Dynamics of Excitons in Semiconductors

Dissertation

zur
Erlangung des Doktorgrades
der Naturwissenschaften
(Dr. rer. nat)

dem Fachbereich Physik
der Philipps-Universität Marburg

vorgelegt von

Markus Stein

aus
Marburg

Marburg, Mai 2019

Vom Fachbereich Physik der Philipps-Universität als Dissertation angenommen
am: 28.06.2019

Erstgutachter: Prof. Dr. Martin Koch
Zweitgutachter: Prof. Dr. Stephan W. Koch

Tag der mündlichen Prüfung: 15.07.2019

Hochschulkennziffer 1180

Zusammenfassung

Diese Dissertation befasst sich mit den spektralen und dynamischen Eigenschaften von Exzitonen und exzitonischen Resonanzen in Halbleitern und Halbleiterheterostrukturen. Ziel ist es, das Wissen über Exzitonen, ihre spektralen Eigenschaften und ihre Dynamik zu erweitern. Grundlage dafür sind die Ergebnisse mehrerer wissenschaftlicher Publikationen auf diesem Fachgebiet, die im Rahmen meiner Doktorarbeit veröffentlicht wurden. Kapitel 1 führt in das Thema ein, indem es die enorme Bedeutung von Halbleitern und halbleiterbasierten Geräten für unsere moderne Gesellschaft hervorhebt. Im Rahmen dessen wird der besondere Einfluss von Exzitonen auf die elektrooptischen Eigenschaften von Halbleitern erörtert und die Relevanz eines tiefgreifenden Verständnisses von Exzitonen, vor allem im Hinblick auf die fortschreitende Miniaturisierung von Halbleiterbauelementen, herausgearbeitet. Kapitel 2 behandelt die physikalischen Grundlagen von Halbleitern und der Wechselwirkung zwischen Licht und Materie, die das theoretische Fundament für die durchgeführten Experimente und deren Analyse bilden. Erläutert werden die verwendeten experimentellen Techniken in Kapitel 3. Ein besonderes Augenmerk richtet sich hier auf die optische Anrege-Terahertz Abfrage Spektroskopie, die in dieser Arbeit hauptsächlich angewendet wird und eine der wichtigsten Techniken zur Untersuchung von Exzitonen und deren Dynamik in Halbleitern darstellt. Die experimentellen Ergebnisse werden anschließend in den Kapiteln 4 bis 7 vorgestellt.

Kapitel 4 demonstriert mittels optischer Anrege-Terahertz Abfrage Spektroskopie, dass nach einer nicht resonanten optischen Anregung zunächst keine Exzitonenpopulation, sondern nur ein Elektron-Loch-Plasma in Germanium Volumenhalbleitern sowie in Germanium und GaInAs Quantenfilmen vorliegt. In allen betrachteten Fällen bilden sich Exzitonen auf einer Zeitskala von mehreren zehn bis hundert Pikosekunden aus einem reinen Elektron-Loch-Plasma. Mehrere Behauptungen und Beobachtungen zu diesem Thema in der Fachliteratur, wonach sich ein großer Anteil an Exzitonen bereits auf einer Sub-Pikosekunden-Zeitskala bilden soll, werden für die hier untersuchten Proben nicht gestützt.[82,188,191] Während in Germanium Volumenhalbleitern sogar eine verzögerte Exzitonenbildung beobachtet wird, beginnt die Ausbildung einer Exzitonenpopulation in GaInAs Quantenfilmen unmittelbar nach einer nicht resonanten optischen Anregung. Dabei können zwei Bildungszeiten bestimmt werden, eine von 14 ps und eine von 344 ps. Des Weiteren werden in diesem Kapitel theoretische Vorhersagen, wonach sich weit unterhalb der Mott-Dichte Exzitonen mit zunehmender Ladungsträgerdichte schneller bilden, bestätigt.

Kapitel 5 konzentriert sich ausschließlich auf die optischen Anrege-Terahertz Abfrage

Experimente am Volumenhalbleiter Germanium. In Abschnitt 5.1 wird eine energetische Aufspaltung der intraexzitonischen $1s-2p$-Resonanz nachgewiesen. Kurz zuvor wurde dieses spektrale Verhalten theoretisch für Germanium vorhergesagt. Demzufolge wird die Aufspaltung der intraexzitonischen Resonanz durch die Anisotropie der effektiven Masse der L-Tal Elektronen herbeigeführt, die zu einer Aufspaltung der Energieniveaus der $2p$-Zustände der Exzitonen führt. Die Ionisierung einer Exzitonenpopulation durch starke THz-Pulse wird in Abschnitt 5.2 betrachtet. Hier konnte nicht nur gezeigt werden, dass die Exzitonenpopulation für Terahertz-Feldstärken von 2,4 kV/cm vollständig ionisiert, sondern es wurden auch die spektralen Eigenschaften des intraexzitonischen Übergangs als Funktion der Feldstärke erfasst. Es stellt sich heraus, dass mit zunehmender Feldstärke des Terahertz-Pulses, also bei zunehmender Ionisierung der Exzitonenpopulation, eine Verbreiterung der intraexzitonischen $1s-2p$-Resonanz erfolgt, die einhergeht mit einer Blauverschiebung von bis zu 10 %. Abschnitt 5.3 erforscht die Streuung von freien Elektronen und Löchern mit einer inkohärenten Population von Exzitonen. Durch die Verwendung von zwei optischen Pulsen wird eine Umgebung geschaffen, in der eine kalte Population von Exzitonen umgeben ist von einem heißen Elektron-Loch-Plasma. Sowohl elastische als auch unelastische Streuprozesse erhöhen die Linienbreite der intraexzitonischen Resonanz, während nur die unelastischen Streuprozesse die Exzitonenpopulation zerstören. Diese einzigartige Methodik erlaubt erstmals die experimentelle Unterscheidung zwischen elastischen und unelastischen Streuprozessen in Halbleitern. Dies liefert eine elastische Streurate von $1,7\cdot10^{-4}$ $\mathrm{cm^3s^{-1}}$ und eine unelastische Streurate von $2,0\cdot10^{-4}\,\mathrm{cm^3s^{-1}}$.

Die kohärente und inkohärente Dynamik von Exzitonen in speziellen Halbleiterheterostrukturen, bei denen die energetisch günstigsten Zustände für Elektronen und Löcher durch eine zwischenliegende Barriere räumlich getrennt sind, wird in Kapitel 6 untersucht. Abschnitt 6.2 demonstriert, dass exzitonische Zustände von räumlich getrennten Elektronen und Löchern eine Resonanz in der linearen Absorption ausbilden können. Dies ermöglicht die resonante Anregung dieser Zustände, so dass die kohärente Lebensdauer solcher exzitonischen Ladungstransferzustände quantifiziert und mit der von regulären exzitonischen Zuständen verglichen werden kann. Die Ergebnisse dieser Untersuchungen mittels Vierwellenmischspektroskopie werden in Abschnitt 6.3 vorgestellt. Neben Quantenschwebungen zwischen den entsprechenden Zuständen der regulären und der Ladungstransfer-Exzitonen ermitteln wir eine Zerfallszeit der kohärenten Polarisation der Ladungstransfer-Exzitonen von 0,4 ps. Dieser Zerfall ist fast dreimal schneller als der Zerfall der kohärenten Polarisation der regulären Exzitonen aus einer Referenzprobe bestehend aus GaInAs Quantenfilmen. Diese kürzere kohärente Lebensdauer der Ladungstransfer-Exzitonen wird auf zusätzliche Streuprozesse an der inneren Grenzfläche zurückgeführt. Die inkohärente Dynamik von Ladungstransfer-Exzitonen wird in Abschnitt 6.4 durch optische Anrege-Terahertz Abfrage Spektroskopie beleuchtet. Intraexzitonische Übergänge offenbaren, dass die Ladungstransfer-Exzitonen eine viel niedrigere $1s-2p$ Übergangsenergie von 3,2 meV haben als die regulären Exzitonen der

Referenzprobe mit 7 meV. Die Ursache dafür ist die reduzierte Coulomb-Wechselwirkung durch die räumliche Trennung der Ladungsträger. Darüber hinaus ermitteln wir eine Rekombinationszeit der Ladungstransfer-Exzitonen von 2,5 ns, die mehr als doppelt so groß ist wie die der regulären Exzitonen der Referenzprobe. Nach optischen Anregungsbedingungen, die energetisch über der Resonanz der Ladungstransfer-Exzitonen liegen, wird zunächst die typische Antwort eines Elektron-Loch-Plasmas beobachtet. In dieser Plasma-ähnlichen Antwort bildet sich eine Schulter auf einer Zeitskala von mehreren hundert Pikosekunden durch die beginnende Bildung einer Population von Ladungstransfer-Exzitonen aus. Innerhalb weniger Nanosekunden entwickelt sich eine Antwort, die nahezu identisch mit der Terahertz-Antwort kurz nach resonanten Anregungsbedingungen ist, was auf eine beinahe reine Population von Ladungstransfer-Exzitonen hindeutet. Der Zerfall der Ladungsträger verschiebt die energetische Position der intraexzitonischen Resonanz auf einer Nanosekundenzeitskala von 2,2 meV bis auf 3,2 meV. Eine solche dichteabhängige Verschiebung der intraexzitonischen Resonanzenergie wird bei regulären Exzitonen in GaInAs Quantenfilmproben nicht beobachtet und ist ein Indikator für einen fermionischeren Charakter von Ladungstransfer-Exzitonen.
Abschließend konzentriert sich Kapitel 7 auf das Verhalten der exzitonischen Absorption in optisch angeregten Halbleiterheterostrukturen. Es zeigt sich, dass die exzitonische Absorption eines Quantenfilms nach der optischen Anregung spektral verschmälert sein kann, was zu einer Erhöhung der Absorptionsspitze führt. Nach der optischen Anregung dauert es mehrere zehn bis hundert Pikosekunden, bis die Linienbreitenverringerung eintritt und unter geeigneten Anregungsbedingungen den Maximalwert der exzitonischen Absorption um mehr als 10 % erhöht. Dieses unerwartete Verhalten der exzitonischen Absorption kann nur in solchen Proben beobachtet werden, die eine räumliche Trennung von Elektronen und Löchern zulassen. Bisher gibt es keine physikalische Erklärung für dieses außergewöhnliche Phänomen.

Author's Contributions

This thesis consists of a comprehensive overview of the most important ideas, experiments and results of my doctoral studies as well as their relevance to the current state of research. The overview is followed by five research publications that are of particular relevance for this thesis and three additional publications.

Relevant Publications in Peer-Review Journals

[I] M. Stein, C. Lammers, P. Springer, P.-H. Richter, S. W. Koch, M. Koch, and M. Kira, „Density-dependent exciton dynamics and L-valley anisotropy in germanium“, Phys. Rev. B 95, 155207 (2017).

[II] M. Stein, C. Lammers, P.-H. Richter, C. Fuchs, W. Stolz, M. Koch, O. Vänskä, M. J. Weseloh, M. Kira, and S. W. Koch, „Dynamics of charge-transfer excitons in type-II semiconductor heterostructures“, Phys. Rev. B 97, 125306 (2018).

[III] M. Stein, C. Lammers, M. J. Drexler, C. Fuchs, W. Stolz, and M. Koch, „Enhanced Absorption by Linewidth Narrowing in Optically Excited Type-II Semiconductor Heterostructures“, Phys. Rev. Lett. 121, 017407 (2018).

[IV] M. Stein, C. Lammers, J. T. Steiner, P.-H. Richter, S. W. Koch, M. Koch, and M. Kira, „Exciton ionization by THz pulses in germanium“, J. Phys. B: At. Mol. Opt. Phys. 51 154001 (2018).

[V] M. Stein, F. Schäfer, and L. Gomell, „Inelastic electron-exciton scattering in bulk germanium“, Phys. Rev. B 99, 144310 (2019).

In Preparation

[VI] P.-H. Richter, M. Stein, C. Lammers, A. Ballabio, D. Chrastina, and M. Koch, „Charge carrier dynamics in Ge quantum wells – comprehensive insights via THz probe spectroscopy“, 2019.

[VII] M. Stein, J. T. Steiner, M. J. Weseloh, M. Kira, and S. W. Koch, „Exciton formation dynamics in GaInAs quantum wells“, 2019.

Additional Publications in Peer-Review Journals

[1] C. Lammers, M. Stein, C. Berger, C. Möller, C. Fuchs, A. Ruiz Perez, A. Rahimi-Iman, J. Hader, J. V. Moloney, W. Stolz, S. W. Koch, and M. Koch, „Gain spectroscopy of a type-II VECSEL chip“, Appl. Phys. Lett. 109, 232107 (2016).

[2] L. Rost, S. Gies, M. Stein, C. Fuchs, S. Nau, P. Kükelhan, K. Volz, W. Stolz, M. Koch, and W. Heimbrodt, „Correlation of optical properties and interface morphology in type-II semiconductor heterostructures“, J. Phys.: Condens. Matter 31 014001 (2018).

[3] N. Pourdavoud, T. Haeger, A. Mayer, P. J. Cegielski, A.-L. Giesecke, R. Heiderhoff, S. Olthof, S. Zaefferer, I. Shutsko, A. Henkel, D. Becker-Koch, M. Stein, M. Cehovski, O. Charfi, H.-H. Johannes, D. Rogalla, M. C. Lemme, M. Koch, Y. Vaynzof, K. Meerholz, W. Kowalsky, H.-C. Scheer, P. Görrn, and T. Riedl, „Room-Temperature Stimulated Emission and Lasing in Recrystallized Cesium Lead Bromide Perovskite Thin Films“, Adv. Mater. 31, 1903717 (2019).

In Preparation

[4] M. Stein, C. Fuchs, W. Stolz, D. M. Mittleman, and M. Koch, „A direct probe of room-temperature quantum tunneling processes in type-II heterostructures using terahertz emission spectroscopy“, submitted to Phys. Rev. Lett. (2019).

[5] W.-R. Hannes, A. Trautmann, M. Stein, F. Schäfer, M. Koch, and T. Meier, „Strongly non-resonant four-wave mixing in semiconductors“, 2019.

Posters and Talks

- M. Stein, C. Fuchs, W. Stolz, and M. Koch, „THz emission from type-II quantum-well heterostructures“, Poster presented by M. Koch at Optical Terahertz Science and Technology Conference (OTST), Santa Fe (2019).

- M. Stein, C. Lammers, P.-H. Richter, C. Fuchs, W. Stolz, M. Koch, O. Vänskä, M. J. Weseloh, M. Kira, and S. W. Koch, „Charge-transfer excitons and their dynamics in semiconductor heterostructures“, Contributed talk by M. Stein at International Conference on Nonlinear Optics and Excitation Kinetics in Semiconductors (NOEKS 14), Berlin (2018).
- M. Stein, C. Lammers, M. Drexler, C. Fuchs, W. Stolz, and M. Koch, „Enhanced excitonic absorption by linewidth narrowing in optically excited type-II semiconductor heterostructures“, Poster presented by M. Stein at International Conference on Nonlinear Optics and Excitation Kinetics in Semiconductors (NOEKS 14), Berlin (2018).
- P.-H. Richter, M. Stein, C. Lammers, C. Fuchs, W. Stolz, M. Koch, O. Vänskä, M. J. Weseloh, M. Kira, and S. W. Koch, „Coherent and incoherent dynamics of charge-transfer excitons“, Keynote talk by P.-H. Richter at 43rd International Conference on Infrared, Millimeter, and Terahertz Waves (IRMMW-THz), Nagoya (2018).
- M. Stein, C. Lammers, P.-H. Richter, P. Springer, S. W. Koch, M. Kira, and M. Koch, „Mass anisotropy in germanium revealed by terahertz spectroscopy“, Poster presented by M. Stein at German THz Conference, Bochum (2017).
- C. Lammers, M. Stein, P.-H. Richter and M. Koch, „Ionization of excitons by strong THz pulses in bulk germanium“, Poster presented by C. Lammers at German THz Conference, Bochum (2017).
- M. Stein, C. Lammers, P.-H. Richter, P. Springer, S. W. Koch, M. Kira, and M. Koch, „Mass anisotropy in germanium revealed by terahertz spectroscopy“, Poster presented by M. Stein at International Conference on Nonlinear Optics and Excitation Kinetics in Semiconductors (NOEKS 13), Dortmund (2016).
- C. Lammers, M. Stein, M. Fey, C. Fuchs, C. Möller, A. Ruiz Perez, C. Berger, A. Rahimi-Iman, J. Hader, J. V. Moloney, S. W. Koch, W. Stolz, and M. Koch, „Time-resolved gain spectroscopy on type-I and type-II VECSEL chips“, Poster presented by C. Lammers at Conference on Lasers and Electro-Optics (CLEO), San Jose (2016).

Original Contributions

The experimental findings presented in this thesis were always preceded by intense discussions with my office partners, primarily C. Lammers and P.-H. Richter, in which we

discussed the experimental results, potential improvements of the experimental setup as well as the possibilities of new experiments and their feasibility. Here, I will present the individual contributions to the respective publications, which are relevant for this thesis.
C. Lammers and myself conceived the experimental measurements for Paper I together. This includes a revision and improvement of the existing optical pump-terahertz probe setup in order to achieve the necessary sensitivity as well as the selection of an appropriate sample. The measurements were carried out by C. Lammers and myself and analyzed together with P.-H. Richter. Afterward, I created a draft of the experimental part of the manuscript, which was first revised by C. Lammers and subsequently by the other experimental co-authors, namely P.-H. Richter and M. Koch. The theoretical contributions to the manuscript are from P. Springer, M. Kira and S. W. Koch. Finally, the entire manuscript was revised by all co-authors.
For Paper II suitable samples had to be designed at first. The design was based on theoretical band structure and terahertz absorption calculations of O. Vänskä and M. J. Weseloh. Together with the requirements of the sample manufacturers C. Fuchs and W. Stolz and the experimental demands on the sample, which were jointly stated by C. Lammers and myself, we finally agreed on a sample which, according to the theoretical predictions, met all requirements. This sample was then fabricated by C. Fuchs. The sample was examined experimentally via optical pump-terahertz probe by C. Lammers, P.-H. Richter and myself, with C. Lammers and myself determining the experimental parameters and evaluating the results together with P.-H. Richter. The four-wave mixing experiments on this sample were suggested by M. Koch and performed and analyzed by C. Lammers and myself. The experimental results were then discussed with M. Koch and the theoreticians and a report of the experimental results was written by C. Lammers and myself. The experimental results were theoretically modeled by O. Vänskä and M. J. Weseloh and graphically illustrated by O. Vänskä. Finally, based on the experimental report and the theoretical modeling, the original version of the manuscript was written by S. W. Koch and edited by all co-authors.
The effect of a linewidth narrowing observed in Paper III was first identified by M. Drexler and myself in experimental data obtained by me via optical pump-optical probe spectroscopy. Subsequently, I was able to work out the observed effect much clearer by conducting optical pump-optical probe measurements under more suitable experimental conditions. The experimental results were discussed in the office together with C. Lammers. This discussions formed the basis for additional experiments to further investigate the physical framework of the observed effect. The original version of the manuscript was written by me and first revised by M. Koch and then by the other co-authors.
The idea for the measurements that formed the experimental basis for Paper IV originated from me. The corresponding measurements were carried out together with C. Lammers and P.-H. Richter and were analyzed by me. Together with C. Lammers I wrote the original version of the manuscript, which formed the basis for the theoretical modeling by J. T. Steiner. The theoretical results were added to the manuscript and it

was revised by all co-authors.
I had the idea for Paper V, conceived the experiments and carried them out with the support of F. Schäfer and L. Gomell. The experimental data were analyzed by F. Schäfer and myself with the support of L. Gomell. Finally, the results were interpreted by me and I wrote the manuscript which was revised by both co-authors.
For the manuscript „Charge carrier dynamics in Ge quantum wells – comprehensive insights via THz probe spectroscopy“, which is currently in preparation, M. Koch acquired the sample that was fabricated by D. Chrastina and A. Ballabio. The experimental investigations were jointly conceived by P.-H. Richter, C. Lammers and myself and carried out by the three of us together for the most part. The experimental data were analyzed by P.-H. Richter, who also has written the original version of the manuscript and executed some of the measurements on his own.
I had the idea for the other manuscript in preparation „Exciton formation dynamics in GaInAs quantum wells“, designed and conducted the experiments and analyzed the data. The experimental results have been modeled theoretically by J. T. Steiner and the manuscript is currently being written together with the co-authors.

Contents

List of Figures

List of Abbreviations

a_B	Bohr radius
AC	alternating current
CB	conduction band
CdSe	cadmium selenide
CdTe	cadmium telluride
CT	charge transfer
CTX	charge-transfer exciton
DC	direct current
DQW	double quantum well
e	elementary charge
E_b	exciton binding energy
eV	electron volt
FWHM	full width at half maximum
FWM	Four-wave mixing
GaAs	gallium arsenide
GaAsSb	gallium arsenide antimonide
GaAsP	gallium arsenide phosphide
GaSb	gallium antimonide
GaSe	gallium selenide
GaP	gallium phosphide
GaInAs	gallium indium arsenide
GaNAs	gallium nitride arsenide
Ge	germanium
hh	heavy-hole
HR-XRD	high-resolution X-ray diffraction

InP	indium phosphide
lh	light-hole
MBE	molecular beam epitaxy
MOVPE	metal organic vapor phase epitaxy
OPA	optical parametric amplifier
OPOP	optical pump-optical probe spectroscopy
OPTP	optical pump-terahertz probe spectroscopy
QW	quantum well
PL	photoluminescence
SBE	Semiconductor Bloch equations
Si	silicon
THz	terahertz
VB	valence band
ZnTe	zinc telluride

1. Introduction

The discovery of semiconductors should prove to be one of, if not the most important discovery for our modern civilization. With the invention of the transistor, the beginning of a technological and digital revolution started, which finally paved the way into today's information age.[127,167] By now, semiconductor-based devices are an essential part of our everyday lives and indispensable for our modern society. However, despite the enormous importance of semiconductors today, their beginnings were rather hesitant. First discoveries of semiconducting properties such as increasing electrical conductivity with increasing temperature[40,69] and photoconductivity[1,51,176] go way back to the 19th century. In 1874, Karl Ferdinand Braun discovered rectification in contacts between metals and various sulfides.[14] The resulting rectifiers should be the first semiconductor devices. However, those discoveries in the 19th century saw little practical use. Moreover, the observed effects were not understood, unreliable, and it was doubtful whether semiconductors existed at all.[145] On the one hand, this was because materials which later turned out to be semiconductors were not yet available in the necessary purity and, on the other hand, because there was no theoretical conception of semiconductors. This changed rapidly when Alan Wilson's band theory of solids was able to explain the difference between metals, semiconductors and insulators.[209,210] Suddenly, many of the observed effects could be explained with his theory. Beyond that, the enormous influence of impurities on the conductivity of semiconductors became apparent. The improved knowledge and the availability of high-quality semiconductor materials finally led to the development of the first transistor in 1947.[9] This was the trigger for explosive progress in semiconductor technology. Within a short time, transistors based on semiconductor materials replaced vacuum tubes as signal amplifiers almost entirely and were widely used in radios, televisions and telephones. Not only did semiconductors increase the performance of those devices, but they also reduced their energy consumption, size and cost.[7,207] These advancements enabled the development of the personal computer and modern wireless communication systems and made them affordable for a large population. Furthermore, it allowed for the development of new technologies. These include the internet, solar cells, light-emitting diodes and intelligent driver assistance systems in cars, to name but a few. The foundation for this development has been and will be the intense research on semiconductor materials providing detailed knowledge of their properties, their functionality and their potential.[77,155] In addition to the exploration of novel material systems with unprecedented characteristics, the progressive miniaturization of semiconductor-based devices confronts scientists with ever new challenges.[58,115,121,132,140] A growing research interest consists in controlling charge carriers on extremely short time and length scales.[28,103,150,164] Here the physical limits are approached increasingly. For example, scientists are already investigating films of a single atomic layer and generating single-cycle light pulses.[6,8,151,160] Not far from these frontiers, far-developed epitaxial techniques such as molecular beam epitaxy and metal organic chemical vapor phase epitaxy already enable the precise production of semiconductor layers in the nanometer and sub-nanometer range on an industrial scale.[15,68,123] Besides, sophisticated imaging techniques such as transmission electron microscopy make it possible to control the manufacturing process up to atomic resolution.[59,200] Femtosec-

ond laser systems offer the possibility to spectroscopically investigate and control the charge carrier dynamics in such advanced semiconductor structures on ultrashort time scales.
In this thesis, spectroscopic methods are driven by a femtosecond laser system to gain new insights into charge carrier dynamics in semiconductors and their heterostructures. Here, the emphasis is on the dynamics of Coulomb bound states of electrons and holes, so-called excitons. In modern low-dimensional semiconductor structures bound states of electrons and holes are of particular relevance. Especially the spatial limitation to smallest length scales increases the Coulomb interaction between electrons and holes and thus the exciton binding energy. This affects the formation dynamics and the stability of these quasiparticles. Since excitons are neutral in charge and therefore insulating, their presence has a significant impact on the electrical properties of semiconductors. In many applications, such as solar cells, that demand a separation of electrons and holes, excitons can be a problem for their performance properties.[24,109] Therefore, the formation and decay dynamics of excitons are of great importance. Since the binding energy of excitons is in the terahertz frequency range in a lot of semiconductors, terahertz spectroscopy is the perfect method to study these quasiparticles via their internal transitions.[99]
Chapter 2 introduces the physical fundamentals of semiconductors and the light-matter interaction, both of which are essential for a comprehensive understanding of excitons and the experimental techniques to explore their dynamics. The spectroscopic techniques, including the aforementioned terahertz spectroscopy, that are used in this thesis to study excitons are discussed in detail in Chapter 3. Beyond that, it is described how physical relevant quantities like absorption or the change of the dielectric function are extracted from the measured data. In the subsequent chapters, the research results of my doctoral studies are presented. Chapter 4 focuses on the formation dynamics of excitons after non-resonant excitation of an unbound electron-hole plasma in semiconductors and semiconductor heterostructures. Chapter 5 starts with an analysis of the spectral properties of intraexcitonic transitions in section 5.1. Afterward, sections 5.2 and 5.3 focus on the possibilities of manipulating an exciton population. While section 5.2 explores the manipulation of an exciton population by strong terahertz fields, section 5.3 studies the consequences of scattering processes of excitons with free charge carriers injected by a femtosecond light pulse. In both cases, the exciton population is destroyed and thus the transition to a conductive phase is achieved. Chapter 6 examines the physics of electrons and holes at an internal interface that allows only one of the two charge carriers to tunnel through. This leads to the possibility that electron and hole are spatially separated in different semiconductor layers. The time scale on which such a spatial separation of charge carriers takes place and how the separation affects the properties of the Coulomb bound quasiparticle, i.e., a charge-transfer exciton, is of particular interest in view of the progressive miniaturization that favors such charge carrier configurations. Additionally, the properties of the internal interfaces are becoming increasingly important. In this regard, the physics of a spatially separated electron-hole pair may offer valuable information about the impact of the morphology of internal interfaces on charge carrier dynamics. Another feature of excitonic states is their particularly strong coupling to the light field and thus their significant influence on the optical properties of semiconductors. The coupling of excitonic states to the light field is investigated in Chapter 7. Here, the coupling after a preceding optical excitation is addressed explicitly in such semiconductor heterostructures the band structure of which allows for spatial separation of the charge carriers.

2. Theoretical background

This chapter is intended to provide a brief introduction to the physical principles that not only form the basis for the experiments carried out but also contribute significantly to the interpretation and the understanding of the experimental results. For this purpose, the basic properties of semiconductors and their heterostructures are discussed first, before the main principles of light-matter interaction are addressed. The starting point for the light-matter interaction are the Semiconductor Bloch equations (SBE) from which the existence of bound states between electrons and holes, i.e., excitons, can be derived. Beyond that, the SBE form the basis to describe the response of a semiconductor in the optical as well as in the terahertz regime.

2.1. Semiconductors

Semiconductors are solids with an electrical conductivity between that of a conductor and an insulator.[168] They feature a band gap between valence and conduction band which typically lies between a few hundred millielectron volts (meV) and about 3 electron volts (eV).[213] This implies that they can be excited by optical or near-infrared laser pulses that raise electrons from the valence into the conduction band.[133] The optical excitation of a semiconductor is the starting point of most experimental investigations carried out for this thesis.
A distinction is made between direct and indirect band gap semiconductors. For direct band gap semiconductors, the maximum energy of the valence band and the minimum energy of the conduction band are at the same wave vector $\vec{k}$. A prominent example for a direct semiconductor is gallium arsenide (GaAs). In indirect band gap semiconductors, the maximum energy of the valence band and the minimum energy of the conduction band are at different wave vectors $\vec{k}$. Prominent examples of indirect semiconductors are silicon (Si) and germanium (Ge). The latter of which is studied intensively in this thesis.

2.1.1. Semiconductor heterostructures

A semiconductor heterostructure is a monocrystalline sequence of semiconductor layers of different compositions and thicknesses. The development of modern epitaxial methods such as molecular beam epitaxy (MBE)[27,68] or metal organic vapor phase epitaxy (MOVPE)[189] enable the production of semiconductor layers with an accuracy of less than one nanometer.[19,178] This also allows the production of low-dimensional systems such as quantum wells (QWs), quantum wires or quantum dots. Here, a two-dimensional layer, a one-dimensional strip, or a zero-dimensional dot of a specific semiconductor is embedded in another semiconductor or semiconductor compound. For such structures with a size in the nanometer range, the quantum nature of particles is becoming increasingly important and influences the electrical and optical properties.[105,136] Particularly worth mentioning here is the so-called „quantum confinement“. Due to the potential of the surrounding semiconductor, charge carriers are spatially confined, e.g., in QWs. This spatial restriction requires the consideration of the wave nature of the charge carriers,

which is obtained by the time-independent Schrödinger equation:[13,128,163]

$$\left[\frac{-\hbar^2}{2\mu}\nabla^2 + V(\vec{r})\right]\psi(\vec{r}) = E\psi(\vec{r}), \tag{2.1}$$

where $\hbar$ is the reduced Planck constant, μ the particle's reduced mass, ∇^2 the Laplacian, V the potential energy, ψ the particle's wave function, E the total energy of the particle and $\vec{r}$ the position. Solutions of this equation are standing waves of quantized energies. In one dimension and with infinitely high potential barriers one yields:

$$E_n = \frac{\hbar^2}{2\mu}\left[\frac{n\pi}{L}\right]^2 \text{ with } n = 1,2,3,... \text{ and } \psi_n = A\ sin\left(\frac{n\pi x}{L}\right). \tag{2.2}$$

Here, L is the length of the box and x is the position. Obviously, the ground state (n=1) of the energy levels is energetically above the bottom of the potential well. This increases the energy of particles in systems of reduced dimensionality, which becomes increasingly important when the spatial confinement gets smaller than the exciton Bohr radius.[195] Furthermore, these energies are connected with states the spatial expansion of which is linked to the potential well. This also leads to a discretization of the density of states.[168] In zero-dimensional systems, there are only discrete states. In one-dimensional systems, the density of states changes with $1/\sqrt{E}$ while it is a step function $[\propto \theta(E)]$ in two dimensions. In three-dimensional systems, though, the density of states has a root-shaped curve $(\propto \sqrt{E})$.
The possibility of precisely depositing different semiconductor layers on top of each other paves the way to tailor the properties of such low-dimensional systems. From the perspective of basic research, those systems are therefore ideal model systems to investigate how

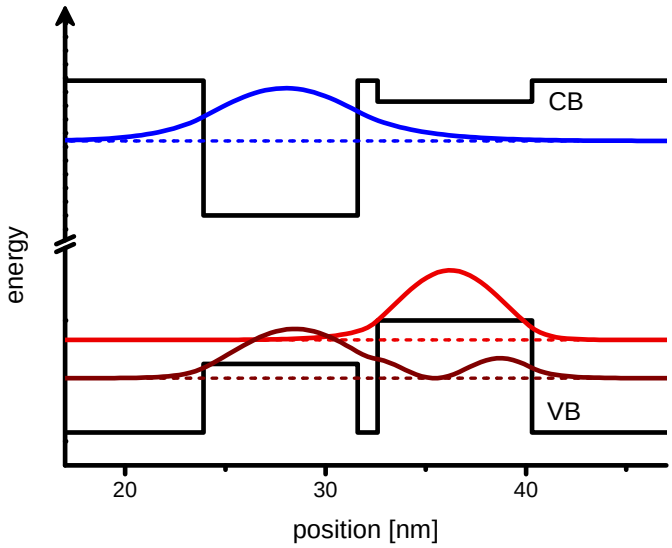

Figure 2.1.: Schematic band structure of a semiconductor heterostructure with a type-II band alignment. The heterostructure consists of two QWs that are separated by a thin barrier between them. The energy levels (dashed lines) are such that the lowest level in the conduction band (CB) and its corresponding wave function (blue line) are predominantly located in one QW while the energetically most favorable state for holes in the valence band (VB) and its wave function (red line) is located in the other.

the electrical and optical properties are altered by the symmetry break. A particularly important structure within the scope of this work is a so-called type-II QW structure. Such type-II semiconductor heterostructures contain two adjacent but different QWs that often include an intermediate barrier between them. The energy levels in the conduction and valence band are designed so that the energetically most favorable state for electrons and holes is in the respective other QW. Figure 2.1 shows an exemplary band structure of such a type-II structure. These structures enable the investigation of charge carrier transfer and recombination across an internal interface as well as the study of bound states of spatially separated electrons and holes, i.e., charge-transfer excitons (CTXs).

2.2. Light-matter interaction in semiconductors

Light-matter interaction forms the basis of all spectroscopic investigations. For this reason, the fundamentals of light-matter interaction are outlined in this section. For a more comprehensive and detailed description of this thematic field, please refer to further literature.[65,92,125,157,192]

2.2.1. Semiconductor Bloch equations

The theoretical description of the interaction between light and matter in semiconductors is based on the semiconductor Bloch equations. They describe the coupling of the electromagnetic field to the electronic system of the semiconductor via a set of coupled nonlinear differential equations.[65,116]
Starting point in the two-band approximation is the Hamiltonian

$$H = H_{el} + H_I, \tag{2.3}$$

where

$$\begin{aligned} H_{el} = &\sum_{\vec{k}} \left(\epsilon_{c,\vec{k}} a^\dagger_{c,\vec{k}} a_{c,\vec{k}} + \epsilon_{v,\vec{k}} a^\dagger_{v,\vec{k}} a_{v,\vec{k}}\right) \\ &+ \frac{1}{2} \sum_{\vec{k},\vec{k}',\vec{q}\neq 0} V_{\vec{q}} \left(a^\dagger_{c,\vec{k}+\vec{q}} a^\dagger_{c,\vec{k}'-\vec{q}} a_{c,\vec{k}'} a_{c,\vec{k}} + a^\dagger_{v,\vec{k}+\vec{q}} a^\dagger_{v,\vec{k}'-\vec{q}} a_{v,\vec{k}'} a_{v,\vec{k}}\right. \\ &\left. + 2 a^\dagger_{c,\vec{k}+\vec{q}} a^\dagger_{v,\vec{k}'-\vec{q}} a_{v,\vec{k}'} a_{c,\vec{k}}\right) \end{aligned} \tag{2.4}$$

describes the electron part of the system via their kinetic and potential energies for the conduction band c and the valence band v. Here, $a^\dagger$ and a are the creation and annihilation operators of the quantum mechanical states, $\epsilon_{c/v,\vec{k}}$ are the single particle energies of an electron with momentum $\vec{k}$ in the respective band and $V_{\vec{q}}$ is the Coulomb matrix element, which is the Fourier transformation of the Coulomb potential in real space. For simplicity's sake, phonon interactions as well as those Coulomb interaction processes that do not conserve the number of particles in each band are not included here.
The Hamiltonian

$$H_I = -\sum_{\vec{k}} E(t) \left(a^\dagger_{c,\vec{k}} a_{v,\vec{k}} d_{cv} + h.c.\right) \tag{2.5}$$

describes the interaction of the semiconductor with the classical electric field $E(t)$ via a dipole transition from the valence to the conduction band with the dipole-transition matrix element d_{cv}. The abbreviation $h.c.$ represents the Hermitian conjugate part. With the full Hamiltonian, it is possible to compute the many-particle dynamics of the system's

relevant microscopic quantities. Those are the microscopic interband polarization $P_{\vec{k}}(t)$ and carrier distributions, i.e., $n_{e,\vec{k}}(t)$ for electrons in the conduction band and $n_{h,\vec{k}}(t)$ for holes in the valence band. They are obtained via their quantum mechanical expectation values as follows:

$$\begin{aligned} n_{e,\vec{k}}(t) &= \langle a^{\dagger}_{c,\vec{k}} a_{c,\vec{k}} \rangle \\ n_{h,\vec{k}}(t) &= 1 - \langle a^{\dagger}_{v,\vec{k}} a_{v,\vec{k}} \rangle \\ P_{\vec{k}}(t) &= \langle a^{\dagger}_{v,\vec{k}} a_{c,\vec{k}} \rangle. \end{aligned} \tag{2.6}$$

The temporal dynamics of the polarization and the charge carrier distribution can be obtained by the Heisenberg equation of motion.[65,92] Separating the equations of motion in products of carrier densities, interband polarizations and an unfactorized rest eventually leads to the SBE:[65]

$$\frac{\partial P_{\vec{k}}}{\partial t} = -i(e_{e,\vec{k}} + e_{h,\vec{k}})P_{\vec{k}} + i(1 - n_{e,\vec{k}} - n_{h,\vec{k}})\omega_{R,\vec{k}} + \frac{\partial P_{\vec{k}}}{\partial t}\,|_{scatt} \tag{2.7}$$

$$\begin{aligned} \frac{\partial n_{e,\vec{k}}}{\partial t} &= -2\,\mathrm{Im}(\omega_{R,\vec{k}} P^{*}_{\vec{k}}) + \frac{\partial n_{e,\vec{k}}}{\partial t}\,|_{scatt} \\ \frac{\partial n_{h,\vec{k}}}{\partial t} &= -2\,\mathrm{Im}(\omega_{R,\vec{k}} P^{*}_{\vec{k}}) + \frac{\partial n_{h,\vec{k}}}{\partial t}\,|_{scatt}\,. \end{aligned} \tag{2.8}$$

Here, $\hbar e_{e,\vec{k}}$ and $\hbar e_{h,\vec{k}}$ are the renormalized single-particle energies and $\omega_{R,\vec{k}}$ is the generalized Rabi frequency

$$\omega_{R,\vec{k}} = \frac{1}{\hbar}\left(d_{cv}E(t) + \sum_{\vec{q}\neq\vec{k}} V_{|\vec{k}-\vec{q}|} P_{\vec{q}} \right), \tag{2.9}$$

that couples the polarization and density equations to the applied field $E(t)$. In particular, the term $-2\,\mathrm{Im}(\omega_{R,\vec{k}} P^{*}_{\vec{k}})$ describes the generation of electrons and holes by the absorption of light while the term $1 - n_{e,\vec{k}} - n_{h,\vec{k}}$ describes the phase-space filling factor. The last terms of the summation in the respective equations in 2.7 and 2.8 are the scattering terms which summarize the unfactorized rest. The scattering terms are responsible for the redistribution processes of electrons in their respective bands as well as in between different bands.
The SBE are the starting point for a microscopic description of linear and nonlinear spectroscopy like four-wave mixing (FWM) or time resolved pump-probe experiments. However, the calculation of the SBE is very complex and especially the scattering terms require further approximations that need to be adapted to the specific problem. A detailed description of some common and useful approximations for the scattering terms can be found in Refs. 65, 91, 157.

2.2.2. Excitons

Assuming a quasi-equilibrium, i.e., the assumption that the scattering processes have already driven the carrier distribution into its thermal Fermi-Dirac distribution, the equations 2.7 and 2.8 simplify to homogeneous equations. Equation 2.7 can now be solved by the eigenvalue problem:

$$(e_{e,\vec{k}} + e_{h,\vec{k}})\phi^{R}_{\lambda}(\vec{k}) - (1 - n_{e,\vec{k}} - n_{h,\vec{k}}) \sum_{\vec{q}\neq\vec{k}} V_{|\vec{k}-\vec{q}|}\phi^{R}_{\lambda}(\vec{q}) = E_{\lambda}\phi^{R}_{\lambda}(\vec{k}). \tag{2.10}$$

Here, $\phi_\lambda^R(\vec{k})$ are the right-handed eigenstates that are related to the eigenvalue E_λ. When no charge carriers are present, i.e., when the semiconductor is unexcited and $n_{e,\vec{k}}$ and $n_{h,\vec{k}}$ are zero, this is the same problem as for atomic hydrogen. A Fourier transformation then yields the Wannier equation in real space:[65]

$$-\left[\frac{\hbar^2\nabla_{\vec{r}}^2}{2m_r}+V(\vec{r})\right]\phi_\lambda^R(\vec{r})=E_\lambda\phi_\lambda^R(\vec{r}), \tag{2.11}$$

with the inverse reduced mass $\frac{1}{m_r}=\frac{1}{m_e}+\frac{1}{m_h}$, which consists of the effective mass of the electron in the conduction band (m_e) and the hole in the valence band (m_h). Solving the Wannier equation in analogy to the problem of the hydrogen atom yields solutions which are bound states of electrons and holes that are attracted to each other by the Coulomb interaction. These bound states are quasiparticles and are known as Wannier excitons. Their binding energies are

$$\begin{aligned} E_n &= E_0\frac{1}{n^2} \text{ in 3D and} \\ E_n &= E_0\frac{1}{(n-1/2)^2} \text{ in 2D, with } n=1,2,\dots\ . \end{aligned} \tag{2.12}$$

Here, $E_0=\frac{m_r e^4}{8h^2\epsilon^2}$ and is the exciton Rydberg energy. Since ϵ is the permittivity of the medium, which in many semiconductors is about a factor of 10 larger than in vacuum, and m_r is the reduced effective mass, the binding energy of many excitons is roughly an order of 1000 lower than that of the hydrogen atom. Therefore, exciton binding energies of many semiconductors are between 1 meV and 20 meV so that their intraexcitonic transitions are accessible via terahertz (THz) radiation.[99] Note that in an ideal two-dimensional case, the binding energy would be a factor of 4 greater than in the three-dimensional case.
In an excited semiconductor the phase-space filling factor $1-n_{e,\vec{k}}-n_{h,\vec{k}}$ in Eq. 2.10 reduces the effective Coulomb interaction and eventually changes its sign for large densities. Thus the effective Coulomb interaction becomes repulsive due to the Fermionic Pauli-blocking effects and consequently prevents the existence of bound excitons.[91] This carrier density-dependent transition from bound excitons to an unbound electron-hole plasma is called Mott transition.[66,94,134]

2.2.3. Optical response

In the linear regime, the optical response of a semiconductor is mainly driven by its linear susceptibility $\chi(\omega)$ which is defined as the constant of proportionality that relates the electric field of the light pulse $E(\omega)$ to the induced macroscopic polarization $P(\omega)$[118]

$$P(\omega)=\epsilon_0\chi(\omega)E(\omega). \tag{2.13}$$

Solving Eq. 2.7 for an unexcited semiconductor in a set of eigenstates $\phi_\lambda^R(\vec{k})$ and replacing the microscopic scattering term by a phenomenological value $i\gamma p_\lambda$ yields the famous Elliott formula for the linear susceptibility:[38]

$$\chi(\omega)=\frac{|d_{cv}|^2}{\epsilon_0}\sum_\lambda\frac{|\phi_\lambda^R(\vec{r}=0)|^2}{E_\lambda-\hbar\omega-i\gamma}. \tag{2.14}$$

Under some few well-founded assumptions, the actual absorption is proportional to the

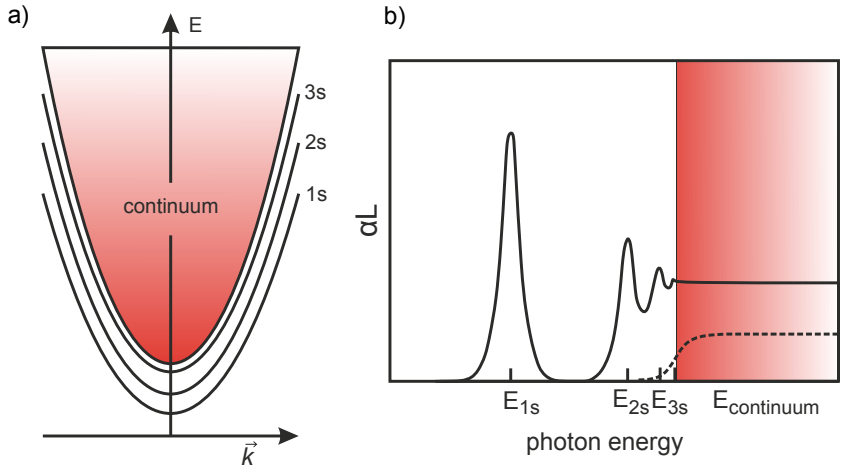

Figure 2.2.: a) Schematic representation of the parabolic dispersion relation of the optically active s-like exciton states. Since the wave vector of photons is negligibly small, only states close to $\vec{k} = 0$ can be excited. b) The corresponding absorption (solid line) of a semiconductor QW. Here, the 1s, 2s and 3s exciton states are visible as individual absorption peaks before the continuum sets in for higher energies. The dashed line shows the absorption without Coulomb interaction. Not only are exciton states below the band edge missing here, but also the absorption above the band edge is reduced. Similar illustrations can be found, among others, in Ref. 125 and Ref. 108.

imaginary part of the linear susceptibility.[65,91] Hence, the absorption of a semiconductor shows resonances when the photon energy $\hbar\omega$ matches the excitonic energies E_λ. The oscillator strength of those resonances is determined by the probability to find the conduction-band electron and the valence-band hole at $\vec{r} = 0$, i.e., within the same lattice unit cell. Since only s-like states are non-zero at $\vec{r} = 0$, the optical excitation contains only these states.[91] The phenomenological variable γ introduces the homogeneous broadening of the resonances that is caused by the complex scattering terms. However, many real semiconductor compounds, especially at low temperatures, are dominated by an inhomogeneous broadening due to local changes of their composition, a non-homogeneous permittivity or, in QW systems, changes in the width of the QW.[197] Figure 2.2 b) shows the absorption close to the band edge of a 2D semiconductor. As can be seen, the Coulomb interaction not only causes absorption below the band edge via bound states but also increases the absorption for photon energies above the band gap via a Coulomb enhancement factor.[65]

Here, interactions with phonons are not included. This is a reasonable estimation for optical transitions close to the band edge of a direct-gap semiconductor since two-quantum processes that include a phonon have a massively reduced transition probability.[65] Nonetheless, such two-quantum processes allow for the excitation of an indirect semiconductor energetically below its direct band gap. Then, in addition to the energy, the appropriate wave vector $\vec{k}$, which is provided by a phonon, must be available as well. The reduced absorption of indirect semiconductors below their direct band gap[213] increases the penetration depth of an optical pulse from the nano- to micrometer regime, which is a typical penetration depth in direct semiconductors, up to the millimeter regime.[159] Thus, a homogeneous excitation profile of a comparatively thick layer is possible in indirect semiconductors.[32] This increase in the depth of interaction enables the high-resolution THz spectroscopy on Ge which is discussed in detail in Chapter 5.

In an excited semiconductor, phase-space filling and Coulomb screening reduce the absorption whereas excitation-induced dephasing broadens the resonances.[79,162,172] The excitation-induced change of the linear absorption of a semiconductor can be investigated via optical pump-optical probe (OPOP) spectroscopy.

2.2.4. Response in the terahertz regime

In contrast to optical excitation, the energy of a photon in the THz regime is not sufficient to overcome the band gap of a semiconductor. However, THz radiation can interact with free charge carriers and bound electron-hole pairs that are already present in the semiconductor, e.g., via a preceding optical pulse. A semiconductor couples to a classical linear polarized electromagnetic field via[91]

$$\left[\frac{\partial^2}{\partial z^2} - \frac{n_{\mathrm{BG}}^2}{c_0^2}\frac{\partial^2}{\partial t^2}\right]\langle A\rangle = -\mu_0 J_{\mathrm{tot}}. \tag{2.15}$$

Here, n_{BG} is the background refractive index, c_0 and μ_0 are the speed of light and the permeability in vacuum, and $\langle A\rangle \equiv \langle A(z,t)\rangle \vec{e}_A$ is the vector potential of the electromagnetic field. In Eq. 2.15 a propagating THz field generates a current J in the semiconductor which couples back to the THz field via Maxwell's wave equation. The total current J_{tot} is given by[187]

$$J_{\mathrm{tot}} = J_{THz} + J_A \equiv \frac{1}{S}\sum_{\vec{k}}\left(j_e(\vec{k})n_{e,\vec{k}} + j_h(\vec{k})n_{h,\vec{k}}\right) - \frac{1}{S}\sum_{\vec{k}}\left(\frac{e^2}{m_e}n_{e,\vec{k}} + \frac{e^2}{m_h}(1-n_{h,\vec{k}})\right)\langle A\rangle, \tag{2.16}$$

with the quantization area S and the current-matrix elements

$$j_e(\vec{k}) \equiv -\frac{|e|\hbar\vec{k}}{m_e}\vec{e}_A \text{ and } j_h(\vec{k}) \equiv \frac{|e|\hbar\vec{k}}{m_h}\vec{e}_A. \tag{2.17}$$

Here, $\vec{e}_A$ is the polarization direction of the THz field and e the elementary charge. The total current J_{tot} is composed of the ponderomotive current J_A and the THz current J_{THz} which couples to the exciton correlations[87,90]

$$c_x^{\vec{q},\vec{k}',\vec{k}} \equiv \triangle\left\langle a^\dagger_{c,\vec{k}}a^\dagger_{v,\vec{k}'}a_{c,\vec{k}+\vec{q}}a_{v,\vec{k}'-\vec{q}}\right\rangle = \left\langle a^\dagger_{c,\vec{k}}a^\dagger_{v,\vec{k}'}a_{c,\vec{k}+\vec{q}}a_{v,\vec{k}'-\vec{q}}\right\rangle - \left\langle a^\dagger_{c,\vec{k}}a^\dagger_{v,\vec{k}'}a_{c,\vec{k}+\vec{q}}a_{v,\vec{k}'-\vec{q}}\right\rangle_{single}.$$

Since the solutions of Eq. 2.10 form a complete exciton-basis, the exciton correlations can be expanded:[91,187]

$$\begin{aligned}\Delta N_{\lambda,\lambda'}(\vec{q}) &= \sum_{\vec{k},\vec{k}'}\phi^L_\lambda(\vec{k})\phi^L_{\lambda'}(\vec{k}')c_x^{\vec{q},\vec{k}'-\vec{q}_h,\vec{k}+\vec{q}_e},\\ c_x^{\vec{q},\vec{k}'-\vec{q}_h,\vec{k}+\vec{q}_e} &= \sum_{\lambda,\lambda'}\phi^R_\lambda(\vec{k})\phi^R_{\lambda'}(\vec{k}')\Delta N_{\lambda,\lambda'}(\vec{q}).\end{aligned} \tag{2.18}$$

Here, $\phi^L_\lambda(\vec{k})$ are the left handed solutions,

$$\vec{q}_e \equiv \frac{m_e}{m_e - m_h}\vec{q} \quad \text{and} \quad \vec{q}_h \equiv -\frac{m_h}{m_e - m_h}\vec{q}.$$

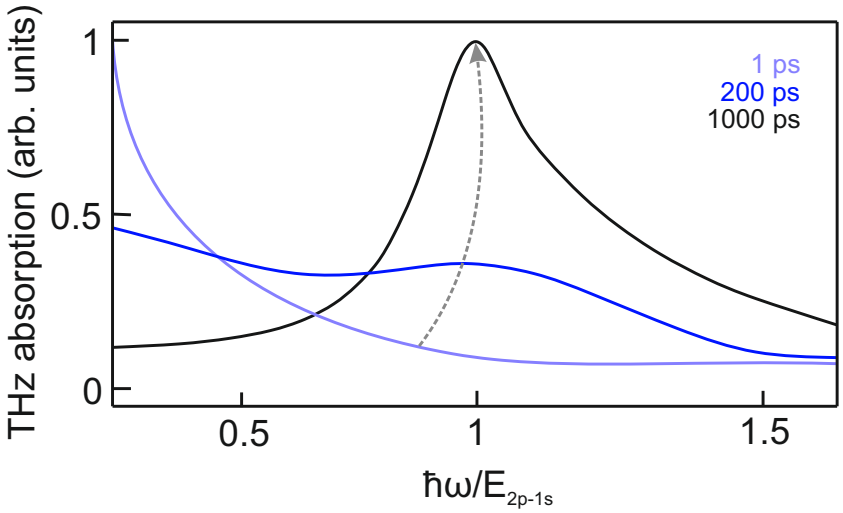

Figure 2.3.: Calculated THz absorption for different time delays after non-resonant excitation conditions. In the first picoseconds (light blue line) the THz response is dominated by the absorption of a correlated electron-hole plasma, which shows no resonance and decreases with increasing energy. On a time scale of several hundred picoseconds, an incoherent exciton population builds up that coexists with the electron-hole plasma (blue line). Finally, almost all electrons and holes are bound into $1s$ excitons, which is reflected in the THz absorption by a pronounced resonance at the energy of the $1s$ to $2p$ transition (black line). In this state the semiconductor is non-conductive and the absorption drops close to zero for energies below the resonance. The illustration is based on calculations in Ref 87.

By using a time derivation of Eq. 2.16, substituting the carrier dynamics of Eq. 2.8[1] and using the exciton-basis expansion of the correlations, the total current J_{tot} is connected to the correlation densities $\Delta n_{\lambda,\lambda'} \equiv \frac{1}{S}\sum_{\vec{q}} \Delta N_{\lambda,\lambda'}(\vec{q})$. With some further transformations,[91] one obtains $J_{tot}(\omega)$ which can be substituted into the susceptibility for the THz regime

$$\chi_{THz}(\omega) = \frac{J_{tot}(\omega)}{\epsilon_0 \omega^2 \langle A(\omega) \rangle}. \tag{2.19}$$

This finally yields[91,183]

$$\begin{aligned}\chi_{THz}(\omega) = \frac{1}{\epsilon_0 \omega^2 S}\frac{1}{\hbar\omega + i\gamma}\sum_{\lambda,\lambda',\vec{q}}\Big[S_{\lambda,\lambda'}(\vec{q},\omega)\Delta N_{\lambda,\lambda'}(\vec{q}) - \left(S_{\lambda,\lambda'}(\vec{q},-\omega)\Delta N_{\lambda,\lambda'}(\vec{q})\right)^*\Big] \\ -\frac{e^2}{\epsilon_0 \omega^2 S}\sum_{\vec{k}}\Big(\frac{n_{e,\vec{k}}}{m_e(\vec{k})} + \frac{n_{h,\vec{k}}}{m_h(\vec{k})}\Big),\end{aligned} \tag{2.20}$$

with the response function

$$S_{\lambda,\lambda'}(\vec{q},\omega) = \sum_{\beta}\frac{(E_{\beta,\vec{q}} - E_{\lambda,\vec{q}})J_{\lambda',\beta}J_{\beta,\lambda}}{E_{\beta,\vec{q}} - E_{\lambda,\vec{q}} - \hbar\omega - i\gamma}. \tag{2.21}$$

It turns out that the response function features discrete resonances that are determined

[1] in a form that includes the two-particle correlations

by the energy separation of different exciton states ($E_{\beta,\vec{q}} - E_{\lambda,\vec{q}}$), i.e., intraexcitonic transitions. The selection rules of those transitions are provided by the product of the current-matrix elements $J_{\lambda',\beta} J_{\beta,\lambda}$. In principle, only those intraexcitonic transitions are allowed in which the angular momentum changes by $\pm\hbar$. Allowed are, e.g., transitions from the $1s$ exciton state to $2p$ or higher p-states. The contributions to the THz susceptibility χ_{THz} are given by the product of the response function with the electron-hole correlations $\Delta N_{\lambda,\lambda'}$. Here, the diagonal correlations $\Delta N_{\lambda,\lambda}$ correspond to bound excitons in the state λ while the non-diagonal elements characterize a correlated electron-hole plasma. The THz susceptibility is connected with the THz absorption $\alpha(\omega)$ via:

$$\alpha(\omega) = \frac{\omega}{c_0 n_{BG}} \mathrm{Im}[\chi_{THz}(\omega)]. \tag{2.22}$$

Figure 2.3 depicts the THz absorption for the transition from a correlated electron-hole plasma (light blue line) into a population of $1s$ excitons (black line).
In contrast to optical spectroscopy methods like OPOP, in which any population of charge carriers affects the response of excitonic states,[22,53,89,99] e.g., via Coulomb screening, optical pump-THz probe (OPTP) spectroscopy detects intraexcitonic transitions only when an exciton population (or polarization) actually exists.[91,187] This characteristic makes THz spectroscopy a very valuable tool to unambiguously prove the existence of exciton populations and to study their formation and decay dynamics.[91,99]

3. Experimental techniques

In the context of this work, different spectroscopic techniques are used to characterize the dynamics of excitons in semiconductors and their heterostructures. In particular, the coherent and incoherent dynamics of excitons and excitonic states are investigated by methods of optical as well as THz spectroscopy. How the different experimental setups are built, how the data are acquired and how they are evaluated is explained in this chapter.

3.1. Optical pump-optical probe spectroscopy

3.1.1. Setup

In optical pump-optical probe spectroscopy, a first laser pulse - the pump - excites the sample before a time-delayed second, significantly weaker laser pulse - the probe - monitors the transmission of the sample.[172] Usually, different time delays between pump and probe can be set by using a mechanical delay line. Most often the change of transmission (or absorption) due to the optical excitation pulse is of interest, which is achieved by comparing the transmission with and without optical excitation. Using a broadband supercontinuum as a probing pulse allows for the analysis of a large spectral range.
In the laboratory this is realized as follows:
A regenerative amplifier system[1] generates approximately 35 fs short laser pulses at a repetition rate of 1 kHz and a central wavelength of 800 nm. A part of the output runs an optical parametric amplifier[2] (OPA). The OPA is able to adjust the central wavelength of the emitted laser pulses in a range from 475 nm to 2600 nm via optical parametric amplification. The output of the OPA is used as the pump pulse, which allows to set the desired excitation conditions for the experiment. The other part of the amplifier output runs over a motorized delay line and an active beam stabilization[3] before a broadband supercontinuum is generated via self-phase modulation in a sapphire crystal.[2,214] After strong attenuation by optical filters, the supercontinuum is focused onto the sample where it spatially overlaps with the optical pump pulse and probes the sample. In order to probe a homogeneous excitation density, the spot size of the excitation pulse is considerably larger than the spot size of the probe pulse. Afterward, the transmitted probe pulse is analyzed by a grating spectrometer with a gallium indium arsenide (GaInAs) detector line that is cooled with liquid nitrogen. The GaInAs photodiodes can detect light in a range from 900 to 1600 nm with high sensitivity. The resolution of the spectrometer is adjustable from 1 nm to approximately 0.1 nm by using different gratings. Usually, pump and probe pulses are polarized cross-linear to each other so that scattered light from the pump pulse can be blocked by a polarization filter in front of the spectrometer. In addition, there is a mechanical shutter in both the pump and the probe beam path so that both paths can be opened and closed separately. A schematic representation of the setup is shown in Fig. 3.1.

[1] Spectra-Physics Spitfire® Ace™
[2] Spectra-Physics TOPAS Prime
[3] TEM-Messtechnik BeamLock®

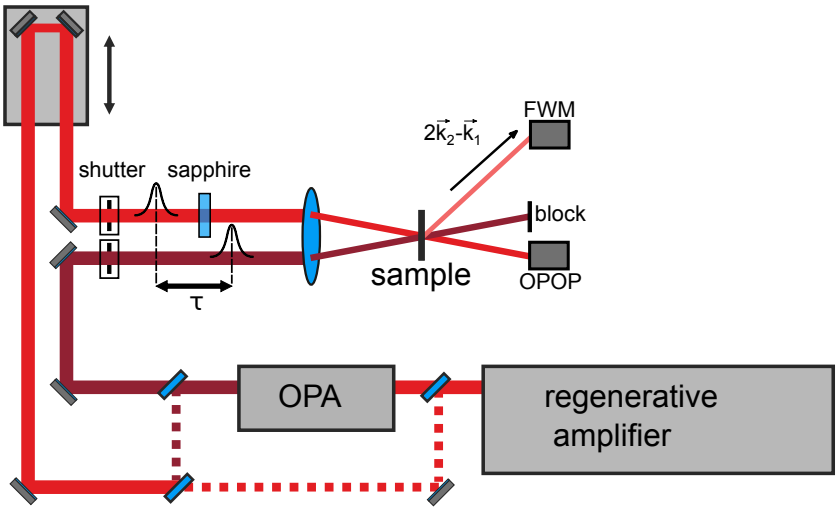

Figure 3.1.: Schematic representation of the optical pump-optical probe setup in combination with a four-wave mixing setup. In a typical OPOP experiment, only the optical pump pulse passes through the OPA, while the probe pulse is already extracted previously by a beam splitter. The probe pulse then travels over a delay line before a sapphire crystal generates the broadband supercontinuum that is focused onto the sample and finally detected by a spectrometer. In a typical FWM experiment, the laser beam from the amplifier is split after the OPA. In this case, there is no sapphire crystal in the setup so that two almost identical pulses are focused onto the sample. Here, however, not the transmitted beam is detected, but the beam diffracted in the direction $2\vec{k}_2 - \vec{k}_1$. Detection is possible with a photodiode or a spectrometer.

3.1.2. Data acquisition

In order to calculate the actual change of the absorption $\Delta\alpha L$ (or the change of the transmission), four measurements are performed for each time delay between pump and probe. Obviously, these are the probe pulse with a blocked pump pulse $T_0(\lambda)$, i.e., the probe of the unexcited sample, and the probe under the impact of the optical excitation $T_p(\lambda)$, i.e., the probe of the excited sample. However, since both the scattered light of the pump pulse and the photoluminescence of the sample are included in the measurement of $T_p(\lambda)$, the measurement is corrected by $T_{PL}(\lambda)$. For the measurement of $T_{PL}(\lambda)$, the probe pulse is blocked, but the beam path of the optical pump is open. Furthermore, the background illumination of the laboratory and the offset of the detector $T_{BG}(\lambda)$ is measured with both mechanical shutters closed. With this data, $\Delta\alpha L$ is calculated via:

$$\Delta\alpha(\lambda)L = -ln\left(\frac{T_p(\lambda) - T_{PL}(\lambda)}{T_0(\lambda) - T_{BG}(\lambda)}\right). \tag{3.1}$$

By using a delay line, these $\Delta\alpha(\lambda)L$ spectra can be recorded for any desired time delay between pump and probe pulse. Here, the delay line allows us to capture a time frame of about 10 ns. The temporal resolution of the setup is fundamentally limited by the length of the optical pulses, which is approximately 60 fs.

3.2. Four-wave mixing spectroscopy

Another optical technique that utilizes at least two optical pulses is four-wave mixing spectroscopy.[29,197] In its simplest form, a first optical pulse $\vec{k}_1$ is used to create a coherent polarization in the sample and a second delayed optical pulse $\vec{k}_2$ interferes with this polarization. Due to the angle of the two pulses to each other, a spatial sinusoidal varying interference pattern is created, which functions as an optical grating. At this optical grating, the second pulse is partially self-diffracted and can be detected amongst others in direction $2\vec{k}_2 - \vec{k}_1$ by a photodiode (or a spectrometer) as shown in Fig. 3.1. The measured time-integrated intensity of the detector $I(\tau_{21})$ is then proportional to:

$$I(\tau_{21}) \propto \int_{-\infty}^{\infty} |P_{NL}^{(3)}(t, \tau_{21})|^2 dt, \tag{3.2}$$

where $P_{NL}^{(3)}$ is the third-order nonlinear polarization. $P_{NL}^{(3)}$ is a product of the two first-order polarizations resulting from the first optical pulse at the time of arrival of the second pulse and the second pulse itself.[125] Accordingly, a diffracted signal can only be detected as long as a coherent polarization is still present when the second pulse arrives. FWM spectroscopy thus measures the loss of optical coherence in the medium. This decoherence is typically caused by elastic and inelastic scattering processes. Therefore, FWM is an excellent complement to linear spectroscopy methods such as linear absorption, as it enables to study scattering processes even in the presence of inhomogeneous broadening.

3.3. Optical pump-terahertz probe spectroscopy

In contrast to optical techniques that cover interband transitions in semiconductors, the low energy THz-photons are sensitive to intraband transitions of free charge carriers and quasiparticles like excitons, polarons and phonons.[99,198] In particular, THz spectroscopy allows us to investigate incoherent excitons by their internal excitonic transitions, which is analogous to atomic absorption spectroscopy.[83] Therefore, OPTP is ideally suited to explore both the formation and decay dynamics of an incoherent exciton population as well as spectral features of intraexcitonic transitions.

3.3.1. Setup

Starting point is again the regenerative amplifier system with its 35 fs short laser pulses at a central wavelength of 800 nm. Those pulses are divided into two parts by a beam splitter. One part - the pump - drives an OPA so that the excitation wavelength can be tuned before it excites the sample. If desired, the spectral width of the pump pulse can be reduced with a pulse shaper, as shown in Fig. 3.2. The pulse shaper decomposes the optical pulse into its spectral components via a grating, so that the optical pulse can be cut to the desired spectral width by razor blades.
The other part of the laser output passes a delay line, which is used to set the time delay between the optical pump and the THz probe, and an active beam stabilization before it is divided by another beam splitter. The largest part of the pulse runs over a second delay line and drives a large aperture GaAs antenna which generates the single-cycle THz pulses. The THz probe pulse is then focused onto the sample via two parabolic mirrors where it spatially overlaps with the optical pump. Afterward, two parabolic mirrors focus the THz probe onto an 800 μm thick ZnTe crystal. Here, the THz pulse spatially overlaps with the remaining third optical pulse and is detected via electro-optical sampling.

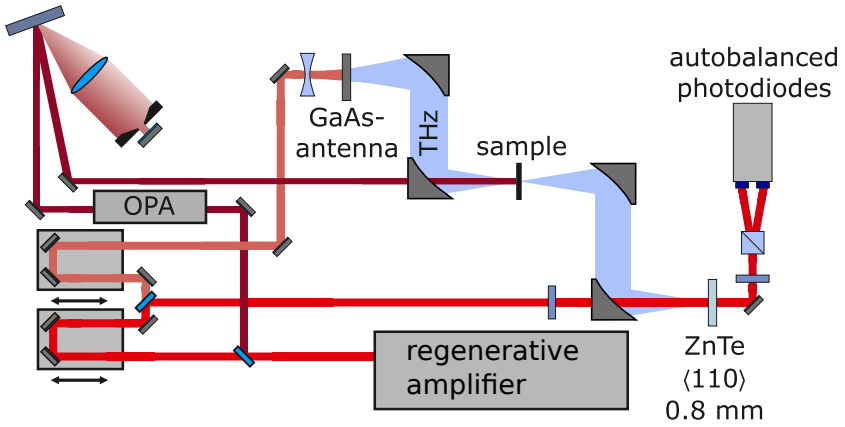

Figure 3.2.: Schematic representation of the optical pump-terahertz probe setup. The initial optical pulse of the regenerative amplifier is divided into three parts. One is used for optical excitation of the sample, one for the generation of the THz pulse and one for detection of the THz pulse via electro-optical sampling. Two delay lines are necessary to set the time delay between optical pump and THz probe pulse as well as to sample the THz pulse electro-optically.

To avoid water vapor absorption, the complete THz path is flooded with dry nitrogen gas.

3.3.2. Generation of single-cycle terahertz pulses

Nowadays, there are many possibilities to generate single-cycle THz pulses out of short laser pulses. For example via laser-induced plasma,[63] the photo-Dember effect,[61,93] optical rectification[153,212] or metallic spintronic emitters.[169] However, in the experiments carried out within this thesis, a photoconductive antenna is used to generate single-cycle THz pulses. Therefore, the working principle of such photoconductive antennas is described in more detail in this section.
A photoconductive antenna consists of a semiconductor material to which an electrode structure is applied in order to create an electric field between the electrodes. An optical pulse with a photon energy greater than the band gap energy of the semiconductor generates charge carriers which are accelerated by the applied electric field in a plane perpendicular to the direction of incidence. This transient electrical current can be described by a Hertzian dipole where the far field has to be:[78]

$$E_{THz}(t) \propto \frac{d}{dt} I_{PC}(t). \tag{3.3}$$

Here, E_{THz} is the electric field of the THz pulse far from the emitter and I_{PC} is the photocurrent of the antenna. Since the radiated electric field is proportional to the temporal change of the current, the radiated spectrum is linked closely to the charge carrier dynamics of the photoconductive antenna. To obtain a radiated maximum in the THz frequency range, the rise and fall times of the current need to be on a pico- or subpicosecond time scale. In addition to short optical excitation pulses, this also requires a short recapture time of the excited charge carriers.[146] This is accomplished by using semiconductor materials with a large number of trapping and recombination centers. In the case of low-temperature-grown GaAs, which is the substrate of the photoconductive antenna used for the measurements presented here, this is obtained by introducing defects

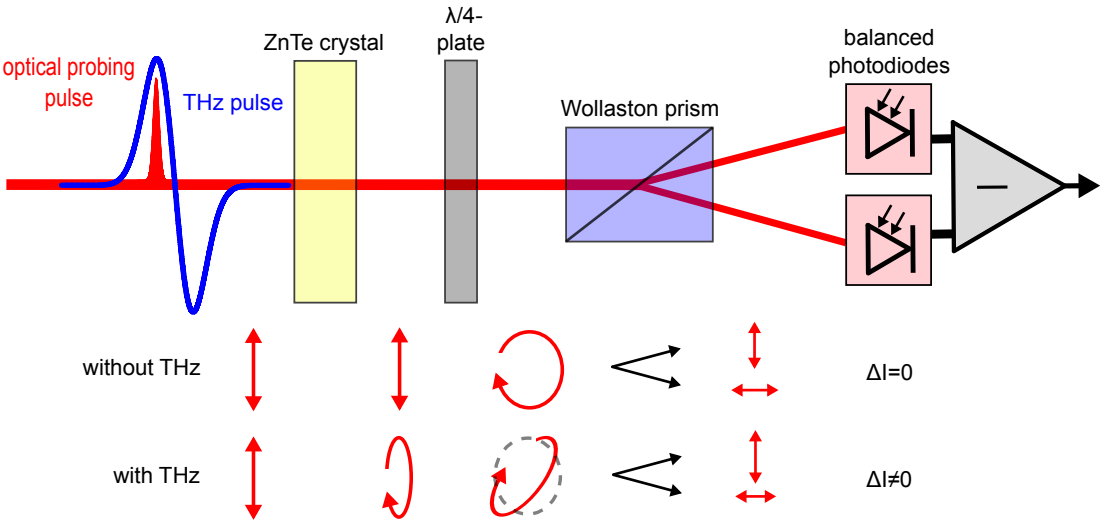

Figure 3.3.: Schematic representation of the electro-optical sampling used for the phase-sensitive detection of the THz radiation. On top, a schematic arrangement of the applied optical and electrical components is illustrated, while the respective polarization of the optical probing pulse with and without THz field is indicated below.

during the growth process at a low temperature. However, to achieve a high THz output power, the mobility of the charge carriers in the semiconductor material should be as high as possible. The combination of high carrier mobility and a short recapture time is a trade-off the optimization of which is still the subject of current research.[10,80,100,101,113]

3.3.3. Phase-sensitive detection of terahertz radiation

The single-cycle THz pulses that are generated by the photoconductive antenna are detected via electro-optical sampling. A schematic of this method is shown in Fig. 3.3. It enables a coherent detection of amplitude and phase of the electric field of the THz pulse.[135,199,211]

For the electro-optical sampling, the THz pulse and a much shorter optical probe pulse are focused on a nonlinear crystal such as ZnTe, GaSe or GaP. In those nonlinear crystals, the birefringence can be modulated by an electric field. This effect is called Pockels effect or linear electro-optic effect.[110] Here, the change of the birefringence (Δn) is linear to the electric field strength (E) of the applied field:[148]

$$\Delta n = \frac{n_0^3}{2} \sum_j r_{ij} E_j. \tag{3.4}$$

Since this modulation of the refractive index occurs almost instantaneously, a short optical probe pulse is able to detect the currently present electric field of the THz pulse. In crystals with a zinc-blende structure like ZnTe, all electro-optic coefficients are zero except $r_{41} = r_{52} = r_{63}$.[146] Accordingly, when the optical pulse is polarized by 45° to the optical axis, it experiences a phase shift of:[148]

$$\Delta\phi = \pi \frac{d}{\lambda} n_0^3 r_{41} E_{THz}(t). \tag{3.5}$$

Here, n_0 is the non-modified refractive index, i.e., without an external electric field, and d is the thickness of the nonlinear crystal.
If no THz field is applied to the ZnTe crystal, the linearly polarized optical pulse is converted into a circularly polarized one by a subsequent quarter-wave plate. A Wollaston prism separates this circularly polarized beam into horizontal and vertical components which are detected by a pair of photodiodes. Since horizontal and vertical components are equally strong in circularly polarized light, both photodiodes receive the same signal and balance each other out. When the transmitting THz pulse exerts an electric field to the ZnTe crystal, elliptically polarized light is generated behind the quarter-wave plate due to the additional phase shift. Here, either the horizontal or the vertical component is more intense, so that there is a difference between the photocurrents of each photodiode. In the small angle approximation this difference of the photocurrents is proportional to the phase shift of the optical pulse and thus to the electric field of the THz pulse:

$$\Delta I \propto sin(\Delta\phi) \approx \Delta\phi \propto E_{THz}(t). \tag{3.6}$$

By changing the time delay between the probing optical pulse and the THz pulse, the entire THz pulse can be sampled. Thus, we receive the full trace of the THz pulse in the time domain.
In addition to the duration of the probing optical pulse, there are other effects which limit the maximum detectable bandwidth of the THz pulse. In particular, a mismatch between the optical group and THz phase velocities and the absorption of the nonlinear ZnTe crystal at THz frequencies should be mentioned here.[5,54,111] Both the phase mismatch and the THz absorption deteriorate for frequencies above 2.5 THz and limit the bandwidth of our setup.[55] The bandwidth can be enhanced by using thinner ZnTe crystals or other nonlinear crystals such as GaP that do not show an increasing absorption above 2.5 THz. However, this is associated with a loss of sensitivity.

3.3.4. Data acquisition

In order to process the differential current ΔI recorded by the balanced photodiodes at a certain position of the second delay line, the current is converted into a voltage by a transimpedance amplifier first. This voltage signal then passes through a boxcar integrator[4], which, however, only has the function to temporally cut the several microseconds short voltage signal out of a millisecond of non-signal. Afterward, the voltage signal is sent to a lock-in amplifier[5]. For operation, the lock-in amplifier requires a modulated signal. This is realized by a mechanical chopper wheel. Depending on the intended measurement, it chops either the THz probe or the optical pump path. Accordingly, the signal output by the lock-in amplifier is proportional to the difference signal between the path blocked by the chopper wheel and the open path. Depending on which path is chopped, one gets:

1. The difference between the transmitted THz field and no THz field at all. This results in the THz pulse $E_{ref}(t)$ when the entire pulse is sampled. In this configuration, the optical pump is blocked.
2. The difference between the transmitted THz field of the excited and the unexcited sample.

[4]Stanford Research Systems SR250 Gated Integrator
[5]Stanford Research Systems SR830 DSP Lock-In Amplifier

Thus, if the entire pulse is sampled, one obtains the pump-induced change of the THz pulse $\Delta E(t)$.

A Fourier transformation of the detected waveforms $E_{ref}(t)$ and $\Delta E(t)$ yields the frequency domain fields of the reference pulse $E_{ref}(\omega)$ as well as its pump-induced change $\Delta E(\omega)$. With this, the excitation-induced absorption $\alpha(\omega)$ and the change of the real part of the dielectric function $\Delta\epsilon(\omega)$ can be calculated:[198]

$$\alpha(\omega) = -\frac{2}{L}\,\mathrm{Re}\left(\frac{\Delta E(\omega)}{E_{ref}(\omega)+\Delta E(\omega)}\right), \tag{3.7}$$

$$\Delta\epsilon(\omega) = \frac{2c_0\sqrt{\epsilon_r}}{\omega L}\,\mathrm{Im}\left(\frac{\Delta E(\omega)}{E_{ref}(\omega)+\Delta E(\omega)}\right). \tag{3.8}$$

Here, L is the thickness of the sample, c_0 is the speed of light in vacuum and ϵ_r the dielectric constant of the material.

4. Exciton formation dynamics

The rapidly advancing development of lasers in the 1960s and 70s soon enabled the generation of short laser pulses in the picosecond and femtosecond time domain.[4] Together with improved measurement techniques, this paved the way for the exploration of dynamic processes on a pico- and subpicosecond time scale. With these achievements, new fields of research emerged, one of which is ultrafast spectroscopy.[49,56] One of the leading research interests of ultrafast spectroscopy are charge carrier dynamics in semiconductors.[144,172] This includes the formation dynamics of excitons in semiconductors and semiconductor quantum wells, which is the subject of particularly controversial discussions. A large number of experimental research results were published on this subject in the 1990s.[11,30,34,35,106,107,141,149,154] The idea behind these experimental efforts was to determine the formation dynamics of an exciton population by detecting its time-resolved photoluminescence, the energy of which was supposed to be below the transition energy of a free electron-hole plasma. A problem of time-resolved photoluminescence spectroscopy is that access is restricted to excitons with a center of mass momentum close to K=0, since only these can recombine radiatively. This complicates the analysis and interpretation of the experimental results. Consequently, exciton formation times determined by time-resolved photoluminescence vary from less than 20 ps to more than 200 ps for GaAs QWs.[11,30,34] Time-resolved photoluminescence as the method of choice for determining exciton formation dynamics suffered a further setback in 1998 when Kira *et al.* showed theoretically that a free electron-hole plasma also emits photoluminescence predominantly at the transition energy of the exciton.[89] Thus, excitonic photoluminescence does not necessarily indicate a population of excitons. Subsequently, this theoretical discovery has been validated experimentally.[22,53] These findings further discredited the inconsistent results of exciton formation times determined by photoluminescence spectroscopy.

Instead, optical pump-terahertz probe spectroscopy should finally provide unambiguous insights into the formation dynamics of an exciton population.[88,99] Terahertz spectroscopy detects the intraexcitonic transitions between 1s excitons and higher states such as 2p. Such intraexcitonic transitions are only possible if an actual population of 1s excitons is present. Furthermore, terahertz spectroscopy is sensitive to excitons of any center of mass momentum. As it turns out, however, OPTP spectroscopy does not show a consistent picture either. While some publications report an ultrafast exciton formation process directly after a non-resonant optical excitation leading to an almost instantaneous population of excitons,[82,83,188] others report an at first pure electron-hole plasma which condenses into an exciton population on a time scale of tens to hundreds of picoseconds.[67,190] Some of these reported differences are certainly related to different characteristics of different material systems, but fundamental discrepancies of the exciton formation dynamics in very similar samples seem rather unlikely.

In this Chapter, I will use OPTP to study the exciton formation dynamics of bulk Ge and GaInAs QWs under non-resonant excitation conditions. Besides the impact of the excitation density, the influence of the excitation energy on the dynamics of exciton formation is investigated. The intention is to finally end the controversy about the exciton formation dynamics in semiconductors that is going on for three decades now.

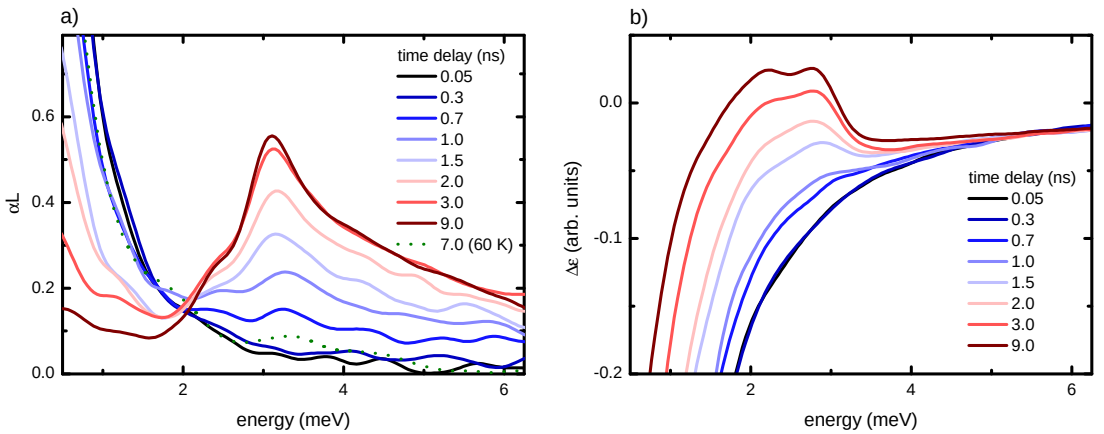

Figure 4.1.: a) THz absorption spectra at 11 K for different time delays between optical pump and THz probe pulses. The dotted curve shows the THz absorption at a temperature of 60 K. b) Change of the real part of the dielectric function for the same time delays. The estimated carrier density is $5 \cdot 10^{14}\mathrm{cm}^{-3}$ which is far below the exciton Mott density in Ge.

4.1. Density-dependent exciton formation in bulk germanium

After an optical excitation at 0.8 eV, i.e., energetically about 55 meV above its indirect band gap, bulk Ge clearly shows the response of a free electron-hole plasma for time delays between the optical pump and the THz probe pulse of 300 ps or less. On the one hand, this is evident in the THz absorption, which is negligibly low for the intraexcitonic resonance around 3.1 meV and, as expected for an electron-hole plasma, increases significantly below 1.5 meV. This is shown in Fig. 4.1 a) where additionally the THz absorption at a temperature of 60 K is given as a dotted line. A comparison shows that the THz response within the first 300 ps at 11 K is very similar to that of a sample temperature of 60 K at which hardly any bound exciton states should be present due to the increased thermal energy. On the other hand, the plasma response becomes apparent in the change of the real part of the dielectric function which shows the typical Drude-like response of unbound electron-hole pairs in the first 300 ps after excitation [see Fig. 4.1 b)]. Both in the absorption and the change of the dielectric function, the responses for time delays of 50 ps and 300 ps are literally identical, which excludes any exciton formation processes on these time scales. A significant change of αL and $\Delta\epsilon$ becomes apparent for a time delay of 700 ps. For this time delay an increased intraexcitonic absorption at 3.1 meV together with an increase of $\Delta\epsilon$ below the intraexcitonic resonance energy is observed. The reason for this is the incipient formation of bound electron-hole pairs, i.e., excitons. These signatures of an exciton population increase in the next nanoseconds in which the unbound electron-hole pairs transform into bound excitons. Finally, 9 ns after the optical excitation an almost pure exciton population is present as discussed in detail in Paper I. In order to investigate the delayed exciton formation in bulk Ge more precisely, we analyze the temporal behavior of the intraexcitonic absorption. For this purpose, we read out the absorption strength at 3.1 meV, which should be approximately proportional to the exciton fraction in bulk Ge. However, the temporal resolution of this method is limited by the number of spectra that can be recorded in finite time. A much higher temporal resolution is possible by linking the exciton fraction to the signal strength at specific points in the time domain of the THz pulse. Instead of scanning the entire time domain, this allows for measurements of transients at a single point in the time domain.

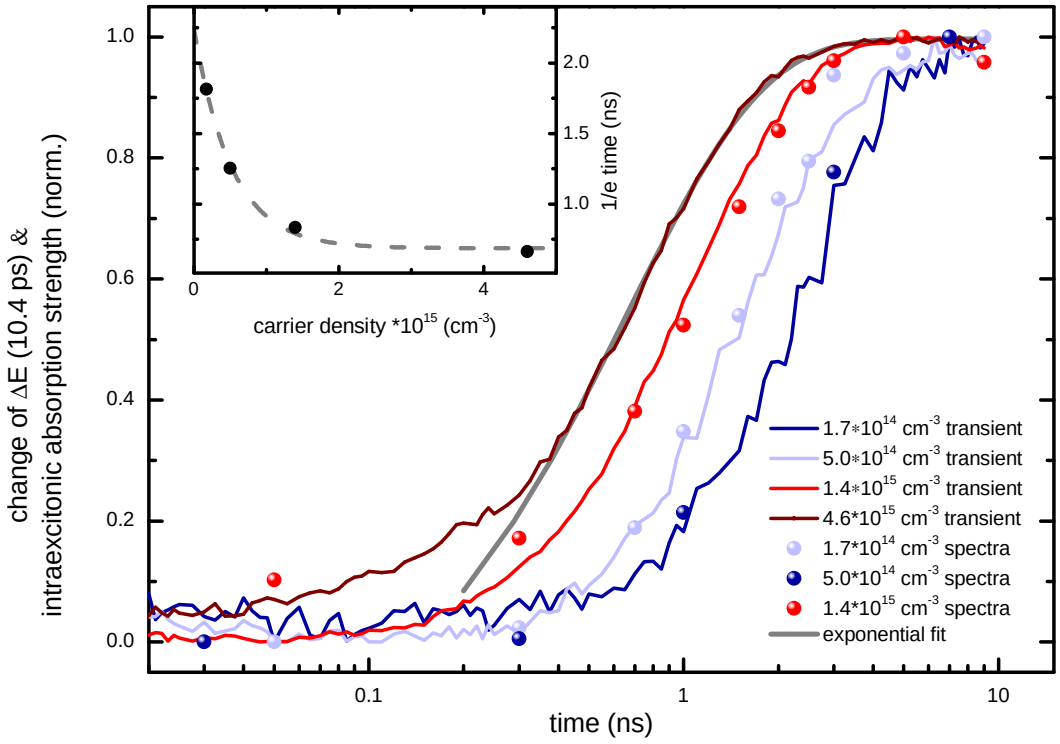

Figure 4.2.: The intraexcitonic absorption strengths are plotted together with transients from the excitation-induced change of the THz pulse for different excitation densities. The spheres are extracted from the intraexcitonic absorption peak at 3.1 meV and the solid curves are from transients at a specific position in the time domain of the THz pulse. Fitting an exponential function (gray line) to the transients gives characteristic times for the buildup of an excitonic response. Those buildup times are plotted in the inset for four different excitation densities.

For a detailed explanation of this experimental approach, see Paper I. In Fig. 4.2 the normalized absorption strength at 3.1 meV is plotted together with the normalized transient of a specific point in the time domain of the THz pulse for different excitation densities. Both approaches agree very well, which further justifies the use of transients to determine the exciton formation dynamics. As already discussed in the context of Fig. 4.1, initially no signs of an exciton population are observed. Instead, the exciton formation is, depending on the carrier density, delayed by several hundred picoseconds. A few hundred picoseconds after first signs of an excitonic response appear, however, a simple exponential function can describe the exciton formation. This allows for the determination of characteristic time constants. While the time constant is nearly 2 ns for the lowest carrier density investigated, it drops to 0.66 ns for the highest density investigated of $4.6 \cdot 10^{15}\mathrm{cm}^{-3}$. For the present carrier densities, which are one to two orders of magnitude below the exciton Mott density,[170] a more rapid exciton formation is observed with increasing carrier density. This is consistent with theoretical investigations.[71]
Thus, no ultrafast exciton formation can be observed in bulk Ge. On the contrary, the exciton formation is delayed. This can be attributed to the fact that the distribution of hot carriers has to cool down first after optical excitation. Subsequently, the formation of an exciton population starts. In this low-density regime, exciton formation occurs earlier and is accelerated with increasing excitation density.

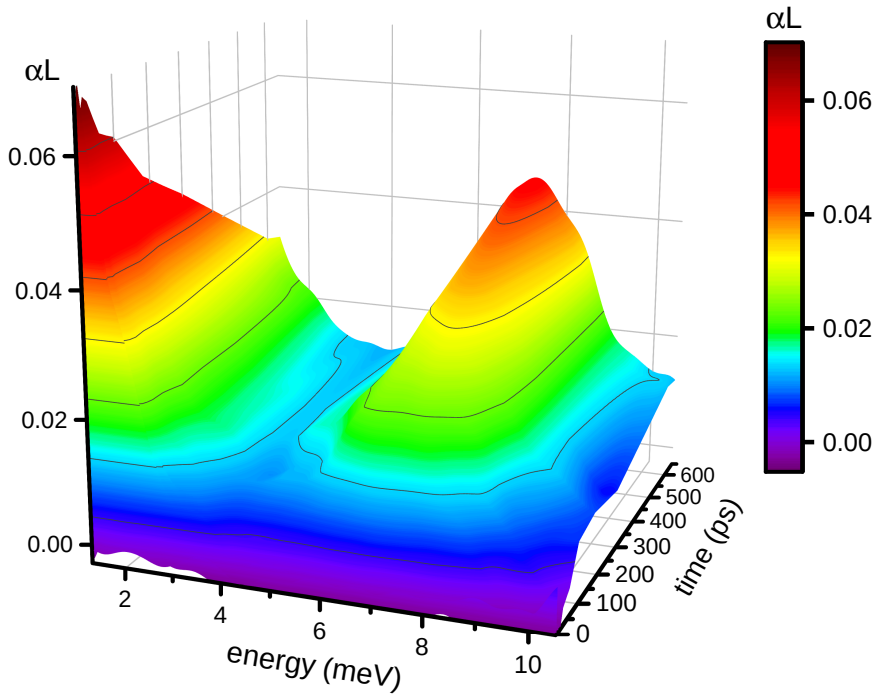

Figure 4.3.: Surface plot of the THz absorption after non-resonant excitation with a photon density of $5.5 \cdot 10^{12}$ photons/cm^2 in a GaInAs QW sample. The optical excitation pulse is energetically 30 meV above the excitonic resonance and has a full width at half maximum of 13 meV. The sample is held at a temperature of 11 K.

4.2. Exciton formation dynamics in GaInAs quantum wells

In addition to bulk Ge, the THz response of GaInAs QWs after non-resonant excitation conditions is investigated. The results shown in Fig. 4.3 are obtained from a sample containing 50 repetitions of 8.65 nm thick GaInAs QWs embedded in 1.35 nm thick layers of GaAs and a strain compensating layer of GaAsP. For further details of the sample, please refer to sample 6 in Ref. 119. Again, immediately after non-resonant excitation, the response of an electron-hole plasma occurs. Characteristic for this is the high absorption for energies below 2 meV. In contrast to bulk Ge, however, a continuous formation of excitons starts directly after the optical excitation, as indicated by the emerging intraexcitonic resonance at 7 meV in Fig. 4.3. As the absorption of the intraexcitonic resonance increases, the absorption of the electron-hole plasma decreases on a time scale of several hundred picoseconds.

In order to investigate the dynamics of the exciton formation more closely, the spectral THz absorption is integrated from 4.75 meV to 9.10 meV. Doing so is a good measure of the intraexcitonic oscillator strength. In Fig. 4.4, the normalized oscillator strength determined by the spectrally integrated THz absorption is displayed together with the transient from a specific point in the time domain of the THz pulse (see Paper I for details about this experimental approach). Once again there is an excellent agreement between both methods. To enable a logarithmic representation, the zero time delay between optical pump and THz probe pulse is shifted to 4 ps. It turns out that the exciton formation starts immediately, as the increase of the intraexcitonic oscillator strength and the increase of the transient in the first picoseconds after optical excitation reveals.

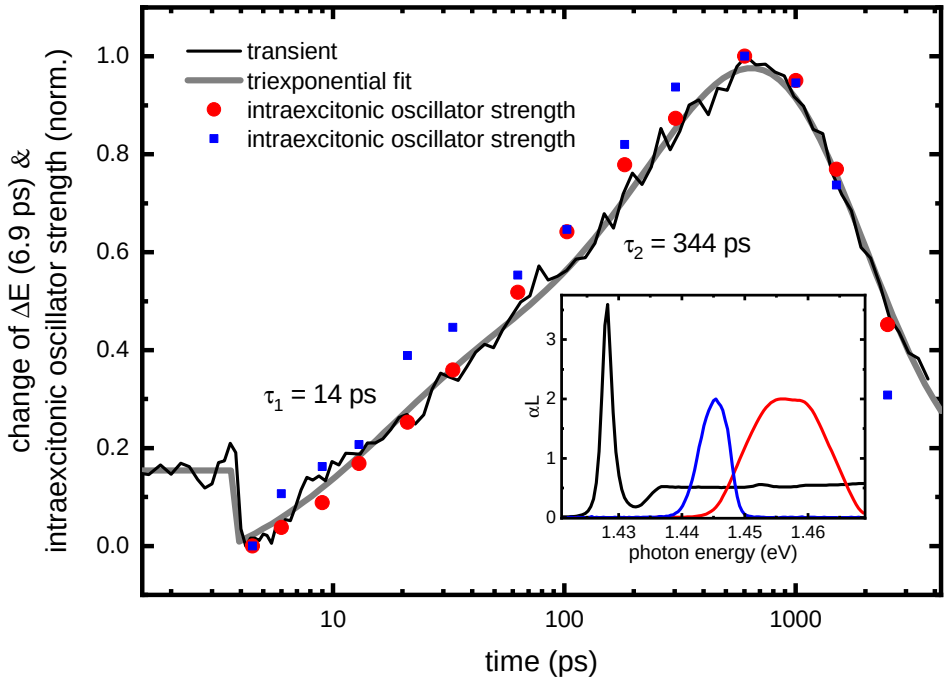

Figure 4.4.: The intraexcitonic oscillator strength is plotted together with a transient from the excitation-induced change of the THz pulse at a position of 6.9 ps in the time domain. The inset shows the linear absorption (black line) of the sample as well as the two non-resonant excitation pulses (red and blue lines). The transients and the red spheres are obtained after non-resonant excitation with a central energy of 1.458 eV, while the blue squares are obtained after excitation with a central energy of 1.445 eV. Adapting a triexponential function to the transient provides two rise times operating at different time scales.

The maximum is reached about 600 ps after excitation and the intraexcitonic oscillator strength and the transient subsequently decrease due to recombination processes. A triexponential function describes the course of the graph very well. One part of the triexponential function describes the radiative and non-radiative decay of the population on a nanosecond time scale. The other two parts of the function are necessary to describe the exciton formation. While a delayed monoexponential function can describe the exciton formation in bulk Ge, two exponential functions are required to describe the exciton formation in GaInAs QWs. As a result, there are two time constants - a lower time constant of about 14 ps and a higher time constant of about 344 ps. This may indicate that two different processes, which operate on different time scales, contribute to the formation of an exciton population in GaInAs QWs.
In the literature, an interaction with optical phonons is often associated with a very fast exciton formation.[11,171,175,193] In order to check whether optical phonons are the reason for the observed fast exciton formation process, the sample is also excited 17 meV above the excitonic resonance (blue squares in Fig. 4.4). This excess energy is well below the energy of an optical phonon (∼30 meV) in GaAs. In this case, however, the course of the intraexcitonic oscillator strength is very similar to that after optical excitation 30 meV above the excitonic resonance. A major contribution of optical phonons to the observed fast exciton formation thus seems unlikely.
Initially after a non-resonant optical excitation, GaInAs QWs show the THz response of

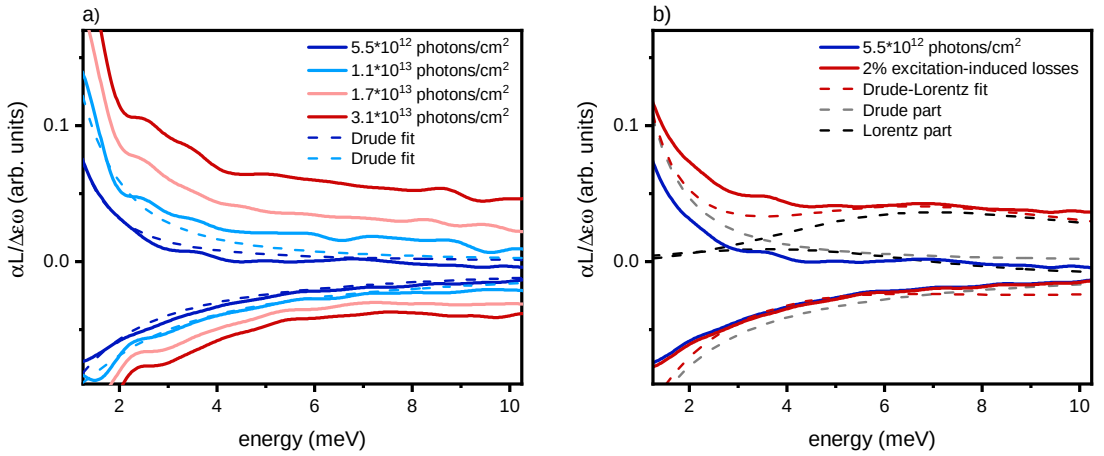

Figure 4.5.: a) The THz absorption is shown together with the change of the real part of the dielectric function for different photon densities 3 ps after a non-resonant optical excitation. For better visualization, the change of the real part of the dielectric function has been multiplied by ω. Exemplarily, a Drude model is adapted to the THz response for two photon densities (dashed lines). b) Out of the THz response for the lowest photon density, the THz response that would be obtained for an additional 2 % excitation-induced loss of the transmitted THz pulse is calculated. A Drude-Lorentz model is adapted to this THz response and is plotted together with the respective components from the Drude and the Lorentzian part.

an electron-hole plasma. However, the formation of an exciton population starts immediately after the optical excitation, so that a small fraction of excitons is already present after a few picoseconds. Nonetheless, it takes several hundred picoseconds until a large proportion of free electron-hole pairs are bound into excitons. The fact that a small part of the electron-hole plasma is bound into excitons very fast may explain why the exciton formation times in comparable QW structures vary from several tens of picoseconds to several hundred picoseconds in the literature.[11,30,34,82] After all, this corresponds quite well to the two time constants that we observe here. Nevertheless, it does not explain the reports of a quasi-instantaneous appearance of high exciton fractions in the range of 40 % after a non-resonant optical excitation in similar QW structures.[82,83]

In this context, it should be noted that increasing excitation densities can lead to an offset in the THz absorption. This is visualized in Fig. 4.5 a), where the THz response is shown 3 ps after non-resonant excitation conditions for different excitation densities. As clearly visible, the THz absorption increases strongly with increasing excitation density. This is partly expected due to the increased number of charge carriers in the sample. However, the THz absorption of an electron-hole plasma is close to zero above 4 meV as can be seen for the lowest photon density of $5.5 \cdot 10^{12}$ photons/cm^2. Therefore, a THz absorption close to zero is also expected from an electron-hole plasma for higher excitation densities at energies above 4 meV. Yet, this expectation does not match our observation. We observe a disproportionate increase of the absorption above 4 meV, i.e., energetically in a domain where absorption due to intraexcitonic transitions is expected. However, this absorption above 4 meV should not lead to the erroneous assumption of a large population of excitons since it is not substantiated by excitonic signatures in the dielectric function change. Instead, the cause is probably an offset in the THz absorption produced by some frequency-independent excitation-induced losses. A plausible explanation may be carrier-

induced reflection or scattering losses. To strengthen this argument, Fig. 4.5 b) shows, in addition to the measured THz response, the response one would obtain when 2 % of the transmitted THz pulse were lost due to frequency-independent excitation-induced losses. It turns out that this changes almost nothing at $\Delta\epsilon \cdot \omega$ but leads to a massive offset in the THz absorption. An offset very similar to the one we observe for increasing photon densities. Please note that the charge carrier density naturally increases with photon density. An increased carrier density, of course, further increases the THz absorption at low energies and lowers $\Delta\epsilon \cdot \omega$. Aside from the offset in the absorption, this is precisely what we observe for increasing photon densities in Fig. 4.5 a).
In particular, the offset in the THz absorption makes it impossible to describe the THz response with the frequently used Drude model. While such a pure Drude model describes the THz response for a photon density of $5.5 \cdot 10^{12}$ photons/cm^2 very well in Fig. 4.5 a), it fails to describe the THz response for higher photon densities adequately. Almost identical observations were made by T. Suzuki and R. Shimano in silicon.[190] For increased excitation densities they find: „The $\Delta\epsilon_1$ spectrum shows a Drude-like response at 10 ps. On the other hand, $\Delta\sigma_1$ has a deviation from the Drude fitting, and it indicates that there is an excitonic correlation.“[190] As already hinted at by T. Suzuki and R. Shimano, such an offset in the absorption (or in $\Delta\sigma_1$) can be described reasonably well by a broad intraexcitonic resonance. This is especially true when only a limited spectral range is available. In Fig. 4.5 b), a Drude-Lorentz model is adapted to the response that one would observe for 2 % excitation-induced losses. While it is impossible to describe this response with a pure Drude model, a large part of an additional Lorentzian component produces a more or less reasonable result. In many cases, such Drude-Lorentz models are used to determine the proportion of an exciton population in the total carrier population. For this purpose, the share of the Lorentzian part in the overall function is linked to the exciton fraction. In the exemplary case presented here, this could lead to a severe overestimation of the exciton population. Furthermore, it enables the interpretation that a significant exciton population exists directly after a non-resonant optical excitation. Thus, the observed excitation-induced THz absorption offset may explain why some studies of intraexcitonic transitions such as Ref. 83 claim to observe enormously high exciton fractions instantaneously after a non-resonant optical excitation.
In the samples investigated within the scope of this work, which include bulk Ge, Ge QWs and different GaInAs QWs, no significant proportion of an exciton population could be observed immediately after a non-resonant optical excitation. Instead, the response of an electron-hole plasma has been observed first in each and every case as long as the excitation densities were well below the Mott density. The observed deviation of the absorption from the Drude model in the energy range of intraexcitonic transitions for elevated excitation densities in Ge and GaInAs QWs is not attributed to an exciton population since clear excitonic signatures in the dielectric function change are missing.

5. Excitons in bulk germanium

The model system most frequently investigated in this work is bulk Ge, which served as a sample in Paper I, Paper IV and Paper V. Therefore, before discussing the individual findings that resulted from this model system, I would first like to address the general benefits of bulk Ge and explain why this of all semiconductor materials has been investigated so often in this thesis.
First of all, the OPTP setup used here is most sensitive in the frequency range from 0.5 to 2 THz. Thus, ideally, the intraexcitonic transitions should also be in this frequency range. This condition is met by bulk Ge, which has an intraexcitonic $1s-2p$ transition at $\sim$0.75 THz;[170,194] however, it is an exclusion criterion for, e.g., Si. Besides, Ge is a monocrystalline semiconductor and can therefore be produced in a particularly pure form. The absence of other elements and the very high structural quality compared to compound semiconductors make it an ideal model system for spectroscopic investigations as unwanted inhomogeneous line broadenings are minimized.[62,64,177] Nevertheless, the decisive advantage of Ge over many other semiconductors such as GaAs, InP, GaSb, CdTe or CdSe is its indirect band gap. The comparatively low absorption coefficient of Ge below its direct band gap allows for a homogeneous optical excitation up to a sample thickness of several millimeters at liquid helium temperatures. Compared to the usual penetration depths of $\sim$1 μm for direct semiconductors, this enables the investigation of significantly thicker samples, which increases the signal strength and thus the signal-to-noise ratio of the THz experiments considerably. Only this high signal-to-noise ratio made it possible to perform the „good-quality THz absorption experiments“ required by Springer *et al.*,[179] which finally provided the experimental confirmation of the theoretically predicted effect of anisotropic effective masses on excitonic properties.[184] The first section starts with these experiments exploring the influence of an L-valley anisotropy in bulk Ge on intraexcitonic transitions, which not only demonstrated the suitability of the model system but also paved the way for further experiments.

5.1. L-valley anisotropy

Ge is an indirect semiconductor with a valence band maximum at the Γ-point and a conduction band minimum in the L-valley. After an optical excitation, all electrons should relax into the L-valley and all holes should relax in the Γ-valley. The L-valley in Ge, however, has a distinctly different curvature depending on the direction of motion in $\vec{k}$-space.[18] This results in a strong effective mass anisotropy. Consequently, the longitudinal effective mass for electrons in the L-valley is with m_l=1.59 m_0 about 20 times greater than the transversal effective mass with m_t=0.0815 m_0.[114,120] Through the Coulomb interaction, electrons and holes in indirect semiconductors can form an exciton where both particles have different momentums. However, the effective mass anisotropy results in exciton wave functions that are no longer symmetric in $\vec{k}$-space, which in turn leads to an energy splitting of the higher quantum states.[179] In particular, this leads to a splitting of the p-states that are relevant for the intraexcitonic $1s-2p$ transition. More precisely, this energetic splitting of the p-states results in a second intraexcitonic $1s-2p$ transition which, if the splitting is large enough, should become visible as a shoulder in the THz

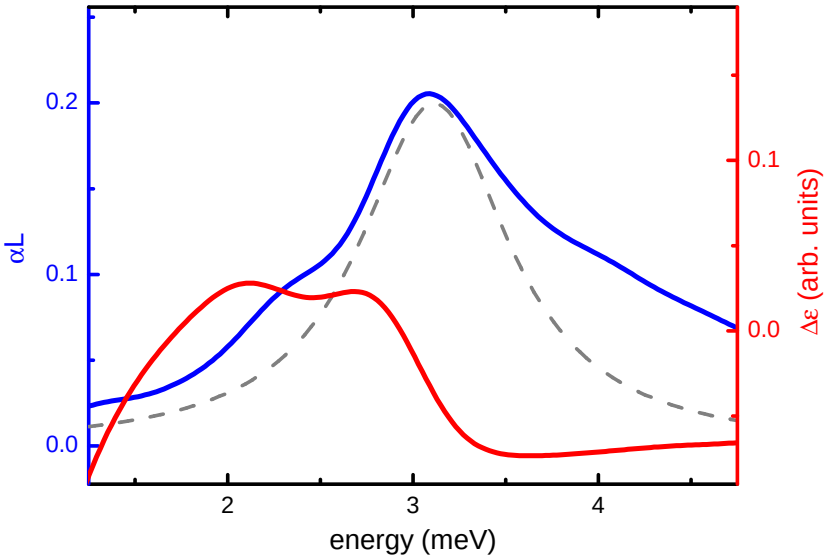

Figure 5.1.: THz absorption (blue) as well as the change of the real part of the dielectric function (red) are shown for a time delay of 7 ns between optical pump and THz probe. A simple Lorentzian function is drawn as a gray dotted line for orientation.

absorption. For a detailed microscopic description of how the effective mass anisotropy affects the excitonic states, please refer to the original publication by Springer *et al.* in Ref. 179.

Inspired and challenged by the theoretical predictions of Springer *et al.*,[179] an initial attempt was made to measure intraexcitonic transitions with our OPTP setup in bulk Ge. For this attempt, we use a 500 μm thick sample of undoped Ge with a room-temperature resistivity of more than 30 Ωcm. There was hope that the linewidth of the intraexcitonic $1s-2p$ transition in a 500 μm thick sample of pure Ge might be small enough to spectrally resolve the predicted shoulder in THz absorption with a sufficiently high signal-to-noise ratio.

For this purpose, the sample was cooled down in a continuous flow liquid-He cryostat to 11 K and optically excited at a central energy of 0.8 eV. This excitation energy is about 80 meV below the direct band gap of Ge. At this photon energy the absorption coefficient of 8.4 cm^{-1} is low enough to allow for an almost homogeneous excitation of the 500 μm thick sample. Within the next nanoseconds after optical excitation, the generated electron-hole plasma cools down and condensates into an almost pure $1s$ exciton population. This $1s$ exciton population is probed by a weak THz pulse 7 ns after the optical excitation.

Due to the intraexcitonic $1s-2p$ resonance, the THz absorption shows a pronounced peak at ~3.1 meV as shown in Fig. 5.1. This peak in the absorption spectrum is accompanied by an oscillatory signature of the change of the dielectric function which is typical for a Lorentzian oscillator.[198] However, the peak in the absorption cannot be described by a simple Lorentzian oscillator. For energies above 3.4 meV the absorption deviates from a Lorentz function. In this range, intraexcitonic transitions to higher quantum states such as $3p$, $4p$ and so on further increase the absorption. Beyond that, the absorption also deviates significantly from the Lorentzian function below the resonance energy and reveals a distinct shoulder at ~2.4 meV. Concurrently, $\Delta\epsilon$ shows another less pronounced oscillatory signature at this energy, which occurs in addition to the promi-

nent oscillatory signature at 3.1 meV. Both are clear indications of a second intraexcitonic $1s-2p$ resonance. This additional resonance energetically below the main resonance was predicted by Springer *et al.*[179] Thus, Springer *et al.* were able to apply their theory, which accounts for the effective mass anisotropy of L-valley electrons, to the experimental data and reached an excellent agreement.[184] The results of this collaboration between experimental and theoretical semiconductor physicists are published in Paper I. Since experimental results and the predictive microscopic theory match very well in the THz absorption, there is high confidence that the observed shoulder at ∼2.4 meV is caused by a second intraexcitonic resonance. The reason for this additional resonance is the effective mass anisotropy of L-valley electrons.

5.2. Exciton ionization by THz pulses

Up to now, the influence of electric fields on the optical properties of semiconductors has been studied intensively from both the theoretical as well as the experimental perspective.[16,50,84,85,124,129,201] For experimental investigations either DC electric fields or electromagnetic pulses from the near- to the far-infrared are used to expose semiconductors to external fields.[26,75,180] Such electric fields have, among other things, an impact on the band gap of semiconductors, their exciton binding energy and the energy of each excitonic state. For example, a static electric field leads to pronounced oscillations in the optical absorption spectrum above and a non-vanishing absorption below the band edge.[52,208] This effect is known as the Franz-Keldysh effect.[50,85] If, instead of a static electric field, a time-dependent electric field is applied, as, e.g., a THz pulse allows, an additional blueshift of the band edge is observed.[81,131,174,180] However, the observed phenomena of this dynamic Franz-Keldysh effect vary depending on the frequency and duration of the time-dependent electric field.[33,138] Detailed investigations focusing on the excitonic $1s$ resonance also show an induced splitting of the resonance due to the AC Stark effect[31,202] as well as Rabi flopping.[39] Unfortunately, it is hard to distinguish between effects on the band gap and effects on the exciton binding energy in all these experiments as optical absorption or transmission experiments often measure a superposition of both. Furthermore, effects on intraexcitonic transitions and optically dark states such as excitonic $2p$ states remain entirely unclear. To overcome these limitations of optical spectroscopy and to literally bring light into the dark states, intraexcitonic transitions are investigated as a function of the field strength of a time-dependent electric field in Paper IV. These experiments are analog to the spectroscopy of the hydrogen atom but energetically scaled down by three orders of magnitude, which makes it considerably easier to apply electric fields that are in the order of magnitude of the ionization field.[41,130]

In Paper IV single-cycle THz pulses of various field strengths are used to probe intraexcitonic transitions in bulk Ge. For this, the Ge sample is cooled to a temperature of 11 K and optically excited at a central energy of 0.8 eV. On a time scale of several nanoseconds, the optically generated electron-hole plasma condenses into bound electron-hole pairs so that after 9 ns an almost pure $1s$ exciton population has formed. This is confirmed by probing the sample with a low field strength THz pulse of 0.12 kV/cm. For this field strength a distinct $1s-2p$ resonance at 3.1 meV is observed in the THz absorption spectrum as shown in Fig. 5.2 a). An almost identical absorption spectrum is found for a field strength of 0.22 kV/cm, which confirms that up to this field strength the THz pulse can be considered as a pure probing pulse. A further increase of the field strength leads to a reduced absorption peak which is accompanied by a broadening. At this point, the

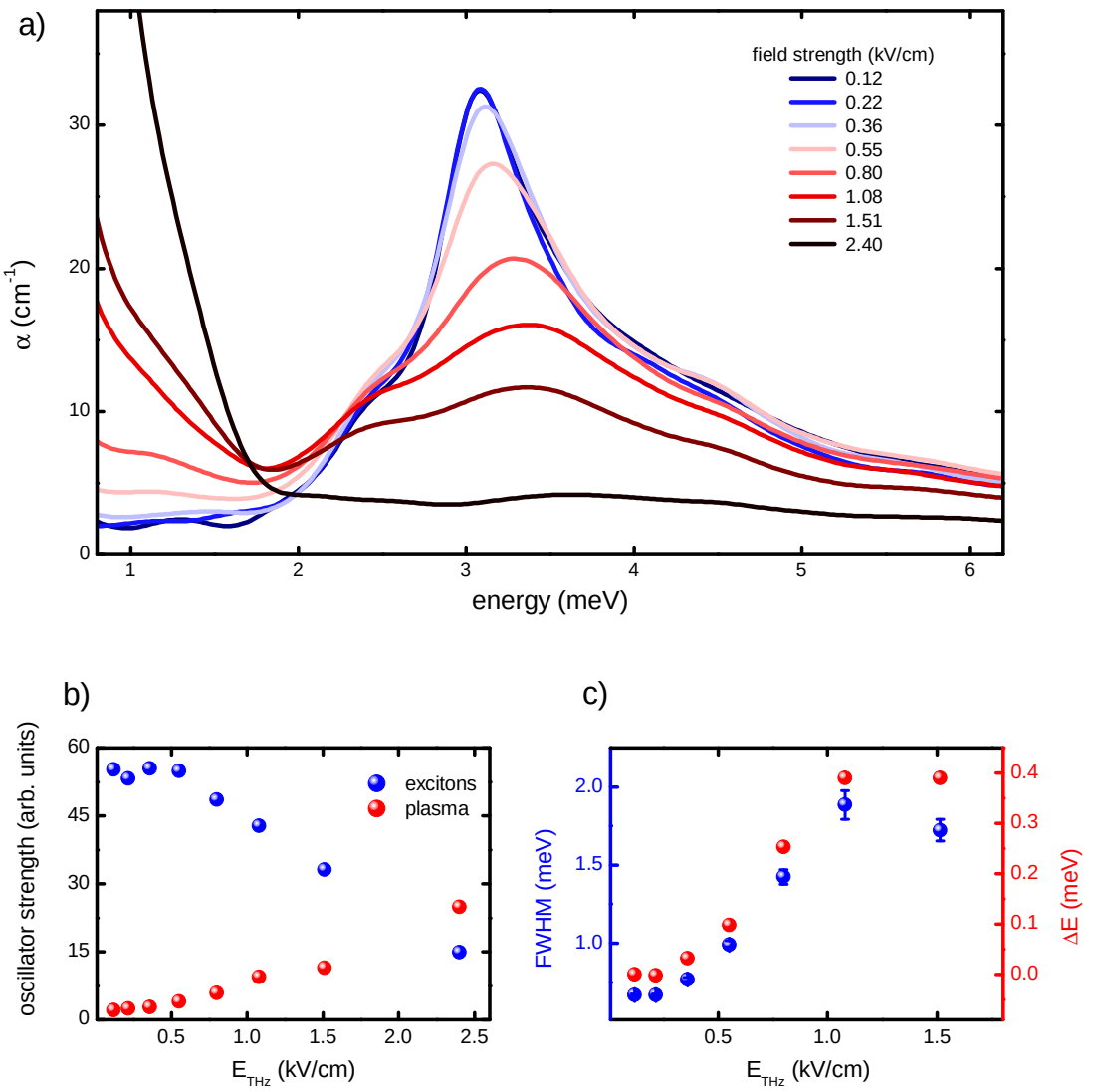

Figure 5.2.: Influence of different strong THz pulses on the intraexcitonic transition. a) The THz absorption spectra for THz pulses of different maximum field strengths are recorded 9 ns after the optical pump excites the sample. b) The oscillator strength of the intraexcitonic transition (blue) integrated from 1.8 to 6 meV and the oscillator strength of the unbound electron-hole plasma (red) integrated from 0.85 to 1.8 meV. While the intraexcitonic oscillator strength stays constant for field strengths up to 0.55 kV/cm and decreases for higher field strengths, the oscillator strength of the electron-hole plasma already increases at low field strengths. c) The FWHM of the intraexcitonic transition (blue) and the relative energetic shift (ΔE) of the intraexcitonic resonance (red) for different maximum THz field strengths. Both increase with increasing THz field strength.

THz pulse is no longer a pure probing pulse but simultaneously interacts with the excitonic states. Since the intraexcitonic oscillator strength remains unchanged up to a field strength of 0.55 kV/cm [see Fig. 5.2 b)], the peak value of the absorption is only reduced because of a homogeneous broadening of the resonance. The reason for this homogeneous broadening is a shortening of the lifetime of a state. Here, most likely, the weaker bound

$2p$ states are field ionized by the THz pulse on time scales shorter than their typical coherent lifetimes. For DC electric fields such an ionization starting at higher excitonic states first is predicted in Ref. 12. Further increasing the field strength reduces not only the peak value of the absorption but also the intraexcitonic oscillator strength. This reduced oscillator strength for field strengths above 0.55 kV/cm is attributed to the incipient ionization of the $1s$ exciton population. The ionization of the exciton population reflects itself in a decrease of the intraexcitonic absorption peak as well as in an increase of the low-energy absorption due to the generated unbound electron-hole plasma. At the highest field strength of 2.4 kV/cm the intraexcitonic resonance vanishes nearly entirely while the plasma response reaches a maximum. Here, the exciton population is ionized almost completely. This is in good agreement with the static electric field necessary to ionize excitons in bulk Ge which is estimated as:[12]

$$E_{ion} = \frac{E_b}{e \cdot a_B} \approx 4\,meV/(e \cdot 24.3\,nm) \approx 1.65\,kV/cm, \tag{5.1}$$

where E_b is the exciton binding energy and a_B is the Bohr radius.
The broadening of the absorption peak due to the reduced lifetime of the excitonic states is illustrated in Fig. 5.2 c). Values for full widths at half maximum (FWHM) are obtained by fitting a sum of two Lorentz functions to the absorption spectrum. For the lowest THz field strength, this yields a linewidth of 0.67 meV. With increasing field strength the linewidth of the intraexcitonic transition increases reaching a value of 1.88 meV at 1.08 kV/cm.
Furthermore, there is a blueshift of the intraexcitonic transition with increasing THz field strength. This is illustrated in Fig. 5.2 c), where the relative energy shift of the absorption peak is plotted as a function of the maximum field amplitude of the THz pulses. Theoretical calculations show a reduction of the exciton binding energy for DC electric fields, which would result in a redshift of the intraexcitonic transition energies.[130] However, since AC fields at THz frequencies are applied here, dynamic effects come into play. Theoretical calculations have shown that the frequency of AC electric fields in relation to the transition frequency plays a decisive role.[138] For THz frequencies (ω_{THz}) slightly below the resonance frequency (ω_{1s-2p}), the AC Stark effect causes a redshift of the $1s$ exciton state whereas the $2p$ state is blueshifted.[33] This increases the energy difference between the $1s$ and the $2p$ state which is consistent with the observed blueshift of the $1s-2p$ resonance. However, for THz frequencies above the resonance frequency, the Stark shifts are in the opposite direction. The broadband THz pulses used here contain frequencies below and above the intraexcitonic resonances. Hence, a superposition of both effects is expected. Nonetheless, in total, a blueshift of the $1s-2p$ resonance is observed. This is evidence that the theoretically predicted shifts for $\omega_{THz} < \omega_{1s-2p}$ outweigh the shifts for $\omega_{THz} > \omega_{1s-2p}$. Consistent with our experimental observation, stronger shifts for $\omega_{THz} < \omega_{1s-2p}$ are also reported in theoretical investigations by Dent *et al.* for field strengths below 2 kV/cm in GaAs QWs (see Fig. 3 in Ref. 33). In total, we observe a blueshift of the $1s-2p$ resonance of up to 0.39 meV for a field strength of 1.08 kV/cm. This is more than 10 % of the $1s-2p$ transition energy. At the same time, the shoulder at ∼2.4 meV, which is caused by the electron effective mass anisotropy in the L-valley, does not show any noticeable shifts. It is conceivable that at this transition energy the predicted redshift for $\omega_{THz} > \omega_{1s-2p}$ compensates the blueshift.
The experimental results are corroborated by a microscopic many-body theory in Paper IV. The theory produces a very similar THz response and in particular, describes the attenuation of the $1s-2p$ resonance due to the exciton ionization very well.[185] Fur-

thermore, the theoretical modeling indicates a blueshift of the intraexcitonic resonance. However, the blueshift and the broadening of the resonance are more pronounced in the experiment. These results further emphasize the need for high-quality experiments for a detailed understanding of many-particle systems in the nonlinear regime.

5.3. Inelastic electron-exciton scattering

When S.G. Elkomoss and G. Munschy theoretically investigated the elastic and inelastic electron-exciton scattering in semiconductors in the late 70s of the 20th century, they stated that in particular experimental data for inelastic scattering are lacking.[36,37] They concluded that „the separation between elastic and inelastic collisions in semiconductors, as in atomic physics, would be of considerable interest“[36] and that their calculations „will have much more interest in the future“.[37] They should be right as in the following decades electron-exciton scattering was studied intensively in semiconductors.[17,46,70,72,97,122,152,166] However, the experimental findings are based either on the analysis of transition linewidths in PL or transmission experiments or on dephasing rates in FWM experiments.[72,97,117,122,166,203,206] Since both elastic and inelastic scattering processes contribute to the dephasing rate, which is directly linked with the homogeneous linewidth, these experimental methods do not allow to distinguish between both scattering processes.[70,206] Instead, they only give access to the total scattering rate. Consequently, an experimental separation between elastic and inelastic electron-exciton scattering processes in semiconductors is still unavailable. In this section, I will show that optical pump-terahertz probe spectroscopy is capable of ending this experimental inaccessibility. Using bulk Ge as an example, I will demonstrate how it is experimentally possible to determine the inelastic and the total electron-exciton scattering rate and thus directly derive the elastic scattering rate.

In order to investigate the electron-exciton scattering in bulk Ge by means of OPTP, the setup has to be extended by a second optical excitation pulse. This is realized by using a beam splitter behind the OPA as shown in Ref. 186. Subsequently, the first optical pulse is used to generate an electron-hole plasma in the sample. At a sample temperature of 11 K, this electron-hole plasma condenses into bound excitons on a time scale of a few nanoseconds as demonstrated in Paper I. Then, when a $1s$ exciton population is present, the second optical pulse generates an electron-hole plasma within this population of $1s$ excitons. How this hot electron-hole plasma interacts with the exciton population is studied by analyzing the response of a probing THz pulse.

In principle, different interactions between the electron-hole plasma and the exciton population are possible. In an elastic scattering process between an electron or hole and an exciton, the scattering partners exchange energy and momentum, but the exciton remains bound.[152] Since the THz pulse probes not only optically active exciton states but also intraexcitonic transitions of excitons of any momentum, elastic scattering should hardly change the oscillator strength of those transitions. However, elastic scattering increases the linewidth of the transition. In contrast, an inelastic scattering process overcomes the Coulomb interaction so that the exciton breaks into an unbound electron-hole pair or scatters into a higher exciton state.[152] Since the response of both, an electron-hole plasma and higher exciton states, differs significantly from the response of a $1s$ exciton population, an inelastic scattering process should be visible in the THz response. To be precise, inelastic scattering is expected to increase the THz absorption at low energies while simultaneously decreasing the strength of the intraexcitonic resonance.

At this point, it should be mentioned that apart from the direct scattering of elec-

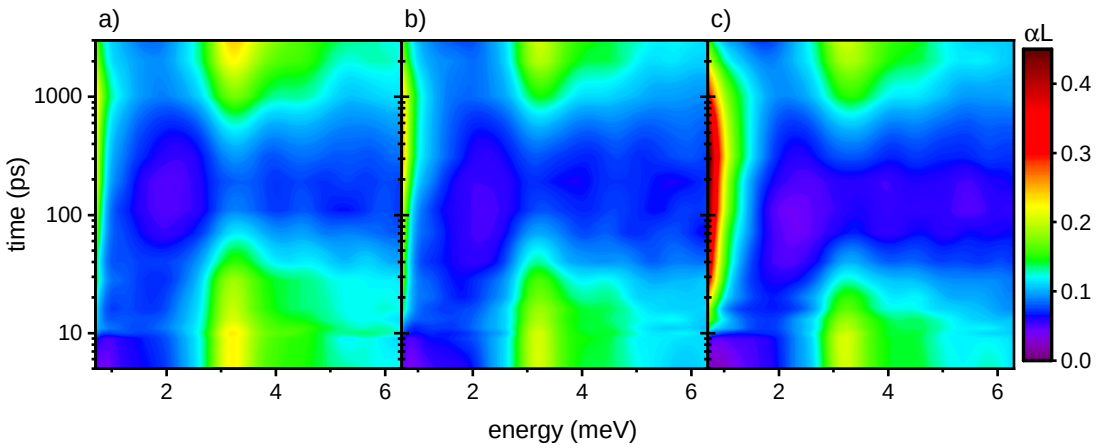

Figure 5.3.: Contour plots of the THz absorption for a constant photon density of the first excitation pulse and photon densities of a) $2.9 \cdot 10^{13}$ photons/cm^2, b) $5.9 \cdot 10^{13}$ photons/cm^2 and c) $1.0 \cdot 10^{14}$ photons/cm^2 for the second optical pulse. The second pulse is delayed by 6.7 ns with respect to the first pulse and its arrival, i.e., a zero time delay between the second optical and the THz probe pulse is set to 10 ps. Before the second pulse excites the sample all three images display a clear intraexcitonic resonance at 3.2 meV which indicates an almost pure 1s exciton population. With the arrival of the second pulse, however, the exciton population decays on a picosecond time scale, which is evident by the decreasing strength of the intraexcitonic resonance and the simultaneous increase of the absorption below 1 meV. This process occurs more rapidly with increasing photon density of the second pulse. Subsequently, the intraexcitonic resonance at 3.2 meV is restored on a nanosecond time scale.

trons or holes with excitons, scattering events between an exciton and a phonon, which is previously emitted by charge carrier relaxation, are also possible. Concerning this, however, theoretical studies show that electron-exciton scattering is much more efficient than exciton-phonon scattering.[152] This may explain why the possibility of an excitation-induced exciton-phonon scattering process is also neglected or not even discussed in other experimental studies.[70,72,97,117,122,166] Nevertheless, it is stated here that it is indistinguishable in the experiment whether an electron or hole scatters directly with the exciton population or whether the charge carriers first emit a phonon which then scatters with the exciton population. Therefore, when the term electron-exciton scattering is used in this thesis, it includes both the direct scattering as well as all scattering effects of the exciton with those phonons that are emitted by the electron.

The expected increase of the absorption at low energies and the simultaneous decrease of the intraexcitonic absorption peak for inelastic scattering processes is precisely what Fig. 5.3 shows. When the second optical pulse excites the sample at 10 ps, the strength of the intraexcitonic resonance at 3.2 meV begins to decrease while the absorption at energies below 1.5 meV increases. Here, the inelastic electron-exciton scattering is caught in the act. After the intraexcitonic resonance decays almost entirely on a time scale of several tens of picoseconds, the resonance reappears on a nanosecond time scale. On this time scale, the exciton population is restored.[184]

To quantify the decay of the exciton population, the intraexcitonic absorption is integrated from 2 meV to 6 meV and plotted against time for different photon densities of the

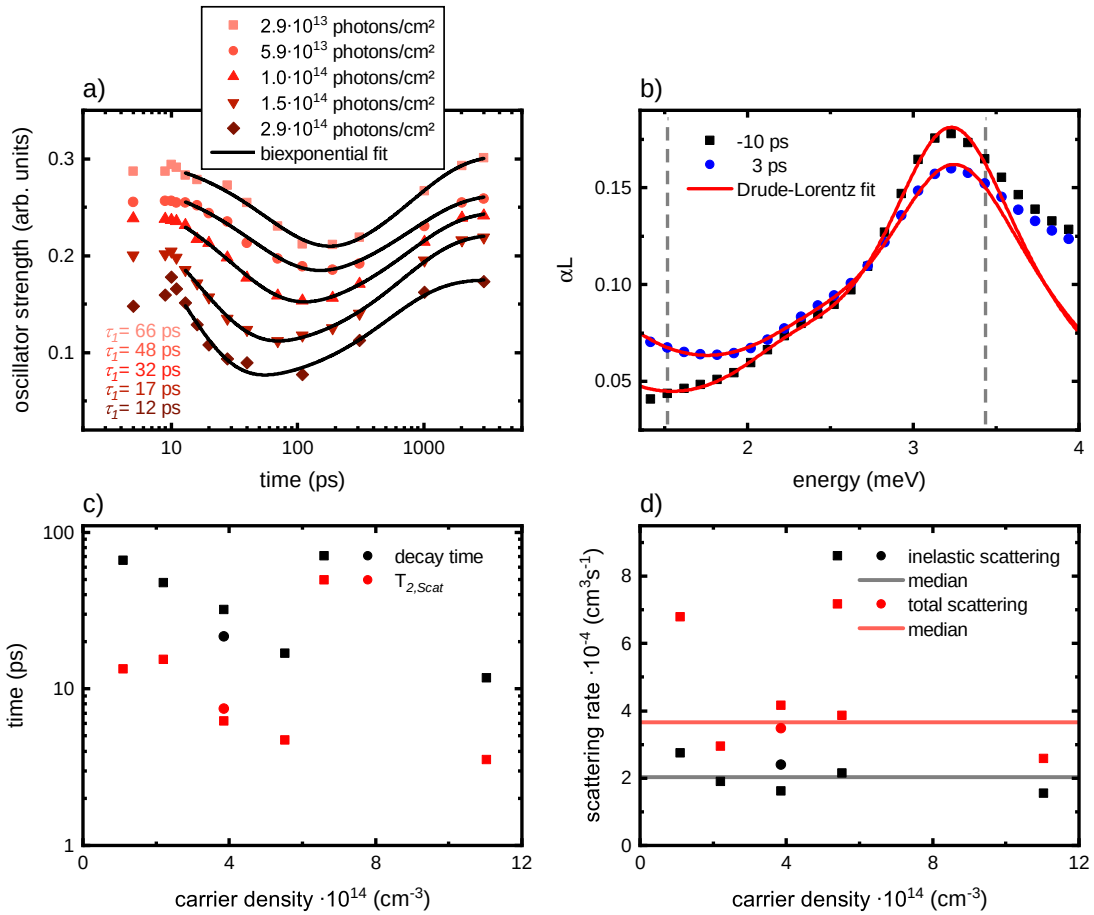

Figure 5.4.: a) Intraexcitonic absorption integrated from 2 meV to 6 meV for a photon density of $9.8 \cdot 10^{13}$ photons/cm^2 of the first optical pulse and five different densities of the second pulse. For better visualization, offsets have been added to the data points of different photon densities. A biexponential fit (black) yields the decay times τ_1. b) Exemplary fit of a Drude-Lorentz model to the intraexcitonic $1s-2p$ transition 10 ps before and 3 ps after the second optical pulse injects an electron-hole plasma. The borders of the fit are marked by vertical gray dashed lines. c) The decay times τ_1 (black data points) from the biexponential fit are plotted together with the dephasing due to electron-exciton scattering $T_{2,Scat}$ (red data points), which is calculated via Eq. 5.4. In addition to the results for a photon density of $9.8 \cdot 10^{13}$ photons/cm^2 (squares), the results for a photon density of $2.8 \cdot 10^{14}$ photons/cm^2 (circles) from the first excitation pulse are shown as well. d) The corresponding inelastic and total scattering rates that are calculated with Eq. 5.2 and Eq. 5.7, respectively, together with the respective median of the data points.

second pulse in Fig. 5.4 a). Fitting a biexponential function yields both the decay time and the reformation time of the exciton population. It turns out that the exciton population decays faster with increasing photon density of the second pulse. Explicitly, the decay time decreases continuously from 66 ps for a photon density of $2.9 \cdot 10^{13}$ photons/cm^2 to 12 ps for a photon density of $2.9 \cdot 10^{14}$ photons/cm^2 from the second pulse. The decay

time is connected with the scattering rate γ via:[166]

$$\gamma = \frac{2}{\tau_1 \cdot n}. \tag{5.2}$$

Here, n is the electron density that is injected into the conduction band by the second optical pulse. Since the decay of the exciton population is caused exclusively by inelastic scattering, it allows for the first time an experimental determination of an inelastic scattering rate in semiconductors. The experimental result is a median inelastic scattering rate of $2.0 \cdot 10^{-4}\,\mathrm{cm^3 s^{-1}}$ as shown in Fig. 5.4 d).
While only inelastic scattering processes destroy the exciton population, all scattering processes affect the linewidth of a transition. Therefore, similar to transmission or PL experiments, the linewidth before and after excitation by the second optical pulse can be used to gain insights about the total scattering rate.[97,122,203] For this, the homogeneous linewidth Δ_{Hom} of the intraexcitonic $1s-2p$ transition 10 ps before and 3 ps, 6 ps and 10 ps after the second pulse excites the sample is determined via a Drude-Lorentz fit, which is exemplary displayed in Fig. 5.4 b) for two time delays. Details about the Drude-Lorentz model are given in Paper V. The homogeneous linewidth Δ_{Hom} of the transition is linked to its dephasing time T_2 via:[70]

$$T_2 = \frac{2}{\Delta_{Hom}}. \tag{5.3}$$

The dephasing time T_2 itself is composed of a natural dephasing time of the transition $T_{2,Nat}$ and an additional dephasing due to the electron-exciton scattering $T_{2,Scat}$. Since the natural dephasing time $T_{2,Nat}$ is obtained from the homogeneous linewidth 10 ps before the second pulse arrives, the dephasing due to electron-exciton scattering can be calculated with:[166]

$$T_{2,Scat} = \frac{T_2 \cdot T_{2,Nat}}{T_{2,Nat} - T_2}. \tag{5.4}$$

The resulting values of $T_{2,Scat}$ are depicted in Fig. 5.4 c) for the respective excitation conditions. However, since the $1s-2p$ transition consists of two states, the $1s$ and the $2p$ state, the lifetime of both is shortened by additional scattering. Accordingly, $T_{2,Scat}$ consists of the additional dephasing due to electron scattering of the $1s$ states $T_{2,Scat,1s}$ as well as the $2p$ states $T_{2,Scat,2p}$:[3]

$${T_{2,Scat}}^{-1} = {T_{2,Scat,1s}}^{-1} + {T_{2,Scat,2p}}^{-1}. \tag{5.5}$$

Under the assumption that both states are equally influenced by scattering one obtains:

$$T_{2,Scat,1s} = 2 \cdot T_{2,Scat}. \tag{5.6}$$

With this the total scattering rate γ_{Tot} of the $1s$ exciton with the additional electron-hole plasma can be calculated:

$$\gamma_{Tot} = \frac{2}{T_{2,Scat,1s} \cdot n} = \frac{1}{T_{2,Scat} \cdot n}. \tag{5.7}$$

In this way, the use of the median yields a total electron-exciton scattering rate of $3.7 \cdot 10^{-4}\,\mathrm{cm^3 s^{-1}}$ as shown in Fig. 5.4 d). This scattering rate is composed of the elastic as well as the inelastic scattering. Since the inelastic scattering rate is determined by the decay of the exciton population, this provides access to the elastic scattering rate as well.

The elastic scattering rate is the difference between the total and the inelastic scattering rate. This results in an elastic scattering rate of $1.7 \cdot 10^{-4}\,\mathrm{cm^3 s^{-1}}$. Accordingly, for the excitation conditions used here with an excess energy of the electron-hole plasma of $\sim$50 meV, the elastic scattering rate is with $1.7 \cdot 10^{-4}\,\mathrm{cm^3 s^{-1}}$ comparable to the inelastic scattering rate of $2.0 \cdot 10^{-4}\,\mathrm{cm^3 s^{-1}}$.
Unfortunately, for this conclusion it is assumed that the $1s$ and $2p$ states have the same scattering rate. Of course, this does not have to be the case. Therefore, the total scattering rate of an electron-hole plasma with $1s$ excitons can probably be determined more precisely by Four-wave mixing experiments as performed by Schultheis *et al.*[166] However, for indirect semiconductors such as Ge, these FWM experiments are not suitable because in this case, an optically induced polarization dephases quasi-instantaneously due to the required interaction with a phonon. Thus, the approach of the spectroscopy of intraexcitonic transitions seems to be the method of choice to gain insights into electron-exciton scattering in indirect semiconductors. Besides, the introduced method to investigate the inelastic electron-exciton scattering processes is, of course, not limited to bulk Ge. Thus, similar measurements on thin direct semiconductor layers or QW structures that can be investigated concurrently by FWM might allow for an even more precise separation of elastic and inelastic scattering processes in the future.

6. Charge-transfer excitons

In today's technological age, the often microscopically small semiconductor devices are indispensable. Despite their widespread use, the market for semiconductor devices continues to grow rapidly.[205] In many cases, the reason for this growth is the improved performance and functionality of the devices, which is made possible by their increasing miniaturization.[20,21,48] Due to this ongoing miniaturization, modern electric and optoelectronic devices often comprise a large number of individual material layers with thicknesses in the nanometer regime.[196,204] As a result, their performance is increasingly dominated by the microscopic properties of the boundaries between adjacent materials.[104] A promising probe of these properties is the so-called charge-transfer exciton (CTX), which is a Coulomb bound quasiparticle where electron and hole are located on opposite sides of an internal interface. Since its wave function extends across an intermediate layer, it contains quantum-level information about the charge transport and internal interfaces.
To study the properties of CTXs, a semiconductor heterostructure is designed where the conduction band minimum and the valence band maximum are on different sides of an intermediate barrier. Here, the attractive Coulomb interaction can lead to the formation of a spatially indirect exciton, i.e., the CTX. The properties and the coherent as well as the incoherent dynamics of CTXs are investigated using both optical and THz spectroscopy techniques which are supported by a microscopic theory.[86,87]

6.1. Sample design

In order to examine CTXs under optimum conditions, a suitable sample is required first. This sample has to meet the mandatory requirement that the conduction band minimum and the valence band maximum are located in spatially separated QWs so that a type-II band alignment exists. In addition, there should be a type-I QW reference sample to provide a direct comparison between charge-transfer and regular excitons. Besides these mandatory conditions, numerous other properties are desirable from an experimental point of view. These would be:

1. The intraexcitonic resonance of the CTX should be between 0.5 and 2 THz to investigate it with the most sensitive settings of our OPTP setup.

2. The CTX should be easily distinguishable from both a regular exciton and a plasma response.

3. The CTX should feature an excitonic $1s$ resonance in the linear absorption to enable resonant excitation conditions.

In cooperation with the group of Prof. W. Stolz from the Laboratory for Structural and Technological Research, who evaluated the possibilities of producing the sample, and the theoretical calculations from the group of Prof. S. W. Koch, we designed a GaInAs/GaAs/GaAsSb heterostructure on a GaAs substrate. To be precise, the theoretical modeling has shown that 8 nm wide QWs with a 1 nm thick GaAs barrier in between

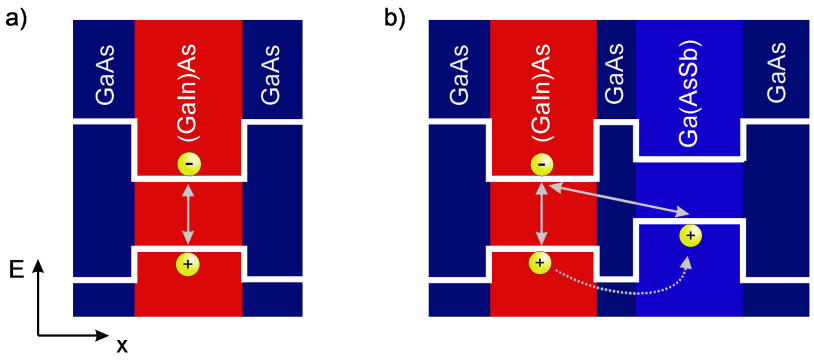

Figure 6.1.: a) The schematic band structure of the type-I heterostructure has a spatially direct transition within the GaInAs layer. The yellow spheres represent electrons in the conduction or holes in the valence band. b) In the type-II heterostructure, holes that are injected into the GaInAs layer can tunnel through the GaAs barrier into the GaAsSb layer. Together with electrons in the conduction band of the GaInAs layer, this enables a spatially indirect transition, which is the energetically lowest transition in this heterostructure.

and In and Sb concentrations of 5 % and 3 %, respectively, would be a good choice.[183] A type-I reference sample is generated by omitting the GaAsSb layer during the growth process. Such a GaInAs QW sample should feature an intraexcitonic resonance around 7 meV (1.69 THz).[60] At the same time, according to the theoretical modeling, the intraexcitonic resonance of the CTX should be 3.6 meV (0.87 THz) for the designed type-II structure. Thus, the intraexcitonic resonances are in the ideal frequency range between 0.5 and 2 THz and are easily distinguishable from each other. Furthermore, for the 1 nm thick GaAs interlayer, the spatial separation should be sufficiently small to see the resonance of the 1s state of the CTX in the linear absorption.
Using the specifications from the theoretical modeling, samples with 50 repetitions of GaInAs/GaAs/GaAsSb double quantum wells (DQWs) were grown embedded in additional GaAs spacer layers to build a stack of uncoupled DQWs. A subsequent analysis of the grown structure with high-resolution X-ray diffraction (HR-XRD) revealed a QW thickness of 7.7 nm separated by a 1 nm thick GaAs interlayer and In and Sb concentrations of 5.8 % and 3.3 % respectively.[183] The type-I reference sample consists of 50 repetitions of the GaInAs QW embedded in GaAs. Figure 6.1 shows a schematic representation of the sample structure together with the band structure for the type-I reference sample [a)] and the type-II sample [b)]. A modeled band structure of the type-II heterostructure together with the corresponding wave functions can be found in Fig. 2.1.

6.2. Absorption of charge-transfer states

The grown samples are optically characterized by linear absorption. Together with the theoretical modeling, this allows for an initial check if the desired band structure has been realized. Figure 6.2 shows the linear absorption of the samples at 10 K. The type-I reference sample, which is depicted in red, reveals the typical absorption of a QW sample with a distinct resonance of the regular 1s exciton at 1.465 eV. For energies below this resonance, the absorption goes towards zero. Above, a step-like character can be suspected before the absorption is dominated by the band edge of the rather thick GaAs substrate. Since the sample with a type-II band alignment also contains

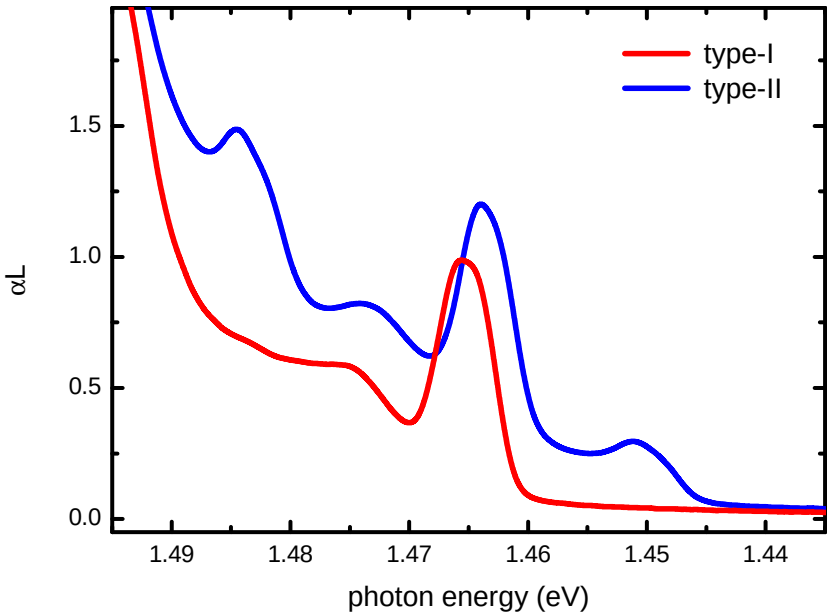

Figure 6.2.: Linear absorption of the type-I reference sample (red) and the type-II heterostructure (blue). The type-I reference shows a distinct resonance at 1.465 eV, which is the excitonic transition in the GaInAs QWs. On the other hand, the type-II heterostructure has the energetically lowest resonance at 1.451 eV. This is the spatially indirect transition of the CTX.

the GaInAs QWs, it shows its distinct excitonic resonance at ∼1,465 eV as well. In addition, however, the type-II heterostructure produces further resonances. Thus, there is an additional resonance at 1.485 eV, which can be related to the direct transition in the GaAsSb QWs, and another resonance at 1.451 eV. Together with the microscopic theory, this much weaker resonance at 1.451 eV can be assigned to the spatially indirect transition from the GaAsSb QW to the GaInAs QW.[183] More precisely, this charge-transfer transition corresponds to the 1s resonance of the CTX. A microscopic modeling of the linear absorption of this sample is presented in Paper II.

6.3. Coherent dynamics of charge-transfer excitons

After identifying the respective resonances utilizing linear absorption and a microscopic theory, the coherent dynamics of these states can be investigated systematically with FWM spectroscopy in self-diffraction geometry. Therefore, the output of a mode-locked titan-sapphire laser emitting pulses with a duration of ∼100 fs and a FWHM of 17 meV at a repetition rate of 80 MHz is used. The emission energy of the laser is tunable which enables different excitation conditions. Two of those excitation conditions are shown in Fig. 6.3 a) in relation to the linear absorption of the type-II heterostructure.

FWM spectroscopy of the conventional type-I reference sample yields a typical signal for resonant excitation conditions.[112,165] The polarization created by the first optical pulse dephases on a time scale of ∼1 ps, as can be seen in Fig. 6.3 c). Since the short but spectral broad pulse creates not only a 1s excitonic polarization but also polarizations of 2s and higher states, an interference of these states occurs. This interference results in a beating pattern that superimposes the exponential decay of the coherent 1s polarization.[47,57,98] The frequency of this beating is ∼1.7 THz which corresponds to an energy

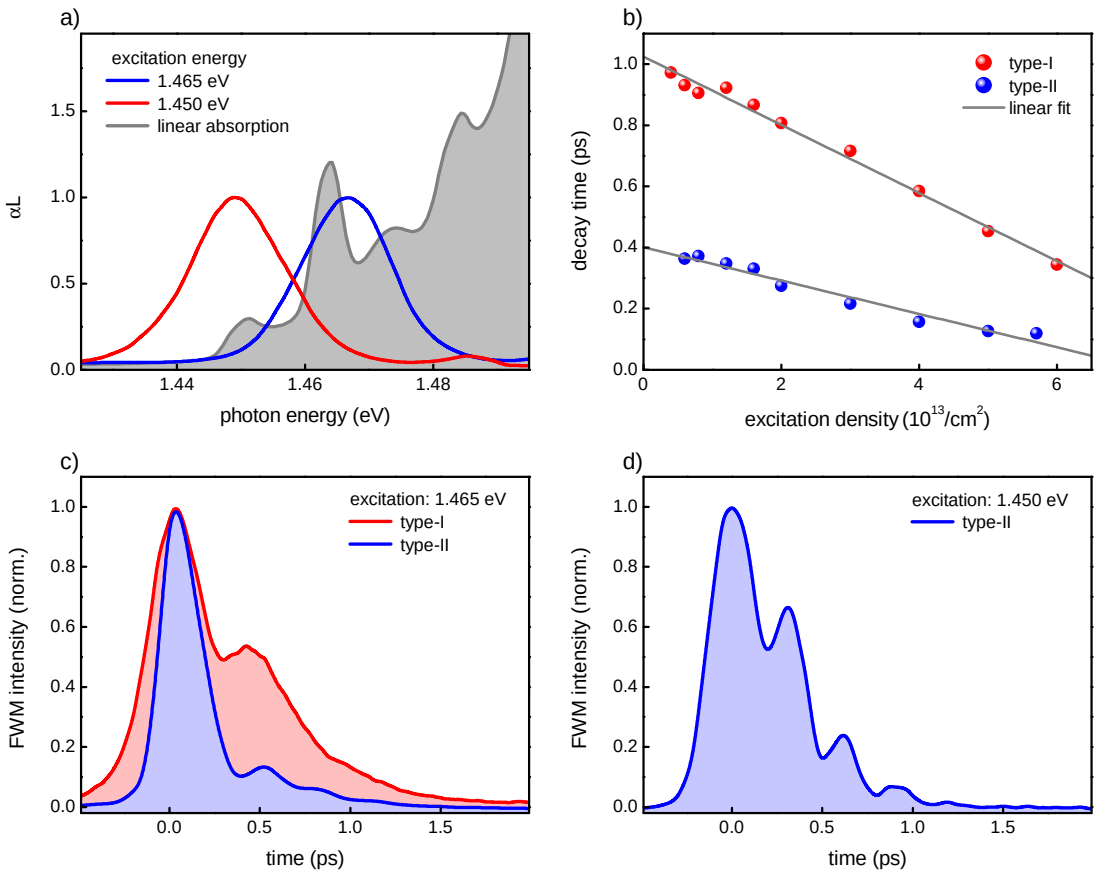

Figure 6.3.: a) Excitation conditions for the FWM experiments in relation to the linear absorption of the type-II heterostructure (gray). By energetically shifting the driving laser pulses, the excitonic resonances are excited to different extents. b) The density-dependent decay times of the FWM signal for the type-I and the type-II sample. The linear fit (gray) extrapolates the respective zero-density decay time. c) FWM transients of the two samples at an excitation energy of 1.465 eV and d) for the type-II heterostructure at an excitation energy of 1.450 eV.

difference of 7 meV between the 1s and 2s exciton state.
In contrast, resonant excitation of the regular exciton at 1.465 eV in the type-II heterostructure shows a different behavior. Here, a very fast decay of the coherent polarization takes place within the first ∼200 fs. This rapid decay is induced by the charge-transfer of holes from the GaInAs layer into the GaAsSb layer, which instantaneously destroys the coherent polarization of the regular exciton. However, when the excitation pulse is tuned to lower energies, the fast initial decay vanishes and a distinct beating signature appears [see Fig. 6.3 d)]. A Fourier transformation of the time trace yields a beating frequency of ∼3.1 THz, which is much higher than the beating frequency of the type-I reference sample. In the type-II sample, an interference between the polarization of regular 1s excitons from the GaInAs layer and the 1s state of CTXs is possible. Linear absorption reveals an energy difference between the resonance of the CTX and the regular exciton of 13 meV (3.15 THz), which fits very well to the observed beating frequency of 3.1 THz. Accordingly, the beating pattern stems from the interference between the coexisting spatially direct and indirect excitonic polarizations, i.e., quantum beats between

regular and CT excitons.[102] Interestingly enough, this beating and thus the polarization of the regular exciton dephases much slower than after its resonant excitation at 1.465 eV. This may be an indication that the existence of a CTX polarization inhibits the decay of the coherent polarization of the regular exciton. Since we hold the charge transfer process responsible for the decay of the coherence of the regular exciton, this also implies that the existence of CTXs inhibits the charge carrier transfer. Hints for such an impact of a CT population on the charge carrier transfer dynamics have already been identified in my master thesis.[181]
Fitting an exponential function to the FWM transients gives the decay time of the coherent polarization which is shown in Fig. 6.3 b). By performing an excitation density series for both, the type-I reference sample and the type-II heterostructure after resonant excitation to the respective lowest resonance, the low-density decay times of the coherence in the individual samples are derived. The result is a low-density decay time of slightly above 1 ps for the coherent polarization of the regular exciton in the reference sample and 0.4 ps for the coherent polarization of the CTX. Thus, the coherent polarization of the CTX is lost almost three times faster than that of the regular exciton in the reference sample. Since, compared to the regular exciton in the type-I sample, the wave function of the CTX is extended over two additional inner interfaces and another material composition, the faster decay can be attributed to additional scattering at internal interfaces. If this is the case, FWM spectroscopy of CTX could be a feasible method to assess the quality and the impact of internal interfaces.

6.4. Incoherent dynamics of charge-transfer excitons

In addition to the coherent dynamics, the incoherent dynamics of excitons are explored via OPTP spectroscopy. The setup is driven by a 1 kHz amplifier system in combination with an OPA. The OPA allows to tune the central frequency of the pulses from the visible to the near infrared range. A subsequent pulse shaper cuts the spectrally broad pulses from the OPA before they excite the sample. This enables a targeted excitation of excitonic resonances that are identified in the linear absorption.
First, consider resonant excitation conditions of the respective energetically lowest resonance. In the type-I reference sample, this corresponds to the resonant excitation of the regular $1s$ exciton, whereas in the type-II heterostructure this is the resonant excitation of the $1s$ state of the CTX. Subsequently, the THz pulse probes the samples 5 ps after the optical excitation. Figure 6.4 illustrates the absorption and the change of the real part of the dielectric function of the two samples in the THz frequency range. For the type-I reference sample, there is a resonance in the THz absorption due to the intraexcitonic $1s-2p$ transition at 7 meV in combination with an oscillatory response of $\Delta\epsilon$. Such a THz response is typical for an almost pure $1s$ exciton population in a type-I QW structure and has been described numerous times in the literature.[60,74,82,165] Furthermore, this transition energy fits perfectly to the beating frequency of 1.7 THz between the excitonic $1s$ and $2s$ state that we observe in the FWM experiments. In contrast, the type-II heterostructure shows a much broader resonance in the absorption with a maximum at 3.3 meV. Again this is connected to an oscillatory signature of $\Delta\epsilon$ with a turning point at 3.3 meV. Apparently, we witness the intraexcitonic resonance of the CTX, which reveals the existence of a CTX population.[99] The spatial separation of electron and hole reduces the Coulomb interaction, which, as predicted by theory, leads to a lower binding energy and thus to a lower energy of the intraexcitonic $1s-2p$ transition compared to the regular exciton in the type-I reference sample.

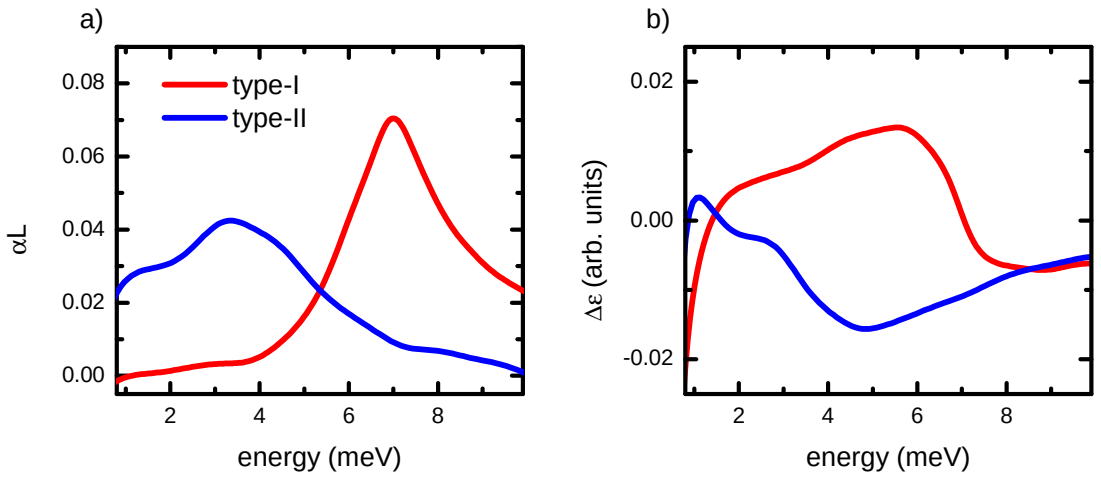

Figure 6.4.: a) THz absorption (αL) and b) the change of the real part of the dielectric function ($\Delta\epsilon$) for the type-I and the type-II heterostructure after resonant excitation to the respective energetically lowest resonance.

At sample temperatures of 10 K and for excitation densities clearly below the Mott density, the observed 1s exciton population should hardly decompose. This is confirmed by the fact that larger time delays between optical pump and THz probe pulse produce the same spectral shape of the response. However, recombination reduces the amplitude of the pump-induced THz response. In this case, the amplitude at any point in the time domain is proportional to the exciton population.[147] This allows the investigation of the recombination dynamics at a high temporal resolution by measuring the transient of the pump-induced change of the THz pulse (ΔE_{THz}) at a prominent feature in the time domain. Figure 6.5 d) shows the measured transients for both samples. Clearly, the population of the type-I sample decays much faster than the population of the type-II sample. Both transients can be described very well by a simple exponential function, as anticipated for a population of excitons.[25] The transients reveal time constants of 1.1 ns and 2.5 ns, respectively. Again, a recombination time of 1.1 ns is typical for a type-I QW structure.[43] The reason for the substantially slower recombination in the type-II heterostructure is the spatially extended wave function of the CTX, which reduces the radiative recombination probability.

Initially, after non-resonant excitation conditions, a Drude-like absorption signature is observed for both samples [see Fig. 6.5 b)]. This indicates the presence of a conductive electron-hole plasma. However, this response is also observed when the type-II heterostructure is excited resonantly to its regular exciton [see Fig. 6.5 a)]. The lack of an intraexcitonic resonance of the regular exciton directly after its resonant excitation is a further indication for the extremely fast decay of regular exciton polarizations in the type-II heterostructure. This is consistent with the observations made under similar excitation conditions via FWM spectroscopy. Most likely the polarization of the regular exciton decays directly into a charge-transfer population due to the fast hole transfer through the 1 nm thick intermediate barrier. Within a few hundred picoseconds after the optical excitation, a shoulder at about 2.5 meV emerges from the initial Drude-like absorption and finally forms a distinct resonance at about 3 meV after 1 ns. Here, the formation process of a 1s CTX population out of an electron-hole plasma and/or higher exciton states is captured. A response that is very consistent with the response observed a few picoseconds after the resonant excitation of the CTX indicates an almost complete

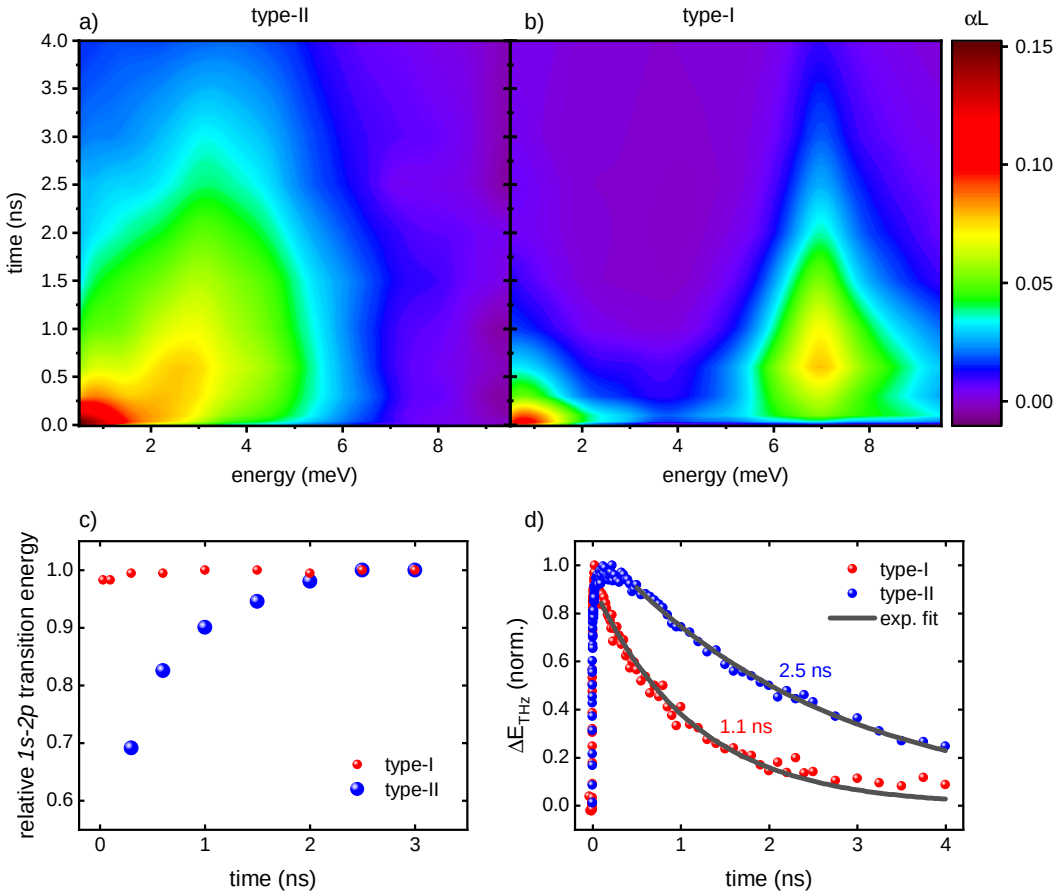

Figure 6.5.: a) Time-resolved THz absorption (αL) of the type-II heterostructure after resonantly exciting its regular exciton. b) Comparable data of the type-I heterostructure after non-resonant excitation conditions. A Drude-like response initially dominates the THz absorption of both before resonances develop on a time scale of several hundred picoseconds. The resonances occur in the vicinity of 3 meV and 7 meV for the type-II and the type-I heterostructure, respectively, and are the consequence of the respective intraexcitonic $1s-2p$ transition. c) The measured $1s-2p$ transition energy in the type-I and the type-II heterostructure relative to 6.99 and 3.17 meV, respectively, is plotted over time. Although the transition energy for the type-I sample remains unchanged, the relative transition energy for the type-II sample is initially only 0.7 before moving towards 1 with increasing time delay and thus decreasing charge carrier density. d) The pump-induced change of the THz pulse (ΔE_{THz}) after resonant excitation to the energetically lowest resonance of the type-I and the type-II sample. After optical excitation, the pump-induced change of the THz pulse decays exponentially (gray fit) with time constants of 1.1 and 2.5 ns.

condensation into the $1s$ state within a few nanoseconds.

The type-I reference sample also shows an exciton formation process out of a Drude-like plasma response on a comparable time scale after non-resonant excitation conditions. In contrast to the type-II heterostructure, however, there is no density-dependent shift of the intraexcitonic resonance energy [see Fig. 6.5 c)]. Similarly, other investigations as well as own investigations on GaInAs QW samples showed no energy shift of the intraex-

citonic resonance either.[60] It seems that an energetic shift of the resonance from 2.2 meV to 3.2 meV, as observed here during the formation process of CTXs, is a specific property of these excitons. Together with the theoretical analysis, the observed energetic shift can be attributed to the Pauli-blocking effect, which indicates that the CTX is more sensitive to its fermionic substructure than the regular exciton. For a more detailed experimental and theoretical analysis of the CTX, please refer to Paper II.

7. Enhanced absorption in type-II heterostructures

Within the scope of this work, type-II heterostructures are also investigated utilizing optical pump-optical probe spectroscopy. In particular, the charge carrier transfer dynamics in type-II heterostructures are analyzed. For this purpose, femtosecond OPOP spectroscopy has proven to be a suitable experimental method.[42,44,45] Our primary focus of the OPOP spectroscopy on type-II heterostructures has been the influence of the morphology of the internal interfaces on charge carrier dynamics. Parts of the results of these studies are published in Ref. 158. However, in the course of these investigations, astonishing spectral signatures have occurred. This chapter deals with these spectral signatures, which indicate an excitation-induced enhancement of the excitonic resonance in the linear absorption of type-II heterostructures.

The samples under study consist of 5 periods of GaInAs/GaAs/GaNAs DQWs embedded in GaAs cap layers. In contrast to the samples presented in Chapter 6, here the electrons in the conduction band of the GaInAs layer can tunnel through the barrier into the GaNAs layer as shown exemplarily in Fig. 7.1 b). Beyond that, due to the greater barrier thicknesses of 1.5 nm, 4.0 nm and 6.0 nm and the deeper potential wells, a spatially indirect transition does not show up in the linear absorption of these samples. This enables the exclusive excitation of charge carriers in the GaInAs QWs. Experimentally, this is implemented by optical excitation at a central energy of 1.34 eV. A white-light supercontinuum then probes the GaInAs QWs. As a reference, samples with a lower N-concentration in the GaNAs layer are used, so that the conduction band minimum is located in the GaInAs layer, as illustrated in Fig. 7.1 a). A more detailed description of

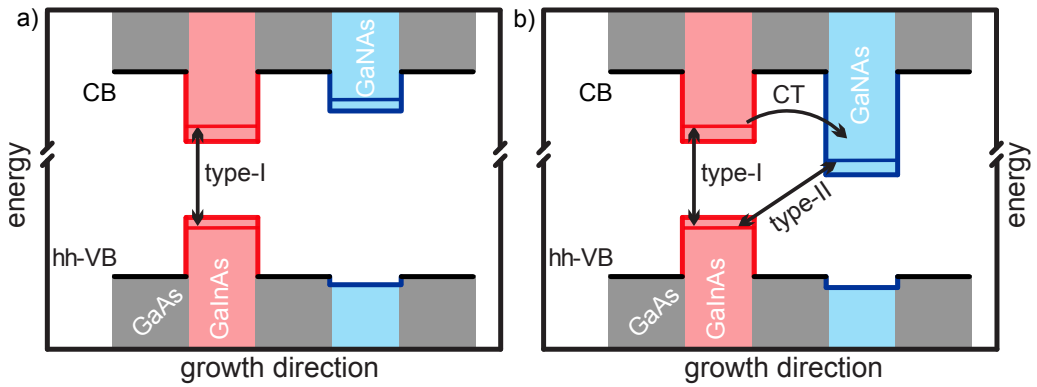

Figure 7.1.: A schematic of the band structures of the GaInAs/GaAs/GaNAs heterostructures. In a) the nitrogen concentration in the GaNAs QWs is so low that the energetically most favorable positions for electrons and holes are located in the GaInAs QWs. In b) the nitrogen concentration is increased so that the minimum of the conduction band is found in the GaNAs QWs. In this scenario, electrons that are injected into the CB of the GaInAs layer can tunnel through the GaAs barrier into the GaNAs layer.

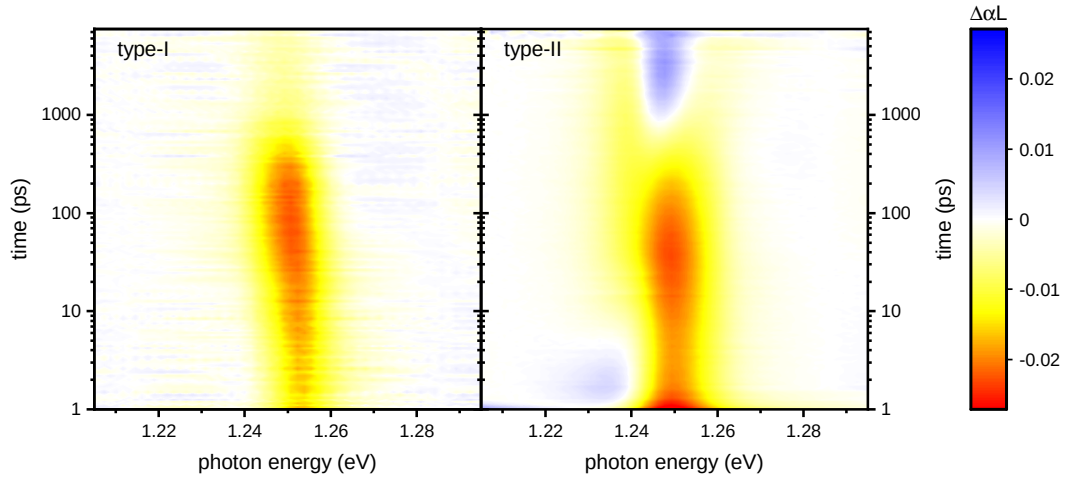

Figure 7.2.: Left panel: Contour plot of the OPOP spectra from a reference sample with a 1.5 nm thick GaAs intermediate barrier and a type-I band alignment. Right panel: Contour plot of a sample with the same barrier thickness but a higher nitrogen concentration, which results in a type-II band alignment. The plot illustrates the pump-induced changes of the optical absorption ($\Delta\alpha L$) for time delays between pump and probe pulse ranging from femtoseconds up to several nanoseconds. The optical excitation is shifted to 1 ps in order to plot a logarithmic time scale.

the sample structure is found in Paper III.
Directly after optical excitation, both the reference samples with a type-I band alignment and the type-II heterostructures show a bleaching signature in the differential absorption at the energy of the excitonic 1s state of the GaInAs QWs. The bleaching signature of the differential absorption can be traced exemplarily for a reference sample and a type-II heterostructure in Fig. 7.2. In OPOP spectroscopy, a bleaching signature is indicated by negative values of the differential absorption ($\Delta\alpha L$). The reduced absorption is the result of phase-space filling and Coulomb screening due to the optical excitation of charge carriers.[73,76,95,161] Within the next picoseconds, the type-II heterostructures show a recovery of the absorption. This recovery of the absorption is caused by the charge carrier transfer from electrons in the GaInAs QWs into the GaNAs QWs.[42,44,45] Accordingly, this recovery does not occur in the reference samples with a type-I band alignment. In addition, the recovery of the absorption becomes slower with increasing barrier thickness in type-II heterostructures.[158,182] To be precise, recovery times of about 300 fs, 1 ps and roughly 15 ps are observed for barrier thicknesses of 1.5 nm, 4.0 nm and 6.0 nm, respectively. For other type-II heterostructures, charge carrier transfer times of the same order of magnitude have been observed in the literature.[137,139,142] Following the carrier transfer, the excited electron-hole plasma cools down on a time scale of tens of picoseconds. The cooling of the electron-hole plasma reduces the excitonic absorption, which can be observed both in the reference samples and in the type-II heterostructures.[126,156,173] After the differential absorption reaches a minimum, the signal recovers for all samples due to recombination.
However, while the signal for type-I samples steadily decreases to zero, a local peak forms in the middle of the excitonic 1s heavy-hole (hh) transition in the type-II heterostructures on a time scale of hundreds of picoseconds. This remarkable feature of a positive differential absorption surrounded by a negative differential absorption denotes a linewidth

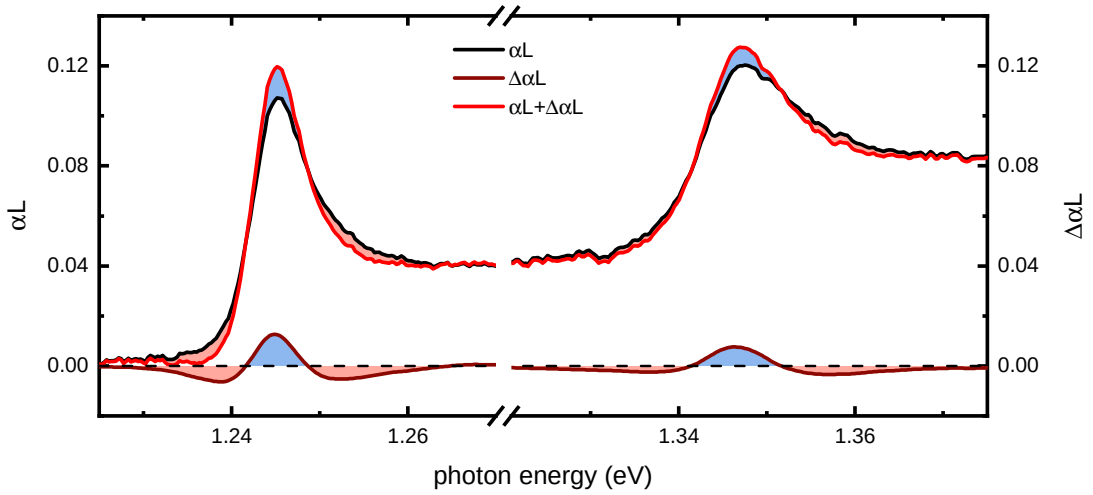

Figure 7.3.: The linear absorption (black line) of a type-II heterostructure with a 6 nm thick GaAs barrier is presented together with its differential absorption (dark red line) and the sum of linear and differential absorption (red line). The unexcited sample (black line) already shows distinct excitonic hh and lh resonances in the optical absorption. Nevertheless, an optical excitation at 1.34 eV with a photon density of $9.1 \cdot 10^{13}$ photons/cm^2 can lead to an even sharper and more pronounced excitonic absorption. The $\Delta\alpha$L signature shown here occurs 5 ns after the optical excitation.

narrowing. In fact, spectral integration over the entire signature provides an integrated differential absorption close to zero. This proves that the linewidth of the excitonic transition has become narrower, whereas the excitonic oscillator strength is unchanged. Such behavior is exceptionally intriguing. In general, the opposite effect is expected from an optical excitation in a semiconductor heterostructure: a line broadening accompanied by a reduction of the oscillator strength.[23,76,96,161]

By changing the experimental parameters, the observed linewidth narrowing is examined more closely. Obviously, the excitation density influences the differential absorption. High excitation densities always lead to a bleaching signature due to the dominant effects of phase-space filling. Sufficiently low carrier densities are therefore necessary to observe an enhanced absorption due to a linewidth narrowing. Yet, a low carrier density is not sufficient. For the sample with a 1.5 nm thick inner GaAs barrier a time of at least 10 ps is necessary for a positive differential absorption to develop. An increase of the charge carrier density delays the appearance of the signature. Nevertheless, the peak value of the positive differential absorption increases with excitation density. Thus it can be excluded that the reason for the delayed appearance at higher excitation densities is solely the need to reduce the number of charge carriers via recombination. Instead, higher carrier densities delay the occurrence but at the same time are, up to a certain density, necessary to increase the signature of a positive differential absorption. Only when the carrier density is too high, recombination is required first in order to reach a lower carrier density at which the phase-space filling no longer dominates the differential absorption. For photon densities of $6.6 \cdot 10^{14}$ photons/cm^2 and $9.1 \cdot 10^{13}$ photons/cm^2 for the respective heterostructures with the 1.5 nm and 6.0 nm GaAs barrier, a value of the differential absorption of up to 0.01 is reached 5 ns after optical excitation. This boosts the excitonic absorption peak by more than 10 %. Figure 7.3 depicts the linear absorption of a type-II sample with a 6.0 nm thick barrier together with its differential

absorption 5 ns after the optical excitation as well as the sum of linear and differential absorption. This illustration highlights the significant pump-induced enhancement of the excitonic resonance due to a linewidth narrowing. Furthermore, it demonstrates that the linewidth narrowing is not limited to the excitonic $1s$ hh resonance but also occurs for the $1s$ light-hole (lh) resonance.

Even though the linewidth narrowing occurs at all barrier thicknesses investigated, its formation dynamics reveal a distinct dependence on the barrier thickness. In fact, a positive differential absorption occurs faster for samples with thinner barriers. This may tempt to make electric field effects due to carrier separation in the type-II heterostructures responsible for the observed effect. Then, on the other hand, the effect should occur quasi-instantaneously with the charge carrier transfer. However, with a time delay of at least 10 ps for the sample with the 1.5 nm and more than 100 ps for the sample with the 6.0 nm barrier until a positive $\Delta\alpha L$ signal appears, the effect of a linewidth narrowing is delayed by at least one order of magnitude to the charge carrier transfer in the respective samples. Moreover, electric field effects should result in spectral shifts of the excitonic resonance.[130,143] Again, such spectral shifts do not occur. Therefore, field effects can be excluded at least as the sole cause of the observed effect. Beyond that, the effect is not limited to the previously considered sample temperatures of 10 K but occurs even faster at higher and ambient temperatures.

Even if no clear physical explanation for the astonishing effect of a linewidth narrowing in optically excited type-II heterostructures could be identified by varying the experimental parameters, at least some conceivable explanations such as field effects could be excluded. For a more detailed discussion as well as more experimental data, the reader is referred to Paper III and the corresponding supplemental material.

In total, we observe a linewidth narrowing in all 9 GaInAs/GaAs/GaNAs type-II heterostructures investigated over the last few years. Recently, we also noticed similar signatures in the differential absorption of GaInAs/GaAs/GaAsSb type-II heterostructures at room temperature. Here it seems that the linewidth narrowing occurs both in the excitonic resonance of the GaInAs and the GaAsSb QWs. However, since the QWs are energetically much closer to each other and are also close to the GaAs substrate, as shown in Fig. 6.2, the investigation of these samples is more challenging. Nonetheless, the effect appears to be independent of whether electrons or holes remain in the respective QW and the evidence increases that an optically induced linewidth narrowing is a universal effect in type-II heterostructures. Future investigations may show whether one of the most fundamental properties of matter - the absorption of light - might be enhanced in a similar way in other type-II-like systems.

8. Summary

This thesis deals with the spectral and dynamic properties of excitons and excitonic resonances in semiconductors and semiconductor heterostructures. The intention is to expand the knowledge about excitons, their spectral properties, and their dynamics. The foundation for this are the results of several scientific publications in this field, which have been published as part of my doctoral studies.
Chapter 1 introduces the topic by highlighting the tremendous importance of semiconductors and semiconductor-based devices for our modern society. In this context, the unique impact of excitons on the electro-optical properties of semiconductors is discussed and the relevance of a profound understanding of excitons, especially concerning the progressive miniaturization of semiconductor devices, is elaborated. Chapter 2 covers the physical principles of semiconductors and light-matter interaction, which form the theoretical backbone for the conducted experiments and their analysis. The applied experimental techniques are explained in Chapter 3. Particular attention is paid to optical pump-terahertz probe spectroscopy, which has been utilized intensively in this work and is one of the most important techniques to study excitons and their dynamics in semiconductors. Afterward, the experimental results are presented in chapters 4 to 7.
Chapter 4 demonstrates via optical pump-terahertz probe spectroscopy that initially after a non-resonant optical excitation there is no exciton population present but only an electron-hole plasma in bulk germanium as well as in germanium and GaInAs quantum wells. In all cases, excitons are formed on a time scale of several tens to hundreds of picoseconds out of a pure electron-hole plasma. Several claims and observations on this topic in the scientific literature according to which a high proportion of excitons forms on a subpicosecond time scale are not supported for the samples investigated here.[82, 188, 191] While in bulk germanium a delayed exciton formation is observed, the exciton formation starts immediately after a non-resonant optical excitation in GaInAs quantum wells. Here, two different time periods, one of 14 ps and one of 344 ps, can be determined for the formation. Furthermore, theoretical predictions that at carrier densities far below the Mott density excitons form faster with increasing charge carrier density are confirmed in this chapter.
Chapter 5 is focused exclusively on optical pump-terahertz probe experiments at bulk germanium. In section 5.1 an energetic splitting of the intraexcitonic $1s-2p$ resonance is detected. Soon before, this spectral behavior was predicted theoretically in germanium. Accordingly, the splitting of the intraexcitonic resonance is caused by the effective mass anisotropy of the L-valley electrons which leads to a splitting of the energy levels of the $2p$ states of the exciton. The ionization of an exciton population by strong terahertz pulses can be observed in section 5.2. Not only ionizes the exciton population for terahertz field strengths of 2.4 kV/cm completely, but also the spectral properties of the intraexcitonic transition are recorded as a function of field strength. It turns out that with increasing field strength of the terahertz pulse, thus for an increasing ionization of the exciton population, there is a broadening of the intraexcitonic $1s-2p$ resonance that is accompanied by a blueshift of up to 10 %. Section 5.3 investigates the scattering of free electrons and holes with an incoherent population of excitons. Utilizing two optical pulses an environment is created in which a cold population of excitons is surrounded

by a hot electron-hole plasma. Both elastic and inelastic scattering processes increase the linewidth of the intraexcitonic resonance, while only inelastic scattering processes destroy the exciton population. This unique method enables the experimental differentiation between elastic and inelastic scattering processes in semiconductors for the first time, yielding an elastic scattering rate of $1.7 \cdot 10^{-4}\,\mathrm{cm^3 s^{-1}}$ and an inelastic scattering rate of $2.0 \cdot 10^{-4}\,\mathrm{cm^3 s^{-1}}$.

The coherent and incoherent dynamics of excitons in special semiconductor heterostructures, where the energetically most favorable states for electrons and holes are spatially separated by an intermediate barrier are studied in Chapter 6. Section 6.2 shows that excitonic states of spatially separated electrons and holes form a resonance in the linear absorption. This allows for the resonant excitation of these states so that the coherent lifetime of such excitonic charge-transfer states can be quantified and compared to that of regular excitonic states. The results of these investigations via four-wave mixing spectroscopy are presented in section 6.3. In addition to a beating between the respective states of the regular and the charge-transfer exciton, we find a decay time of the coherent polarization of the charge-transfer exciton of 0.4 ps. This decay is almost three times faster than the decay of the coherent polarization of the regular exciton from a GaInAs quantum well reference sample. This shorter coherent lifetime of charge-transfer excitons is attributed to additional scattering processes at the inner interface. The incoherent dynamics of charge-transfer excitons are examined in section 6.4 by optical pump-terahertz probe spectroscopy. Intraexcitonic transitions reveal that the charge-transfer excitons have a much lower $1s-2p$ transition energy of 3.2 meV than the regular excitons of the reference sample with 7 meV. The reason for this is the reduced Coulomb interaction due to the spatial separation of the charge carriers. Furthermore, we find a recombination time of the charge-transfer excitons of 2.5 ns, which is more than twice as long as that of regular excitons in the reference sample. After optical excitation conditions that are energetically above the resonance of the charge-transfer exciton, at first, the typical response of an electron-hole plasma is observed. In this plasma-like response, a shoulder forms on a time scale of several hundred picoseconds due to the incipient formation of a population of charge-transfer excitons. Within a few nanoseconds, a response develops which is nearly identical to the terahertz response shortly after resonant excitation conditions, indicating an almost pure population of charge-transfer excitons. The decay of the charge carriers shifts the energetic position of the intraexcitonic resonance on a nanosecond time scale from 2.2 meV to 3.2 meV. Such a density-dependent shift of the intraexcitonic resonance energy is not observed for regular excitons in GaInAs quantum well samples and is indicative of a more fermionic character of charge-transfer excitons.

Finally, Chapter 7 is focused on the behavior of the excitonic absorption in optically excited semiconductor heterostructures. It turns out that the excitonic absorption of a quantum well can be spectrally narrowed after optical excitation, resulting in an increased absorption peak. It takes several tens to hundreds of picoseconds after the optical excitation until the linewidth narrowing occurs and, under suitable excitation conditions, enhances the excitonic absorption peak by more than 10 %. This unexpected behavior of the excitonic absorption can only be observed in those samples that allow for a spatial separation of electrons and holes. So far, there is no physical explanation for this remarkable phenomenon.

Bibliography

[1] W. G. Adams and R. E. Day. V. The action of light on selenium. *Proceedings of the Royal Society of London*, 25(171-178):113–117, 1877.

[2] R. R. Alfano. *The Supercontinuum Laser Source: The Ultimate White Light.* Springer New York, 2016.

[3] D. L. Andrews and A. A. Demidov. *An Introduction to Laser Spectroscopy: Second Edition.* Springer US, 2012.

[4] D. H. Auston, S. L. Shapiro, D. J. Bradley, A. J. Campillo, K. Eisenthal, E. P. Ippen, D. v. der Linde, and C. V. Shank. *Ultrashort Light Pulses: Picosecond Techniques and Applications.* Topics in Applied Physics. Springer Berlin Heidelberg, 2013.

[5] H. J. Bakker, G. C. Cho, H. Kurz, Q. Wu, and X.-C. Zhang. Distortion of terahertz pulses in electro-optic sampling. *J. Opt. Soc. Am. B*, 15(6):1795–1801, Jun 1998.

[6] A. A. Balandin, S. Ghosh, W. Bao, I. Calizo, D. Teweldebrhan, F. Miao, and C. N. Lau. Superior thermal conductivity of single-layer graphene. *Nano Letters*, 8(3):902–907, 2008. PMID: 18284217.

[7] B. J. Baliga. *Fundamentals of Power Semiconductor Devices.* Springer International Publishing, 2019.

[8] A. Baltuška, Th. Udem, M. Uiberacker, M. Hentschel, E. Goulielmakis, Ch. Gohle, R. Holzwarth, V. S. Yakovlev, A. Scrinzi, T. W. Hänsch, and F. Krausz. Attosecond control of electronic processes by intense light fields. *Nature*, 421(6923):611, 2003.

[9] J. Bardeen and W. H. Brattain. The transistor, a semi-conductor triode. *Phys. Rev.*, 74:230–231, Jul 1948.

[10] C. W. Berry, N. Wang, M. R. Hashemi, M. Unlu, and M. Jarrahi. Significant performance enhancement in photoconductive terahertz optoelectronics by incorporating plasmonic contact electrodes. *Nature Communications*, 4:1622, 2013.

[11] P. W. M. Blom, P. J. van Hall, C. Smit, J. P. Cuypers, and J. H. Wolter. Selective exciton formation in thin GaAs/$Al_xGa_{1-x}As$ quantum wells. *Phys. Rev. Lett.*, 71:3878–3881, Dec 1993.

[12] Daniel F. Blossey. Wannier exciton in an electric field. I. Optical absorption by bound and continuum states. *Phys. Rev. B*, 2:3976–3990, Nov 1970.

[13] B. H. Bransden and C. J. Joachain. *Quantum Mechanics.* Prentice Hall, 2000.

[14] F. Braun. Ueber die Stromleitung durch Schwefelmetalle. *Annalen der Physik*, 229(12):556–563, 1875.

[15] W. G. Breiland, M. E. Coltrin, J. R. Creighton, H. Q. Hou, H. K. Moffat, and J. Y. Tsao. Organometallic vapor phase epitaxy (OMVPE). *Materials Science and Engineering: R: Reports*, 24(6):241–274, 1999.

[16] J. Callaway. Optical absorption in an electric field. *Phys. Rev.*, 130(2):549, 1963.

[17] V. Capozzi, L. Pavesi, and J. L. Staehli. Exciton-carrier scattering in gallium selenide. *Phys. Rev. B*, 47(11):6340, 1993.

[18] M. Cardona and F. H. Pollak. Energy-band structure of germanium and silicon: The k·p method. *Phys. Rev.*, 142:530–543, Feb 1966.

[19] P. Caroff, J. B. Wagner, K. A. Dick, H. A. Nilsson, M. Jeppsson, K. Deppert, L. Samuelson, L. R. Wallenberg, and L.-E. Wernersson. High-quality InAs/InSb nanowire heterostructures grown by metal–organic vapor-phase epitaxy. *Small*, 4(7):878–882, 2008.

[20] R. K. Cavin, P. Lugli, and V. V. Zhirnov. Science and engineering beyond Moore's law. *Proceedings of the IEEE*, 100(Special Centennial Issue):1720–1749, 2012.

[21] H. K. Charles and G. K. Sujan. Microelectronic packaging: Electrical interconnections. In *Reference Module in Materials Science and Materials Engineering*. Elsevier, 2016.

[22] S. Chatterjee, C. Ell, S. Mosor, G. Khitrova, H. M. Gibbs, W. Hoyer, M. Kira, S. W. Koch, J. P. Prineas, and H. Stolz. Excitonic photoluminescence in semiconductor quantum wells: Plasma versus excitons. *Phys. Rev. Lett.*, 92:067402, Feb 2004.

[23] D. S. Chemla, D. Miller, P. Smith, A. Gossard, and W. Wiegmann. Room temperature excitonic nonlinear absorption and refraction in GaAs/AlGaAs multiple quantum well structures. *IEEE Journal of Quantum Electronics*, 20(3):265–275, 1984.

[24] W. Chen, T. Xu, F. He, W. Wang, C. Wang, J. Strzalka, Y. Liu, J. Wen, D. J. Miller, J. Chen, K. Hong, L. Yu, and S. B. Darling. Hierarchical nanomorphologies promote exciton dissociation in polymer/fullerene bulk heterojunction solar cells. *Nano Letters*, 11(9):3707–3713, 2011.

[25] A. Chernikov. Time-resolved photoluminescence spectroscopy of semiconductors for optical applications beyond the visible spectral range. *Philipps-University Marburg*, 2011.

[26] A. H. Chin, J. M. Bakker, and J. Kono. Ultrafast electroabsorption at the transition between classical and quantum response. *Phys. Rev. Lett.*, 85:3293–3296, Oct 2000.

[27] A. Y. Cho and J. R. Arthur. Molecular beam epitaxy. *Progress in Solid State Chemistry*, 10:157 – 191, 1975.

[28] T. L. Cocker, D. Peller, P. Yu, J. Repp, and R. Huber. Tracking the ultrafast motion of a single molecule by femtosecond orbital imaging. *Nature*, 539(7628):263, 2016.

[29] S. T. Cundiff. Coherent spectroscopy of semiconductors. *Opt. Express*, 16(7):4639–4664, Mar 2008.

[30] T. C. Damen, J. Shah, D. Y. Oberli, D. S. Chemla, J. E. Cunningham, and J. M. Kuo. Dynamics of exciton formation and relaxation in GaAs quantum wells. *Phys. Rev. B*, 42:7434–7438, Oct 1990.

[31] J. R. Danielson, Y.-S. Lee, J. P. Prineas, J. T. Steiner, M. Kira, and S. W. Koch. Interaction of strong single-cycle terahertz pulses with semiconductor quantum wells. *Phys. Rev. Lett.*, 99:237401, Dec 2007.

[32] W. C. Dash and R. Newman. Intrinsic optical absorption in single-crystal germanium and silicon at 77 K and 300 K. *Phys. Rev.*, 99:1151–1155, Aug 1955.

[33] C. J. Dent, B. N. Murdin, and I. Galbraith. Phase and intensity dependence of the dynamical Franz-Keldysh effect. *Phys. Rev. B*, 67:165312, Apr 2003.

[34] B. Deveaud, B. Sermage, and D. S. Katzer. Free exciton versus free carrier luminescence in a quantum well. *Le Journal de Physique IV*, 3(C5):C5–11, 1993.

[35] R. Eccleston, R. Strobel, W. W. Rühle, J. Kuhl, B. F. Feuerbacher, and K. Ploog. Exciton dynamics in a GaAs quantum well. *Phys. Rev. B*, 44:1395–1398, Jul 1991.

[36] S. G. Elkomoss and G. Munschy. Electron-exciton elastic scattering cross sections in the central field and the exchange approximations. *Journal of Physics and Chemistry of Solids*, 38(6):557–563, 1977.

[37] S. G. Elkomoss and G. Munschy. Electron-exciton inelastic collision cross sections for different semiconductors. *Journal of Physics and Chemistry of Solids*, 40(6):431–438, 1979.

[38] R. J. Elliott. Intensity of optical absorption by excitons. *Phys. Rev.*, 108:1384–1389, Dec 1957.

[39] B. Ewers, N. S. Köster, R. Woscholski, M. Koch, S. Chatterjee, G. Khitrova, H. M. Gibbs, A. C. Klettke, M. Kira, and S. W. Koch. Ionization of coherent excitons by strong terahertz fields. *Phys. Rev. B*, 85:075307, Feb 2012.

[40] M. Faraday. *On a New Law of Electric Conduction; On Conducting Power Generally.* Royal Society, 1833.

[41] J. Fauchier and J. D. Dow. An analytic approach to the hydrogen stark effect in weak, strong, and ultrastrong fields. *Phys. Rev. A*, 9:98–107, Jan 1974.

[42] J. Feldmann, E. O. Göbel, and K. Ploog. Ultrafast optical nonlinearities of type-II $Al_xGa_{1-x}As$/AlAs multiple quantum wells. *Applied Physics Letters*, 57(15):1520–1522, 1990.

[43] J. Feldmann, G. Peter, E. O. Göbel, P. Dawson, K. Moore, C. Foxon, and R. J. Elliott. Linewidth dependence of radiative exciton lifetimes in quantum wells. *Phys. Rev. Lett.*, 59:2337–2340, Nov 1987.

[44] J. Feldmann, R. Sattmann, E. O. Göbel, J. Kuhl, J. Hebling, K. Ploog, R. Muralidharan, P. Dawson, and C. T. Foxon. Subpicosecond real-space charge transfer in type-II GaAs/AlAs superlattices. *Phys. Rev. Lett.*, 62:1892–1895, Apr 1989.

[45] J. Feldmann, R. Sattmann, E. O. Göbel, J. Nunnenkamp, J. Kuhl, J. Hebling, K. Ploog, R. Muralidharan, P. Dawson, and C. T. Foxon. Γ-X transfer rates in type-II (Al)GaAs/AlAs superlattices. *Solid-State Electronics*, 32(12):1713 – 1717, 1989. Special Issue Hot Carriers in Semiconductors.

[46] Y.-P. Feng and H. N. Spector. Scattering of excitons by free carriers in semiconducting quantum well structures. *Journal of Physics and Chemistry of Solids*, 48(7):593–601, 1987.

[47] B. F. Feuerbacher, J. Kuhl, R. Eccleston, and K. Ploog. Quantum beats between the light and heavy hole excitons in a quantum well. *Solid State Communications*, 74(12):1279 – 1283, 1990.

[48] G. Fiori, F. Bonaccorso, G. Iannaccone, T. Palacios, D. Neumaier, A. Seabaugh, S. K. Banerjee, and L. Colombo. Electronics based on two-dimensional materials. *Nature Nanotechnology*, 9(10):768, 2014.

[49] G. Fleming. Chemical applications of ultrafast spectroscopy. 1986.

[50] W. Franz. Einfluß eines elektrischen Feldes auf eine optische Absorptionskante. *Zeitschrift für Naturforschung A*, 13(6):484–489, 1958.

[51] C. E. Fritts. On a new form of selenium cell, and some electrical discoveries made by its use. *American Journal of Science*, (156):465–472, 1883.

[52] A. Frova, P. Handler, F. A. Germano, and D. E. Aspnes. Electro-absorption effects at the band edges of silicon and germanium. *Phys. Rev.*, 145:575–583, May 1966.

[53] I. Galbraith, R. Chari, S. Pellegrini, P. J. Phillips, C. J. Dent, A. F. G. van der Meer, D. G. Clarke, A. K. Kar, G. S. Buller, C. R. Pidgeon, B. N. Murdin, J. Allam, and G. Strasser. Excitonic signatures in the photoluminescence and terahertz absorption of a $GaAs/Al_xGa_{1-x}As$ multiple quantum well. *Phys. Rev. B*, 71:073302, Feb 2005.

[54] G. Gallot and D. Grischkowsky. Electro-optic detection of terahertz radiation. *J. Opt. Soc. Am. B*, 16(8):1204–1212, Aug 1999.

[55] G. Gallot, J. Zhang, R. W. McGowan, T.-I. Jeon, and D. Grischkowsky. Measurements of the THz absorption and dispersion of ZnTe and their relevance to the electro-optic detection of THz radiation. *Applied Physics Letters*, 74(23):3450–3452, 1999.

[56] E. O. Göbel. Ultrafast spectroscopy of semiconductors. In *Festkörperprobleme 30*, pages 269–294. Springer, 1990.

[57] E. O. Göbel, K. Leo, T. C. Damen, J. Shah, S. Schmitt-Rink, W. Schäfer, J. F. Müller, and K. Köhler. Quantum beats of excitons in quantum wells. *Phys. Rev. Lett.*, 64:1801–1804, Apr 1990.

[58] M. A. Green, A. Ho-Baillie, and H. J. Snaith. The emergence of perovskite solar cells. *Nature Photonics*, 8(7):506, 2014.

[59] T. Grieb, K. Müller, R. Fritz, M. Schowalter, N. Neugebohrn, N. Knaub, K. Volz, and A. Rosenauer. Determination of the chemical composition of GaNAs using STEM HAADF imaging and STEM strain state analysis. *Ultramicroscopy*, 117:15–23, 2012.

[60] T. Grunwald, T. Jung, D. Köhler, S. W. Koch, G. Khitrova, H. M. Gibbs, R. Hey, and S. Chatterjee. Measurement of intraexcitonic transition signatures via THz time-domain spectroscopy: A GaAs/(AlGa)As – (GaIn)As/GaAs comparison. *physica status solidi c*, 6(2):500–503, 2009.

[61] P. Gu, M. Tani, S. Kono, K. Sakai, and X.-C. Zhang. Study of terahertz radiation from InAs and InSb. *Journal of Applied Physics*, 91(9):5533–5537, 2002.

[62] R. N. Hall and T. J. Soltys. High purity germanium for detector fabrication. *IEEE Transactions on Nuclear Science*, 18(1):160–165, Feb 1971.

[63] H. Hamster, A. Sullivan, S. Gordon, W. White, and R. W. Falcone. Subpicosecond, electromagnetic pulses from intense laser-plasma interaction. *Phys. Rev. Lett.*, 71:2725–2728, Oct 1993.

[64] W. L. Hansen. High-purity germanium crystal growing. *Nuclear Instruments and Methods*, 94(2):377 – 380, 1971.

[65] H. Haug and S. W. Koch. *Quantum Theory of the Optical and Electronic Properties of Semiconductors: Fivth Edition.* 2009.

[66] H. Haug and S. Schmitt-Rink. Electron theory of the optical properties of laser-excited semiconductors. *Progress in Quantum Electronics*, 9(1):3 – 100, 1984.

[67] E. Hendry, M. Koeberg, and M. Bonn. Exciton and electron-hole plasma formation dynamics in ZnO. *Phys. Rev. B*, 76:045214, Jul 2007.

[68] M. A. Herman and H. Sitter. *Molecular Beam Epitaxy: Fundamentals and Current Status.* Springer Series in Materials Science. Springer Berlin Heidelberg, 2012.

[69] J. W. Hittorf. *Ueber das elektrische Leitungsvermögen des Schwefelsilbers und Halbschwefelkupfers.* 1851.

[70] A. Honold, L. Schultheis, J. Kuhl, and C. W. Tu. Collision broadening of two-dimensional excitons in a GaAs single quantum well. *Phys. Rev. B*, 40(9):6442, 1989.

[71] W. Hoyer, M. Kira, and S. W. Koch. Influence of coulomb and phonon interaction on the exciton formation dynamics in semiconductor heterostructures. *Phys. Rev. B*, 67:155113, Apr 2003.

[72] D. Huang, H. Y. Chu, Y. C. Chang, R. Houdré, and H. Morkoç. Excitonic absorption in modulation-doped $GaAs/Al_xGa_{1-x}As$ quantum wells. *Phys. Rev. B*, 38:1246–1250, Jul 1988.

[73] D. Huang, J.-I. Chyi, and H. Morkoç. Carrier effects on the excitonic absorption in GaAs quantum-well structures: Phase-space filling. *Phys. Rev. B*, 42:5147–5153, Sep 1990.

[74] R. Huber, R. A. Kaindl, B. A. Schmid, and D. S. Chemla. Broadband terahertz study of excitonic resonances in the high-density regime in $GaAs/Al_xGa_{1-x}As$ quantum wells. *Phys. Rev. B*, 72:161314, Oct 2005.

[75] S. Hughes and D. S. Citrin. Creation of highly anisotropic wave packets in quantum wells: Dynamical Franz-Keldysh effect in the optical and terahertz regimes. *Phys. Rev. B*, 59(8):R5288, 1999.

[76] S. Hunsche, K. Leo, H. Kurz, and K. Köhler. Exciton absorption saturation by phase-space filling: Influence of carrier temperature and density. *Phys. Rev. B*, 49:16565–16568, Jun 1994.

[77] M. Iansiti and J. West. From physics to function: An empirical study of research and development performance in the semiconductor industry. *Journal of Product Innovation Management*, 16(4):385–399.

[78] J. D. Jackson. *Classical Electrodynamics, 3rd Ed.* Wiley India Pvt. Limited, 2007.

[79] F. Jahnke, M. Kira, S. W. Koch, G. Khitrova, E. K. Lindmark, T. R. Nelson, Jr., D. V. Wick, J. D. Berger, O. Lyngnes, H. M. Gibbs, and K. Tai. Excitonic nonlinearities of semiconductor microcavities in the nonperturbative regime. *Phys. Rev. Lett.*, 77:5257–5260, Dec 1996.

[80] M. Jarrahi. Advanced photoconductive terahertz optoelectronics based on nano-antennas and nano-plasmonic light concentrators. *IEEE Transactions on Terahertz Science and Technology*, 5(3):391–397, May 2015.

[81] A. P. Jauho and K. Johnsen. Dynamical Franz-Keldysh effect. *Phys. Rev. Lett.*, 76:4576–4579, Jun 1996.

[82] R. A. Kaindl, M. A. Carnahan, D. Hägele, R. Lövenich, and D. S. Chemla. Ultrafast terahertz probes of transient conducting and insulating phases in an electron–hole gas. *Nature*, 423(6941):734, 2003.

[83] R. A. Kaindl, D. Hägele, M. A. Carnahan, and D. S. Chemla. Transient terahertz spectroscopy of excitons and unbound carriers in quasi-two-dimensional electron-hole gases. *Phys. Rev. B*, 79:045320, Jan 2009.

[84] L. V. Keldysh. Behavior of non-metallic crystals in strong electric fields. *Soviet Journal of Experimental and Theoretical Physics*, 6:763, 1958.

[85] L. V. Keldysh. The effect of a strong electric field on the optical properties of insulating crystals. *Sov. Phys. JETP*, 7(5):788–790, 1958.

[86] M. Kira, W. Hoyer, and S. W. Koch. Microscopic theory of the semiconductor terahertz response. *physica status solidi (b)*, 238(3):443–450.

[87] M. Kira, W. Hoyer, and S. W. Koch. Terahertz signatures of the exciton formation dynamics in non-resonantly excited semiconductors. *Solid State Communications*, 129(11):733 – 736, 2004.

[88] M. Kira, W. Hoyer, T. Stroucken, and S. W. Koch. Exciton formation in semiconductors and the influence of a photonic environment. *Phys. Rev. Lett.*, 87:176401, Oct 2001.

[89] M. Kira, F. Jahnke, and S. W. Koch. Microscopic theory of excitonic signatures in semiconductor photoluminescence. *Phys. Rev. Lett.*, 81:3263–3266, Oct 1998.

[90] M. Kira and S. W. Koch. Microscopic theory of optical excitations, photoluminescence, and terahertz response in semiconductors. *The European Physical Journal D - Atomic, Molecular, Optical and Plasma Physics*, 36(2):143–157, Nov 2005.

[91] M. Kira and S. W. Koch. Many-body correlations and excitonic effects in semiconductor spectroscopy. *Progress in Quantum Electronics*, 30(5):155 – 296, 2006.

[92] M. Kira and S. W. Koch. *Semiconductor Quantum Optics*. Cambridge University Press, 2011.

[93] G. Klatt, F. Hilser, W. Qiao, M. Beck, R. Gebs, A. Bartels, K. Huska, U. Lemmer, G. Bastian, M. B. Johnston, M. Fischer, J. Faist, and T. Dekorsy. Terahertz emission from lateral photo-dember currents. *Opt. Express*, 18(5):4939–4947, Mar 2010.

[94] C. Klingshirn and H. Haug. Optical properties of highly excited direct gap semiconductors. *Physics Reports*, 70(5):315 – 398, 1981.

[95] W. H. Knox, R. L. Fork, M. C. Downer, D. A. B. Miller, D. S. Chemla, C. V. Shank, A. C. Gossard, and W. Wiegmann. Femtosecond dynamics of resonantly excited excitons in room-temperature GaAs quantum wells. *Phys. Rev. Lett.*, 54:1306–1309, Mar 1985.

[96] W. H. Knox, C. Hirlimann, D. A. B. Miller, J. Shah, D. S. Chemla, and C. V. Shank. Femtosecond excitation of nonthermal carrier populations in GaAs quantum wells. *Phys. Rev. Lett.*, 56:1191–1193, Mar 1986.

[97] M. Koch, R. Hellmann, G. Bastian, J. Feldmann, E. O. Göbel, and P. Dawson. Enhanced energy and phase relaxation of excitons in the presence of bare electrons. *Phys. Rev. B*, 51:13887–13890, May 1995.

[98] M. Koch, G. von Plessen, J. Feldmann, and E. O. Göbel. Excitonic quantum beats in semiconductor quantum-well structures. *Chemical Physics*, 210(1):367 – 388, 1996. Confined Excitations in Molecular and Semiconductor Nanostructures.

[99] S. W. Koch, M. Kira, G. Khitrova, and H. M. Gibbs. Semiconductor excitons in new light. *Nature Materials*, 5(7):523, 2006.

[100] R. B. Kohlhaas, R. J. B. Dietz, S. Breuer, S. Nellen, L. Liebermeister, M. Schell, and B. Globisch. Improving the dynamic range of InGaAs-based THz detectors by localized beryllium doping: up to 70 dB at 3 THz. *Opt. Lett.*, 43(21):5423–5426, Nov 2018.

[101] R. B. Kohlhaas, B. Globisch, S. Nellen, L. Liebermeister, M. Schell, P.-H. Richter, M. Koch, M. P. Semtsiv, and W. T. Masselink. Rhodium doped InGaAs: A superior ultrafast photoconductor. *Applied Physics Letters*, 112(10):102101, 2018.

[102] O. Kojima, K. Mizoguchi, and M. Nakayama. Quantum beats of type-I and type-II excitons in an $In_xGa_{1-x}As$/GaAs strained single quantum well. *Journal of Applied Physics*, 112(4):043522, 2012.

[103] F. Krausz and M. I. Stockman. Attosecond metrology: from electron capture to future signal processing. *Nature Photonics*, 8(3):205, 2014.

[104] H. Kroemer. Nobel lecture: Quasielectric fields and band offsets: teaching electrons new tricks. *Rev. Mod. Phys.*, 73:783–793, Oct 2001.

[105] C. S. S. R. Kumar. *Semiconductor Nanomaterials*. Nanomaterials for Life Sciences. Wiley, 2010.

[106] R. Kumar, A. S. Vengurlekar, S. S. Prabhu, J. Shah, and L. N. Pfeiffer. Picosecond time evolution of free electron-hole pairs into excitons in GaAs quantum wells. *Phys. Rev. B*, 54:4891–4897, Aug 1996.

[107] J. Kusano, Y. Segawa, Y. Aoyagi, S. Namba, and H. Okamoto. Extremely slow energy relaxation of a two-dimensional exciton in a GaAs superlattice structure. *Phys. Rev. B*, 40:1685–1691, Jul 1989.

[108] C. Lammers. Über die Dynamik des Charge-Transfer-Exzitons. Dissertation, Philipps Universität Marburg, 2017.

[109] J. Lee, K. Vandewal, S. R. Yost, M. E. Bahlke, L. Goris, M. A. Baldo, J. V. Manca, and T. Van Voorhis. Charge transfer state versus hot exciton dissociation in polymer-fullerene blended solar cells. *Journal of the American Chemical Society*, 132(34):11878–11880, 2010.

[110] Y. S. Lee. *Principles of Terahertz Science and Technology.* Lecture Notes in Physics. Springer US, 2009.

[111] A. Leitenstorfer, S. Hunsche, J. Shah, M. C. Nuss, and W. H. Knox. Detectors and sources for ultrabroadband electro-optic sampling: Experiment and theory. *Applied Physics Letters*, 74(11):1516–1518, 1999.

[112] K. Leo, E. O. Göbel, T. C. Damen, J. Shah, S. Schmitt-Rink, W. Schäfer, J. F. Müller, K. Köhler, and P. Ganser. Subpicosecond four-wave mixing in GaAs/$Al_xGa_{1-x}As$ quantum wells. *Phys. Rev. B*, 44:5726–5737, Sep 1991.

[113] S. Lepeshov, A. Gorodetsky, A. Krasnok, E. Rafailov, and P. Belov. Enhancement of terahertz photoconductive antenna operation by optical nanoantennas. *Laser & Photonics Reviews*, 11(1):1600199.

[114] B. W. Levinger and D. R. Frankl. Cyclotron resonance measurements of the energy band parameters of germanium. *Journal of Physics and Chemistry of Solids*, 20(3):281 – 288, 1961.

[115] L. Li, Y. Yu, G. J. Ye, Q. Ge, X. Ou, H. Wu, D. Feng, X. H. Chen, and Y. Zhang. Black phosphorus field-effect transistors. *Nature Nanotechnology*, 9(5):372, 2014.

[116] M. Lindberg and S. W. Koch. Effective bloch equations for semiconductors. *Phys. Rev. B*, 38:3342–3350, Aug 1988.

[117] W. Liu, D. Jiang, K. Luo, Y. Zhang, and X. Yang. Broadening of the excitonic linewidth due to scattering of two-dimensional free carriers. *Applied Physics Letters*, 67(5):679–681, 1995.

[118] V. Lucarini, J. J. Saarinen, K. E. Peiponen, and E. M. Vartiainen. *Kramers-Kronig Relations in Optical Materials Research.* Springer Series in Optical Sciences. Springer Berlin Heidelberg, 2006.

[119] S. Lutgen, T. F. Albrecht, T. Marschner, W. Stolz, and E. O. Göbel. Optical properties of symmetrically strained (GaIn)As/Ga(PAs) superlattices grown by metalorganic vapour phase epitaxy. *Solid-State Electronics*, 37(4):905 – 909, 1994.

[120] O. Madelung. *Semiconductors: Group IV Elements and III-V Compounds.* Data in Science and Technology. Springer Berlin Heidelberg, 2012.

[121] K. F. Mak, C. Lee, J. Hone, J. Shan, and T. F. Heinz. Atomically thin MoS_2: A new direct-gap semiconductor. *Phys. Rev. Lett.*, 105:136805, Sep 2010.

[122] A. Manassen, E. Cohen, A. Ron, E. Linder, and L. N. Pfeiffer. Exciton and trion spectral line shape in the presence of an electron gas in GaAs/AlAs quantum wells. *Phys. Rev. B*, 54:10609–10613, Oct 1996.

[123] C. Mattevi, H. Kim, and M. Chhowalla. A review of chemical vapour deposition of graphene on copper. *Journal of Materials Chemistry*, 21(10):3324–3334, 2011.

[124] T. Meier, F. Rossi, P. Thomas, and S. W. Koch. Dynamic localization in anisotropic coulomb systems: Field induced crossover of the exciton dimension. *Phys. Rev. Lett.*, 75:2558–2561, Sep 1995.

[125] T. Meier, P. Thomas, and S. W. Koch. *Coherent Semiconductor Optics: From Basic Concepts to Nanostructure Applications*. Springer Berlin Heidelberg, 2007.

[126] K. Meissner, B. Fluegel, R. Binder, S. W. Koch, G. Khitrova, and N. Peygambarian. Comparison of optical nonlinearities of type-II and type-I quantum wells. *Applied Physics Letters*, 59(3):259–261, 1991.

[127] B. Merritt. *The Digital Revolution*. Synthesis Lectures on Emerging Engineering Technologies. Morgan & Claypool Publishers, 2016.

[128] A. Messiah. *Quantum Mechanics*. Dover Books on Physics. Dover Publications, 2014.

[129] D. A. B. Miller, D. S. Chemla, T. C. Damen, A. C. Gossard, W. Wiegmann, T. H. Wood, and C. A. Burrus. Band-edge electroabsorption in quantum well structures: The quantum-confined Stark effect. *Phys. Rev. Lett.*, 53:2173–2176, Nov 1984.

[130] D. A. B. Miller, D. S. Chemla, T. C. Damen, A. C. Gossard, W. Wiegmann, T. H. Wood, and C. A. Burrus. Electric field dependence of optical absorption near the band gap of quantum-well structures. *Phys. Rev. B*, 32:1043–1060, Jul 1985.

[131] Y. Mizumoto, Y. Kayanuma, A. Srivastava, J. Kono, and A. H. Chin. Dressed-band theory for semiconductors in a high-intensity infrared laser field. *Phys. Rev. B*, 74:045216, Jul 2006.

[132] J. E. Moore. The birth of topological insulators. *Nature*, 464(7286):194, 2010.

[133] T. S. Moss, G. J. Burrell, and B. Ellis. *Semiconductor Opto-Electronics*. Elsevier Science, 2013.

[134] N. F. Mott. Metal-insulator transition. *Rev. Mod. Phys.*, 40:677–683, Oct 1968.

[135] A. Nahata, D. H. Auston, T. F. Heinz, and C. Wu. Coherent detection of freely propagating terahertz radiation by electro-optic sampling. *Applied Physics Letters*, 68(2):150–152, 1996.

[136] H. S. Nalwa. *Nanostructured Materials and Nanotechnology*. Academic Press, 2002.

[137] M. Nido, M. G. W. Alexander, W. W. Rühle, T. Schweizer, and K. Köhler. Non-resonant electron and hole tunneling times in GaAs/$Al_{0.35}Ga_{0.65}As$ asymmetric double quantum wells. *Applied Physics Letters*, 56(4):355–357, 1990.

[138] K. B. Nordstrom, K. Johnsen, S. J. Allen, A.-P. Jauho, B. Birnir, J. Kono, T. Noda, H. Akiyama, and H. Sakaki. Excitonic dynamical Franz-Keldysh effect. *Phys. Rev. Lett.*, 81:457–460, Jul 1998.

[139] T. B. Norris, X. J. Song, W. J. Schaff, L. F. Eastman, G. Wicks, and G. A. Mourou. Tunneling escape time of electrons from a quantum well under the influence of an electric field. *Applied Physics Letters*, 54(1):60–62, 1989.

[140] K. S. Novoselov, A. K. Geim, S. V. Morozov, D. Jiang, Y. Zhang, S. V. Dubonos, I. V. Grigorieva, and A. A. Firsov. Electric field effect in atomically thin carbon films. *Science*, 306(5696):666–669, 2004.

[141] S. Nüsse, P. Haring Bolivar, H. Kurz, V. Klimov, and F. Levy. Carrier cooling and exciton formation in GaSe. *Phys. Rev. B*, 56:4578–4583, Aug 1997.

[142] D. Y. Oberli, J. Shah, T. C. Damen, C. W. Tu, T. Y. Chang, D. A. B. Miller, J. E. Henry, R. F. Kopf, N. Sauer, and A. E. DiGiovanni. Direct measurement of resonant and nonresonant tunneling times in asymmetric coupled quantum wells. *Phys. Rev. B*, 40:3028–3031, Aug 1989.

[143] G. R. Olbright, W. S. Fu, J. F. Klem, H. M. Gibbs, G. Khitrova, R. Pon, B. Fluegel, K. Meissner, N. Peyghambarian, R. Binder, I. Galbraith, and S. W. Koch. Nonlinear optical properties of type-II quantum wells. *Phys. Rev. B*, 44:3043–3053, Aug 1991.

[144] A. Othonos. Probing ultrafast carrier and phonon dynamics in semiconductors. *Journal of Applied Physics*, 83(4):1789–1830, 1998.

[145] W. Pauli. Scientific correspondence with Bohr, Einstein, Heisenberg ao, Volume II: 1930–1939, 1985.

[146] K. E. Peiponen, A. Zeitler, and M. Kuwata-Gonokami. *Terahertz Spectroscopy and Imaging*. Springer Series in Optical Sciences. Springer Berlin Heidelberg, 2012.

[147] C. Pöllmann, P. Steinleitner, U. Leierseder, P. Nagler, G. Plechinger, M. Porer, R. Bratschitsch, C. Schüller, T. Korn, and R. Huber. Resonant internal quantum transitions and femtosecond radiative decay of excitons in monolayer WSe_2. *Nature Materials*, 14(9):889, 2015.

[148] P. E. Powers. *Fundamentals of Nonlinear Optics*. CRC Press, 2011.

[149] S. S. Prabhu, A. S. Vengurlekar, and J. Shah. Picosecond-luminescence study of exciton formation dynamics in CdSe. *Phys. Rev. B*, 53:R10465–R10468, Apr 1996.

[150] K. E. Priebe, C. Rathje, S. V. Yalunin, T. Hohage, A. Feist, S. Schäfer, and C. Ropers. Attosecond electron pulse trains and quantum state reconstruction in ultrafast transmission electron microscopy. *Nature Photonics*, 11(12):793, 2017.

[151] B. Radisavljevic, A. Radenovic, J. Brivio, V. Giacometti, and A. Kis. Single-layer MoS_2 transistors. *Nature Nanotechnology*, 6(3):147, 2011.

[152] G. Ramon, A. Mann, and E. Cohen. Theory of neutral and charged exciton scattering with electrons in semiconductor quantum wells. *Phys. Rev. B*, 67:045323, Jan 2003.

[153] A. Rice, Y. Jin, X. F. Ma, X.-C. Zhang, D. Bliss, J. Larkin, and M. Alexander. Terahertz optical rectification from ⟨110⟩ zinc-blende crystals. *Applied Physics Letters*, 64(11):1324–1326, 1994.

[154] D. Robart, X. Marie, B. Baylac, T. Amand, M. Brousseau, G. Bacquet, G. Debart, R. Planel, and J. M. Gerard. Dynamical equilibrium between excitons and free carriers in quantum wells. *Solid state communications*, 95(5):287–293, 1995.

[155] N. Rosenberg. *Why do firms do basic research (with their own money)?*, pages 225–234. World Scientific, 2010.

[156] H. Roskos, B. Rieck, A. Seilmeier, and W. Kaiser. Cooling of a carrier plasma in germanium investigated with subpicosecond infrared pulses. *Applied Physics Letters*, 53(24):2406–2408, 1988.

[157] F. Rossi and T. Kuhn. Theory of ultrafast phenomena in photoexcited semiconductors. *Rev. Mod. Phys.*, 74:895–950, Aug 2002.

[158] L. Rost, S. Gies, M. Stein, C. Fuchs, S. Nau, P. Kükelhan, K. Volz, W. Stolz, M. Koch, and W. Heimbrodt. Correlation of optical properties and interface morphology in type-II semiconductor heterostructures. *Journal of Physics: Condensed Matter*, 31(1):014001, 2018.

[159] S. Sanguinetti, M. Guzzi, E. Gatti, and M. Gurioli. *Characterization of Semiconductor Heterostructures and Nanostructures: Chapter 12. Photoluminescence Characterization of Structural and Electronic Properties of Semiconductor Quantum Wells.* Elsevier Science, 2013.

[160] G. Sansone, E. Benedetti, F. Calegari, C. Vozzi, L. Avaldi, R. Flammini, L. Poletto, P. Villoresi, C. Altucci, R. Velotta, S. Stagira, S. De Silvestri, and M. Nisoli. Isolated single-cycle attosecond pulses. *Science*, 314(5798):443–446, 2006.

[161] S. Schmitt-Rink, D. S. Chemla, and D. A. B. Miller. Linear and nonlinear optical properties of semiconductor quantum wells. *Advances in Physics*, 38(2):89–188, 1989.

[162] H. C. Schneider, W. W. Chow, and S. W. Koch. Excitation-induced dephasing in semiconductor quantum dots. *Phys. Rev. B*, 70:235308, Dec 2004.

[163] E. Schrödinger. Quantisierung als Eigenwertproblem. *Annalen der Physik*, 385(13):437–490.

[164] O. Schubert, M. Hohenleutner, F. Langer, B. Urbanek, C. Lange, U. Huttner, D. Golde, T. Meier, M. Kira, S. W. Koch, and R. Huber. Sub-cycle control of terahertz high-harmonic generation by dynamical Bloch oscillations. *Nature Photonics*, 8(2):119, 2014.

[165] L. Schultheis, A. Honold, J. Kuhl, K. Köhler, and C. W. Tu. Optical dephasing of homogeneously broadened two-dimensional exciton transitions in GaAs quantum wells. *Phys. Rev. B*, 34:9027–9030, Dec 1986.

[166] L. Schultheis, J. Kuhl, A. Honold, and C. W. Tu. Ultrafast phase relaxation of excitons via exciton-exciton and exciton-electron collisions. *Phys. Rev. Lett.*, 57:1635–1638, Sep 1986.

[167] K. Schwab. *The Fourth Industrial Revolution.* Crown Publishing Group, 2017.

[168] K. Seeger. *Semiconductor Physics: An Introduction.* Advanced Texts in Physics. Springer, 2004.

[169] T. Seifert, S. Jaiswal, U. Martens, J. Hannegan, L. Braun, P. Maldonado, F. Freimuth, A. Kronenberg, J. Henrizi, I. Radu, E. Beaurepaire, Y. Mokrousov, P. M. Oppeneer, M. Jourdan, G. Jakob, D. Turchinovich, L. M. Hayden, M. Wolf, M. Münzenberg, M. Kläui, and T. Kampfrath. Efficient metallic spintronic emitters of ultrabroadband terahertz radiation. *Nature Photonics*, 10(7):483–488, 2016.

[170] F. Sekiguchi and R. Shimano. Excitonic correlation in the Mott crossover regime in Ge. *Phys. Rev. B*, 91:155202, Apr 2015.

[171] P. E. Selbmann, M. Gulia, F. Rossi, E. Molinari, and P. Lugli. Coupled free-carrier and exciton relaxation in optically excited semiconductors. *Phys. Rev. B*, 54:4660–4673, Aug 1996.

[172] J. Shah. *Ultrafast Spectroscopy of Semiconductors and Semiconductor Nanostructures*. Springer Series in Solid-State Sciences. Springer Berlin Heidelberg, 2013.

[173] C. V. Shank, R. L. Fork, R. F. Leheny, and J. Shah. Dynamics of photoexcited GaAs band-edge absorption with subpicosecond resolution. *Phys. Rev. Lett.*, 42:112–115, Jan 1979.

[174] K. Shinokita, H. Hirori, M. Nagai, N. Satoh, Y. Kadoya, and K. Tanaka. Dynamical Franz–Keldysh effect in GaAs/AlGaAs multiple quantum wells induced by single-cycle terahertz pulses. *Applied Physics Letters*, 97(21):211902, 2010.

[175] K. Siantidis, V. M. Axt, and T. Kuhn. Dynamics of exciton formation for near band-gap excitations. *Phys. Rev. B*, 65:035303, Dec 2001.

[176] W. Smith. *The action of light on selenium*. 1876.

[177] H. Spieler. *Semiconductor Detector Systems*. Oxford science publications. OUP Oxford, 2005.

[178] D. Spirkoska, J. Arbiol, A. Gustafsson, S. Conesa-Boj, F. Glas, I. Zardo, M. Heigoldt, M. H. Gass, A. L. Bleloch, S. Estrade, M. Kaniber, J. Rossler, F. Peiro, J. R. Morante, G. Abstreiter, L. Samuelson, and A. Fontcuberta i Morral. Structural and optical properties of high quality zinc-blende/wurtzite GaAs nanowire heterostructures. *Phys. Rev. B*, 80:245325, Dec 2009.

[179] P. Springer, S. W. Koch, and M. Kira. Excitonic terahertz absorption in semiconductors with effective-mass anisotropies. *J. Opt. Soc. Am. B*, 33(7):C30–C38, Jul 2016.

[180] A. Srivastava, R. Srivastava, J. Wang, and J. Kono. Laser-induced above-band-gap transparency in GaAs. *Phys. Rev. Lett.*, 93:157401, Oct 2004.

[181] M. Stein. Ladungsträgerdynamik in räumlich indirekten Halbleiterheterostrukturen. Masterarbeit, Philipps Universität Marburg, 2015.

[182] M. Stein, C. Lammers, M. J. Drexler, C. Fuchs, W. Stolz, and M. Koch. Enhanced absorption by linewidth narrowing in optically excited type-II semiconductor heterostructures. *Phys. Rev. Lett.*, 121:017401, Jul 2018.

[183] M. Stein, C. Lammers, P.-H. Richter, C. Fuchs, W. Stolz, M. Koch, O. Vänskä, M. J. Weseloh, M. Kira, and S. W. Koch. Dynamics of charge-transfer excitons in type-II semiconductor heterostructures. *Phys. Rev. B*, 97:125306, Mar 2018.

[184] M. Stein, C. Lammers, P. Springer, P.-H. Richter, S. W. Koch, M. Koch, and M. Kira. Density-dependent exciton dynamics and L-valley anisotropy in germanium. *Phys. Rev. B*, 95:155207, Apr 2017.

[185] M. Stein, C. Lammers, J. T. Steiner, P-H Richter, S. W. Koch, M. Koch, and M. Kira. Exciton ionization by THz pulses in germanium. *Journal of Physics B: Atomic, Molecular and Optical Physics*, 51(15):154001, Jul 2018.

[186] M. Stein, F. Schäfer, and L. Gomell. Inelastic electron-exciton scattering in bulk germanium. *Phys. Rev. B*, 99:144310, Apr 2019.

[187] J. T. Steiner, M. Kira, and S. W. Koch. Optical nonlinearities and Rabi flopping of an exciton population in a semiconductor interacting with strong terahertz fields. *Phys. Rev. B*, 77:165308, Apr 2008.

[188] P. Steinleitner, P. Merkl, P. Nagler, J. Mornhinweg, C. Schüller, T. Korn, A. Chernikov, and R. Huber. Direct observation of ultrafast exciton formation in a monolayer of WSe_2. *Nano Letters*, 17(3):1455–1460, 2017. PMID: 28182430.

[189] G. B. Stringfellow. *Organometallic Vapor-Phase Epitaxy: Theory and Practice*. Elsevier Science, 1999.

[190] T. Suzuki and R. Shimano. Time-resolved formation of excitons and electron-hole droplets in Si studied using terahertz spectroscopy. *Phys. Rev. Lett.*, 103:057401, Jul 2009.

[191] J. Szczytko, L. Kappei, J. Berney, F. Morier-Genoud, M. T. Portella-Oberli, and B. Deveaud. Determination of the exciton formation in quantum wells from time-resolved interband luminescence. *Phys. Rev. Lett.*, 93:137401, Sep 2004.

[192] T. Takagahara. *Quantum Coherence Correlation and Decoherence in Semiconductor Nanostructures*. Elsevier Science, 2003.

[193] A. Thilagam. Exciton formation assisted by longitudinal optical phonons in monolayer transition metal dichalcogenides. *Journal of Applied Physics*, 120(12):124306, 2016.

[194] T. Timusk. Far-infrared absorption study of exciton ionization in germanium. *Phys. Rev. B*, 13:3511–3514, Apr 1976.

[195] A. Tiwari, A. K. Mishra, H. Kobayashi, and A. P. F. Turner. *Intelligent Nanomaterials: Processes, Properties, and Applications*. Wiley, 2012.

[196] K. Tomioka, M. Yoshimura, and T. Fukui. A III–V nanowire channel on silicon for high-performance vertical transistors. *Nature*, 488(7410):189, 2012.

[197] K. T. Tsen. *Ultrafast Phenomena in Semiconductors*. Springer New York, 2012.

[198] R. Ulbricht, E. Hendry, J. Shan, T. F. Heinz, and M. Bonn. Carrier dynamics in semiconductors studied with time-resolved terahertz spectroscopy. *Rev. Mod. Phys.*, 83:543–586, Jun 2011.

[199] J. Valdmanis and G. Mourou. Subpicosecond electrooptic sampling: Principles and applications. *IEEE Journal of Quantum Electronics*, 22(1):69–78, January 1986.

[200] S. Van Aert, K. J. Batenburg, M. D. Rossell, R. Erni, and G. Van Tendeloo. Three-dimensional atomic imaging of crystalline nanoparticles. *Nature*, 470(7334):374, 2011.

[201] G. von Plessen, T. Meier, M. Koch, J. Feldmann, P. Thomas, S. W. Koch, E. O. Göbel, K. W. Goossen, J. M. Kuo, and R. F. Kopf. Exciton ionization induced by an electric field in a strongly coupled GaAs/$Al_xGa_{1-x}As$ superlattice. *Phys. Rev. B*, 53:13688–13693, May 1996.

[202] M. Wagner, H. Schneider, D. Stehr, S. Winnerl, A. M. Andrews, S. Schartner, G. Strasser, and M. Helm. Observation of the intraexciton Autler-Townes effect in GaAs/AlGaAs semiconductor quantum wells. *Phys. Rev. Lett.*, 105:167401, Oct 2010.

[203] D. R. Wake, H. W. Yoon, J. P. Wolfe, and H. Morkoç. Response of excitonic absorption spectra to photoexcited carriers in GaAs quantum wells. *Phys. Rev. B*, 46:13452–13460, Nov 1992.

[204] M. M. Waldrop. The chips are down for Moore's law. *Nature News*, 530(7589):144, 2016.

[205] C.-T. Wang and C.-S. Chiu. Competitive strategies for Taiwan's semiconductor industry in a new world economy. *Technology in Society*, 36:60 – 73, 2014.

[206] H. Wang, K. Ferrio, D. G. Steel, Y. Z. Hu, R. Binder, and S. W. Koch. Transient nonlinear optical response from excitation induced dephasing in GaAs. *Phys. Rev. Lett.*, 71:1261–1264, Aug 1993.

[207] J. C. Whitaker. *Microelectronics*. Electronics Handbook Series. CRC Press, 2005.

[208] R. Williams. Electric field induced light absorption in CdS. *Phys. Rev.*, 117:1487–1490, Mar 1960.

[209] A. H. Wilson. The theory of electronic semi-conductors.-II. *Proceedings of the Royal Society of London. Series A, Containing Papers of a Mathematical and Physical Character*, 134(823):277–287, 1931.

[210] A. H. Wilson. The theory of electronic semi-conductors. *Proceedings of the Royal Society of London. Series A, Containing Papers of a Mathematical and Physical Character*, 133(822):458–491, 1931.

[211] Q. Wu and X.-C. Zhang. Free-space electro-optic sampling of terahertz beams. *Applied Physics Letters*, 67(24):3523–3525, 1995.

[212] K.-L. Yeh, M. C. Hoffmann, J. Hebling, and K. A. Nelson. Generation of 10μJ ultrashort terahertz pulses by optical rectification. *Applied Physics Letters*, 90(17):171121, 2007.

[213] P. YU and M. Cardona. *Fundamentals of Semiconductors: Physics and Materials Properties*. Graduate Texts in Physics. Springer, 2010.

[214] A. M. Zheltikov. *Physics-Uspekhi*, 49(6):605, 2006.

Relevant Publications

I. Density-dependent exciton dynamics and *L*-valley anisotropy in germanium

M. Stein, C. Lammers, P. Springer, P.-H. Richter, S. W. Koch, M. Koch, and M. Kira, Phys. Rev. B 95, 155207 (2017)

Abstract

Optical pump-THz probe spectroscopy is used to investigate the exciton formation dynamics and its intensity dependence in bulk Ge. Associated with the intraexcitonic $1s-2p$ transition, the gradual buildup of an absorption peak around 3.1 meV (0.75 THz) signifies a delayed exciton formation after optical pump which is accelerated for higher excitation densities. Analyzing the spectral shape of this THz absorption resonance, two distinct resonances are found which are attributed to the mass anisotropy of L-valley electrons via a microscopic theory.

DOI: 10.1103/PhysRevB.95.155207

URL: `https://link.aps.org/doi/10.1103/PhysRevB.95.155207`

PHYSICAL REVIEW B **95**, 155207 (2017)

Density-dependent exciton dynamics and L-valley anisotropy in germanium

M. Stein,* C. Lammers, P. Springer,† P.-H. Richter, S. W. Koch, and M. Koch
Department of Physics and Material Sciences Center, Philipps-Universität Marburg, Renthof 5, 35032 Marburg, Germany

M. Kira
Center for Ultrafast Optical Science, University of Michigan, Ann Arbor, Michigan 48109, USA
(Received 18 November 2016; revised manuscript received 5 March 2017; published 26 April 2017)

Optical pump-THz probe spectroscopy is used to investigate the exciton formation dynamics and its intensity dependence in bulk Ge. Associated with the intraexcitonic $1s$-$2p$ transition, the gradual buildup of an absorption peak around 3.1 meV (0.75 THz) signifies a delayed exciton formation after optical pump which is accelerated for higher excitation densities. Analyzing the spectral shape of this THz absorption resonance, two distinct resonances are found which are attributed to the mass anisotropy of L-valley electrons via a microscopic theory.

DOI: 10.1103/PhysRevB.95.155207

I. INTRODUCTION

Electrons and holes in photoexcited semiconductors can form bound pairs of hydrogenlike excitons due to the attractive Coulomb interaction. For decades, techniques such as linear absorption [1,2] time-resolved photoluminescence [3–5], pump-probe spectroscopy [6,7], and four-wave mixing [8–10] have been used to study these quasiparticles intensively. As a consequence, most aspects and many important details of the light-matter interaction phenomena in semiconductors are now well understood [11–13].

However, despite all these studies, the conditions and dynamical characteristics of exciton formation are still discussed controversially. The microscopic analysis of Kira *et al.* [14] showed that the formation time of excitons cannot simply be deduced from the buildup of a luminescence peak at the spectral position of the excitonic transition. As an alternative method, it was suggested to monitor the appearance of the $1s$-$2p$ intraexcitonic resonance which can only occur if an optically induced coherent excitonic polarization and/or incoherent excitonic populations are present in the material [15]. For most of the popular semiconductor materials, the observation of this resonance requires the use of optical pump and terahertz (THz) probe spectroscopy. Provided with a suitable time resolution, this technique allows for the investigation of the formation and decay of the characteristic intraexcitonic transitions [16].

In fact, the optical pump and THz probe approach was pioneered in 1994 by Groeneveld and Grischkowsky [17], well before the above-mentioned theoretical work [14]. Groeneveld and Grischkowsky studied the $1s$-$2p$ transition of heavy-hole excitons in GaAs/AlGaAs multiple quantum wells. Although the signal-to-noise ratio and the analysis of the results was rather limited at that time, these investigations were the first experiments of this kind. About ten years later, similar experiments with a much improved resolution were performed by Kaindl *et al.* [18] and Huber *et al.* [19], who observed the buildup and decay of excitonic populations in GaAs/AlGaAs multiple quantum wells.

In subsequent years, also indirect semiconductors have been studied. Suzuki and Shimano investigated the formation of excitons and electron-hole droplets [20] and the cooling dynamics of the optically excited carriers [21] in Si. Furthermore, Sekiguchi and Shimano monitored intraexcitonic transitions in Ge, focusing in particular on the Mott transition [22]. Besides that, steady state experiments on Ge using conventional far-infrared techniques were performed in 1976 by Timusk [23].

Both Si and Ge show a strong electron mass anisotropy in their side valleys. For Ge, for instance, it has been known since the 1970's that this anisotropy leads to a splitting of the $1s$ excitonic resonance in the absorption spectrum [24]. To allow for the modeling of the THz response of such indirect semiconductors with anisotropic effective masses, a microscopic theory was developed recently [25]. The numerical studies predict a characteristic modification of the $1s$-$2p$ transition resonance which arises from the asymmetric parabolicity of the L valley in the conduction band. In particular, $2p$ excitons energetically split, resulting in two resonances in the THz absorption spectrum. However, such a double resonance structure has not yet been observed experimentally.

In this paper, we investigate the dynamics of exciton formation in bulk Ge for different excitation densities using optical pump and THz probe spectroscopy. We show that the exciton formation occurs faster when the excitation density is increased. Additionally, we unambiguously identify the unique double resonance attributed to the L-valley mass anisotropy.

II. EXPERIMENTAL DETAILS

We use a sample of undoped n-type Ge with a thickness of $l = 500\ \mu$m and a room-temperature resistivity of larger than 30 Ω cm for our experiments. A schematic of the indirect band structure of Ge can be seen in Fig. 1(a). The sample is cooled down to 11 K in a continuous flow liquid-He cryostat.

A 1 kHz Ti:sapphire regenerative amplifier system provides 35 fs pulses spectrally centered around 800 nm. The pulse train is split into three parts. After frequency conversion in an optical parametric amplifier to 0.8 eV (1550 nm), the first part optically excites the Ge crystal in the low-energy tail

*markus.stein@physik.uni-marburg.de
†Present address: Institute of Technical Physics, German Aerospace Center, Paffenwaldring 38-40, 70569 Stuttgart, Germany.

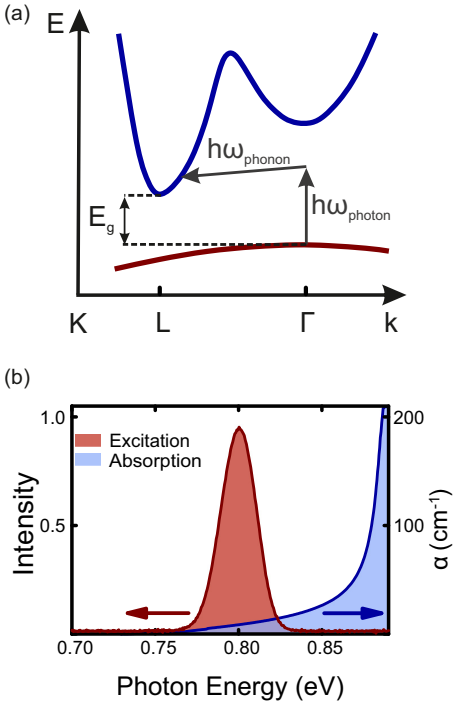

FIG. 1. (a) A sketch of the indirect band structure of Ge shows an electron mass anisotropy in the L valley. This means that the parabolicity of the L valley is asymmetric for different directions in k space. (b) The Ge sample is optically excited around 0.8 eV (red curve). Here, the measured absorption of Ge (blue curve) is relatively low. The excitation energy is barely above the indirect band gap.

of the measured absorption spectrum [see Fig. 1(b)]. As this excitation is only 55 meV above the indirect band gap, the absorption coefficient is low (8.4 cm^{-1}). This ensures a high penetration depth of the pump beam and therefore a nearly homogeneous excitation profile in the propagation direction. With a diameter of 3.5 mm the optical pump spot is laterally larger than the THz probe spot.

The second part of the pulse train excites a low-temperature (LT)-grown large aperture GaAs antenna which emits THz pulses with fields up to 15 kV/cm [26,27]. Field strengths of less than 0.5 kV/cm are used to ensure that the THz field acts as a probe and does not ionize the excitons [26]. The third part of the pulse train is used to record the THz probe pulse via electro-optical sampling by means of an 800 μm thick ZnTe crystal [28]. A pair of autobalanced photodiodes are used to sample the wave form of the THz field. The THz part of our setup is purged with nitrogen in order to get rid of water vapor absorption. This setup, which is depicted in Fig. 2, can detect THz pulses with a bandwidth ranging from 0.4 to 12 meV (0.1 to 3 THz) and a sufficiently high signal-to-noise ratio. We measured a time window of 21 ps with the THz pulse roughly centered in the middle of this window. Afterwards, we applied a Hanning window function to our data. A Fourier transformation of these wave forms yields the frequency domain fields of the reference pulse $E(\omega)$ as well

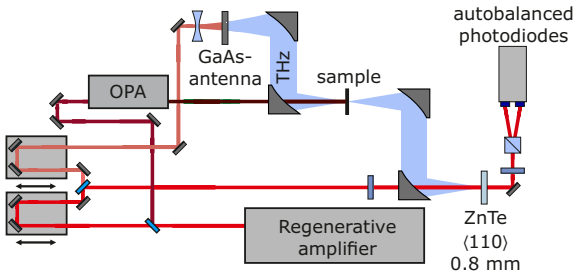

FIG. 2. A schematic of the experimental optical pump and THz probe setup. The THz section is purged with dry nitrogen to avoid THz absorption in water vapor.

as its pump-induced change $\Delta E(\omega)$. The absorption $\alpha(\omega)$ as well as the change of the real part of the dielectric function $\Delta\epsilon(\omega)$ are given by [29]

$$\alpha(\omega) = \frac{2}{l}\,\mathrm{Re}\left(\frac{\Delta E(\omega)}{E(\omega)}\right), \tag{1}$$

$$\Delta\epsilon(\omega) = \frac{2c_0\sqrt{\epsilon_r}}{\omega l}\,\mathrm{Im}\left(\frac{\Delta E(\omega)}{E(\omega)}\right), \tag{2}$$

where c_0 is the speed of light in vacuum and ϵ_r the dielectric constant of the material.

III. RESULTS

To study exciton formation times, it is useful to analyze the THz probe spectra at several instants after the optical pulse has excited the Ge sample [see Fig. 3(a)]. Here, the carrier density is estimated to be $5 \times 10^{14}/\mathrm{cm}^3$, i.e., far below the exciton Mott density in Ge, which, according to Sekiguchi and Shimano, is roughly at $1 \times 10^{16}/\mathrm{cm}^3$. We can see in Fig. 3(a)

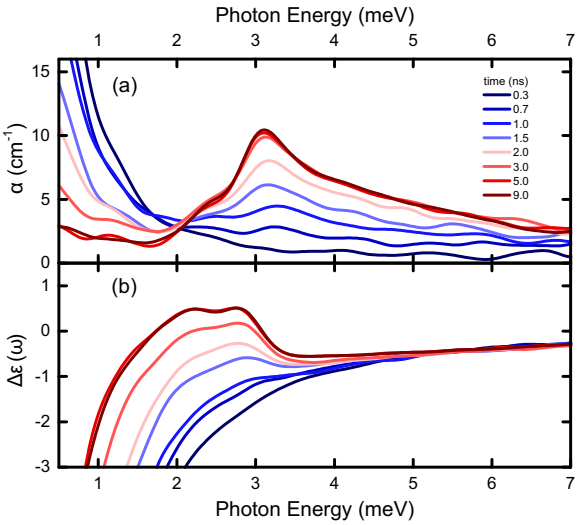

FIG. 3. (a) THz absorption spectra for different time delays between optical excitation and THz probe pulses. (b) Change of the real part of the dielectric function for the same time delays.

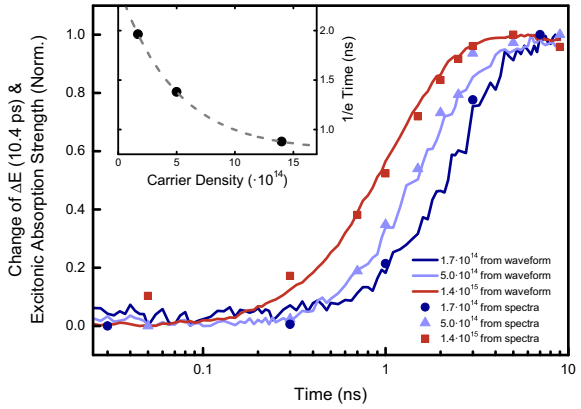

FIG. 4. Rise time of the excitonic response gained by two different methods. Symbols were extracted from the absorption strength of the excitonic resonance, while solid curves are extracted from transients at a temporal positon of 10.4 ps in the THz pulse. The inset shows buildup times for three different excitation densities obtained by ordinary exponential fits of the transients.

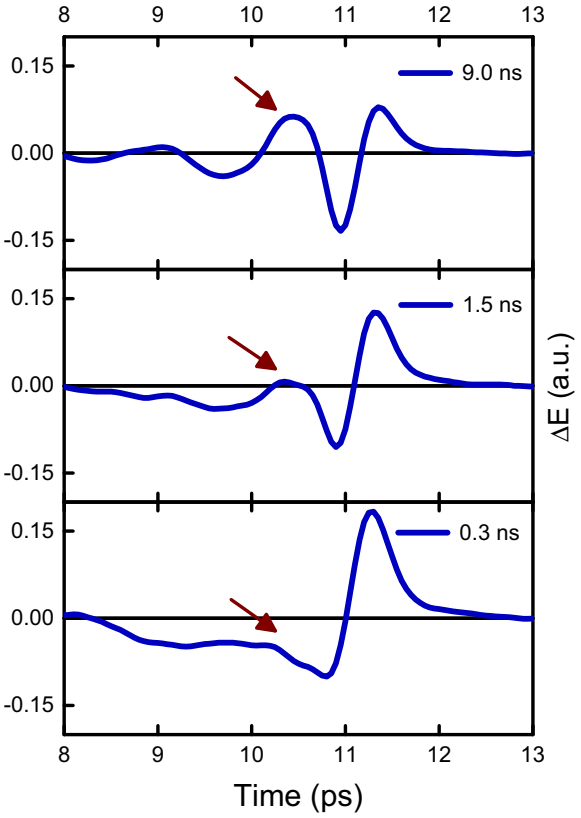

FIG. 5. Wave forms of the pump-induced change of the probing THz pulses for different times after excitation. The exciton formation can be monitored at certain temporal positions of the wave form. Most noticeable is the change of the wave form at 10.4 ps, while the system develops from an electron-hole plasma into bound excitons.

that shortly after the excitation, the THz absorption spectra are dominated by the response of an electron-hole plasma which gives rise to strong absorption below photon energies of 1.5 meV. The corresponding change of the dielectric function shows a negative response [see Fig. 3(b)], which is characteristic for an electron-hole plasma [29].

However, within a few nanoseconds the contribution of the electron-hole plasma decreases until it becomes insignificant after 5 ns. Simultaneously, we observe the formation of excitons, as indicated by the occurrence of a prominent absorption peak around 3.1 meV, which is associated with the intraexcitonic $1s$-$2p$ transition and agrees with earlier findings [22,23]. Furthermore, the change of the dielectric function shows an oscillatory signature at this energy, which is typical for a Lorentzian oscillator [29]. An additional absorption resonance appears at 2.4 meV, which is also accompanied by an oscillatory signature of the dielectric function.

A. Formation dynamics

To discuss the exciton dynamics, we notice that the first excitonic signatures are visible as a weak peak in the absorption spectrum around 3.3 meV for a pump-probe time delay of 0.7 ns. This peak evolves into a clear excitonic resonance reaching 50% of its final absorption strength around 1.5 ns after excitation. It takes up to 5 ns until the excitonic peak reaches its final oscillator strength and the final features of a significant electron-hole plasma vanish almost completely. For the temporally adjacent 4 ns, no evidence of recombination or formation of any further many-particle states such as biexcitons or electron-hole droplets can be observed.

To quantify these results, we read out the absorption at 3.1 meV for different time delays, subtract a weak offset from the plasma response at 50 ps, and finally normalize the data. In Fig. 4, we show the temporal evolution of the excitonic absorption strength for different excitation densities (symbols). Even though it is possible to extract an exciton formation time with this method, the time resolution is limited by the low number of spectra that can be measured within a reasonable time. To follow the dynamics of the exciton formation with a much better time resolution, we use an alternative experimental route. This method exploits a prominent feature in the pump-induced change of the THz wave forms which can be attributed to the buildup of exciton populations. For illustration purposes, Fig. 5 shows the pump-induced change of three THz pulses transmitted through the sample after 0.3, 1.5, and 9 ns, respectively. At 0.3 ns we see the pump-induced electric field oscillation of a pure or almost pure plasma response, while at 9 ns the oscillation of an almost pure excitonic response is shown. These two wave forms differ in particular at 10.4 ps. For simplicity, we assume that only two states exist in our system, a plasma state and an exciton state. Both contribute to the response at 10.4 ps. By a simple superposition of both responses we then can describe every mixture of those two states, e.g., the response at 1.5 ns can also be described by a superposition of 50% of the plasma response at 0.3 ns and 50% of the excitonic response at 9 ns. As a consequence, the value of the change of the electric field $\Delta E(t)$ at 10.4 ps continuously changes from

negative to positive when the system goes from the plasma state into an excitonic state. Hence, we are confident that the signal amplitude at this time delay is a fairly good measure for the exciton fraction in our system. Using this method, Fig. 4 illustrates the normalized change of $\Delta E(10.4\ \text{ps})$, shown as solid lines, along with the previous results obtained from the spectral absorption represented by symbols. Symbols and solid lines are in good agreement with one another, which suggests that the signal at 10.4 ps is indeed a good indicator for the exciton fraction.

Fitting ordinary exponential functions, we find the characteristic exciton formation times ranging from 1.96 ns for the lowest density to 0.88 ns for the highest density investigated. Hence, our experimental observations are in agreement with previous theoretical predictions in Ref. [30] that assert an accelerated exciton formation for an increased excitation density. The accelerated formation in this low-density regime is a consequence of the rising probability that electrons and holes find scattering partners necessary for the formation process.

Note that in contrast to the experiments on direct III-V semiconductors [31], we do not observe any noticeable exciton fraction for early times—neither in the spectra nor in the transients. We find here that the formation of excitons in Ge starts only after 200–700 ps, depending on the carrier density. This delayed start of the formation process is consistent with the typical cooling dynamics of excited charge carrier systems mediated by acoustic phonons [32].

B. *L*-valley anisotropy

Besides the experimental extraction of relevant time scales, a comparison to theoretically predicted absorption line shapes was performed. For this purpose, a generalized Wannier equation approach which accounts for the mass anisotropy of L-valley electrons is used [25].

This method is based on an expansion of the exciton wave function into spherical harmonics and introduces an energetic splitting of the $2p_0$ and $2p_{\pm1}$ exciton states. Effective electron masses and dielectric constants determine the extent of the splitting. At a single L valley, the selection rules prohibit the $1s$-$2p_0$ ($1s$-$2p_{\pm}1$) transition, except for a purely parallel (perpendicular) polarization of the probe field with respect to the ellipsoidal axis of the conduction band. However, the total THz response contains components from both polarizations due to the fourfold degeneracy of the L valley in Ge. As a result, the THz absorption is dominated by two distinct resonances. Since the resonance at 2.4 meV has a lower absorption coefficient, it leads to a shoulder on the low-energy side of the THz absorption spectrum. Our absorption spectrum measurement has a 2.9% relative accuracy at the 2.4 meV shoulder, and our theory analysis suggests the shoulder rises 59.4% above a single-Lorentzian result. Since experiment and theory show an excellent agreement at the shoulder, our comparison identifies the existence of two separate exciton resonances with a high confidence. Figure 6 presents a comparison of the computed absorption (shaded area) with the experimental spectrum 7 ns after the optical excitation (solid line). The excellent agreement was obtained using effective L-valley electron masses $m_\perp = 0.05m_0$ and $m_\parallel = 1.74m_0$, a hole mass of $m_\text{h} = 0.337m_0$, as well as a dielectric constant $\epsilon_\text{r} = 16.2$. In addition to the total spectrum, its decomposition into that part originating from parallel (dotted lines) and perpendicular (dashed lines) THz field polarization is shown. The values for the effective masses and the dielectric constant can be found in either Refs. [33] or [34]. There is one exception, which is the electron mass in the perpendicular (Γ-to-K) direction, which was assumed to be $0.05m_0$. In the literature this value varies around $0.08m_0$. It is necessary to adjust this value to reproduce the excellent agreement with the experiment. A likely reason is the band structure, which is assumed to be parabolic in our theory, but is not parabolic in reality.

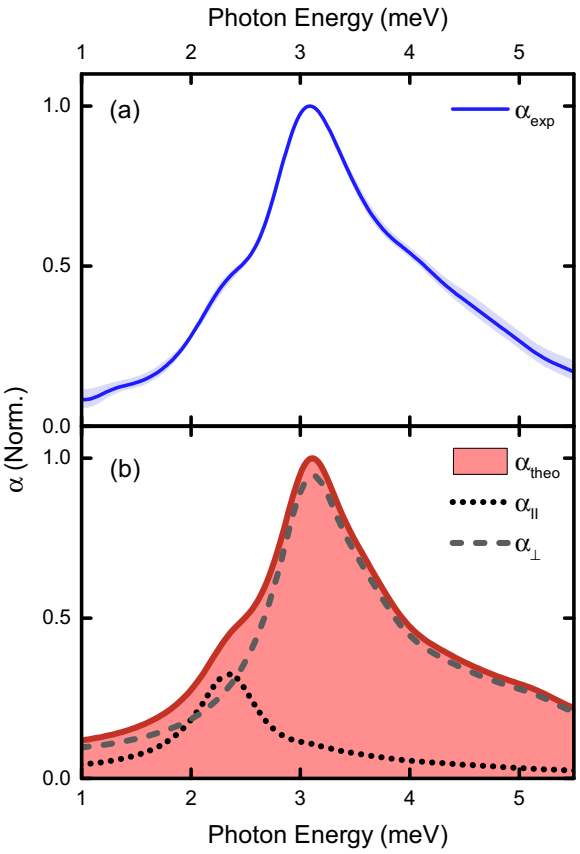

FIG. 6. Comparison between the experimental and theoretical results. (a) The measured spectrum (solid line) was taken 7 ns after optical excitation. The brighter line represents the standard error of the measurement. (b) The theoretical spectrum (shaded area) is a superposition of absorption spectra for parallel (dotted) and perpendicular (dashed) polarization.

IV. CONCLUSION

In summary, we performed optical pump and THz probe spectroscopy to study the dynamics of exciton formation in bulk Ge. The presence of excitons can be concluded from the occurrence of an absorption peak around 3.1 meV

(0.75 THz) associated with the intraexcitonic $1s$-$2p$ transition. We find that exciton formation starts several hundred picoseconds after nonresonant excitation and attribute this delay to the fact that the carrier distribution needs to cool down first via acoustic phonons. Our experimental observations are consistent with the theoretical prediction that exciton formation occurs faster for increased excitation densities. Furthermore, we show that the $1s$-$2p$ transition is composed of two distinct resonances which arise from the mass anisotropy of L-valley electrons.

ACKNOWLEDGMENTS

We acknowledge financial support from the Deutsche Forschungsgemeinschaft via the Collaborative Research Center 1083 (DFG:SFB1083).

[1] H. Haug, *Optical Nonlinearities and Instabilities in Semiconductors* (Elsevier, Amsterdam, 2012).
[2] T. Kazimierczuk, D. Fröhlich, S. Scheel, H. Stolz, and M. Bayer, Nature (London) **514**, 343 (2014).
[3] J. Feldmann, G. Peter, E. O. Göbel, P. Dawson, K. Moore, C. Foxon, and R. J. Elliott, Phys. Rev. Lett. **59**, 2337 (1987).
[4] B. Deveaud, F. Clérot, N. Roy, K. Satzke, B. Sermage, and D. S. Katzer, Phys. Rev. Lett. **67**, 2355 (1991).
[5] S. Imhof, C. Wagner, A. Thränhardt, A. Chernikov, M. Koch, N. S. Köster, S. Chatterjee, S. W. Koch, O. Rubel, X. Lu, S. R. Johnson, D. A. Beaton, and T. Tiedje, Appl. Phys. Lett. **98**, 161104 (2011).
[6] W. H. Knox, C. Hirlimann, D. A. B. Miller, J. Shah, D. S. Chemla, and C. V. Shank, Phys. Rev. Lett. **56**, 1191 (1986).
[7] A. P. Heberle, J. J. Baumberg, and K. Köhler, Phys. Rev. Lett. **75**, 2598 (1995).
[8] H. Wang, M. Jiang, and D. G. Steel, Phys. Rev. Lett. **65**, 2835 (1990).
[9] M. Koch, J. Feldmann, E. O. Göbel, P. Thomas, J. Shah, and K. Köhler, Phys. Rev. B **48**, 11480 (1993).
[10] S. T. Cundiff, T. Zhang, A. D. Bristow, D. Karaiskaj, and X. Dai, Acc. Chem. Res. **42**, 1423 (2009).
[11] M. Kira, F. Jahnke, W. Hoyer, and S. W. Koch, Prog. Quantum Electron. **23**, 189 (1999).
[12] M. Kira and S. W. Koch, Prog. Quantum Electron. **30**, 155 (2006).
[13] M. Kira and S. W. Koch, *Semiconductor Quantum Optics* (Cambridge University Press, Cambridge, UK, 2009).
[14] M. Kira, F. Jahnke, and S. W. Koch, Phys. Rev. Lett. **81**, 3263 (1998).
[15] M. Kira, W. Hoyer, T. Stroucken, and S. W. Koch, Phys. Rev. Lett. **87**, 176401 (2001).
[16] S. W. Koch, M. Kira, G. Khitrova, and H. Gibbs, Nat. Mater. **5**, 523 (2006).
[17] R. Groeneveld and D. Grischkowsky, J. Opt. Soc. Am. B **11**, 2502 (1994).
[18] R. A. Kaindl, M. A. Carnahan, D. Hägele, R. Lövenich, and D. S. Chemla, Nature (London) **423**, 734 (2003).
[19] R. Huber, R. A. Kaindl, B. A. Schmid, and D. S. Chemla, Phys. Rev. B **72**, 161314 (2005).
[20] T. Suzuki and R. Shimano, Phys. Rev. Lett. **103**, 057401 (2009).
[21] T. Suzuki and R. Shimano, Phys. Rev. B **83**, 085207 (2011).
[22] F. Sekiguchi and R. Shimano, Phys. Rev. B **91**, 155202 (2015).
[23] T. Timusk, Phys. Rev. B **13**, 3511 (1976).
[24] A. Frova, G. A. Thomas, R. E. Miller, and E. O. Kane, Phys. Rev. Lett. **34**, 1572 (1975).
[25] P. Springer, S. W. Koch, and M. Kira, J. Opt. Soc. Am. B **33**, C30 (2016).
[26] B. Ewers, N. S. Köster, R. Woscholski, M. Koch, S. Chatterjee, G. Khitrova, H. M. Gibbs, A. C. Klettke, M. Kira, and S. W. Koch, Phys. Rev. B **85**, 075307 (2012).
[27] M. J. Drexler, R. Woscholski, S. Lippert, W. Stolz, A. Rahimi-Iman, and M. Koch, Phys. Rev. B **90**, 195304 (2014).
[28] A. Nahata, A. S. Weling, and T. F. Heinz, Appl. Phys. Lett. **69**, 2321 (1996).
[29] R. Ulbricht, E. Hendry, J. Shan, T. F. Heinz, and M. Bonn, Rev. Mod. Phys. **83**, 543 (2011).
[30] W. Hoyer, M. Kira, and S. W. Koch, Phys. Rev. B **67**, 155113 (2003).
[31] R. A. Kaindl, D. Hägele, M. A. Carnahan, and D. S. Chemla, Phys. Rev. B **79**, 045320 (2009).
[32] K. Kash and J. Shah, Appl. Phys. Lett. **45**, 401 (1984).
[33] R. Poerschke and O. Madelung, *Data in Science and Technology, Semiconductors, Group IV Elements and III-V Compounds* (Springer, Berling, 1991).
[34] U. Rössler, D. Strauch, H. Landolt, and R. Börnstein, in *Semiconductors: Group IV Elements, IV-IV and III-V Compounds. Part A: Lattice Properties*, edited by O. Madelung, U. Rössler, and M. Schulz (Springer, Berlin, 2001).

II. Dynamics of charge-transfer excitons in type-II semiconductor heterostructures

M. Stein, C. Lammers, P.-H. Richter, C. Fuchs, W. Stolz, M. Koch, O. Vänskä, M. J. Weseloh, M. Kira, and S. W. Koch, Phys. Rev. B 97, 125306 (2018)

Abstract

The formation, decay, and coherence properties of charge-transfer excitons in semiconductor heterostructures are investigated by applying four-wave-mixing and terahertz spectroscopy in combination with a predictive microscopic theory. A charge-transfer process is identified where the optically induced coherences decay directly into a charge-transfer electron-hole plasma and exciton states. It is shown that charge-transfer excitons are more sensitive to the fermionic electron-hole substructure than regular excitons.

DOI: 10.1103/PhysRevB.97.125306

URL: `https://link.aps.org/doi/10.1103/PhysRevB.97.125306`

Dynamics of charge-transfer excitons in type-II semiconductor heterostructures

M. Stein,[1] C. Lammers,[1] P.-H. Richter,[1] C. Fuchs,[1] W. Stolz,[1] M. Koch,[1] O. Vänskä,[1] M. J. Weseloh,[1] M. Kira,[2] and S. W. Koch[1]
[1]*Department of Physics and Material Sciences Center, Philipps-Universität Marburg, Renthof 5, 35032 Marburg, Germany*
[2]*Center for Ultrafast Optical Science, University of Michigan, Ann Arbor, Michigan 48109, USA*

(Received 19 December 2017; revised manuscript received 12 February 2018; published 26 March 2018)

The formation, decay, and coherence properties of charge-transfer excitons in semiconductor heterostructures are investigated by applying four-wave-mixing and terahertz spectroscopy in combination with a predictive microscopic theory. A charge-transfer process is identified where the optically induced coherences decay directly into a charge-transfer electron-hole plasma and exciton states. It is shown that charge-transfer excitons are more sensitive to the fermionic electron-hole substructure than regular excitons.

DOI: 10.1103/PhysRevB.97.125306

I. INTRODUCTION

Most modern electric and optoelectronic devices consist of sophisticated heterostructures, the performance of which is dominated by the charge transport through the interfaces between the constituents [1–5]. Therefore the properties of these internal interfaces between solids become increasingly important with the continuing progress of device miniaturization [6–8]. This is particularly relevant in semiconductor heterostructures because they often comprise hundreds of individual layers with thicknesses in the nanometer regime [2,9].

For the *in situ* characterization of the inner boundaries between the different materials, it is desirable to identify interface-specific excitations that are accessible by suitable optical techniques to control both physical and chemical processes. A prominent example is the charge-transfer exciton (CTX), i.e., the Coulomb-bound quasiparticle where the electron and hole are located at the opposite sides of an internal interface. Therefore the CTX-formation dynamics not only contains quantum-level information about electron transport but also about the interface. In addition to being a promising probe of the microscopic interface properties, the CTX plays an important role in the charge-transfer (CT) process of heterojunction solar cells as well [10–13].

So-called type-II quantum-well (QW) heterostructures are ideally suited for the studies on CTXs and their dynamical properties [14,15]. In such systems, the conduction-band minimum and the valence-band maximum are localized at different sides of the internal interface such that the energetically lowest electron-hole transitions are indirect in real space and the attractive Coulomb interaction can give rise to a stable CTX, also referred to as type-II exciton.

Experimentally, the formation and decay dynamics of excitonic populations are optimally studied by combining conventional optical techniques, i.e., pump-probe, four-wave mixing (FWM), and luminescence measurements, with direct quasiparticle spectroscopy using terahertz (THz) light sources [16]. In our investigations, we apply these techniques for experimental characterization. We use a microscopic quantum theory [17–19] for the design and metal-organic chemical vapor deposition (MOCVD) fabrication for the growth of a GaAs/InGaAs/GaAsSb type-II double-quantum-well (DQW) structure that exhibits a CTX resonance in its linear absorption spectrum. This feature makes it possible for us to perform optical studies for a wide range of conditions, including resonant CTX excitation. In samples without CTX resonance, the formation of CTX populations is usually a multistep process where optical excitation induces a type-I interband transition followed by a CT process across the internal interface.

II. SAMPLE DESIGN

We design a DQW structure to have a pronounced type-II character while still retaining enough overlap between the ground-state electron and hole wave functions, allowing for optically active CT states. Since the CTX resonance should be distinguishable in the THz-absorption spectra from the direct-exciton resonance as well as from the Drude-like plasma response [19], we need to tailor the $1s$-to-$2p$ transition energies of the CTX states to be in the vicinity of 4 meV. This situation can be optimized by tuning the detailed material compositions and the layer thicknesses.

For the CTX, thicker layers result in a decrease of the Coulomb interaction between electrons and holes, which in turn leads to a smaller $1s-2p$ transition energy. At the same time, the thickness should not be too large as this suppresses the electron-hole wave-function overlap. In other words, increasing the thickness of both QWs of the structure reduces the intraexcitonic transition energies of the CTXs whereas for the direct exciton mainly the thickness of the InGaAs QW is relevant. On the other hand, the QWs should not be too thick since this causes many energetically close-by confinement levels, which makes a specific excitation of certain resonances cumbersome. Additionally, we require the lowest energy exciton to be a CT state. Overall, this leads to a rather complex optimization process between the thicknesses of the different active layers and the InGaAs-GaAsSb material compositions.

We approach the structure-design optimization problem by calculating the single-particle energies and wave functions based on an eight-band model of the $\mathbf{k}\cdot\mathbf{p}$ theory for

semiconductor heterostructures (see, e.g., Ref. [20]), where we include the effects of strain [21,22] and use the spherical approximation [18]. After numerically testing a variety of combinations, we conclude that in a suitable structure roughly 8-nm-thick QWs should be separated by an approximately 1-nm-thick interlayer. Good choices for the In and the Sb concentrations are in the vicinity of 5% and 3%, respectively.

On the basis of this modeling, a sample was grown using MOCVD. Characterization of the experimental sample yields a realized well thickness of 7.7 nm, an interlayer thickness of 1 nm, and In and Sb concentrations of 5.8% and 3.3%, respectively. For this set of structure parameters, we again compute the band structure via the 8×8 Hamiltonian using the material parameters suggested in Ref. [23] with exceptions that we increased the GaAsSb band-gap energy by 3.5 meV and decreased the InGaAs band gap by 5 meV to match the two lowest resonances of optical absorption between theory and experiment. This minor tuning of the band gaps is well inside the uncertainties of the experimentally deduced band-gap bowing parameters of the GaAsSb and InGaAs ternary compounds. From the numerical solution of the 8×8 Hamiltonian, we extract the confinement functions, band-edge energies, effective masses, and dipoles that we use as an input for our microscopic theory in Sec. V.

III. SAMPLE FABRICATION AND CHARACTERIZATION

We carry out the sample growth by applying metal organic vapor phase epitaxy (MOVPE) in an AIXTRON AIX 200 Gas Foil Rotation® (GFR) reactor system. We chose hydrogen as the carrier gas and set the reactor pressure to $p_R = 50$ mbar. As group-V precursors, we use tertiarybutylarsine (TBAs), tertiarybutylphosphine (TBP), and triethylantimony (TESb). Triethylgallium (TEGa) and trimethylindium (TMIn) are the group-III precursors. We remove the native oxide layer from the double-side polished exact GaAs (001) substrates by applying a TBAs-stabilized bake-out procedure prior to the epitaxial growth of the active region. The active region consists of 50 repetitions of InGaAs/GaAs/GaAsSb DQWs. In between the DQW active regions, we grow tensile strained GaAs/GaAsP/GaAs barriers in order to compensate the compressive strain of the active region. *We also fabricate a type-I reference sample in a similar manner to that of the aforementioned type-II sample, but exclude the GaAsSb QWs as well as the GaAs interlayer.* We make the structures at a growth temperature of $T_g = 550\,^{\circ}$C and chose group-V/group-III gas phase ratios of 3.0, 4.8, and 4.0 for GaAsP, InGaAs, and GaAsSb, respectively.

We use a high-resolution x-ray diffraction (HR-XRD) with a Panalytical X'Pert Pro system for the structural characterization and atomic force microscopy (AFM) in a Digital Instruments NanoScope IIIa to analyze the quality of the epitaxial surface. We obtain the layer thicknesses and compositions from measurements of the $\omega - 2\theta$ diffraction pattern around the (004) reflection in combination with theoretical modeling. Figure 1(a) shows a comparison of the experimental and simulated HR-XRD intensity (I) patterns of the type-II sample. The 5 μm $\times$ 5 μm scan of the type-II sample [Fig. 1(b)] reveals a smooth and well defined surface with a root-mean-square roughness of 0.3 nm despite the complex structure of the layer stack.

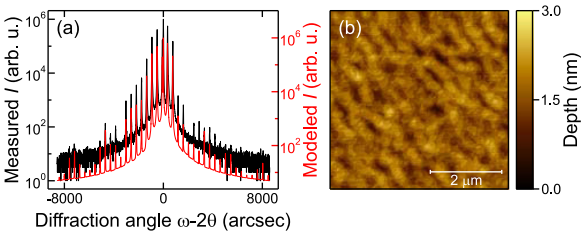

FIG. 1. Structural characterization of the type-II sample using HR-XRD and AFM. (a) The comparison of the experimental (black) and modeled (red) HR-XRD pattern of the type-II sample yields an excellent agreement and allows for a full determination of the structural parameters. (b) The AFM scan of the type-II sample reveals a smooth surface with a root-mean-square roughness of 0.3 nm.

IV. EXPERIMENTS

A. Four-wave mixing spectroscopy

We investigate the coherent dynamics of the regular type-I and the CT excitons by FWM experiments in self-diffraction geometry [24–26], using the output of a mode-locked titan-sapphire laser emitting 100-fs pulses with a repetition rate of 80 MHz. The emission energy is tunable and enables different excitation conditions. We superimposed laser pulses with wave vectors k_1 and k_2 on the sample. If the temporal delay between the pulses is smaller than or in the order of the phase relaxation time, this gives rise to a diffracted signal in the direction corresponding to $2k_2 - k_1$ (see Fig. 2). A photodiode measures the time-integrated diffracted signal as a function of the delay time between the pulses.

B. Optical-pump–THz-probe spectroscopy

We perform the optical-pump–THz-probe measurements [27–29] to study the intraexcitonic transitions for both the regular type-I and the CT excitons. For this purpose, we use the output of a 1-kHz titanium-sapphire regenerative amplifier system with 35-fs pulses spectrally centered around 1.55 eV. The pulse train is split into three parts. After frequency conversion in an optical parametric amplifier, the first part runs through a

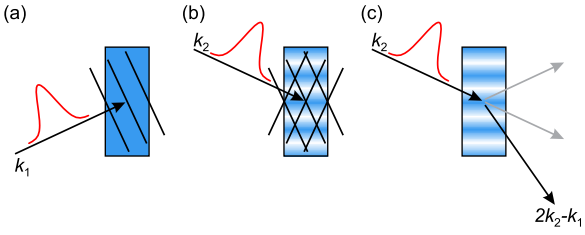

FIG. 2. (a) The first optical pulse k_1 induces a coherent polarization in the sample. (b) The second pulse k_2 interacts with this polarization and creates a spatially modulated population. (c) At the same time, parts of the second pulse are diffracted by the laser induced grating.

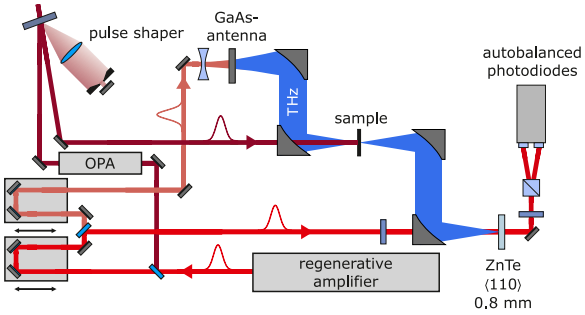

FIG. 3. Schematic of the optical-pump–THz-probe setup. Charge carriers are injected into the sample by a near-infrared pump beam of an optical parametric amplifier that is spectrally narrowed to 5 meV by a pulse shaper. Illumination of a large aperture GaAs antenna generates THz pulses. After passing the sample, these pulses are detected via electro-optical sampling by means of a ZnTe crystal and a pair of autobalanced photodiodes.

pulse shaper, creating spectrally narrow pulses at the desired energy required for photoexcitation of the respective sample. The second part of the amplifier output excites a LT-grown large aperture GaAs-antenna [30], which emits THz pulses with field strengths up to 15 kV/cm ranging from 0.4–12.4 meV (0.1–3 THz). The third part records THz wave forms via electro-optical sampling by means of an 800-μm-thick ZnTe crystal and autobalanced photodiodes. The THz beam path of our setup is purged with nitrogen in order to eliminate water vapor absorption. Figure 3 depicts a schematic of the optical-pump–THz-probe setup.

Fourier transformation of the detected wave forms yields the frequency domain fields of the reference pulse $E(\omega)$ as well as its pump induced change $\Delta E(\omega)$. The absorption $\alpha(\omega)$ as well as the change of the real part of the dielectric function $\Delta\epsilon(\omega)$ follow from

$$\alpha(\omega) = \frac{2}{l}\mathrm{Re}\left[\frac{\Delta E(\omega)}{E(\omega)+\Delta E(\omega)}\right],$$

$$\Delta\epsilon(\omega) = \frac{2c_0\sqrt{\epsilon_r}}{\omega l}\mathrm{Im}\left[\frac{\Delta E(\omega)}{E(\omega)+\Delta E(\omega)}\right],$$

where l is the thickness of the DQWs, c_0 is the speed of light in vacuum, and ϵ_r the dielectric constant of the material.

V. MICROSCOPIC THEORY

To microscopically model the optical and terahertz responses of CTX in the type-II QW structure, we generalize the approach of Refs. [18,19,31] to the electron-electron interactions through interfaces. This theory is then numerically evaluated to design the required type-II structure as well as to interpret the experimental results.

A. Excitation quantum kinetics

In QW structures, we can define the electronic state $i = (\boldsymbol{\lambda},\mathbf{k}_\parallel)$ via the band index $\boldsymbol{\lambda} = (\lambda,n)$ and the QW-plane crystal momentum $\hbar\mathbf{k}_\parallel$ [17,18]. Here, the band index $\boldsymbol{\lambda} = (\lambda,n)$ identifies the state to be either in a valence ($\lambda = v$) or in a conduction ($\lambda = c$) band while n gives the exact confinement level inside λ. The single-particle properties of homogeneously excited systems [18,19] follow from

$$P^{\lambda,\lambda'}_{\mathbf{k}_\parallel} \equiv \langle \hat{a}^\dagger_{\lambda,\mathbf{k}_\parallel}\hat{a}_{\lambda',\mathbf{k}_\parallel}\rangle \ (\lambda\neq\lambda'),$$

$$f^{\lambda}_{\mathbf{k}_\parallel} \equiv \langle \hat{a}^\dagger_{\lambda,\mathbf{k}_\parallel}\hat{a}_{\lambda,\mathbf{k}_\parallel}\rangle \ (\lambda = c),$$

$$f^{\lambda}_{\mathbf{k}_\parallel} \equiv 1-\langle \hat{a}^\dagger_{\lambda,\mathbf{k}_\parallel}\hat{a}_{\lambda,\mathbf{k}_\parallel}\rangle \ (\lambda = v),$$

where the Fermi operators $\hat{a}_{\lambda,\mathbf{k}_\parallel}$ and $\hat{a}^\dagger_{\lambda',\mathbf{k}_\parallel}$ relate $P^{\lambda,\lambda'}_{\mathbf{k}_\parallel}$ to the interband polarization and $f^{\lambda}_{\mathbf{k}_\parallel}$ to the electron ($\lambda = c$) or hole ($\lambda = v$) occupations. Analogously, the true two-body correlations are defined by

$$c^{\mathbf{q}_\parallel,\mathbf{k}'_\parallel,\mathbf{k}_\parallel}_{\lambda_1,\lambda_2;\lambda_3,\lambda_4} \equiv \Delta\langle \hat{a}^\dagger_{\lambda_1,\mathbf{k}_\parallel}\hat{a}^\dagger_{\lambda_2,\mathbf{k}'_\parallel}\hat{a}_{\lambda_3,\mathbf{k}'_\parallel+\mathbf{q}_\parallel}\hat{a}_{\lambda_4,\mathbf{k}_\parallel-\mathbf{q}_\parallel}\rangle.$$

The fully systematic quantum kinetics of these quantities are derived in Ref. [19], yielding the semiconductor Bloch equations [32]

$$\mathrm{i}\hbar\frac{\partial}{\partial t}P^{\lambda,\lambda'}_{\mathbf{k}_\parallel} = [\tilde{E}_{\lambda',\mathbf{k}_\parallel}+\tilde{E}_{\lambda,\mathbf{k}_\parallel}]P^{\lambda,\lambda'}_{\mathbf{k}_\parallel} - \left(1-f^{\lambda}_{\mathbf{k}_\parallel}-f^{\lambda'}_{\mathbf{k}_\parallel}\right) \times\left[E(t)D_{\lambda',\lambda}(\mathbf{k}_\parallel)+\sum_{\mathbf{k}'_\parallel}V^{\lambda;\lambda'}_{\mathbf{k}_\parallel-\mathbf{k}'_\parallel}P^{\lambda,\lambda'}_{\mathbf{k}'_\parallel}\right]+\Gamma^{\lambda,\lambda'}_{\mathbf{k}_\parallel}, \tag{1}$$

$$\frac{\partial}{\partial t}f^{\lambda}_{\mathbf{k}_\parallel} = \frac{2}{\hbar}\mathrm{Im}\left[\sum_{\eta\neq\lambda}\left[E(t)D_{\eta,\lambda}(\mathbf{k}_\parallel)+\sum_{\mathbf{k}'_\parallel}V^{\lambda;\eta}_{\mathbf{k}_\parallel-\mathbf{k}'_\parallel}P^{\lambda,\eta}_{\mathbf{k}'_\parallel}\right]\times P^{\eta,\lambda}_{\mathbf{k}_\parallel} - \sum_{\eta,\mathbf{k}'_\parallel}\sum_{\mathbf{q}_\parallel}V^{\lambda;\eta}_{\mathbf{k}_\parallel-\mathbf{k}'_\parallel-\mathbf{q}_\parallel}c^{\mathbf{q}_\parallel,\mathbf{k}'_\parallel,\mathbf{k}_\parallel}_{\lambda,\eta;\lambda,\eta}\right] \ (\lambda = c), \tag{2}$$

$$\frac{\partial}{\partial t}f^{\lambda}_{\mathbf{k}_\parallel} = \frac{2}{\hbar}\mathrm{Im}\left[\sum_{\eta\neq\lambda}\left[E(t)D_{\lambda,\eta}(\mathbf{k}_\parallel)+\sum_{\mathbf{k}'_\parallel}V^{\lambda;\eta}_{\mathbf{k}_\parallel-\mathbf{k}'_\parallel}P^{\eta,\lambda}_{\mathbf{k}'_\parallel}\right]\times P^{\lambda,\eta}_{\mathbf{k}_\parallel} + \sum_{\eta,\mathbf{k}'_\parallel}\sum_{\mathbf{q}_\parallel}V^{\lambda;\eta}_{\mathbf{k}_\parallel-\mathbf{k}'_\parallel-\mathbf{q}_\parallel}c^{\mathbf{q}_\parallel,\mathbf{k}'_\parallel,\mathbf{k}_\parallel}_{\lambda,\eta;\lambda,\eta}\right] \ (\lambda = v) \tag{3}$$

for the singlets. For the exciton correlation

$$c^{\mathbf{q}_\parallel,\mathbf{k}'_\parallel,\mathbf{k}_\parallel}_{\lambda,\lambda'} \equiv c^{\mathbf{q}_\parallel,\mathbf{k}'_\parallel,\mathbf{k}_\parallel}_{\lambda,\lambda';\lambda,\lambda'} \ (\lambda = c\,,\lambda' = v),$$

we obtain

$$\begin{aligned}\mathrm{i}\hbar\frac{\partial}{\partial t}c^{\mathbf{q}_\parallel,\mathbf{k}'_\parallel,\mathbf{k}_\parallel}_{\lambda,\lambda'} &= [\tilde{E}_{\lambda,\mathbf{k}'_\parallel+\mathbf{q}_\parallel}+\tilde{E}_{\lambda',\mathbf{k}_\parallel-\mathbf{q}_\parallel}-\tilde{E}_{\lambda',\mathbf{k}'_\parallel}-\tilde{E}_{\lambda,\mathbf{k}_\parallel}]\\ &\times c^{\mathbf{q}_\parallel,\mathbf{k}'_\parallel,\mathbf{k}_\parallel}_{\lambda,\lambda'} - A(t)j_{\lambda,\lambda'}(\mathbf{k}'_\parallel+\mathbf{q}_\parallel-\mathbf{k}_\parallel)c^{\mathbf{q}_\parallel,\mathbf{k}'_\parallel,\mathbf{k}_\parallel}_{\lambda,\lambda'}\\ &+\left(1-f^{e,\lambda}_{\mathbf{k}'_\parallel}-f^{h,\lambda'}_{\mathbf{k}_\parallel-\mathbf{q}_\parallel}\right)\sum_{\mathbf{l}_\parallel}V^{\lambda';\lambda}_{\mathbf{l}_\parallel-\mathbf{k}_\parallel}c^{\mathbf{q}_\parallel,\mathbf{k}'_\parallel,\mathbf{l}_\parallel}_{\lambda,\lambda'}\\ &-\left(1-f^{e,\lambda}_{\mathbf{k}'_\parallel+\mathbf{q}_\parallel}-f^{h,\lambda'}_{\mathbf{k}'_\parallel}\right)\sum_{\mathbf{l}_\parallel}V^{\lambda;\lambda'}_{\mathbf{l}_\parallel-\mathbf{k}'_\parallel}c^{\mathbf{q}_\parallel,\mathbf{l}_\parallel,\mathbf{k}_\parallel}_{\lambda,\lambda'}\\ &-S^{\mathbf{q}_\parallel,\mathbf{k}'_\parallel,\mathbf{k}_\parallel}_{\lambda,\lambda'}+D^{\mathbf{q}_\parallel,\mathbf{k}'_\parallel,\mathbf{k}_\parallel}_{\lambda,\lambda';\mathrm{rest}}+T^{\mathbf{q}_\parallel,\mathbf{k}'_\parallel,\mathbf{k}_\parallel}_{\lambda,\lambda'}.\end{aligned} \tag{4}$$

Here, we introduced the renormalized band dispersion

$$\tilde{E}_{\lambda,\mathbf{k}_\parallel} \equiv E_{\lambda,\mathbf{k}_\parallel} - \sum_{\mathbf{k}'_\parallel} V^{\lambda;\lambda}_{\mathbf{k}_\parallel-\mathbf{k}'_\parallel} f^{\lambda}_{\mathbf{k}'_\parallel} \quad (\lambda = c)\,,$$

$$\tilde{E}_{\lambda,\mathbf{k}_\parallel} \equiv -E_{\lambda,\mathbf{k}_\parallel} - \sum_{\mathbf{k}'_\parallel} V^{\lambda;\lambda}_{\mathbf{k}_\parallel-\mathbf{k}'_\parallel} f^{\lambda}_{\mathbf{k}'_\parallel} \quad (\lambda = v)$$

with the single-particle electronic energies $E_{\lambda,\mathbf{k}_\parallel}$ and the Coulomb-matrix element $V^{\lambda;\lambda'}_{\mathbf{q}_\parallel} \equiv V^{\lambda,\lambda;\lambda',\lambda'}_{\mathbf{q}_\parallel}$ defined by

$$V^{\lambda_1,\lambda_2;\lambda_3,\lambda_4}_{\mathbf{q}_\parallel} \equiv \frac{e^2}{2\epsilon_0\epsilon_{\mathrm{BG}}\mathcal{S}|\mathbf{q}_\parallel|} w_{\lambda_1,\lambda_2} w_{\lambda_3,\lambda_4} \times \int dz dz' g_{\lambda_1,\lambda_2}(z) g_{\lambda_3,\lambda_4}(z') e^{-|\mathbf{q}_\parallel||z-z'|}$$

with $g_{\lambda,\lambda'}(z) \equiv \xi^{\star}_{\lambda}(z)\xi_{\lambda'}(z)$, where $\xi_{\lambda}(z)$ is the confinement function of the band $\boldsymbol{\lambda}$. The electronic charge is denoted by e, ϵ_0 is the vacuum permittivity, $\mathcal{S}$ is the quantization area, ϵ_{BG} is the background screening constant of the structure, and $w_{\lambda,\lambda'}$ is the unit-cell overlap integral between the crystal-periodic Bloch functions [17,18,33]. Furthermore, $E(t)$ is an optical field, and we denote the vector potential of the THz field by $A(t)$. The optical field couples to the system via the dipole-matrix element

$$D_{\lambda,\lambda'}(\mathbf{k}_\parallel) \equiv g_{\lambda,\lambda'} d_{\lambda,\lambda'}(\mathbf{k}_\parallel)\,, \quad g_{\lambda,\lambda'} \equiv \int dz\, g_{\lambda,\lambda'}(z)$$

and the THz coupling is mediated by the intraband current-matrix element

$$j_{\lambda}(\mathbf{k}_\parallel) \equiv e\frac{\hbar\mathbf{k}_\parallel}{m_{\lambda}} \cdot \mathbf{e}_A\,.$$

Here, $d_{\lambda,\lambda'}(\mathbf{k}_\parallel)$ is the unit-cell dipole-matrix element, m_{λ} is the effective mass of band $\boldsymbol{\lambda}$, and $\mathbf{e}_A$ is the polarization vector of the THz fields [17–19].

In the semiconductor Bloch equations, where

$$\Gamma^{\lambda,\lambda'}_{\mathbf{k}_\parallel} \equiv \sum_{\eta,\mathbf{k}'_\parallel} \sum_{\mathbf{q}_\parallel\neq 0} \left[V^{\lambda';\eta}_{\mathbf{q}_\parallel} c^{\mathbf{q}_\parallel,\mathbf{k}'_\parallel,\mathbf{k}_\parallel}_{\lambda,\eta;\eta,\lambda'} - V^{\lambda;\eta}_{\mathbf{q}_\parallel} c^{\mathbf{q}_\parallel,\mathbf{k}'_\parallel-\mathbf{q}_\parallel,\mathbf{k}_\parallel+\mathbf{q}_\parallel}_{\lambda,\eta;\eta,\lambda'} \right],$$

the singlets couple to the doublets, which introduces microscopic screening, energy and field renormalizations, as well as dephasing for the singlets [19,34]. The doublet dynamics includes a current-matrix element $j_{\lambda,\lambda'}(\mathbf{k}_\parallel) \equiv j_{\lambda}(\mathbf{k}_\parallel) - j_{\lambda'}(\mathbf{k}_\parallel)$ and a singlet source:

$$S^{\mathbf{q}_\parallel,\mathbf{k}'_\parallel,\mathbf{k}_\parallel}_{\lambda,\lambda'} = V^{\lambda;\lambda'}_{\mathbf{k}'_\parallel+\mathbf{q}_\parallel-\mathbf{k}_\parallel} \{ f^{\lambda}_{\mathbf{k}'_\parallel+\mathbf{q}_\parallel} f^{\lambda'}_{\mathbf{k}'_\parallel} (1 - f^{\lambda}_{\mathbf{k}_\parallel} - f^{\lambda'}_{\mathbf{k}_\parallel-\mathbf{q}_\parallel}) - f^{\lambda}_{\mathbf{k}_\parallel} f^{\lambda'}_{\mathbf{k}_\parallel-\mathbf{q}_\parallel} (1 - f^{\lambda}_{\mathbf{k}'_\parallel+\mathbf{q}_\parallel} - f^{\lambda'}_{\mathbf{k}'_\parallel}) \}.$$

In Eq. (4), $T^{\mathbf{q}_\parallel,\mathbf{k}'_\parallel,\mathbf{k}_\parallel}_{\lambda,\lambda'}$ introduces the coupling to the triplet contributions and $D^{\mathbf{k}'_\parallel,\mathbf{k}_\parallel}_{\lambda,\lambda';\mathrm{rest}}$ includes the doublet couplings that can be omitted in the main-sum approximation [18,19]. In our further analysis and explicit numerical evaluations, we replace the contributions of the doublet and triplet couplings, $\Gamma^{\lambda,\lambda'}_{\mathbf{k}_\parallel}$ and $T^{\mathbf{q}_\parallel,\mathbf{k}'_\parallel,\mathbf{k}_\parallel}_{\lambda,\lambda'}$, via phenomenological dephasing factors γ_D and γ_T, respectively. Additionally, the electron-electron and hole-hole correlations in Eq. (4) that provide a screening of the THz currents [19] are described with a phenomenological screening factor γ_J.

B. Linear responses

References [18,31,35] introduce a convenient and straightforward method to derive wave equations for the vector potential and/or electric field interacting with a semiconductor system. This is done by starting from a minimal substitution Hamiltonian where the classical field is replaced via its quantized version. After solving the quantum dynamics of the electromagnetic field operators, the classical equations follow by taking the expectation values.

For a multiband type-II heterostructure, this approach yields the wave equations

$$\left(\frac{\partial^2}{\partial z^2} - \frac{n^2_{\mathrm{BG}}}{c_0^2}\frac{\partial^2}{\partial t^2}\right) E(t) = \mu_0 \frac{\partial^2}{\partial t^2} P_{\mathrm{opt}}\,,$$

$$\left(\frac{\partial^2}{\partial z^2} - \frac{n^2_{\mathrm{BG}}}{c_0^2}\frac{\partial^2}{\partial t^2}\right) A(t) = -\mu_0 J_{\mathrm{tot}}$$

for the electric field and the vector potential in the cases of optical or THz excitations, respectively. In these equations, n_{BG} is the background refractive index of the QW structure and μ_0 is the vacuum permeability. The macroscopic polarization

$$P_{\mathrm{opt}} \equiv \frac{1}{\mathcal{S}} \sum_{\mathbf{k}_\parallel} \left[\sum_{\lambda\in v} \sum_{\lambda'\in c} D_{\lambda,\lambda'}(\mathbf{k}_\parallel) P^{\lambda,\lambda'}_{\mathbf{k}_\parallel} + \sum_{\lambda\in c} \sum_{\lambda'\in v} D_{\lambda,\lambda'}(\mathbf{k}_\parallel) P^{\lambda,\lambda'}_{\mathbf{k}_\parallel} \right] \tag{5}$$

is determined by the expectation values of the microscopic polarization [17,18]. The total current, driven by the THz field, is

$$J_{\mathrm{THz}} \equiv \frac{1}{\mathcal{S}} \sum_{\lambda,\mathbf{k}_\parallel} j_{\lambda}(\mathbf{k}_\parallel) f^{\lambda}_{\mathbf{k}_\parallel} - \frac{1}{\mathcal{S}} \sum_{\lambda,\mathbf{k}_\parallel} \frac{e^2}{m_{\lambda}} f^{\lambda}_{\mathbf{k}_\parallel} A(t). \tag{6}$$

With all these ingredients, we can identify the frequency dependent linear susceptibilities

$$\chi_{\mathrm{opt}}(\omega) = \frac{P_{\mathrm{opt}}(\omega)}{\varepsilon_0 E(\omega)}, \tag{7}$$

$$\chi_{\mathrm{THz}}(\omega) = \frac{J_{\mathrm{THz}}(\omega)}{\varepsilon_0 \omega^2 A(\omega)}, \tag{8}$$

under either the optical or the THz excitation, respectively. From these, $\alpha(\omega) = \frac{\omega}{n_{\mathrm{BG}} c_0}\mathrm{Im}[\chi(\omega)]$ yields the absorption with either $\chi = \chi_{\mathrm{opt}}$ or $\chi = \chi_{\mathrm{THz}}$.

C. Responses in the exciton basis

The homogeneous part of Eq. (1) without correlations constitutes the Wannier equation [17,18]

$$(\tilde{E}_{\lambda,\mathbf{k}_\parallel} + \tilde{E}_{\lambda',\mathbf{k}_\parallel}) \phi^{\lambda,\lambda'}_{R;\nu}(\mathbf{k}_\parallel) - \left(1 - f^{\lambda}_{\mathbf{k}_\parallel} - f^{\lambda'}_{\mathbf{k}_\parallel}\right) \times \sum_{\mathbf{l}_\parallel} V^{\lambda;\lambda'}_{\mathbf{k}_\parallel-\mathbf{l}_\parallel} \phi^{\lambda,\lambda'}_{R;\nu}(\mathbf{l}_\parallel) = E^{\lambda,\lambda'}_{\nu} \phi^{\lambda,\lambda'}_{R;\nu}(\mathbf{k}_\parallel) \tag{9}$$

that is a generalized eigenvalue problem with the right-handed solution $\phi^{\lambda,\lambda'}_{R;\nu}(\mathbf{k}_\parallel)$ related to the eigenvalue $E^{\lambda,\lambda'}_{\nu}$. The left-handed solutions $\phi^{\lambda,\lambda'}_{L;\nu}(\mathbf{k}_\parallel)$ are connected to the right-handed

ones via the equation

$$\phi^{\lambda,\lambda'}_{L;\nu}(\mathbf{k}_\parallel) = \frac{\phi^{\lambda,\lambda'}_{R;\nu}(\mathbf{k}_\parallel)}{1 - f^{\lambda}_{\mathbf{k}_\parallel} - f^{\lambda'}_{\mathbf{k}_\parallel}}.$$

After using the freedom to choose the eigenstates $\phi^{\lambda,\lambda'}_{R;\nu}(\mathbf{k}_\parallel)$ to be real, the exciton wave functions are normalized so that

$$\sum_{\mathbf{k}_\parallel} \phi^{\lambda,\lambda'}_{L;\nu}(\mathbf{k}_\parallel)\phi^{\lambda,\lambda'}_{R;\nu'}(\mathbf{k}_\parallel) = \delta_{\nu,\nu'}.$$

The solutions of Eq. (9) can be identified as the exciton states that describe how an electron in band λ and a hole in band λ' are bound together with the exciton energy $E^{\lambda,\lambda'}_{\nu}$ [17,18].

As the exciton solutions form a complete basis, we can expand polarizations

$$P^{\lambda,\lambda'}_{\mathbf{k}_\parallel} = \sum_{\nu} p^{\lambda,\lambda'}_{\nu}\phi^{\lambda,\lambda'}_{R;\nu}(\mathbf{k}_\parallel), \quad p^{\lambda,\lambda'}_{\nu} = \sum_{\mathbf{k}_\parallel} \phi^{\lambda,\lambda'}_{L;\nu}(\mathbf{k}_\parallel)P^{\lambda,\lambda'}_{\mathbf{k}_\parallel}$$

and exciton correlations

$$\Delta N^{\lambda,\lambda'}_{\nu,\nu'}(\mathbf{q}_\parallel) = \sum_{\mathbf{k}_\parallel,\mathbf{k}'_\parallel} \phi^{\lambda,\lambda'}_{L;\nu}(\mathbf{k}_\parallel)\phi^{\lambda,\lambda'}_{L;\nu'}(\mathbf{k}'_\parallel)c^{\mathbf{q}_\parallel,\mathbf{k}'_\parallel-\mathbf{q}_h,\mathbf{k}_\parallel+\mathbf{q}_e}_{\lambda,\lambda'},$$

$$c^{\mathbf{q}_\parallel,\mathbf{k}'_\parallel-\mathbf{q}_h,\mathbf{k}_\parallel+\mathbf{q}_e}_{\lambda,\lambda'} = \sum_{\nu,\nu'} \phi^{\lambda,\lambda'}_{R;\nu}(\mathbf{k}_\parallel)\phi^{\lambda,\lambda'}_{R;\nu'}(\mathbf{k}'_\parallel)\Delta N^{\lambda,\lambda'}_{\nu,\nu'}(\mathbf{q}_\parallel),$$

where

$$\mathbf{q}_e \equiv \frac{m_\lambda}{m_\lambda - m_{\lambda'}}\mathbf{q}_\parallel, \quad \mathbf{q}_h \equiv -\frac{m_{\lambda'}}{m_\lambda - m_{\lambda'}}\mathbf{q}_\parallel.$$

By studying the electron-hole pair-correlation function [18,19], we conclude that the diagonal $\Delta N^{\lambda,\lambda'}_{\nu,\nu}(\mathbf{q}_\parallel)$ define the center-of-mass distribution of ν exciton while the nondiagonal $\Delta N^{\lambda,\lambda'}_{\nu,\nu'\neq\nu}(\mathbf{q}_\parallel)$ are related to some other type of correlated electron-hole quasiparticle configuration. The densities of both types of these correlations are given by

$$\Delta n^{\lambda,\lambda'}_{\nu,\nu'} \equiv \frac{1}{\mathcal{S}}\sum_{\mathbf{q}_\parallel} \Delta N^{\lambda,\lambda'}_{\nu,\nu'}(\mathbf{q}_\parallel). \tag{10}$$

After transforming Eqs. (1) and (5) into frequency space, we use the exciton-basis expansion of the microscopic polarization to solve $P_{\mathrm{opt}}(\omega)$ in terms of the excitonic solutions. Substitution of this result into Eq. (7) gives the Elliott formula [17,18]

$$\chi_{\mathrm{opt}}(\omega) = \frac{1}{\mathcal{S}\varepsilon_0}\sum_{\lambda\in c}\sum_{\lambda'\in v}\sum_{\nu} \frac{\left|\sum_{\mathbf{k}_\parallel}\phi^{\lambda,\lambda'}_{R;\nu}(\mathbf{k}_\parallel)D_{\lambda',\lambda}(\mathbf{k}_\parallel)\right|^2}{E^{\lambda,\lambda'}_{\nu} - \hbar\omega - \mathrm{i}\gamma_D},$$

for the optical susceptibility.

The derivation of the exciton-basis formula for the THz susceptibility is more complicated than the above derivation of $\chi_{\mathrm{opt}}(\omega)$, but follows a similar procedure. First, we take a time derivative of J_{THz} in Eq. (6), substitute the carrier-dynamics of Eqs. (2) and (3) into it, and then use the exciton-basis expansion of the correlations, which results in the coupling of J_{THz} to the correlation densities $\Delta n^{\lambda,\lambda'}_{\nu,\nu'}$. In the next step, we split $\Delta n^{\lambda,\lambda'}_{\nu,\nu'}$ into two parts where one is quasistationary and the other includes the linear response. We get the dynamics of the linear-response part of $\Delta n^{\lambda,\lambda'}_{\nu,\nu'}$ from Eq. (4) after transforming it into the exciton basis. In the last step, we Fourier transform $\frac{\partial}{\partial t}\Delta n^{\lambda,\lambda'}_{\nu,\nu'}$ (of the linear-response part) and substitute it into the Fourier transformation of the previously obtained J_{THz} to obtain the final form of $J_{\mathrm{THz}}(\omega)$ that is then substituted into Eq. (8). All these steps yield

$$\chi_{\mathrm{THz}}(\omega) = \frac{1}{\varepsilon_0\omega^2}\frac{1}{\hbar\omega + \mathrm{i}\gamma_J}\sum_{\substack{\lambda\in c\\ \lambda'\in v}}\sum_{\nu,\nu'}\left[T^{\lambda,\lambda'}_{\nu,\nu'}(\omega)\Delta n^{\lambda,\lambda'}_{\nu,\nu'} - \left(T^{\lambda,\lambda'}_{\nu,\nu'}(-\omega)\Delta n^{\lambda,\lambda'}_{\nu,\nu'}\right)^\star\right] - \frac{e^2}{\varepsilon_0\omega^2\mathcal{S}}\sum_{\lambda,\mathbf{k}_\parallel}\frac{f^{\lambda}_{\mathbf{k}_\parallel}}{m_\lambda}, \tag{11}$$

where the generic THz response function $T^{\lambda,\lambda'}_{\nu,\nu'}(\omega)$ is given by

$$T^{\lambda,\lambda'}_{\nu,\nu'}(\omega) \equiv \sum_{\eta}\frac{\left(E^{\lambda,\lambda'}_{\eta} - E^{\lambda,\lambda'}_{\nu}\right)J^{\lambda,\lambda'}_{\nu,\eta}J^{\lambda,\lambda'}_{\eta,\nu'}}{E^{\lambda,\lambda'}_{\eta} - E^{\lambda,\lambda'}_{\nu} - \hbar\omega - \mathrm{i}\gamma_T},$$

including the excitonic current-matrix element

$$J^{\lambda,\lambda'}_{\nu,\nu'} \equiv \sum_{\mathbf{k}_\parallel}\phi^{\lambda,\lambda'}_{L;\nu}(\mathbf{k}_\parallel)j_{\lambda,\lambda'}(\mathbf{k}_\parallel)\phi^{\lambda,\lambda'}_{R;\nu'}(\mathbf{k}_\parallel).$$

While deriving the above equation for $\chi_{\mathrm{THz}}(\omega)$, we keep only the terms related to the linear response and use the main-sum approximation.

The $\chi_{\mathrm{THz}}(\omega)$ includes contributions given by the nondiagonal $\Delta n^{\lambda,\lambda'}_{\nu,\nu'\neq\nu}$ electron-hole correlations that are not connected to the exciton densities. To estimate these correlations, we use the approach that yields the correlated electron-hole plasma quasiparticle configuration [18,19]. This is done by solving the steady state solution of Eq. (4) in the exciton basis without THz field and with constant carrier densities, yielding

$$\Delta N^{\lambda,\lambda'}_{\nu,\nu'}(\mathbf{q}_\parallel) = \frac{E^{\lambda,\lambda'}_{\nu} - E^{\lambda,\lambda'}_{\nu'}}{E^{\lambda,\lambda'}_{\nu'} - E^{\lambda,\lambda'}_{\nu} - \mathrm{i}\gamma_{\mathrm{P}}}S^{\lambda,\lambda'}_{\nu,\nu'}(\mathbf{q}_\parallel),$$

where the related triplet coupling is described by γ_{P}. Here, we have used the main-sum approximation and

$$S^{\lambda,\lambda'}_{\nu,\nu'}(\mathbf{q}_\parallel) \equiv \sum_{\mathbf{k}_\parallel}\phi^{\lambda,\lambda'}_{L;\nu}(\mathbf{k}_\parallel)f^{\lambda}_{\mathbf{k}_\parallel+\mathbf{q}_e}f^{\lambda'}_{\mathbf{k}_\parallel-\mathbf{q}_h}\phi^{\lambda,\lambda'}_{L;\nu'}(\mathbf{k}_\parallel)$$

is the singlet-source term. The correlation density $\Delta n^{\lambda,\lambda'}_{\nu,\nu'\neq\nu}$ that can exist in the system, whenever we have nonzero electron-hole occupations, follows from here via Eq. (10).

D. Self-consistent exciton states

To model experimental $\chi_{\mathrm{THz}}(\omega)$ via the introduced exciton-basis equations, we need several parameters. These include the three dephasing factors (γ_{T}, γ_{J}, and γ_{P}), the total density of carriers in each band, and the fraction of them that is bound to excitons. Additionally, we assume that the exciton and unbound-carrier distributions can be described by the Bose-Einstein and Fermi-Dirac distributions, respectively.

For the exciton-bound carrier distributions we use the self-consistent equations [36]

$$f^{\lambda}_{\mathbf{k}_\parallel} = \frac{1}{2} \pm \frac{1}{2}\sqrt{1 - 4\sum_{\lambda'\in v,\mathbf{k}'_\parallel} c^{\mathbf{k}_\parallel-\mathbf{k}'_\parallel,\mathbf{k}'_\parallel,\mathbf{k}_\parallel}_{\lambda,\lambda'}} \quad (\lambda = c), \tag{12}$$

$$f^{\lambda}_{\mathbf{k}_\parallel} = \frac{1}{2} \pm \frac{1}{2}\sqrt{1 - 4\sum_{\lambda'\in c,\mathbf{k}'_\parallel} c^{\mathbf{k}'_\parallel-\mathbf{k}_\parallel,\mathbf{k}_\parallel,\mathbf{k}'_\parallel}_{\lambda',\lambda}} \quad (\lambda = v) \tag{13}$$

to estimate the minimum electron and hole occupations required for the existence of the corresponding electron-hole correlations. For sufficiently low exciton densities with narrow distributions, the above equations yield approximately $f_{\mathbf{k}_\parallel}^{\lambda\in c} = \sum_{\lambda'\in v,\nu} \Delta n_{\nu,\nu}^{\lambda,\lambda'} |\phi_{R;\nu}^{\lambda,\lambda'}(\mathbf{k}_\parallel)|^2$ and $f_{\mathbf{k}_\parallel}^{\lambda\in v} = \sum_{\lambda'\in c,\nu} \Delta n_{\nu,\nu}^{\lambda',\lambda} |\phi_{R;\nu}^{\lambda',\lambda}(\mathbf{k}_\parallel)|^2$ that clearly show the connection between the carrier distributions, exciton densities, and exciton wave functions.

At elevated carrier densities and exciton fractions, this connection complicates the solution of the exciton states from Eq. (9), where several contributions depend on the electron and hole occupations. Most importantly, the Coulomb interaction is renormalized by the phase-space filling factor $1 - f_{\mathbf{k}_\parallel}^{\lambda} - f_{\mathbf{k}_\parallel}^{\lambda'}$ that is a direct consequence of the Pauli-blocking effect related to the fermionic substructure of excitons [18,19]. To include the Pauli blocking properly, we iteratively solve the coupled set of Eqs. (9), (12), and (13) for each set of assumed carrier densities and exciton fractions of the system.

VI. RESULTS AND ANALYSIS

In both, the type-I and type-II structures, we probe the formation and decay dynamics of coherent and incoherent excitons by FWM and THz spectroscopies. In these experiments that are all performed at 10 K, we excite the QWs by an optical pulse and probe the sample either via FWM or by THz pulses with time delays Δt_{FWM} and Δt_{THz}, respectively. In the type-II sample, the pump induces regular and CT polarizations in fractions determined by the spectral overlap of the pump with the sample absorption. Via the polarizations, the pump generates populations of electrons and holes. On a picosecond time scale, the holes will relax toward their ground-state in the GaAsSb QW [37–39]. During this time and up to nanoseconds, the build-up of correlations between electron-hole pairs occurs, leading to the formation of incoherent exciton populations [40–44]. The THz probe induces intraexcitonic transitions, e.g., from the excitonic $1s$ to the $2p$ state, which can be detected from the transmitted THz pulse.

To characterize our type-II sample, we measure [Fig. 4(a)]; shaded blue curve] and microscopically model [Fig. 4(b)] its optical absorbance. The experiment-theory comparison confirms that the lowest resonance (at 1.451 eV) originates from the InGaAs/GaAsSb CTX and the second resonance (at 1.464 eV) from the regular exciton of the InGaAs QW. Consequently, in the type-I reference sample only one resonance is present; the one from the InGaAs QW at 1.464 eV [see Fig. 8(a) in Appendix B]. While the CTX absorbs roughly four times less than the direct exciton, it is still clearly visible in the spectra, allowing us to resonantly excite both exciton types by tuning the excitation energy.

Figures 4(c)–4(e) show the intensity of the FWM signal from the type-II sample as a function of the delay time Δt_{FWM} when we tune the excitation energy E_P of the 17 meV broad pump pulse [Fig. 4(a); red curve] to 1.450 eV [Fig. 4(c)], 1.455 eV [Fig. 4(d)], or 1.465 eV [Fig. 4(e)]. The spectrally broad pump pulse is used to maximize the time resolution in order to track the subpicosecond dynamics of the FWM signatures. With excitation energies between 1.450 and 1.460 eV, we excite CT and regular polarizations. For this E_P range,

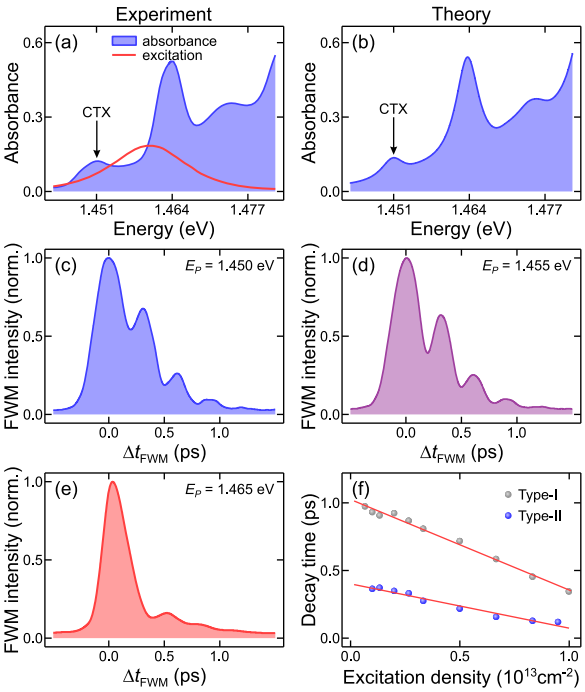

FIG. 4. Linear absorption and coherent dynamics of CTXs. Both (a) experimental and (b) theoretical linear absorption spectra show the CTX resonance. (c)–(e) The intensity of the FWM signal is shown for three different excitation conditions obtained in the type-II sample by tuning the excitation energy E_P of the pump pulse [(a), red curve]. (f) The deduced polarization decay times in the type-I (grey spheres) and type-II (blue spheres) samples are plotted as functions of the pump-pulse excitation density. A linear extrapolation (red lines) yields the decay times of 1.1 ps and 0.41 ps under low excitation conditions, i.e., for negligible densities.

we observe a clear beating pattern in the FWM signal at a frequency corresponding to the energy of 13.9 meV. This correlates well with the energy difference of the CTX and the regular exciton in the linear absorption spectrum. Thus we ascribe the beating pattern to the interference between the coexisting direct and CT excitonic polarizations [45].

For a resonant excitation at the type-I exciton [E_P = 1.465 eV; Fig. 4(e)], the FWM signal shows a very fast initial decay, which is almost independent of the excitation density. We attribute this to a very fast loss of regular-exciton polarizations within this sample. In particular, by combining this with our analysis of the THz results, we conclude that the fast initial decay of the regular-exciton polarization results from a fast CT of holes through the interface. Afterwards, the low fraction of the created CTX polarization gets visible and decays on a time scale that is independent from the central energy of the pump pulse. Thus the CTX coherence time is not affected by the regular polarization while the existence of the CTX polarization contributes to the decay of the regular coherences; see Appendix A for details of the analysis. In particular, the coherence of the regular exciton in the type-II sample decays very fast within the first 0.2 ps when no or almost

no CTX polarization coexists. However, when regular and CT exciton polarizations coexist, we observe a beating pattern between both polarizations that decays on a 0.4 ps time scale. Hence we conclude that the existence of CTX polarizations seems to inhibit the fast decay of regular exciton coherences.

Also our type-I sample produces a FWM-beating pattern for resonant excitation conditions [see Fig. 7(a) in Appendix A]. Here, the beating pattern results from an interference between the $1s$ excitonic polarization and polarizations of $2s$ and higher states, which are excited by the spectrally broad pulse. Consequently, the frequency of the beating pattern corresponds to the 7 meV energy difference between the $1s$ and $2s$ exciton states [25].

Figure 4(f) compares the decay times of the FWM signals in the type-I (grey spheres) and type-II (blue spheres) structures as a function of excitation density of the pump pulse after resonant excitation to their respective lowest resonances. As the data is extrapolated to zero density, we find low-density decay times of 0.4 and 1.1 ps for the type-II and type-I samples, respectively (see Appendix A). In other words, the coherence of the CTX polarization is lost almost three times faster than the coherence in the type-I sample. Since the CTX is spread over three different material compositions, crosses four interfaces, and features a larger Bohr radius than a regular exciton, we attribute the faster decay to an increased broadening and additional scattering at the interfaces. Similarly, the CTX resonance in the absorption spectrum is broader than the regular exciton resonance [see Figs. 8(a) and 8(b) in Appendix B].

After the coherent polarization is lost, we systematically determine the formation dynamics of an incoherent CTX population via a set of optical-pump–THz-probe experiments in the type-II sample. Figures 5(a) and 5(b) present the measured and modeled THz absorbances as function of the delay time Δt_{THz} and the THz photon energy $\hbar\omega_{\mathrm{THz}}$ after exciting the type-II sample resonantly ($E_P = 1.464$ eV) to its regular exciton with a photon density of 1.6×10^{12} cm^{-2} (see Appendix B for more details on the excitation conditions). For the shortest delay times, the THz-absorbance spectrum shows

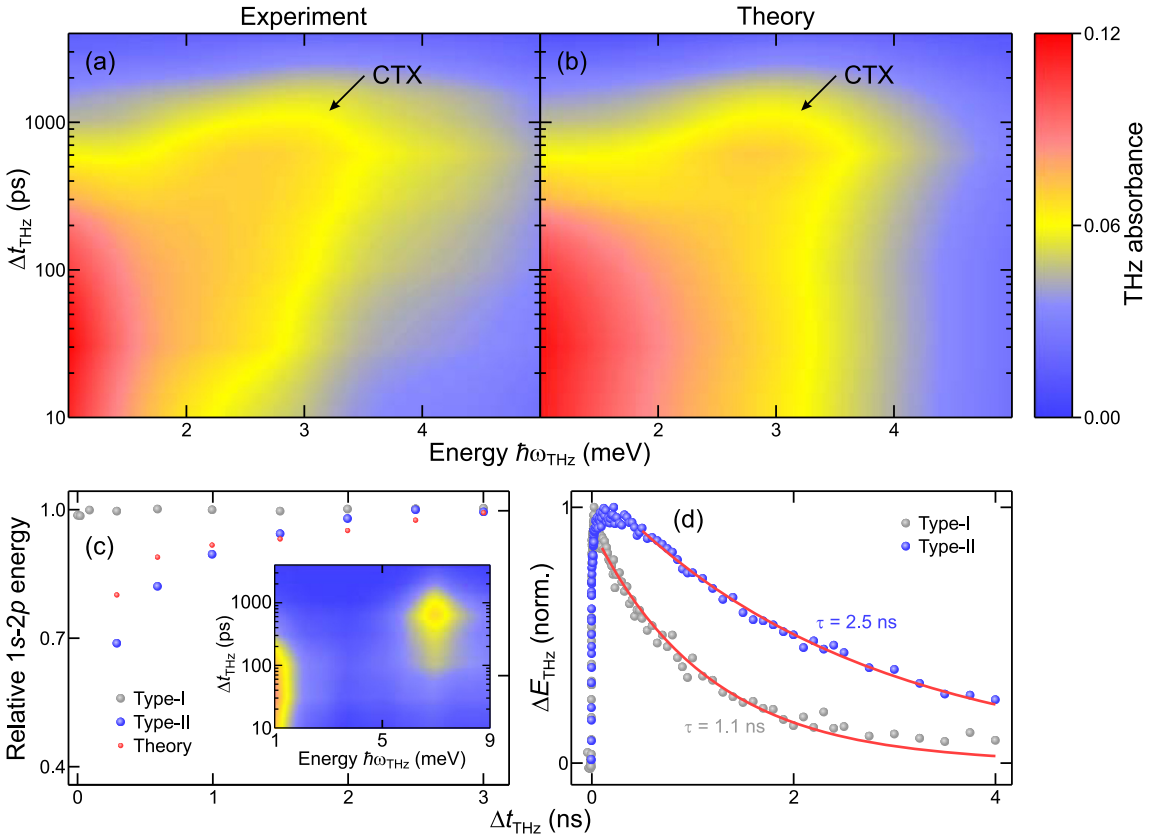

FIG. 5. Time-resolved THz response of the intraexcitonic CTX transition. (a) Experimental and (b) theoretical THz absorbance spectra as functions of the delay time Δt_{THz} and the photon energy $\hbar\omega_{\mathrm{THz}}$ after resonantly exciting the type-I exciton. At early times, the response shows a predominantly Drude-like character, which develops into a clear CTX $1s-2p$ resonance feature at 2.2 meV after $\Delta t_{\mathrm{THz}} = 300$ ps. As this resonance grows, it shifts toward $\hbar\omega_{\mathrm{THz}} = 3.2$ meV. (c) The measured $1s-2p$ resonance energy in type-I (grey spheres) and type-II (blue spheres) structures relative to 6.97 and 3.18 meV, respectively. The red dots show the results from the theoretical modeling of the type-II structure and the inset presents the THz absorbance of the type-I sample after nonresonant excitation. (d) The measured maximal change of the transmitted THz pulses ΔE_{THz} after resonant excitation to the lowest resonances of the type-I (grey spheres) and type-II (blue spheres) samples. The exponential fits (lines) yield decay times of $\tau = 1.1$ and 2.5 ns.

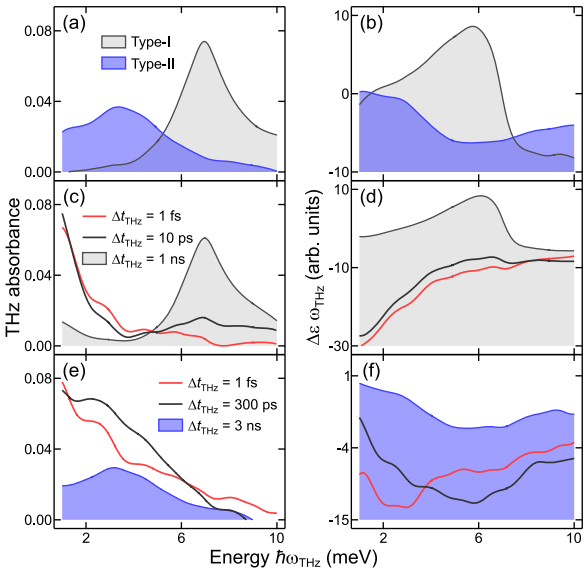

FIG. 6. Dynamical THz response in type-I vs type-II samples. Shortly (5 ps) after the resonant excitation to the lowest resonance, (a) the THz absorbance and (b) the differential dielectric function $\Delta\epsilon\omega_{\mathrm{THz}}$ of the type-I (gray) and type-II (blue) samples show a predominantly excitonic response. After the initial plasma response, the time evolution (c) of the THz absorbance and (d) of $\Delta\epsilon\omega_{\mathrm{THz}}$ for the type-I sample, after nonresonant excitation, clearly show the build-up of the intraexcitonic $1s-2p$ transition peak. In the type-II sample, the CTX resonance emerges in the temporal evolution (e) of the THz absorbance and (f) of the $\Delta\epsilon\omega_{\mathrm{THz}}$ on a nanosecond-time scale after its resonant excitation at the type-I exciton.

a Drude-like signature with a rich substructure, including a noticeable shoulder in the vicinity of $\hbar\omega_{\mathrm{THz}} = 2.5$ meV as can be traced in Fig. 6(e), which shows selected cuts from Fig. 5(a). Around $\Delta t_{\mathrm{THz}} = 300$ ps, this shoulder transforms into a resonance at $\hbar\omega_{\mathrm{THz}} = 2.2$ meV. During the following nanoseconds, this peak becomes more pronounced and shifts toward higher energies. Our theoretical results in Fig. 5(b) not only corroborate the experiments, but they also connect the observed temporally developing resonance to the CTX $1s-2p$ transition.

Figure 5(c) shows the experimental and theoretical $1s-2p$ resonance positions of the type-II structure (blue spheres and red dots, respectively) as well as the experimental $1s-2p$ resonance position of the type-I structure (grey spheres) as a function of Δt_{THz}. We extract the experimental peak positions for the type-II (type-I) sample from the data of Fig. 5(a) [insert of Fig. 5(c); type-I THz absorbance after nonresonant excitation], while the theoretical peak positions are from the data of Fig. 5(b). The data are normalized to their respective maximum $1s-2p$ resonance energies. Since the constituent electron and hole in a CTX are located at the opposite sides of an internal interface, their mutual Coulomb attraction is reduced relative to the case of regular excitons. Consequently, the CTX binding energy is smaller than in regular excitons, which in our case leads to the difference between the low-density $1s-2p$ resonance energies of 3.2 and 7.0 meV of the CTX and regular excitons, respectively.

A small binding energy results in a large Bohr radius, which in turn enhances the non-Bosonic exciton characteristics. These non-Bosonic features include the Pauli-blocking effect that weakens the attraction between electrons and holes in the form of a Fermi pressure. When the electrons and holes are accumulated at separate spatial locations of the system, the repulsive Fermi pressure is increased simultaneously as the attractive Coulomb interaction is reduced. In the Wannier equation (9), these effects enter via the phase-space filling factor $1 - f^{\lambda}_{\mathbf{k}_\parallel} - f^{\lambda'}_{\mathbf{k}_\parallel}$ while the accumulative effect is described in Sec. V D.

In Fig. 5(c), both samples are excited to comparable carrier densities of 1.5×10^{10} cm^{-2} (see Appendix B), but only the CTX resonance shows a pronounced shift as the densities decay. [We connect the different time delays shown in Fig. 5(c) to carrier densities in Appendix C; see especially Fig. 10.] Our theoretical analysis corroborates the experimental results and clearly shows that the shift mainly stems from the described Pauli blocking, unambiguously indicating that CTX properties are more sensitive to its fermionic substructure than those of the type-I exciton. Furthermore, in our modeling, we find that the strength of the Pauli-blocking effect essentially depends on such cooling-dynamic quantities as the exciton fraction, the temperature of the carriers, and the exciton distribution; although, the carrier density is the leading term.

In Appendix B, we estimate the Mott densities of our type-I and type-II samples to be 8.0×10^{10} and 3.6×10^{10} cm^{-2}, respectively. According to these values, we are well below the Mott region in both samples; more significantly in the type-I sample. In other studies of similar type-I samples, a significant shift of the $1s-2p$ resonance is only seen when the carrier densities are close to our estimation of the Mott density of 8.0×10^{10} cm^{-2} [46] or a shift of the resonance is not observed at all [47]. However, in Ref. [46], a comparable shift as seen for the CTX in Fig. 5(c) is achieved in a type-I sample. Yet, this requires changes of the carrier densities from 2.0×10^{10} cm^{-2} to more than 1×10^{11} cm^{-2}, which is above our estimation of the Mott density for such a type-I structure. In addition, the shift is accompanied by a strong broadening of the resonance. In Ref. [47], only a broadening of the resonance is observed without any noticeable shift for a sample of GaInAs QWs. In our CTX studies, we observe a shift of the resonance even though we are more than a factor of 2 below the estimated Mott density. During the strong shift for delay times from 0.3 to 2.0 ns the carrier density only varies by a factor of 2 as can be seen in Fig. 10. Furthermore, a strong broadening of the resonance is not observed in our CTX results of Fig. 5(a). This comparison indicates that CTXs are not only more sensitive to fermionic effects than regular excitons compared to an absolute carrier density, but also with respect to their respective Mott densities.

For additional information on the formation and decay dynamics of the pump induced THz response, we analyze ΔE_{THz}, i.e., the maximum change in the temporal wave form of the transmitted THz pulse between the excited and unexcited samples [48,49] as described in Appendix C. Figure 5(d) shows ΔE_{THz} as a function of the pump-probe delay time in type-I (grey spheres) and type-II (blue spheres) structures

after resonant excitation to their respective lowest resonances. Under these excitation conditions, the build-up of the THz response occurs on a picosecond time scale before it decays exponentially (red curves) with time constants of $\tau = 1.1$ ns and $\tau = 2.5$ ns for the type-I and type-II samples, respectively. Similar decay times are also observed for the excitation conditions of Fig. 5(a) and the insert of Fig. 5(c), showing that these time scales are characteristic for the decay dynamics of the regular and the CT excitons in the samples investigated.

Our setup allows us to compare the temporal evolution of the THz absorbance (left column in Fig. 6) and the differential dielectric function $\Delta\epsilon$ multiplied with ω_{THz} (right column in Fig. 6) after resonant and nonresonant excitations. By multiplying $\Delta\epsilon$ with ω_{THz}, we compensate the leading $1/\omega_{\mathrm{THz}}$ dependency of $\Delta\epsilon$ at low frequencies for illustrative purposes. As we can see in the top row of Fig. 6, the type-I (grey) and type-II (blue) samples show excitonic signatures already 5 ps after resonant optical excitation to the respective energetically lowest absorption peaks. We find a clear $1s-2p$ resonance in the THz absorbance accompanied by the dispersive signature in $\Delta\epsilon\omega_{\mathrm{THz}}$. These features are indicative of the polarization-to-population conversion where CT and regular coherences directly decay into the corresponding correlated exciton populations [50].

In the middle row of Fig. 6, the temporal evolution of the THz response is shown for the type-I sample after nonresonant excitation. Immediately after the excitation (red lines), we see the typical Drude-like features originating from the generated electron-hole plasma. On a picosecond time scale ($\Delta t_{\mathrm{THz}} = 10$ ps; black lines), the $1s-2p$ resonance in the absorbance and the dispersive feature in $\Delta\epsilon\omega_{\mathrm{THz}}$ start to emerge around $\hbar\omega_{\mathrm{THz}} = 7$ meV. Once the delay time reaches $\Delta t_{\mathrm{THz}} = 1$ ns, the functional forms of the absorbance and $\Delta\epsilon\omega_{\mathrm{THz}}$ are very close to those in Figs. 6(a) and 6(b), indicating a clear dominance of the exciton over the plasma response. These findings are characteristic for the exciton formation process after nonresonant excitation where the pump generated polarization first decays into an electron-hole plasma followed by type-I exciton formation on a nanosecond time scale [42,44].

The lowest row in Fig. 6 depicts the CTX formation process in the type-II sample after resonant optical excitation around 1.464 eV, i.e., at the type-I exciton resonance. Immediately after the excitation (red lines), we basically see Drude-like signatures, however, $\Delta\epsilon\omega_{\mathrm{THz}}$ has a prominent turn to positive values at the lowest energies which is absent in the type-I response in Fig. 6(d). This feature remains clearly visible in $\Delta\epsilon\omega_{\mathrm{THz}}$ until the emergence of the $1s-2p$ CTX resonance around $\Delta t_{\mathrm{THz}} = 300$ ps (black curves).

Our microscopic theory relates this peculiar response in $\Delta\epsilon\omega_{\mathrm{THz}}$ to energetically higher CTX states. The energetically higher CTX states feature a similar absorption as the correlated electron-hole plasma. However, their $\Delta\epsilon\omega_{\mathrm{THz}}$ response can differ significantly. While plasma typically shows a negative $\Delta\epsilon\omega_{\mathrm{THz}}$ response [see Fig. 6(d)] energetically higher CTX states offer a positive contribution at low energies. These contributions are responsible for the turn of $\Delta\epsilon\omega_{\mathrm{THz}}$ toward positive values below 2 meV. At later times, the strength of the response of higher-CTXs decreases and eventually merges with the emerging $1s$-CTX response. This behavior relates to the cooling of the exciton distribution accompanied by the increasing binding energy of the $1s$ CTX. Subsequently, the $1s$ population builds-up such that around $\Delta t_{\mathrm{THz}} = 3$ ns (blue shaded curves) the THz signatures approach the type-II results of Figs. 6(a) and 6(b).

Surprisingly, we find that an extensive theory-experiment comparison cannot show *any* distinguishable signatures of the type-I exciton in the THz response of the type-II sample even for the shortest delay times. This is consistent with the very fast decay of the type-I coherences observed in the FWM experiments [Fig. 4(e)] only if the type-I exciton polarization does not decay into an incoherent type-I exciton population but into a CT population instead. Hence we have the interesting scenario where the resonantly induced type-I coherences in our type-II sample directly decay into CT exciton and plasma populations, indicating that the CT process proceeds faster than the formation of the type-I exciton populations.

VII. SUMMARY

In conclusion, we have studied the formation and decay dynamics of coherent and incoherent CTX populations in a type-II double-QW structure by utilizing FWM and THz spectroscopies. Our experimental studies are supported by a microscopic theory that unambiguously assigns the detected type-II signals to CT excitons. In particular, we could verify the formation of CTX populations in our sample and could determine their formation and decay dynamics. These studies clearly demonstrate that direct and indirect CTX spectroscopy yields valuable information on the microscopic details of the CT process. Furthermore, the direct observation of CTX resonances and their combined optical, FWM and THz spectroscopy marks the way towards systematic studies of the buried internal interface excitations in modern heterostructure systems.

ACKNOWLEDGMENTS

This work is a project of the Collaborative Research Center SFB 1083 funded by the Deutsche Forschungsgemeinschaft.

M.S. and C.L. contributed equally to the experimental part of this work.

APPENDIX A: DECAY TIMES IN FWM SPECTROSCOPY

We perform FWM experiments for a series of different excitation conditions, i.e., different excitation densities and energies. Decay times are extracted by applying exponential fits to the FWM transients for each excitation density. These exponential fits are shown exemplary in Fig. 7 for both samples as red lines. Density-dependent decay times of the type-I and the type-II QW samples are linearly extrapolated to yield the corresponding decay times under very low excitation conditions [24,51]. This is done to exclude the influence of excitation induced dephasing so that both samples can be compared at negligible densities. Excitation induced dephasing is mainly caused by scattering events of the created exciton polarizations with electrons and other excitons and reduces the observed decay times [52].

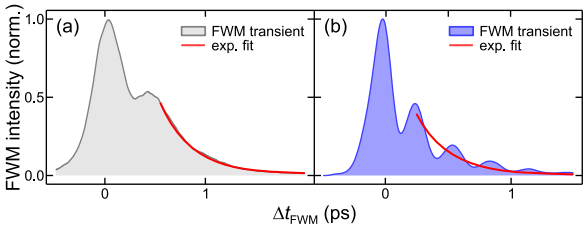

FIG. 7. FWM transient of the (a) type-I and (b) type-II heterostructures after resonant excitation close to their respective lowest resonances, i.e., close to 1.465 and 1.450 eV. The decay time is extracted by applying an exponential fit (red curves).

Tuning the excitation energy of our broad pump pulse enables us to strengthen certain polarizations within our samples in favor of others. This helps us to identify the contributions of certain resonances to the FWM signal. Furthermore, it enables us to estimate their decay times and check if the decay is affected by the existence of the other polarizations.

APPENDIX B: EXCITATION CONDITIONS FOR THz-PROBE SPECTROSCOPY

A pulse shaper is used to create spectrally narrow pulses at the desired energies. For nonresonant excitation of the type-I QW sample, we use a pulse energy of 1.475 eV and a photon density of 3.6×10^{12} cm^{-2}. In Fig. 8(a), we show the spectrum of the 5 meV broad pump pulse together with the linear absorption spectrum of the type-I sample. For excitation of the type-II sample at 1.464 eV, i.e., resonant to the type-I exciton, we use a photon density of 1.6×10^{12} cm^{-2}. The spectrum of the optical pulse is shown in light red in Fig. 8(b).

The photon densities of the optical excitation pulses are carefully chosen so that in both samples a similar amount of charge carriers is injected. The comparable amount of charge carriers is checked by a similar amplitude of ΔE_{THz} in the time domain as well as a similar strength of the plasma response at early times. Taking reflection losses into account, we estimate the injected carrier density per QW to 1.5×10^{10} cm^{-2}, which is in good agreement with the initial carrier density of 1.3×10^{10} cm^{-2} found in the theoretical modeling of the THz response.

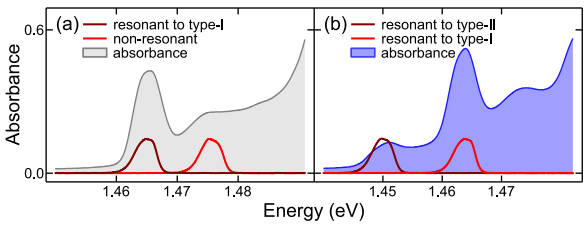

FIG. 8. The linear absorption spectra (a) of the type-I and (b) of the type-II samples. The spectra of the pump pulses for resonant excitation with respect to the energetically lowest exciton transitions are shown in dark red. The nonresonant excitation pulse of the type-I sample as well as the excitation pulse of the type-II sample that is resonant to its regular exciton are shown in light red.

When approaching the Mott-transition regime, it is beneficial to compare the photoinduced carrier density with the Mott density [46]. However, the determination of the Mott density n_{M} is somewhat ambiguous. One way to approximate it in two-dimensional systems is to relate it to the inverse of the exciton Bohr radius a_B via $n_{\mathrm{M}} = 1/(\pi a_B^2)$. From our numerical modeling, we extract the effective bulk Bohr radii, which are twice the actual two-dimensional values [17], of 19.9 and 29.6 nm for the type-I and type-II excitons in the corresponding samples, respectively. These yield estimated Mott densities of $n_{\mathrm{M}} = 8.0 \times 10^{10}$ and 3.6×10^{10} cm^{-2}.

An alternative approach to study the carrier density needed for the Mott-transition regime is obtained by considering the limit where the $1s$ exciton merges with the continuum. Our modeling yields a robust estimation of $n_{\mathrm{M}} = 7.5 \times 10^{10}$cm^{-2} for the regular exciton and $n_{\mathrm{M}} = 3.5 \times 10^{10}$ cm^{-2} for CTX. These compare well with our previous estimations of n_{M} as well as with the Mott densities specified by others for similar type-I [46,53] and type-II [54] structures. In particular, the Mott density determined in Ref. [54] fits well to our estimation of the type-II structure when their Mott density is scaled with respect to the higher exciton binding energy of our sample. Thus we evaluate the Mott density in our type-II sample to be around $n_{\mathrm{M}} = 3.6 \times 10^{10}$ cm^{-2}. This is more than a factor of two above the injected carrier density.

APPENDIX C: THz TRANSIENTS

To follow the dynamics of the exciton formation and recombination after resonant excitation, we measure the transients of the pump induced change ΔE_{THz} at prominent features of the THz wave form as can be seen in Fig. 9. The magnitude of this feature is proportional to the excitonic absorption strength and, under resonant excitation conditions well below the Mott density, directly related to the exciton population [48]. As the exciton population decays due to recombination processes, the magnitude of this feature drops. A transient at this temporal position in the time domain is therefore suitable to monitor the recombination of the exciton population.

However, changes in the spectral shape of the THz response can drastically affect the formation- and decay-dynamic results obtained with this method. Thus, after nonresonant excitation, we focus our studies of the ΔE_{THz} change to delay times

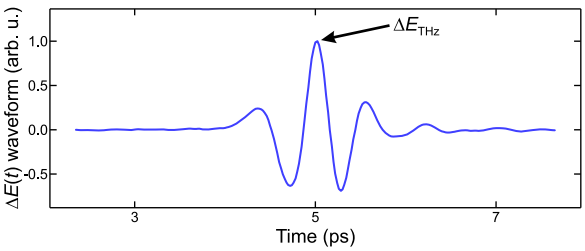

FIG. 9. The measured wave form displays the change of the THz pulse due to the resonantly pumped sample for a pump-probe delay of 5 ps. In our experimental analysis, we measure the transients at the maximal change of the transmitted THz field at a temporal position of 5 ps.

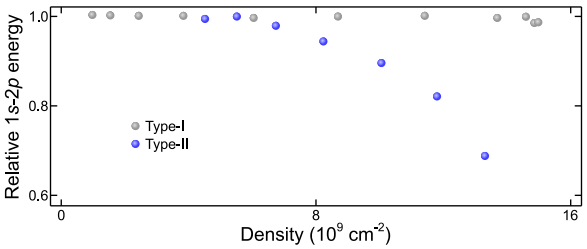

FIG. 10. Carrier density dependence of the $1s-2p$ resonance energy in type-I (grey spheres) and type-II (blue spheres) structures relative to 6.97 and 3.18 meV, respectively.

(Δt_{THz}) above 1.5 ns. At this time and later, the spectral shape of the THz response remains rather unchanged. After resonant excitation to the energetically lowest resonance of the sample, this condition is already reached within several picoseconds so that the analysis of the decay dynamics of ΔE_{THz} as shown in Fig. 5(d) can start shortly after excitation.

Furthermore, the decay times we receive with this method enable us to calculate the charge carrier density for each time delay between the optical-pump and THz-probe pulses. Assuming an initial carrier density of 1.5×10^{10} cm^{-2} for both samples after nonresonant excitation, we show the carrier density dependent shift of the relative $1s-2p$ resonance of Fig. 5(c) in Fig. 10.

[1] A. Dodabalapur, L. Torsi, and H. E. Katz, Science **268**, 270 (1995).
[2] K. Tomioka, M. Yoshimura, and T. Fukui, Nature (London) **488**, 189 (2012).
[3] X. Zou, J. Wang, C.-H. Chiu, Y. Wu, X. Xiao, C. Jiang, W.-W. Wu, L. Mai, T. Chen, J. Li, J. C. Ho, and L. Liao, Adv. Mater. **26**, 6255 (2014).
[4] H. Zhou, Q. Chen, G. Li, S. Luo, T. B. Song, H. S. Duan, Z. Hong, J. You, Y. Liu, and Y. Yang, Science **345**, 542 (2014).
[5] J. Krüger, R. Plass, L. Cevey, M. Piccirelli, M. Grätzel, and U. Bach, Appl. Phys. Lett. **79**, 2085 (2001).
[6] H. Kroemer, Rev. Mod. Phys. **73**, 783 (2001).
[7] M. M. Waldrop, Nature (London) **530**, 144 (2016).
[8] R. K. Cavin, P. Lugli, and V. V. Zhirnov, Proc. IEEE **100**, 1720 (2012).
[9] P. M. Koenraad and M. E. Flatté, Nat. Mater. **10**, 91 (2011).
[10] A. E. Jailaubekov, A. P. Willard, J. R. Tritsch, W. L. Chan, N. Sai, R. Gearba, L. G. Kaake, K. J. Williams, K. Leung, P. J. Rossky, and X. Zhu, Nat. Mater. **12**, 66 (2013).
[11] G. Grancini, M. Maiuri, D. Fazzi, A. Petrozza, H. J. Egelhaaf, D. Brida, G. Cerullo, and G. Lanzani, Nat. Mater. **12**, 29 (2013).
[12] A. J. Heeger, Adv. Mater. **26**, 10 (2014).
[13] M. Gerhard, A. P. Arndt, I. A. Howard, A. Rahimi-Iman, U. Lemmer, and M. Koch, J. Phys. Chem. C **119**, 28309 (2015).
[14] L. V. Butov, A. Zrenner, G. Abstreiter, G. Böhm, and G. Weimann, Phys. Rev. Lett. **73**, 304 (1994).
[15] D. Snoke, S. Denev, Y. Liu, L. Pfeiffer, and K. West, Nature (London) **418**, 754 (2002).
[16] S. W. Koch, M. Kira, G. Khitrova, and H. M. Gibbs, Nat. Mater. **5**, 523 (2006).
[17] H. Haug and S. W. Koch, *Quantum Theory of the Optical and Electronic Properties of Semiconductors*, 5th ed. (World Scientific Publishing, Singapore, 2009).
[18] M. Kira and S. W. Koch, *Semiconductor Quantum Optics* (Cambridge University Press, Cambridge, 2012).
[19] M. Kira and S. W. Koch, Prog. Quantum Electron. **30**, 155 (2006).
[20] W. W. Chow and S. W. Koch, *Semiconductor-Laser Fundamentals: Physics of the Gain Materials* (Springer, Berlin, Heidelberg, New York, 1999).
[21] G. L. Bir and G. E. Pikus, *Symmetry and Strain-induced Effects in Semiconductors* (Wiley, New York, 1974).
[22] C. G. Van de Walle, Phys. Rev. B **39**, 1871 (1989).
[23] I. Vurgaftman, J. R. Meyer, and L. R. Ram-Mohan, J. Appl. Phys. **89**, 5815 (2001).
[24] A. Honold, L. Schultheis, J. Kuhl, and C. W. Tu, Phys. Rev. B **40**, 6442 (1989).
[25] M. Koch, G. von Plessen, J. Feldman, and E. O. Göbel, Chem. Phys. **210**, 367 (1996).
[26] S. T. Cundiff, Opt. Express **16**, 4639 (2008).
[27] K. P. H. Lui and F. A. Hegmann, Appl. Phys. Lett. **78**, 3478 (2001).
[28] P. U. Jepsen, D. G. Cooke, and M. Koch, Laser Photonics Rev. **5**, 124 (2011).
[29] R. Ulbricht, E. Hendry, J. Shan, T. F. Heinz, and M. Bonn, Rev. Mod. Phys. **83**, 543 (2011).
[30] A. Dreyhaupt, S. Winnerl, T. Dekorsy, and M. Helm, Appl. Phys. Lett. **86**, 121114 (2005).
[31] M. Kira, W. Hoyer, and S. W. Koch, Phys. Status Solidi B **238**, 443 (2003).
[32] M. Lindberg and S. W. Koch, Phys. Rev. B **38**, 3342 (1988).
[33] O. Vänskä, I. Tittonen, S. W. Koch, and M. Kira, Phys. Rev. Lett. **114**, 116802 (2015).
[34] R. P. Smith, J. K. Wahlstrand, A. C. Funk, R. P. Mirin, S. T. Cundiff, J. T. Steiner, M. Schafer, M. Kira, and S. W. Koch, Phys. Rev. Lett. **104**, 247401 (2010).
[35] M. Kira, F. Jahnke, W. Hoyer, and S. W. Koch, Prog. Quantum Electron. **23**, 189 (1999).
[36] M. Mootz, M. Kira, and S. W. Koch, New J. Phys. **15**, 093040 (2013).
[37] J. Shah, A. Pinczuk, A. C. Gossard, and W. Wiegmann, Phys. Rev. Lett. **54**, 2045 (1985).
[38] J. F. Ryan, R. A. Taylor, A. J. Turberfield, A. Maciel, J. M. Worlock, A. C. Gossard, and W. Wiegmann, Phys. Rev. Lett. **53**, 1841 (1984).
[39] Y. Rosenwaks, M. C. Hanna, D. H. Levi, D. M. Szmyd, R. K. Ahrenkiel, and A. J. Nozik, Phys. Rev. B **48**, 14675 (1993).
[40] R. H. M. Groeneveld and D. Grischkowskyt, J. Opt. Soc. Am. B **11**, 2502 (1994).
[41] R. A. Kaindl, M. A. Carnahan, D. Hägele, R. Lövenich, and D. S. Chemla, Nature (London) **423**, 734 (2003).
[42] M. Kira, W. Hoyer, and S. W. Koch, Solid State Commun. **129**, 733 (2004).

[43] T. Suzuki and R. Shimano, Phys. Rev. Lett. **103**, 057401 (2009).
[44] R. A. Kaindl, D. Hägele, M. A. Carnahan, and D. S. Chemla, Phys. Rev. B **79**, 045320 (2009).
[45] O. Kojima, K. Mizoguchi, and M. Nakayama, J. Appl. Phys. **112**, 043522 (2012).
[46] R. Huber, R. A. Kaindl, B. A. Schmid, and D. S. Chemla, Phys. Rev. B **72**, 161314 (2005).
[47] T. Grunwald, T. Jung, D. Köhler, S. W. Koch, G. Khitrova, H. M. Gibbs, R. Hey, and S. Chatterjee, Phys. Status Solidi C **6**, 500 (2009).
[48] C. Poellmann, P. Steinleitner, U. Leierseder, P. Nagler, G. Plechinger, M. Porer, R. Bratschitsch, C. Schüller, T. Korn, and R. Huber, Nat. Mater. **14**, 889 (2015).
[49] M. Stein, C. Lammers, P. Springer, P. H. Richter, S. W. Koch, M. Koch, and M. Kira, Phys. Rev. B **95**, 155207 (2017).
[50] M. Kira and S. W. Koch, Phys. Rev. Lett. **93**, 076402 (2004).
[51] R. Hellmann, M. Koch, J. Feldmann, S. T. Cundiff, E. O. Göbel, D. R. Yakovlev, A. Waag, and G. Landwehr, Phys. Rev. B **48**, 2847 (1993).
[52] L. Schultheis, J. Kuhl, A. Honold, and C. W. Tu, Phys. Rev. Lett. **57**, 1635 (1986).
[53] L. Kappei, J. Szczytko, F. Morier-Genoud, and B. Deveaud, Phys. Rev. Lett. **94**, 147403 (2005).
[54] G. Kiršanskė, P. Tighineanu, R. S. Daveau, J. Miguel-Sánchez, P. Lodahl, and S. Stobbe, Phys. Rev. B **94**, 155438 (2016).

III. Enhanced Absorption by Linewidth Narrowing in Optically Excited Type-II Semiconductor Heterostructures

M. Stein, C. Lammers, M. J. Drexler, C. Fuchs, W. Stolz, and M. Koch, Phys. Rev. Lett. 121, 017407 (2018)

Abstract

We experimentally report a surprising linewidth narrowing of the direct exitonic 1s heavy-hole transition in a type-II quantum well system. This narrowing, which builds up on a pico- to nanosecond timescale, causes a transient enhanced absorption at the spectral peak position of the excitonic resonance. We discuss how this effect depends on experimental parameters such as excitation density, temperature, and barrier width. We cannot attribute this effect to known physical mechanisms.

DOI: 10.1103/PhysRevLett.121.017401

URL: `https://link.aps.org/doi/10.1103/PhysRevLett.121.017401`

Enhanced Absorption by Linewidth Narrowing in Optically Excited Type-II Semiconductor Heterostructures

M. Stein,* C. Lammers, M. J. Drexler, C. Fuchs, W. Stolz, and M. Koch
Department of Physics and Material Sciences Center, Philipps-Universität Marburg, Renthof 5, 35032 Marburg, Germany

(Received 14 March 2018; published 2 July 2018)

We experimentally report a surprising linewidth narrowing of the direct exitonic 1 *s* heavy-hole transition in a type-II quantum well system. This narrowing, which builds up on a pico- to nanosecond timescale, causes a transient enhanced absorption at the spectral peak position of the excitonic resonance. We discuss how this effect depends on experimental parameters such as excitation density, temperature, and barrier width. We cannot attribute this effect to known physical mechanisms.

DOI: 10.1103/PhysRevLett.121.017401

Quantum well (QW) based semiconductor heterostructures are ideal model systems to study the properties of low-dimensional carrier systems. Recently, so called type-II structures, which were studied intensively in the late 1980s and early 1990s [1–9], gained attention again as prototypical structures for charge-transfer states [10–15]. They can serve as well-defined high quality model systems to study, e.g., the impact of the interface morphology on charge-transfer processes, which are of importance for nearly all electronic and optoelectronic devices [16]. Type-II semiconductor heterostructures contain two adjacent but different QWs, often with a barrier between them. The energy levels in the conduction and valence band are designed such that for a particular photon energy only one QW is excited and that subsequently either electrons or holes find energetically more favorable states in the other QW and undergo a spatial charge transfer. One powerful experimental method to gain insights into their physics is ultrafast optical pump-probe spectroscopy [1,6,17]. After optical excitation excitonic lines can exhibit reduced absorption, shifts, and broadening [2–4,17]. These signatures are associated with optical nonlinearities arising from the many-particle nature of the system [18–20]. These are phase-space filling, band gap renormalization, screening and excitation induced dephasing.

In this Letter we report an induced absorption of the excitonic resonance due to a linewidth narrowing. The effect, which arises several ten to hundred picoseconds after optical excitation, is observed at the direct type-I 1 *s* heavy-hole (hh) resonance in a type-II QW structure.

We study a set of three different type-I and type-II QW structures, consisting of 5 periods of $Ga_{1-x}In_xAs/GaAs/GaN_yAs_{1-y}$ layers with a cap layer of 45 nm GaAs and a buffer layer of 250 nm GaAs grown on GaAs substrate. The thickness of the intermediate GaAs barrier is $d_{GaAs} = 1.5$ nm (samples *A* and *B*) and $d_{GaAs} = 6.0$ nm (sample *C*) as confirmed by TEM and XRD measurements. Further structural parameters such as the nitrogen concentration (N_N) are listed in Table I. Linear absorption is measured using a tungsten light source focused to a 60 μm large spot and an optical spectrum analyzer. The carrier dynamics are studied using optical pump-white light probe spectroscopy. The setup is operated by a titan-sapphire laser based regenerative amplifier system, which delivers laser pulses with an energy of 5 mJ and a temporal duration of 35 fs with a repetition rate of 1 kHz. Central photon energies can be tuned via an optical parametric amplifier. A small fraction of the amplifier output experiences a variable delay before being focused onto a sapphire crystal in order to generate white-light supercontinuum probe pulses. The spectra of the transmitted white light are recorded by a spectrometer which contains a liquid nitrogen cooled (GaIn)As line detector and has a spectral resolution of 1 nm. The experiments shown are performed at 10 K in a liquid helium cryostat.

The linear absorption spectra of sample *B* and sample *C*, both with a type-II band alignment, are shown in Fig. 1 as solid lines. A schematic band diagram of these samples and the corresponding wave functions are given in the inset of Fig. 1. The minimum energy level of the conduction band is found in the Ga(NAs) QWs while the valence band maximum is in the (GaIn)As layers. Because of the small valence band offset of the Ga(NAs) QWs [21], confined hole states are expected only in the (GaIn)As QWs. Since the indium content and the well width are nearly the same for both samples, both spectra show an absorption peak

TABLE I. Structural parameters from TEM and HR-XRD studies for the set of type-I and type-II QW systems.

Sample	d_{GaAs} (nm)	N_{In} (%)	N_N (%)	$d_{(GaIn)As}$ (nm)	$d_{Ga(NAs)}$ (nm)	Band alignment
A	1.5	24.0	0.6	10.0	7.4	Type-I
B	1.5	23.5	4.8	10.3	4.5	Type-II
C	6.0	23.6	5.0	10.5	4.6	Type-II

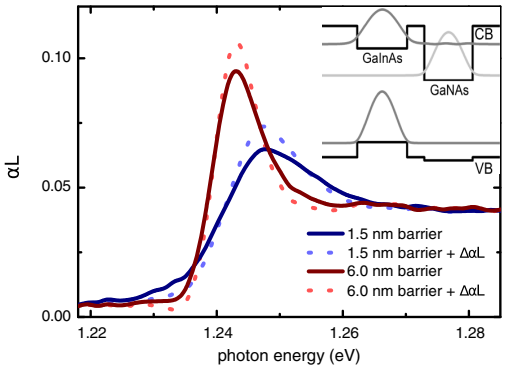

FIG. 1. Solid lines: Linear absorption spectra of the QW samples with a type-II band alignment and 1.5 nm (blue, sample *B*) and 6.0 nm (red, sample *C*) thick barriers, respectively. Dashed lines: Sum of the linear absorption and its respective differential absorption for a pump-probe delay of 5 ns. The inset is a schematic of the band diagram together with the corresponding wave functions.

around 1.245 eV. This absorption peak, which results from the 1 *s* hh exciton in the (GaIn)As QWs, is noticeably slimmer and more pronounced for sample *C* with a 6.0 nm thick barrier. In this case the transition is mainly inhomogeneously broadened and best described by a Gaussian function with a full width at half maximum (FWHM) of 8.3 meV. (See Supplemental Material [22] for details of the fit functions.) In the case of sample *B* the same absorption peak experiences an additional homogeneous broadening which results from the fast electron transfer from the (GaIn)As QWs to the Ga(NAs) QWs. Therefore, the line shape of the 1 *s* exciton transition of sample *B* is best reproduced by a convolution of a Gaussian and a Lorentzian, thus a Voigt profile. Here, the Lorentzian part of the best fit has a broadening of 6.0 meV which corresponds to a dephasing time of 220 fs. The broadening of the Gaussian part is 12.4 meV which results in a FWHM of ~15.9 meV. To analyze the charge carrier dynamics, we perform optical pump-optical probe (OPOP) measurements under cross-linear-polarized excitation. The excitation spectrum is centered at 1.34 eV. This energy excites charge carriers in the (GaIn)As QWs but above its excitonic 1 *s* hh resonance. In Fig. 2 a contour plot of the OPOP measurements is shown for sample *B* with a type-II band alignment (right panel). For comparison, we also plot the OPOP data obtained from the type-I structure (sample *A*) in the left panel. For both samples we observe a negative differential absorption ($\Delta\alpha L$) directly after optical excitation which arises from phase-space filling. For the type-II heterostructure a fast initial recovery is observed within the first picosecond after excitation which is caused by the transfer of electrons through the barrier into the Ga(NAs) QWs [1,28]. An exponential fit to the transient (see inset of Fig. 3) yields a transfer time of 300 fs, which is in good agreement with the dephasing time of 220 fs we received from the linewidth analysis. Once this initial electron transfer is completed in sample *B*, we observe a second minimum in the $\Delta\alpha L$ signal around 40 ps as the initially hot carrier distribution cools down [28–30]. Cooling of the excited charge carriers also leads to a minimum in the reference sample at ~75 ps. The faster cooling dynamics in the type-II sample are attributed to the fact that only holes remain in the (GaIn)As QWs [31–33]. Afterwards, the negative $\Delta\alpha L$ signature recovers for both samples on a timescale of hundreds of picoseconds due to recombination

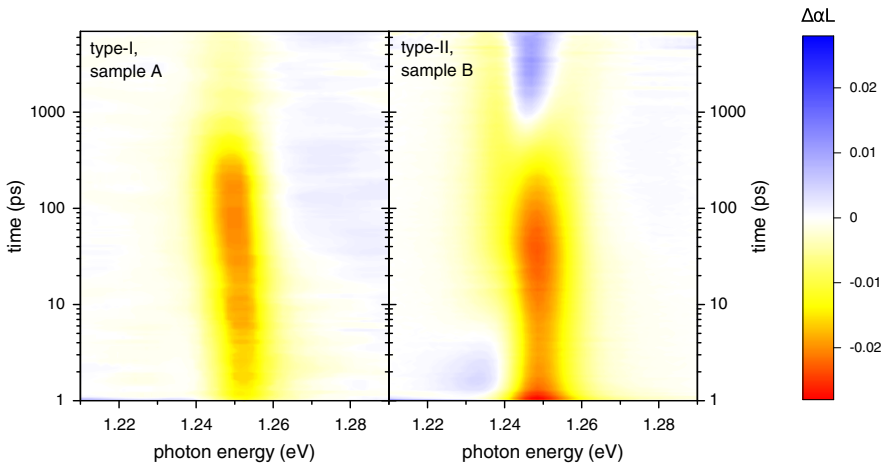

FIG. 2. Left panel: Contour plot of the optical pump-optical probe spectra for the reference sample *A* with a type-I band alignment. Right panel: Contour plot for sample *B* with a type-II band alignment and a 1.5 nm thick GaAs barrier. The plot illustrates the changes of the absorption ($\Delta\alpha L$) after an optical excitation for time delays ranging from femtoseconds to several nanoseconds. In order to plot a logarithmic time scale the optical excitation is set to 1 ps.

processes of the excited charge carriers and/or the population of trap states.

The remarkable feature reported here is a local peak in the differential absorption of sample B. It occurs after 1 ns and is energetically positioned at the 1 s hh transition. This peak reaches its maximum ~3 ns after excitation and sustains at this level for the next 4 ns. The positive $\Delta\alpha L$ signature is surrounded by a negative differential absorption which is a typical signature of a linewidth narrowing. Such an induced absorption is absent in the type-I sample. The formation of this positive $\Delta\alpha L$ signature out of a pure bleaching signature is further highlighted in Fig. 3 where we plot the $\Delta\alpha L$ spectra for a series of discrete time delays. For a time delay of 200 ps we observe a broad negative signal arising from phase-space filling. With progressing time a local maximum arises within this bleaching signal at 1.244 eV which is already very noticeable at 500 ps. As this local maximum evolves into a prominent peak in the $\Delta\alpha L$ spectrum on a nanosecond timescale it shifts to 1.247 eV, which is close to the central position of the bleaching signature at 1.248 eV. For a time delay above 1 ns the absorption is enhanced at this peak while it is decreased above and below this local maximum. A spectral integration over the whole region from 1.215 to 1.28 eV gives an integrated $\Delta\alpha L$ signal close to zero (see the inset of Fig. 3). Since the integrated signature is zero for late times, the oscillator strength of the excitonic 1 s hh transition is not increased. Hence, we conclude that the locally enhanced absorption is caused by a linewidth narrowing. However, such a signature of a linewidth narrowing is not observed for type-I heterostructures, neither in our type-I reference nor in the literature. Here, the negative $\Delta\alpha L$ signature just disappears on a nanosecond timescale which is a typical recombination time for type-I QW samples.

We now discuss how the observed linewidth narrowing depends on experimental parameters. First, we investigate how the buildup of the linewidth narrowing depends on the carrier density. Figure 4 shows the evolution of the $\Delta\alpha L$ signal for three different excitation densities. Here we observe that the positive $\Delta\alpha L$ arises later for an increased carrier density. Nevertheless, the amplitude of the signature increases with excitation density. It reaches a value of 0.01 at late times for a photon density of 6.6×10^{14} photons/cm^2. This corresponds to more than 10% of the excitonic absorption at its peak value.

To investigate the influence of the sample temperature on the observed feature we have performed additional experiments for 40, 120, and 200 K (the results of this experiments are shown in the Supplemental Material [22]). We observe a positive $\Delta\alpha L$ signal for all temperatures. Thus, we can exclude that the formation of quasiparticles like charge-transfer excitons is responsible for the observed signature. Moreover, we find that the signature of an enhanced absorption builds up faster with increasing temperature.

The experiments shown so far are carried out with a photon energy of 1.34 eV which, at 10 K, corresponds to an excess energy of 90 meV. To investigate the impact of the optical excitation energy we also performed experiments with a photon energy of 1.25 eV, which is resonant to the 1 s hh transition. For comparable charge carrier densities we find that the positive $\Delta\alpha L$ signal evolves at the same time (see Supplemental Material [22]). We therefore conclude that the excitation energy is not a decisive parameter for the observations presented here.

Finally, we focus on structural sample parameters. The most important parameter is the intermediate GaAs barrier

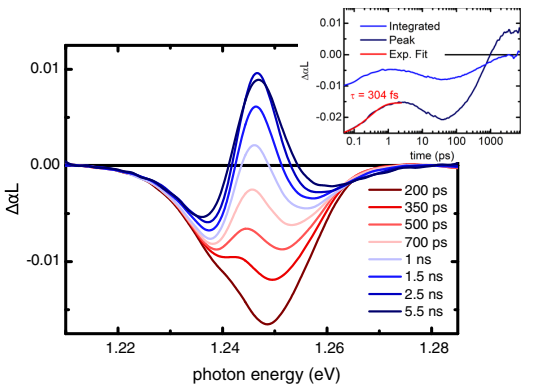

FIG. 3. Differential absorption spectra of sample B for different time delays. The inset shows transients at 1.248 eV (peak) as well as integrated over the whole bleaching signature from 1.215 to 1.28 eV (integrated).

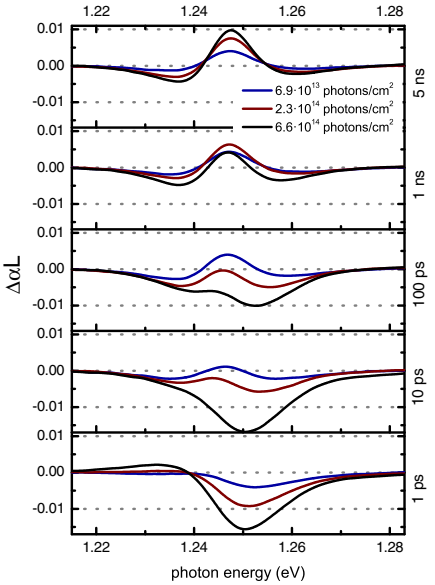

FIG. 4. Differential absorption spectra of sample B for three different excitation densities.

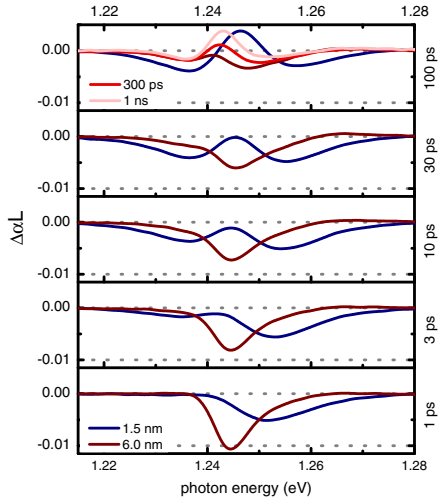

FIG. 5. Comparison of the differential absorption spectra of both samples with a type-II band alignment, i.e., sample B with a barrier width of 1.5 nm and sample C with a barrier width of 6.0 nm.

width as it largely determines the transfer and recombination dynamics in the sample [5]. For a thicker barrier the transfer time as well as the recombination lifetime are enhanced. Figure 5 shows a comparison between sample B and sample C with barrier widths of 1.5 and 6.0 nm, respectively. The experiments have been performed with comparable excitation densities of 1.1×10^{14} photons/cm^2 for sample B and 6.3×10^{13} photons/cm^2 for sample C. A locally enhanced absorption is observed for both samples. Yet, the occurrence of this signature is delayed for sample C in comparison to sample B. This is not surprising as charge transfer and recombination are slower for the thick barrier sample. However, it is surprising that a positive $\Delta\alpha L$ signature occurs several hundred picoseconds later in sample C even though the charge transfer itself happens within tens of picoseconds as OPOP transients reveal.

The above data clearly demonstrate a reduction of the excitonic linewidth after optical excitation in type-II heterostructures. At present we have no microscopic explanation for this surprising effect. The spectral width of excitonic lines results from homogeneous and inhomogeneous broadening. The latter arises from structural inhomogeneities such as compositional disorder or well width fluctuations. The homogeneous linewidth is associated with the coherent lifetime of an optically excited state via $\Gamma_{\mathrm{hom}} = (2\hbar/T_2)$, where Γ_{hom} is the homogeneous linewidth and T_2 is the so-called dephasing time. In a type-I structure the dephasing time is determined by carrier-phonon and carrier-carrier scattering. For low excitation densities and at low temperatures one typically finds dephasing times of a few picoseconds for excitonic hh transitions [34–36]. In a type-II structure the spatial transfer of charge carriers also destroys the coherence. For our sample with a 1.5 nm barrier we determine a transfer time of 300 fs corresponding to an homogeneous linewidth of 4.3 meV by OPOP spectroscopy and an homogeneous linewidth of 6.0 meV corresponding to a dephasing time of 220 fs by a line shape analysis of the linear absorption spectrum. Therefore, we conclude that the fast transfer of charge carriers is mainly responsible for the destruction of the coherence in this sample. If for some unknown reason the dephasing time of the weakly excited sample would increase to roughly 1 ps this could explain the observed linewidth narrowing of ~2.9 meV. This implies that the transfer time would have to increase from 300 fs to above 1 ps. Yet, we observe a linewidth narrowing for sample C as well. Here, the linewidth is reduced by 0.9 meV. However, the main absorption peak of sample C can only be described by an inhomogeneous broadening and already features a transfer time in the ps range so that a further increase will not affect its linewidth. Since it is very unlikely that the surprising effect of a linewidth narrowing is caused by two different mechanisms in both samples, we exclude that it arises from an altered transfer time in the excited sample.

It is well known that electric fields in the growth direction lead to a broadening of the excitonic linewidth [37,38]. Hence, it is conceivable that the unexcited QW structure is slightly tilted, e.g., as a consequence of unwanted background doping. If this initial field is compensated by the charge carrier concentration in the two neighboring QWs the excitonic resonances could be narrowed since the structure would be untilted. Yet, the field induced linewidth broadening is always associated with a spectral shift [37]. As we do not observe any spectral shifts for the densities investigated (see Fig. 4), we exclude that field-induced effects are responsible for the linewidth narrowing. In addition, field-induced effects would directly couple to the transfer of charge carriers through the barrier. However, such a direct coupling of the linewidth narrowing to the charge transfer is not observed. While the charge transfer takes place on a picosecond to subpicosecond timescale, it takes several hundred picoseconds until the linewidth narrowing occurs.

Hence, we cannot attribute our experimental observations to any known physical mechanisms. We hope that the experimental observations reported here will stimulate theoretical investigations in the future.

In conclusion, we observe the astonishing buildup of an enhanced absorption due to a linewidth narrowing at low carrier densities in type-II QW heterostructures. In particular this means that the excitonic resonance in the linear absorption is spectrally sharper in the excited sample than in the unexcited sample. Such a signature does not occur in a type-I reference sample. It takes several tens to hundreds of picoseconds for the enhanced absorption to develop and it can reach up to 10% of the linear absorption of the

samples investigated. The reported signature arises faster for lower carrier densities, higher sample temperatures, and for samples with a lower intermediate barrier thickness. Since type-II semiconductor heterostructures are prototypical structures for a vast number of systems with charge-transfer states, we believe that our findings will stimulate similar investigations on other charge-transfer systems, such as donor-acceptor systems or heterojunction solar cells, where the spatial charge transfer through an interface is essential for their operation.

This work is a project of the Collaborative Research Center SFB 1083 funded by the Deutsche Forschungsgemeinschaft.

*markus.stein@physik.uni-marburg.de

[1] J. Feldmann, R. Sattmann, E. O. Göbel, J. Kuhl, J. Hebling, K. Ploog, R. Muralidharan, P. Dawson, and C. T. Foxon, Phys. Rev. Lett. **62**, 1892 (1989).
[2] G. R. Olbright, W. S. Fu, A. Owyoung, J. F. Klem, R. Binder, I. Galbraith, and S. W. Koch, Phys. Rev. Lett. **66**, 1358 (1991).
[3] G. R. Olbright, W. S. Fu, J. F. Klem, H. M. Gibbs, G. Khitrova, R. Pon, B. Fluegel, K. Meissner, N. Peyghambarian, R. Binder, I. Galbraith, and S. W. Koch, Phys. Rev. B **44**, 3043 (1991).
[4] K. Meissner, B. Fluegel, R. Binder, S. W. Koch, G. Khitrova, and N. Peygambarian, Appl. Phys. Lett. **59**, 259 (1991).
[5] I. Galbraith, P. Dawson, and C. T. Foxon, Phys. Rev. B **45**, 13499 (1992).
[6] J. Feldmann, J. Nunnenkamp, G. Peter, E. Göbel, J. Kuhl, K. Ploog, P. Dawson, and C. T. Foxon, Phys. Rev. B **42**, 5809 (1990).
[7] I. H. Libon, S. Baumgärtner, M. Hempel, N. E. Hecker, J. Feldmann, M. Koch, and P. Dawson, Appl. Phys. Lett. **76**, 2821 (2000).
[8] R. Binder, I. Galbraith, and S. W. Koch, Phys. Rev. B **44**, 3031 (1991).
[9] L. V. Butov, A. Zrenner, G. Abstreiter, G. Böhm, and G. Weimann, Phys. Rev. Lett. **73**, 304 (1994).
[10] D. Snoke, S. Denev, Y. Liu, L. Pfeiffer, and K. West, Nature (London) **418**, 754 (2002).
[11] O. Vänskä, I. Tittonen, S. W. Koch, and M. Kira, Phys. Rev. Lett. **114**, 116802 (2015).
[12] C. Berger, C. Möller, P. Hens, C. Fuchs, W. Stolz, S. W. Koch, A. R. Perez, J. Hader, and J. V. Moloney, AIP Adv. **5**, 047105 (2015).
[13] C. Möller, C. Fuchs, C. Berger, A. R. Perez, M. Koch, J. Hader, J. V. Moloney, S. W. Koch, and W. Stolz, Appl. Phys. Lett. **108**, 071102 (2016).
[14] C. Lammers, M. Stein, C. Berger, C. Möller, C. Fuchs, A. R. Perez, A. Rahimi-Iman, J. Hader, J. V. Moloney, W. Stolz, S. W. Koch, and M. Koch, Appl. Phys. Lett. **109**, 232107 (2016).
[15] M. Stein, C. Lammers, P.-H. Richter, C. Fuchs, W. Stolz, M. Koch, O. Vänskä, M. J. Weseloh, M. Kira, and S. W. Koch, Phys. Rev. B **97**, 125306 (2018).
[16] H. Kroemer, Rev. Mod. Phys. **73**, 783 (2001).
[17] A. Alexandrou, M. K. Jackson, D. Hulin, N. Magnea, H. Mariette, and Y. M. d'Aubigné, Phys. Rev. B **50**, 2727 (1994).
[18] M. Kira and S. Koch, Prog. Quantum Electron. **30**, 155 (2006).
[19] H. Haug and S. W. Koch, Excitonic optical stark effect, *Quantum Theory of the Optical and Electronic Properties of Semiconductors*, 5th ed. (World Scientific, Singapore, 2009), pp. 235–267.
[20] J. Shah, *Ultrafast Spectroscopy of Semiconductors and Semiconductor Nanostructures*, Springer Series in Solid-State Sciences (Springer, New York, 1999).
[21] I. Vurgaftman and J. R. Meyer, J. Appl. Phys. **94**, 3675 (2003).
[22] See Supplemental Material at http://link.aps.org/supplemental/10.1103/PhysRevLett.121.017401, which includes Refs. [8,23–27], for details of the fit functions used for the linewidth analysis and additional experimental data.
[23] R. Steel and J. Torrie, *Principles and Procedures of Statistics: With Special Reference to the Biological Sciences* (McGraw-Hill, New York, 1960).
[24] J. Olivero and R. Longbothum, J. Quant. Spectrosc. Radiat. Transfer **17**, 233 (1977).
[25] S. D. Baranovskii, R. Eichmann, and P. Thomas, Phys. Rev. B **58**, 13081 (1998).
[26] O. Rubel, M. Galluppi, S. Baranovskii, K. Volz, L. Geelhaar, H. Riechert, P. Thomas, and W. Stolz, J. Appl. Phys. **98**, 063518 (2005).
[27] O. Rubel, S. D. Baranovskii, K. Hantke, B. Kunert, W. W. Rühle, P. Thomas, K. Volz, and W. Stolz, Phys. Rev. B **73**, 233201 (2006).
[28] K. Meissner, B. Fluegel, R. Binder, S. W. Koch, G. Khitrova, and N. Peygambarian, Appl. Phys. Lett. **59**, 259 (1991).
[29] C. V. Shank, R. L. Fork, R. F. Leheny, and J. Shah, Phys. Rev. Lett. **42**, 112 (1979).
[30] H. Roskos, B. Rieck, A. Seilmeier, and W. Kaiser, Appl. Phys. Lett. **53**, 2406 (1988).
[31] J. Shah, A. Pinczuk, A. C. Gossard, and W. Wiegmann, Phys. Rev. Lett. **54**, 2045 (1985).
[32] H. J. Polland, W. W. Rühle, J. Kuhl, K. Ploog, K. Fujiwara, and T. Nakayama, Phys. Rev. B **35**, 8273 (1987).
[33] R. A. Höpfel, J. Shah, and A. C. Gossard, Phys. Rev. Lett. **56**, 765 (1986).
[34] R. Hellmann, M. Koch, J. Feldmann, S. T. Cundiff, E. O. Göbel, D. R. Yakovlev, A. Waag, and G. Landwehr, Phys. Rev. B **48**, 2847 (1993).
[35] L. Schultheis, A. Honold, J. Kuhl, K. Köhler, and C. W. Tu, Phys. Rev. B **34**, 9027 (1986).
[36] M. Koch, G. von Plessen, J. Feldmann, and E. O. Göbel, Chem. Phys. **210**, 367 (1996), confined Excitations in Molecular and Semiconductor Nanostructures.
[37] D. A. B. Miller, D. S. Chemla, T. C. Damen, A. C. Gossard, W. Wiegmann, T. H. Wood, and C. A. Burrus, Phys. Rev. B **32**, 1043 (1985).
[38] C. F. Klingshirn, *Semiconductor Optics* (Springer Science & Business Media, New York, 2012).

III.1. Supplemental material

M. Stein, C. Lammers, M. J. Drexler, C. Fuchs, W. Stolz, and M. Koch, Phys. Rev. Lett. 121, 017407 (2018)

Abstract

This supplemental material presents background information on the fit functions used for the linewidth analysis as well as additional results that may be important for future researches in the field. Those results include the temperature dependence and the excitation energy dependence of the linewidth narrowing as well as the influence on the light-hole transition.

DOI: 10.1103/PhysRevLett.121.017401

URL: `https://link.aps.org/doi/10.1103/PhysRevLett.121.017401`

Supplemental Material: Enhanced absorption by linewidth narrowing in optically excited type-II semiconductor heterostructures

M. Stein,* C. Lammers, M. J. Drexler, C. Fuchs, W. Stolz, and M. Koch
Department of Physics and Material Sciences Center,
Philipps-Universität Marburg, Renthof 5, 35032 Marburg, Germany
(Dated: June 7, 2018)

This supplemental material presents background information on the fit functions used for the linewidth analysis as well as additional results that may be important for future researches in the field. Those results include the temperature dependence and the excitation energy dependence of the linewidth narrowing as well as the influence on the light-hole transition.

LINEWIDTH ANALYSIS

Figure 1 shows the linear absorption spectra of both samples with a type-II band alignment around their heavy-hole (hh) exciton transition of the GaInAs QWs. Although the GaInAs QWs of both samples are grown with identical parameters the absorption differs significantly. The differences are caused by the GaAs barriers of different thicknesses. The sample with the 6.0 nm thick barrier has a resonance of the hh exciton of the GaInAs QWs at 1.243 eV. The exciton resonance is inhomogeneously broadened and thus best described by a Gaussian function

$$f_G(E) = f_0 + \frac{A}{\sqrt{2\pi\sigma^2}} \cdot exp\left[-0.5 \cdot \left(\frac{E - E_c}{\sigma} \right)^2 \right],$$

with the offset $f_0 = 0.0048$, the area $A = 0.84\,meV$, the center energy $E_c = 1.2432\,eV$ and the standard deviation $\sigma = 3.04\,meV$. The full width at half maximum (FWHM) of this function is 8.33 meV and the coefficient of determination R^2 between the measurement and the Gaussian fit function is 0.9985 [1].
The exciton resonance of the sample with a type-II band alignment and an 1.5 nm barrier is homogeneously as well as inhomogeneously broadened. Therefore the resonance is described best neither by a pure Gaussian nor by a pure Lorentzian function. Instead, the convolution of a Gaussian and a Lorentzian, i.e. a Voigt profile, describes the resonance well. The best fit is provided by the function

$$f_V(E) = f_0 + \frac{2A \cdot ln(2) \cdot \omega_L}{\pi^{1.5} \cdot \omega_G^2} \cdot \int_{-\infty}^{\infty} \frac{e^{-t^2}}{\left(\sqrt{ln(2)} \cdot \frac{\omega_L}{\omega_G}\right)^2 + \left(\sqrt{4ln(2)} \cdot \frac{E - E_c}{\omega_G} - t\right)^2} dt,$$

with the offset $f_0 = 0.0041$, the area $A = 1.22\,meV$, the center energy $E_c = 1.2479\,eV$, the Gaussian FWHM $\omega_G = 12.41\,meV$ and the Lorentzian FWHM $\omega_L = 6.03\,meV$. The FWHM of this function is approximately given by Ref. [2] as

$$FWHM \approx 0.5346\omega_L + \sqrt{0.2166\omega_L^2 + \omega_G^2} = 15.95\,meV.$$

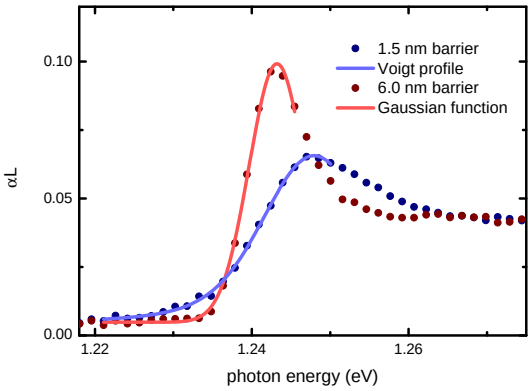

Figure 1: Linear absorption spectra of the samples with a type-II band alignment (dots) and the respective fit functions (solid lines). The absorption spectra are measured at a temperature of 10 K.

The homogeneous broadening of 6.03 meV corresponds to a dephasing time T_2 of 218.3 fs. The relation is $T_2 = \frac{2\hbar}{\omega_L}$.

TEMPERATURE DEPENDENCE

To exclude a correlation between the observed signature and the formation of bound electron-hole pairs, the experiment is performed at different temperatures. As shown in Fig. 2, the signature of an enhanced absorption is observed at all temperatures investigated. At temperatures of 200 K the thermal energy is too high for the formation excitons or charge transfer excitons. Therefore we can exclude that the formation of bound electron-hole pairs is related to the observed signature. However, at an increased temperature, a positive $\Delta\alpha$L signature arises faster, even though the excited charge carrier density is also increased. The increased charge carrier density is indicated by the larger $\Delta\alpha$L bleaching signature in the first picoseconds after excitation. As already shown in the manuscript, the formation time of a positive $\Delta\alpha$L signature increases when the charge carrier density is increased. Therefore it is surprising that a positive $\Delta\alpha$L signature occurs faster for elevated temperatures. Thus, a faster formation with increasing temperature may be seen as an indication that the population of localized states or even deeper trap states could play a role in the formation of an enhanced absorption. At elevated temperatures the mobility of the charge carriers is increased so that localized states are populated faster [3–5]. However, it is completely unclear by which physical mechanism the population of localized or trap states could reduce the linewidth of an excitonic resonance.

EXCITATION ENERGY DEPENDENCE

To study the influence of the photon energy of the optical pump pulse on the formation dynamics of the linewidth narrowing we use two different excitation conditions. In one case the optical pump spectrum has a central energy of 1.25 eV which is resonant to the excitonic resonance in the GaInAs QW. In the other case the central energy of the optical pump pulse is 1.34 eV which creates charge carriers within the GaInAs QW but with an excess energy

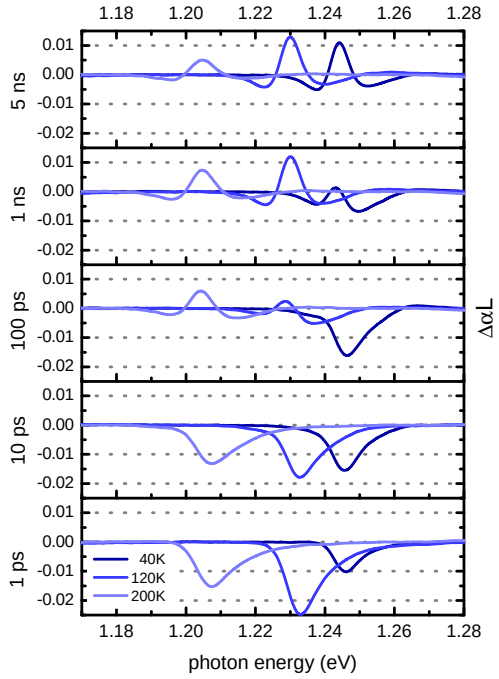

Figure 2: Dynamics of the differential absorption of sample C with a 6.0 nm barrier for three different crystal lattice temperatures.

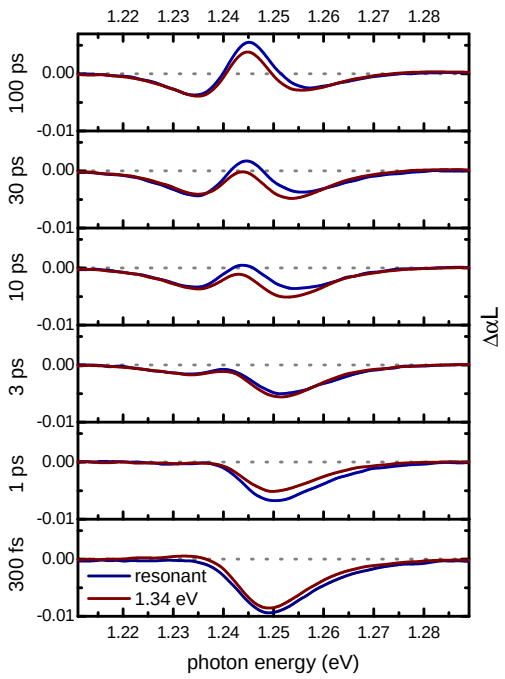

Figure 3: Comparison of the differential absorption in sample B with a 1.5 nm barrier for two different photon energies.

of $\sim$ 90 meV. The results are shown in Fig. 3. For both excitation conditions it takes roughly 30 ps until a positive $\Delta\alpha$L signature evolves. The build up of the linewidth narrowing and the resulting spectra are very similar for both excitation conditions.

EFFECTS ON THE LIGHT-HOLE RESONANCE

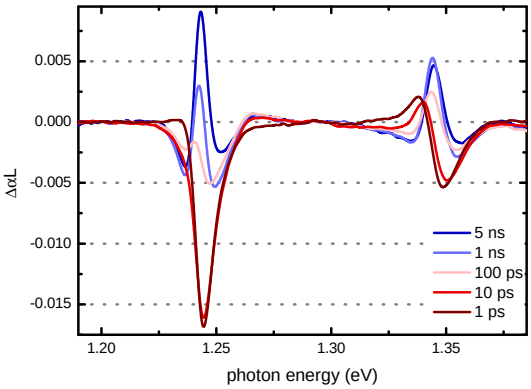

Figure 4: Differential absorption spectra of the heavy- and the light-hole transition for various time delays.

Finally, we check if the signature of a linewidth narrowing only evolves for the hh transition at $\sim$ 1.25 eV or if the same signature of a linewidth narrowing affects also the light-hole (lh) transition at $\sim$ 1.35 eV. In Fig. 4 the $\Delta\alpha$L spectra of sample C with the 6.0 nm barrier are shown for different time delays between the optical pump and the optical probe pulse. Here, the spectra are shown over an energetically broader range that also includes the lh transition at $\sim$ 1.35 eV. For time delays of several nanoseconds, we observe in principle the same $\Delta\alpha$L signature of a linewidth narrowing for hh and lh transition. However, this signature evolves even faster for the lh transition. Furthermore, a pure bleaching signature that is visible for the hh transition in the first picoseconds after excitation is not observed for the lh transition. Here, a superposition of a redshift and a bleaching of the excitonic resonance is apparent in the first picoseconds after excitation. Since the phase-space filling is greatly reduced in the lh compared to the hh, the screening by the hh plasma is not balanced. This unbalance between screening and phase-space filling causes a redshift [6].

* Electronic address: markus.stein@physik.uni-marburg.de

[1] R. Steel and J. Torrie, *Principles and procedures of statistics: with special reference to the biological sciences* (McGraw-Hill, 1960), URL https://books.google.de/books?id=o6FpAAAAMAAJ.

[2] J. Olivero and R. Longbothum, Journal of Quantitative Spectroscopy and Radiative Transfer **17**, 233 (1977), ISSN 0022-4073, URL http://www.sciencedirect.com/science/article/pii/0022407377901613.

[3] S. Baranovskii, R. Eichmann, and P. Thomas, Physical Review B **58**, 13081 (1998).

[4] O. Rubel, M. Galluppi, S. Baranovskii, K. Volz, L. Geelhaar, H. Riechert, P. Thomas, and W. Stolz, Journal of applied physics **98**, 063518 (2005).

[5] O. Rubel, S. Baranovskii, K. Hantke, B. Kunert, W. Rühle, P. Thomas, K. Volz, and W. Stolz, Physical Review B **73**, 233201 (2006).

[6] R. Binder, I. Galbraith, and S. W. Koch, Phys. Rev. B **44**, 3031 (1991), URL https://link.aps.org/doi/10.1103/PhysRevB.44.3031.

IV. Exciton ionization by THz pulses in germanium

M. Stein, C. Lammers, J. T. Steiner, P.-H. Richter, S. W. Koch, M. Koch, and M. Kira, J. Phys. B: At. Mol. Opt. Phys. 51 154001 (2018)

Abstract

After optical pumping, strong single cycle THz pulses are used to probe and manipulate excitons in bulk germanium. For strong THz fields a significant broadening and bleaching of the $1s-2p$ THz absorption peak is observed. The experimental results are analyzed using a microscopic many-body theory attributing the observations to a shortening of the excitonic state lifetime and eventual exciton ionization. Simultaneously, the AC THz Stark effect leads to a shift in the $1s-2p$ transition energy.

DOI: 10.1088/1361-6455/aabac7

URL: `https://doi.org/10.1088%2F1361-6455%2Faabac7`

IOP Publishing Journal of Physics B: Atomic, Molecular and Optical Physics
J. Phys. B: At. Mol. Opt. Phys. **51** (2018) 154001 (5pp) https://doi.org/10.1088/1361-6455/aabac7

Exciton ionization by THz pulses in germanium

M Stein[1], C Lammers[1], J T Steiner[1], P-H Richter[1], S W Koch[1], M Koch[1] and M Kira[2]

[1] Department of Physics and Material Sciences Center, Philipps-Universität Marburg, Renthof 5, D-35032 Marburg, Germany
[2] Electrical Engineering & Computer Science, Department of Physics, University of Michigan, Ann Arbor, MI 48109, United States of America

E-mail: markus.stein@physik.uni-marburg.de

Received 28 November 2017, revised 23 March 2018
Accepted for publication 29 March 2018
Published 9 July 2018

Abstract

After optical pumping, strong single cycle THz pulses are used to probe and manipulate excitons in bulk germanium. For strong THz fields a significant broadening and bleaching of the 1*s*–2*p* THz absorption peak is observed. The experimental results are analyzed using a microscopic many-body theory attributing the observations to a shortening of the excitonic state lifetime and eventual exciton ionization. Simultaneously, the ac THz Stark effect leads to a shift in the 1*s*–2*p* transition energy.

Keywords: excitons, THz spectroscopy, semiconductor physics

(Some figures may appear in colour only in the online journal)

1. Introduction

Optical excitation of semiconductors induces an interband polarization which allows for the generation of electrons and holes in their respective bands. The long-range Coulomb interaction between these quasi-particles can lead to the formation of bound pair states, i.e. excitons, which represent the most fundamental many-body correlation in semiconductors [1–3]. With the advent of THz spectroscopy [4], the observation of hydrogen-like internal quantum transitions of excitons became possible [5, 6].

In the last decade, intra-excitonic transitions have been studied in quantum wells [7] as well as in the bulk semiconductors silicon [8], germanium [9, 10], gallium arsenide [11] and cuprous oxide [12]. In contrast to probing excitons by means of weak THz fields, strong THz fields lead to the excitation of high energy states and even to the ionization of the quasi-particles [11, 13–15].

In this work, we apply THz spectroscopy to probe internal excitonic transitions in optically excited bulk germanium as a function of the ac field strength. Whereas the THz pulse acts as a weak probe for the lowest field strength, i.e. when the maximum field amplitude is less than $0.12\,\mathrm{kV\,cm^{-1}}$, it leads to an almost complete ionization of the excitons for the highest field strength of $2.4\,\mathrm{kV\,cm^{-1}}$. Between those extrema, we observe a broadening, a bleaching and a shift of the excitonic 1*s*–2*p* transition with increasing THz field strength. The experimental results are analyzed using a microscopic many-body theory.

2. Experimental details

The sample studied is a $L = 500\,\mu$m thick piece of undoped germanium held at 10 K in a continuous flow liquid He cryostat. The germanium is excited by an ultrashort optical pulse centered around 0.8 eV (1550 nm) which has been generated via frequency conversion from the output of a 1 kHz titanium–sapphire regenerative amplifier system. The spectrum of the exciting laser pulse and the absorption spectrum of the sample are shown in figure 1. Since the linear absorption of germanium around 0.8 eV is relatively low with $\sim 8.4\,\mathrm{cm^{-1}}$, we create an almost homogeneous carrier density along the cross section of the sample. Explicitly, the carrier

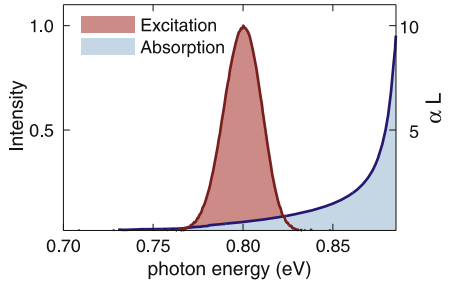

Figure 1. The absorption spectrum of germanium (shaded blue) shows a relatively low indirect absorption around 0.8 eV. In order to assure an almost homogeneous excitation of the entire sample, the central energy of the excitation pulse (shaded red) is set to this value.

density declines to roughly $2/3$ of the initial carrier density throughout the cross section of the sample.

The experimental setup is schematically shown in figure 2. We use an excitation density of 8.3×10^{13} photons cm^{-2}. For the THz pulses, we choose a delay of 9 ns since previous experiments [10] have shown that at those experimental conditions an almost pure incoherent population of 1s-excitons has formed. The THz pulses are generated using a LT-grown large aperture GaAs antenna that is excited by the fundamental laser pulse emitted by the femtosecond amplifier system, which delivers pulses with a duration of 35 fs and a central energy of 1.55 eV (800 nm). A portion of the fundamental laser pulse is used for electro-optic detection of the THz pulse in an 800 μm thick ZnTe crystal. Fourier transformation of the measured waveforms yields the frequency domain fields of the reference pulse $E(\omega)$ as well as its pump induced change $\Delta E(\omega)$. The THz absorption $\alpha(\omega)$ is extracted as [16]

$$\alpha(\omega) = \frac{2}{L}\,\mathrm{Re}\left(\frac{\Delta E(\omega)}{E(\omega) + \Delta E(\omega)}\right). \tag{1}$$

3. Theory

As is well known [17], the valence band in Ge is isotropic with mass $m_h = 0.33\, m_0$ (bare electron mass m_0) while the conduction-band is anisotropic and the masses are $m_{e,x} = m_{e,y} = 0.0815\, m_0$ and $m_{e,z} = 1.59\, m_0$ at the L-valley. Since the anisotropy plays only a minor role for our current studies, we simplify the calculations by assuming $m_e = 1.25 \times 0.0815\, m_0 = 0.1019\, m_0$ in all directions. In other words, we ignore the L-valley anisotropy with the consequence that the computed spectra show only the main $1s$–$2p$ absorption peak at 3.1 meV without the shoulder at 2.4 meV [10, 18].

In our calculations, the THz response follows from Maxwell's wave equation

$$\left[\nabla^2 + \frac{n_0^2}{c^2}\frac{\partial^2}{\partial t^2}\right] A_{\mathrm{THz}} = -\mu_0 (J_{\mathrm{THz}} + J_A) \tag{2}$$

for the THz vector potential A_{THz}, which is related to the THz electric field via $E_{\mathrm{THz}} = -\frac{\partial}{\partial t} A_{\mathrm{THz}}$. Here, c is the speed of light, n_0 is the background refractive index and μ_0 is the vacuum permittivity. The right-hand side of (2) contains the THz current $J_{\mathrm{THz}} = 1/\mathcal{V} \sum_{\lambda=\{e,h\},\mathbf{k}} j_\lambda(\mathbf{k}) f_{\mathbf{k}}^\lambda$ which results from the many-body dynamics of exciton populations. We defined the quantization volume $\mathcal{V}$, the current-matrix element $j_\lambda(\mathbf{k}) = e\hbar\mathbf{k}\cdot\mathbf{e}_P/m_\lambda$ with the effective mass m_λ, the polarization direction of the THz field $\mathbf{e}_P$ and the electron charge $e = -|e|$ as well as the electron $f_{\mathbf{k}}^e = \langle a_{c,\mathbf{k}}^\dagger a_{c,\mathbf{k}}\rangle$ and hole distribution $f_{\mathbf{k}}^h = \langle a_{v,\mathbf{k}} a_{v,\mathbf{k}}^\dagger\rangle$. Here, the electronic excitations are described by fermion operators $a_{c(v),\,\mathbf{k}}$ and $a_{c(v),\mathbf{k}}^\dagger$ for an electron with momentum $\mathbf{k}$ in the conduction (valence) band. It also contains the ponderomotive current $J_A = -e^2 n A_{\mathrm{THz}}/\mu$ with the density n and with the reduced effective mass $\mu^{-1} = m_e^{-1} + m_h^{-1}$ of electrons and holes which does not couple to the many-body dynamics. For the thin sample considered here, the reemitted field ΔE is proportional to the total induced current $J_{\mathrm{THz}} + J_A$ and determines the THz absorption $\alpha(\omega)$ via (1) [19, 20].

The THz current is determined by the semiconductor-Bloch equations for the carrier distributions which do not directly couple to the THz field [19, 20]

$$\hbar\frac{\partial}{\partial t} f_{\mathbf{k}}^e = -2\,\mathrm{Im}\left[\sum_{\mathbf{k}',\mathbf{q}} V_{\mathbf{k}-\mathbf{k}'-\mathbf{q}} c_X^{\mathbf{q},\mathbf{k}',\mathbf{k}}\right] + \Gamma_{c,c;\mathrm{Coul}}^{\mathrm{rest}} + \Gamma_{c,c;\mathrm{phon}} \tag{3}$$

and similarly for $f_{\mathbf{k}}^h$. Here, we defined the excitonic correlations

$$\begin{aligned} c_X^{\mathbf{q},\mathbf{k}',\mathbf{k}} &= \Delta\langle a_{c,\mathbf{k}}^\dagger a_{v,\mathbf{k}'}^\dagger a_{c,\mathbf{k}'+\mathbf{q}} a_{v,\mathbf{k}-\mathbf{q}}\rangle \\ &= \langle a_{c,\mathbf{k}}^\dagger a_{v,\mathbf{k}'}^\dagger a_{c,\mathbf{k}'+\mathbf{q}} a_{v,\mathbf{k}-\mathbf{q}}\rangle - \langle a_{c,\mathbf{k}}^\dagger a_{v,\mathbf{k}'}^\dagger a_{c,\mathbf{k}'+\mathbf{q}} a_{v,\mathbf{k}-\mathbf{q}}\rangle_S \end{aligned}$$

where the factorized single-particle contribution (subscript S) is removed from the full correlation, the Coulomb-matrix element $V_{\mathbf{k}}$ as well as the remaining Coulomb-scattering contributions $\Gamma_{c,c;\mathrm{Coul}}^{\mathrm{rest}}$ and the phonon-scattering contributions $\Gamma_{c,c;\mathrm{phon}}$.

The THz dynamics results from the excitonic correlations c_X which directly couple to A_{THz}

$$\begin{aligned} \mathrm{i}\hbar\frac{\partial}{\partial t} c_X^{\mathbf{q},\mathbf{k}',\mathbf{k}} = {} & [\Delta E^{\mathbf{q},\mathbf{k}',\mathbf{k}} - j_\mu(\mathbf{k}' + \mathbf{q} - \mathbf{k}) A_{\mathrm{THz}}] c_X^{\mathbf{q},\mathbf{k}',\mathbf{k}} \\ & + (1 - f_{\mathbf{k}}^e - f_{\mathbf{k}-\mathbf{q}}^h) \sum_{\mathbf{l}} V_{\mathbf{l}-\mathbf{k}} c_X^{\mathbf{q},\mathbf{k}',\mathbf{l}} \\ & - (1 - f_{\mathbf{k}'+\mathbf{q}}^e - f_{\mathbf{k}'}^h) \sum_{\mathbf{l}} V_{\mathbf{l}-\mathbf{k}'} c_X^{\mathbf{q},\mathbf{l},\mathbf{k}} \\ & + S^{\mathbf{q},\mathbf{k}',\mathbf{k}} + D_{X,\mathrm{rest}}^{\mathbf{q},\mathbf{k}',\mathbf{k}} + T^{\mathbf{q},\mathbf{k}',\mathbf{k}} \end{aligned} \tag{4}$$

with the kinetic energy of the two-particle state $\Delta E^{\mathbf{q},\mathbf{k}',\mathbf{k}}$, the current-matrix element $j_\mu(\mathbf{k}) = j_e(\mathbf{k}) + j_h(\mathbf{k})$, the Coulomb-induced in and out scattering of single-particle quantities $S^{\mathbf{q},\mathbf{k}',\mathbf{k}}$, the remaining two-particle contributions $D_{X,\mathrm{rest}}^{\mathbf{q},\mathbf{k}',\mathbf{k}}$ and the three-particle Coulomb and phonon terms $T^{\mathbf{q},\mathbf{k}',\mathbf{k}}$.

We can introduce the transformation into the exciton basis

$$\Delta N_{\alpha,\beta}(\mathbf{q}) = \sum_{\mathbf{k},\mathbf{k}'} \phi_\alpha^L(\mathbf{k}) \phi_\beta^L(\mathbf{k}') c_X^{\mathbf{q},\mathbf{k}'-\mathbf{q}_h,\mathbf{k}+\mathbf{q}_e}, \tag{5}$$

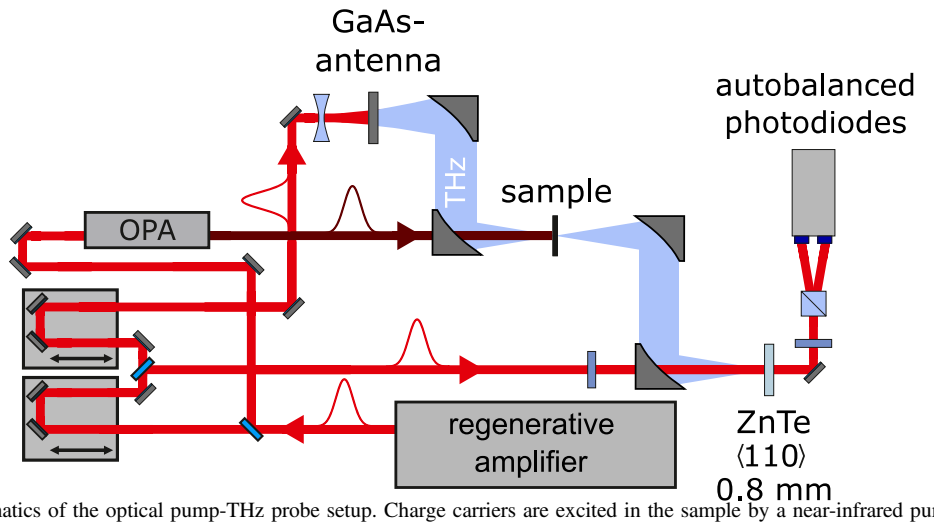

Figure 2. Schematics of the optical pump-THz probe setup. Charge carriers are excited in the sample by a near-infrared pump beam of an optical parametric amplifier. THz pulses are generated by illuminating a large aperture GaAs antenna. After passing the sample, these pulses are detected via electro-optical sampling in a ZnTe crystal and a pair of auto-balanced photodiodes.

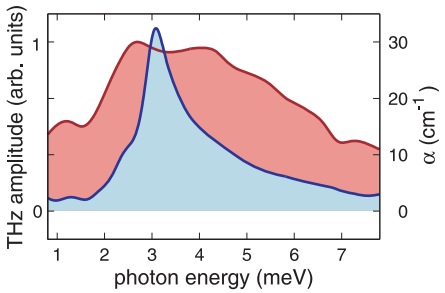

Figure 3. The THz absorption spectrum (blue) for the weakest field strength. The 1*s*–2*p* transition can be seen at 3.1 meV as a pronounced peak in the absorption spectrum. A Fourier transformed spectrum of the reference pulse (red) shows the frequencies of the driving THz pulse.

where $\mathbf{q}_e = m_e/(m_e + m_h)q$ and $\mathbf{q}_h = m_h/(m_e + m_h)q$ and where the excitonic wavefunction $\phi^L_\alpha(\mathbf{k}) = \phi^R_\alpha(\mathbf{k})/(1 - f^e_\mathbf{k} - f^h_\mathbf{k})$ is related to the solution of the Wannier equation

$$(\epsilon^e_\mathbf{k} + \epsilon^h_\mathbf{k})\phi^R_\alpha(\mathbf{k}) - (1 - f^e_\mathbf{k} - f^h_\mathbf{k})\sum_\mathbf{l} V_{\mathbf{l}-\mathbf{k}}\phi^R_\alpha(\mathbf{l}) = E_\alpha\phi^R_\alpha(\mathbf{k}) \tag{6}$$

with the kinetic energy $\epsilon^\lambda_\mathbf{k} = \hbar^2\mathbf{k}^2/(2m_\lambda) - \sum_{\mathbf{k}'} V_{\mathbf{k}-\mathbf{k}'} f^\lambda_{\mathbf{k}'}$ and with the energy E_α of exciton state α.

The diagonal parts $\Delta N_{\alpha,\alpha}(\mathbf{q})$ define the center-of-mass momentum distribution of the α-exciton and non-diagonal parts $\Delta N_{\alpha,\beta\neq\alpha}(\mathbf{q})$ exciton-transition correlations [20].

The density of incoherent 1*s*-excitons is $n_{1s} = \frac{1}{\mathcal{V}}\sum_\mathbf{q} \Delta N_{1s,1s}(\mathbf{q}) = x_{1s}n$ with the quantization volume $\mathcal{V}$ and the 1*s*-exciton fraction x_{1s}.

4. Results and analysis

Via the optical excitation of the Ge sample by an ultrashort optical pulse with a central photon energy of 0.8 eV, we create an unbound electron–hole plasma. On a timescale of several ns, this plasma condenses into bound electron–hole pairs as discussed in detail in [10]. This configuration is the initial condition for the THz probe pulse which has a 9 ns delay and a low field strength of 0.12 kV cm^{-1}. For this field strength, one observes a distinct 1*s*–2*p* resonance at 3.1 meV. The frequency spectrum of the THz pulse in comparison to the intra-excitonic resonance is shown in figure 3.

Increasing the THz intensity, we notice a significant change of the sample's response as can be seen in figure 4(a). In particular, we observe a decrease of the 1*s*–2*p* absorption peak as well as an increase of the low frequency absorption. These features signify exciton ionization leading to the formation of an unbound electron–hole plasma.

Figure 4(b) shows that the 1*s*–2*p* absorption peak already decreases at field strengths above 0.36 kV cm^{-1}. However, the intra-excitonic oscillator strength, which is shown in figure 5(a), remains constant for field strengths up to 0.55 kV cm^{-1} while it decreases for higher field strengths. We conclude that the THz field acts as a true probe pulse in bulk germanium for strengths up to 0.22 kV cm^{-1}. For higher field strengths up to 0.55 kV cm^{-1}, the excitonic 1s-2p resonance first broadens until the 1s-exciton population is ionized for even stronger THz fields. Finally, for the highest field strength of 2.4 kV cm^{-1}, we see that the 1*s*–2*p* absorption vanishes almost completely, whereas the plasma response reaches its maximum.

The broadening of the excitonic resonance is traced in detail in figure 5(b). Values for fullwidths at half maximum

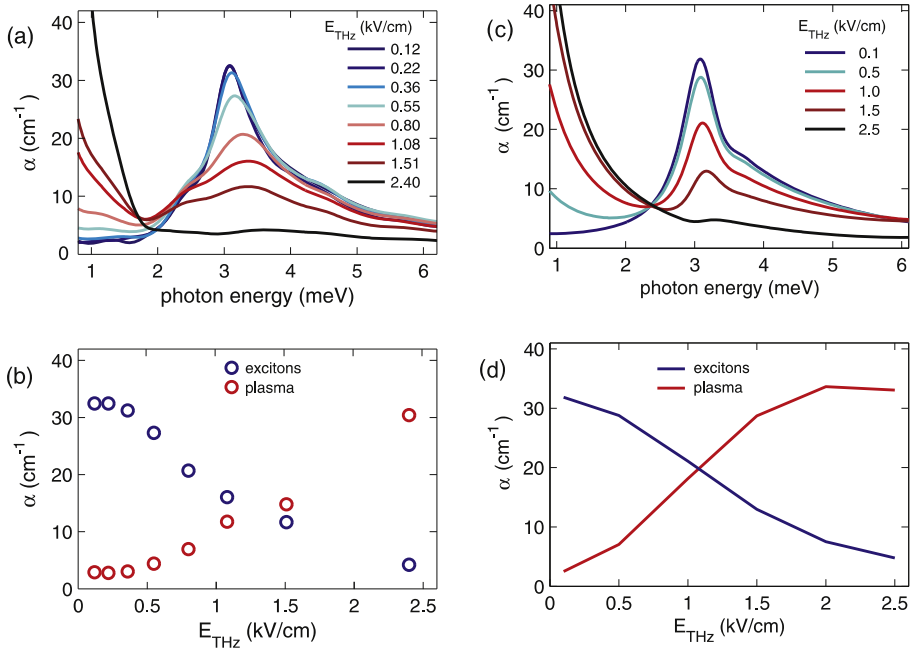

Figure 4. THz absorption for different THz field strengths for experiment (left) and theory (right). (a), (c) The THz absorption spectra $\alpha(\omega)$ for different maximum THz field strengths (in the experiment, they are recorded 9 ns after the optical pump excites the sample). (b), (d) Bleaching of the 1*s*–2*p* resonance (blue, $\alpha(\omega)$ taken at 3.1 meV and slightly higher values as the peak shifts) and emergence of a Drude-like response (red, $\alpha(\omega)$ taken at 1.15 meV) for increasing maximum THz field strengths.

are obtained by fitting a sum of two Lorentz functions to the absorption peaks. For the lowest THz field strengths up to 0.22 kV cm^{-1}, a broadening of 0.67 meV is obtained and, as the field strength rises, this value increases up to a broadening of 1.88 meV for 1.08 kV cm^{-1}. Here, the field ionization results in a reduced lifetime of exciton states which leads to a broadening of the 1*s*–2*p* transition.

In figure 5(c), we plot the energy shift of the 1*s*–2*p* absorption peak as a function of the maximum field amplitude of the THz pulses. We notice a blueshift of the 1*s*–2*p* transition with increasing THz field strength due to the THz ac Stark effect [21–23]. This shift reaches a value of 0.39 meV for a field strength of 1.08 kV cm^{-1} which is more than 10% of the initial 1*s*–2*p* transition energy. Again, the 1*s*–2*p* resonance does not shift until the field strength exceeds 0.22 kV cm^{-1}. This further affirms that up to this field strength true probing conditions exist.

In order to corroborate the interpretation of our experimental results, we evaluate our theory assuming an initial density $n_{1s} = 1.3 \times 10^{13}$ cm^{-3} of incoherent 1*s*-excitons. We match the THz pulse shape to the experimental one in order to obtain the theoretical THz response for different THz intensities shown in figures 4(c) and (d). Besides the absence of the low energy shoulder due to the neglect of the conduction-band anisotropy, we notice that the computed THz response is very similar to the experimental results shown in figures 4(a) and (b). In particular, we observe a pronounced peak from the 1*s*–2*p* exciton absorption for weak THz fields and a Drude-like response from unbound, i.e., ionized exciton populations for strong THz fields. In between, the bleaching of the 1*s*–2*p* absorption peak is very similar to that observed in the experiments, as can be seen by a comparison of figure 4(b) and 4(d). Furthermore, our calculations reproduce the broadening of the 1*s*–2*p* resonance and show a weak blueshift of the 1*s*–2*p* frequency for higher THz intensities.

5. Conclusion

In conclusion, our experiments show the ionization of an incoherent excitonic population. We observe a broadening of the intra-excitonic transition as well as a blueshift of the resonance for increased THz field strength. The broadening is explained by a reduced lifetime of the exciton states due to field ionization whereas the blueshift is caused by the ac Stark effect. For a field strength of 2.4 kV cm^{-1}, the exciton itself is ionized and an almost pure plasma response is observed. The experimental observations are qualitatively reproduced by our microscopic theory. Future experiments with a narrowband THz pump beam and a weak broadband THz probe may give further insights on how the THz frequency impacts the shift behavior of the intra-excitonic resonances.

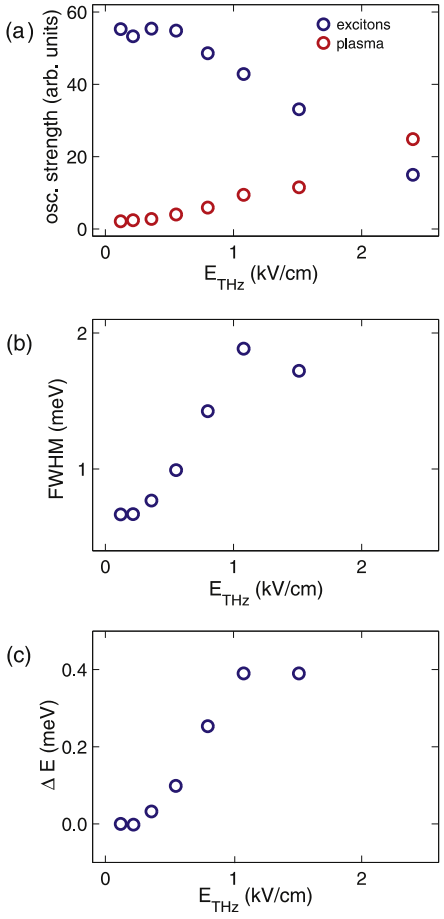

Figure 5. (a) The oscillator strength of the intra-excitonic transition integrated from 1.8 to 6 meV as a function of the maximum THz field strength (blue). It stays constant for field strengths up to 0.55 kV cm^{-1} and decreases for higher field strengths. The oscillator strength of the unbound electron–hole plasma (red) integrated from 0.85 to 1.8 meV increases already at low field strengths. (b) The FWHM of the intra-excitonic transition and (c) the relative energetic shift of the excitonic resonance for different maximum THz field strengths. Both increase with the THz field strength.

Acknowledgments

This work is a project of the Collaborative Research Center SFB 1083 funded by the Deutsche Forschungsgemeinschaft.

ORCID iDs

C Lammers https://orcid.org/0000-0002-7942-8629

References

[1] Elliott R J 1957 *Phys. Rev.* **108** 1384
[2] Feldmann J, Peter G, Göbel E O, Dawson P, Moore K, Foxon C and Elliott R J 1987 *Phys. Rev. Lett.* **59** 2337
[3] Kira M, Jahnke F and Koch S W 1998 *Phys. Rev. Lett.* **81** 3263
[4] Grischkowsky D, Keiding S, Van Exter M and Fattinger C 1990 *J. Opt. Soc. Am.* B **7** 2006–15
[5] KaindI R A, Carnahan M A, Hagele D, Lovenich R and Chemla D S 2003 *Nature* **423** 734
[6] Koch S W, Kira M, Khitrova G and Gibbs H M 2006 *Nat. Mater.* **5** 523
[7] Rice W D *et al* 2013 *Phys. Rev. Lett.* **110** 137404
[8] Suzuki T and Shimano R 2009 *Phys. Rev. Lett.* **103** 057401
[9] Sekiguchi F and Shimano R 2015 *Phys. Rev.* B **91** 155202
[10] Stein M, Lammers C, Springer P, Richter P H, Koch S W, Koch M and Kira M 2017 *Phys. Rev.* B **95** 155207
[11] Sekiguchi F, Mochizuki T, Kim C, Akiyama H, Pfeiffer L N, West K W and Shimano R 2017 *Phys. Rev. Lett.* **118** 067401
[12] Leinß S, Kampfrath T, Volkmann K V, Wolf M, Steiner J T, Kira M, Koch S W, Leitenstorfer A and Huber R 2008 *Phys. Rev. Lett.* **101** 246401
[13] Shinokita K, Hirori H, Nagai M, Satoh N, Kadoya Y and Tanaka K 2010 *Appl. Phys. Lett.* **97** 211902
[14] Ewers B, Köster N S, Woscholski R, Koch M, Chatterjee S, Khitrova G, Gibbs H, Klettke A C, Kira M and Koch S W 2012 *Phys. Rev.* B **85** 075307
[15] Drexler M J, Woscholski R, Lippert S, Stolz W, Rahimi-Iman A and Koch M 2014 *Phys. Rev.* B **90** 195304
[16] Ulbricht R, Hendry E, Shan J, Heinz T F and Bonn M 2011 *Rev. Mod. Phys.* **83** 543
[17] Madelung O 1991 *Semiconductors: Group IV Elements and III–V Compounds* (*Data in Science and Technology*) (Heidelberg: Springer)
[18] Springer P, Koch S W and Kira M 2016 *J. Opt. Soc. Am.* B **33** C30–8
[19] Kira M and Koch S W 2006 *Prog. Quantum Electron.* **30** 155–296
[20] Steiner J T, Kira M and Koch S W 2008 *Phys. Rev.* B **77** 165308
[21] Bakos J S 1977 *Phys. Rep.* **31** 209–35
[22] Nordstrom K B, Johnsen K, Allen S, Jauho A P, Birnir B, Kono J, Noda T, Akiyama H and Sakaki H 1998 *Phys. Rev. Lett.* **81** 457
[23] Dent C J, Murdin B N and Galbraith I 2003 *Phys. Rev.* B **67** 165312

V. Inelastic electron-exciton scattering in bulk germanium

M. Stein, F. Schäfer, and L. Gomell, Phys. Rev. B 99, 144310 (2019)

Abstract

We investigate the destructive inelastic as well as the elastic scattering of a hot electron-hole plasma with an incoherent exciton population in bulk Ge by means of optical pump - terahertz probe spectroscopy. An incoherent exciton population evolves from a first optical pulse while a delayed second optical pulse creates the electron-hole plasma. The interaction of the plasma with the exciton population is monitored via the intraexcitonic transitions by a probing terahertz pulse. Analyzing the density-dependent decay of the intraexcitonic transitions after the arrival of the second optical pulse yields an inelastic scattering rate of $2.0 \times 10^{-4}\,\mathrm{cm^3 s^{-1}}$. An analysis of the corresponding linewidth of the $1s-2p$ transition yields a total scattering rate of $3.7 \times 10^{-4}\,\mathrm{cm^3 s^{-1}}$. This allows us to experimentally distinguish between elastic and inelastic scattering and we obtain an elastic scattering rate of $1.7 \times 10^{-4}\,\mathrm{cm^3 s^{-1}}$.

DOI: 10.1103/PhysRevB.99.144310

URL: `https://link.aps.org/doi/10.1103/PhysRevB.99.144310`

Inelastic electron-exciton scattering in bulk germanium

M. Stein,* F. Schäfer, and L. Gomell
Department of Physics and Material Sciences Center, Philipps-Universität Marburg, Renthof 5, 35032 Marburg, Germany

(Received 28 February 2019; revised manuscript received 9 April 2019; published 25 April 2019)

We investigate the destructive inelastic as well as the elastic scattering of a hot electron-hole plasma with an incoherent exciton population in bulk Ge by means of optical pump-terahertz probe spectroscopy. An incoherent exciton population evolves from a first optical pulse while a delayed second optical pulse creates the electron-hole plasma. The interaction of the plasma with the exciton population is monitored via the intraexcitonic transitions by a probing terahertz pulse. Analyzing the density-dependent decay of the intraexcitonic transitions after the arrival of the second optical pulse yields an inelastic scattering rate of $2.0 \times 10^{-4}\,\mathrm{cm}^3\,\mathrm{s}^{-1}$. An analysis of the corresponding linewidth of the $1s-2p$ transition yields a total scattering rate of $3.7 \times 10^{-4}\,\mathrm{cm}^3\,\mathrm{s}^{-1}$. This allows us to experimentally distinguish between elastic and inelastic scattering and we obtain an elastic scattering rate of $1.7 \times 10^{-4}\,\mathrm{cm}^3\,\mathrm{s}^{-1}$.

DOI: 10.1103/PhysRevB.99.144310

I. INTRODUCTION

Carrier scattering determines the operation and the performance of many semiconductor based devices like transistors, solar cells, or lasers [1–8]. At high carrier concentrations, e.g., effects like kinetic hole burning, carrier capture, and carrier relaxation govern the operation of semiconductor lasers [9–14]. Therefore, a detailed knowledge of scattering processes is of great interest for the optimization of many semiconductor devices. Ultrafast spectroscopy is a viable tool to gain insights into those scattering mechanisms. In the past, especially two methods were used to investigate scattering events between charge carriers and excitons experimentally. Those are optical pump-optical probe spectroscopy, in particular four-wave-mixing spectroscopy (FWM), and time-resolved photoluminescence (TRPL) spectroscopy [15–23]. In FWM experiments the scattering of charge carriers or incoherent excitons with coherent exciton polarizations has been investigated [24]. Here, scattering leads to a dephasing of the optically induced polarization. Accordingly, the dephasing time of a $1s$ exciton polarization is analyzed in the presence of an electron-hole plasma or incoherent excitons that can be injected by an additional prepulse [16,17,24]. Since the dephasing time is inversely connected to the homogeneous linewidth, the homogeneous line broadening of an excitonic transition also gives access to electron-exciton scattering. This is exploited in TRPL and optical transmission experiments by analyzing the linewidth of excitonic transitions [17,19,21,25–28]. Again, additional excitation pulses can be used to create the desired environment [17,19]. Unfortunately, by analyzing transition linewidths and/or dephasing times, the insights are limited to the influence of scattering events on discrete quantum states. A discrete state of, e.g., an exciton can already be destroyed by elastic scattering processes in which the exciton remains bound and only observes a change of momentum. However, a destructive inelastic scattering process in which the exciton overcomes the attractive Coulomb interaction and breaks into an unbound electron-hole pair has the same effect as elastic scattering in these FWM or TRPL experiments [29]. Therefore, it is hard to distinguish between elastic and inelastic scattering processes with those methods. Consequently, little is known experimentally about destructive inelastic scattering, its efficiency, especially in comparison to elastic scattering processes, and how electron-exciton scattering affects the decay of exciton populations [30].

Another spectroscopic technique to study many-particle interactions is optical pump-terahertz probe spectroscopy. Since its pioneering works in the 1980s and early 90s [31–35], optical pump-terahertz probe spectroscopy has proven to be a powerful method for investigating intraband charge carrier interactions in semiconductors and their quasiparticles such as excitons [36–39]. Here, we use optical pump-terahertz probe spectroscopy to study the lifetime as well as the intraexcitonic linewidth of an incoherent exciton population under the impact of a hot electron-hole plasma. Therefore, a second optical pulse injects additional carriers which interact with an incoherent population of excitons that arose from a previous optical pulse. Probing the intraexcitonic $1s-2p$ transition and analyzing its density-dependent decay and its linewidth after the arrival of the second optical pulse provides insights into the destructive inelastic as well as the total scattering rate. This enables the experimental differentiation between elastic and inelastic scattering processes.

II. EXPERIMENTAL DETAILS

The sample investigated is a piece of nominally undoped n-type germanium (Ge) with a thickness of $L = 500\,\mu\mathrm{m}$ and a room temperature resistivity larger than $30\,\Omega\,\mathrm{cm}$. The sample is held at 10 K in a continuous flow liquid-He cryostat.

The experimental setup is schematically shown in Fig. 1(c). The experiment is performed with a 1 kHz titanium-sapphire-based regenerative amplifier system which provides 35 fs

*markus.stein@physik.uni-marburg.de

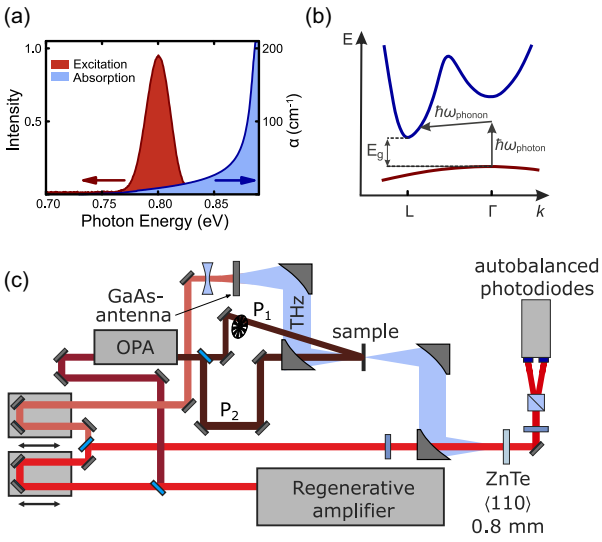

FIG. 1. (a) The linear absorption of the sample (blue) is plotted together with the spectrum of the optical excitation pulse (red). (b) Schematic of the excitation process and the indirect band structure of Ge. (c) A schematic of the experimental optical pump-THz probe setup. The THz section is purged with dry nitrogen gas to avoid THz absorption by water vapor.

pulses spectrally centered around 800 nm. This pulse train is split into three parts. One part of the pulse excites a LT-grown large aperture GaAs antenna. The antenna emits ∼1 ps long terahertz (THz) pulses, which probe the sample's intraexcitonic $1s-2p$ transition and, hence, indicate the presence of an incoherent exciton population. The second part of the pulse is used as a gate pulse to record the THz pulse via electro optical sampling in an 800 μm thick ⟨110⟩ cut ZnTe crystal [40,41]. A pair of autobalanced photodiodes is used to detect the THz field-induced changes of the gate pulse polarization which enables the sampling of the THz waveform. To get rid of water vapor absorption we purge the THz part of our setup with nitrogen gas. The photon energy of the third part of the pulse is converted in an optical parametric amplifier (OPA) to 0.795 eV (1560 nm) with a full width at half maximum (FWHM) of 31 meV and a pulse duration of roughly 60 fs. Thereafter, the pulse is split into two by a beam splitter. One part (P_1) is mechanically chopped and excites the Ge crystal under an angle of ∼20°. Since we optically excite the sample energetically below its direct band gap, the absorption coefficient is low with 7.5 cm^{-1}, which ensures a homogeneous excitation profile in propagation direction. This first pulse P_1 generates an electron-hole plasma, which after 6.7 ns has converted nearly completely into an incoherent population of excitons as previous experiments have shown [42]. With a time delay of 6.7 ns relative to the first optical pulse, the second pulse P_2 provides an additional excitation of the sample [see Fig. 1(c)]. This second beam again generates an electron-hole plasma that interacts with the incoherent population of excitons. In our experiment we can, hence, directly probe how the incoherent exciton population decays via scattering with free carriers. Furthermore, we can monitor the linewidth of the intraexcitonic transition and follow the subsequent reformation of incoherent excitons.

Our setup allows us to detect THz pulses with a bandwidth ranging from 1–12 meV. A time window of 16.5 ps is measured with the THz pulse centered in the middle of this window. Afterwards, a Hanning window function is applied to the measured waveforms before Fourier transformation into the frequency domain. This yields the frequency domain fields of the reference pulse $E(\omega)$ and the pump-induced change $\Delta E(\omega)$ of the first excitation pulse. The absorption $\alpha(\omega)$ as well as the change of the real part of the dielectric function $\Delta\epsilon_1(\omega)$ are given by [43]

$$\alpha(\omega) = 2\Delta\sigma_1(\omega) = \frac{2}{L}\,\mathrm{Re}\left(\frac{\Delta E(\omega)}{E(\omega)+\Delta E(\omega)}\right), \tag{1}$$

$$\Delta\epsilon_1(\omega) = \frac{2c_0\sqrt{\epsilon_r}}{\omega L}\,\mathrm{Im}\left(\frac{\Delta E(\omega)}{E(\omega)+\Delta E(\omega)}\right), \tag{2}$$

where c_0 is the speed of light in vacuum and ϵ_r is the dielectric constant of the material.

In order to determine the specified photon densities, the knife-edge method has been used to measure the width of both the optical and the THz pulse. Under the assumption of perfect spatial overlap, it is determined which portion of the lateral 3 mm large optical pulse lies within the FWHM of the 1 mm large THz pulse. Together with the power of the optical pulse, which has been determined by a thermal power meter, the photon density per pulse ρ is calculated for the FWHM of the THz pulse. Using the spectrum of the optical pulse $I_0(\omega)$ and the measured linear absorption of the sample $\alpha(\omega)$, the absorption for each frequency is weighted with the respective intensity of the spectrum to obtain the average absorption of the optical pulse A_{avg}:

$$A_{\mathrm{avg}} = \frac{\sum_\omega (I_0(\omega) - I_0(\omega)\cdot e^{-\alpha(\omega)L})}{\sum_\omega I_0(\omega)} = 0.293. \tag{3}$$

Together with the photon density ρ, the sample thickness L, and the reflectance R, the charge carrier density n can be calculated:

$$n = \frac{(\rho - \rho R)\cdot A_{\mathrm{avg}}}{L}. \tag{4}$$

Here, a value of 0.36 is used for the reflectance of Ge.

III. RESULTS

To study the inelastic scattering process of an unbound electron-hole plasma with an incoherent exciton population, we analyze the response of the probing THz pulse shortly before and after the second optical pulse injects an electron-hole plasma. As the injected charge carriers collide with the existing exciton population different scattering mechanisms are possible [29,30,44,45]. An elastic scattering process may change the momentum and the kinetic energy of the exciton but will not destroy the Coulomb bound electron-hole pair [29,44]. Since the probing THz pulse detects intraexcitonic transitions from excitons of all center-of-mass momentums, such elastic scattering processes will hardly change the oscillator strength of the intraexcitonic transition.

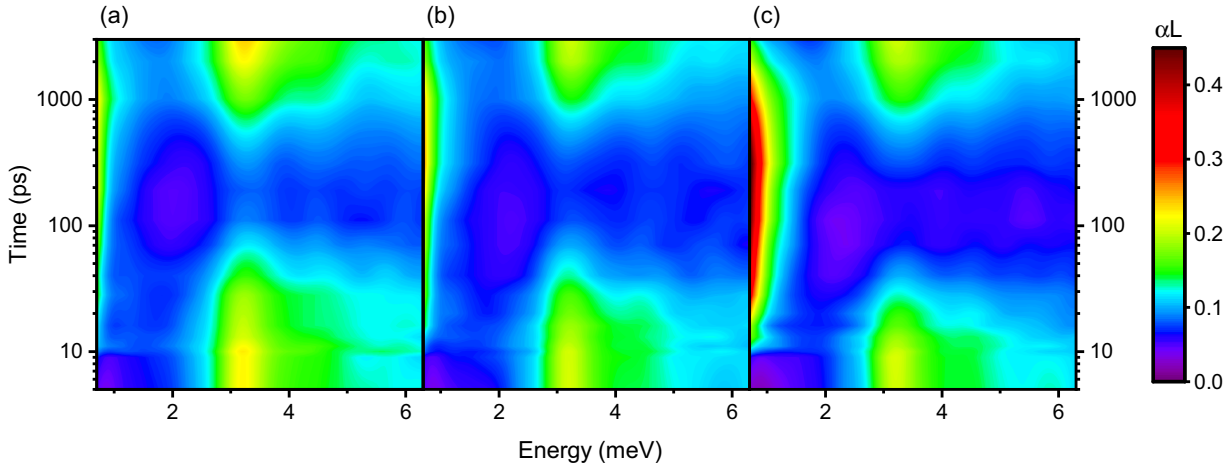

FIG. 2. Contour plots of the THz absorption for a constant photon density of the first excitation pulse P_1 of 9.8×10^{13} photons/cm^2 and photon densities of (a) 2.9×10^{13} photons/cm^2, (b) 5.9×10^{13} photons/cm^2, and (c) 1.0×10^{14} photons/cm^2 for the second optical pulse P_2. The second pulse is delayed by 6.7 ns with respect to the first optical pulse. A time delay of zero between the second optical pulse and the THz pulse is set to 10 ps on the time axis to allow for a logarithmic representation. Before the second optical pulse excites the sample, all graphs show a pronounced intraexcitonic resonance at 3.2 meV. With the excitation from the second optical pulse at 10 ps, the amplitude of the resonance decreases on a time scale of tens of picoseconds, while simultaneously the absorption increases at low energies. This process occurs more rapidly with increasing photon density of the second pulse. It takes a few hundred picoseconds for the intraexcitonic resonance to build up again and about 3 ns to reach a similar level as before the excitation of the second pulse.

However, elastic scattering processes increase the linewidth of the transition. In contrast, destructive inelastic scattering processes overcome the Coulomb interaction and the exciton breaks into a free electron-hole pair [29]. As the plasma response of an unbound electron-hole pair differs significantly from intraexcitonic transitions, we are able to clearly identify the inelastic scattering by means of THz probe spectroscopy.

Figure 2 shows contour plots of the THz absorption for a photon density of 9.8×10^{13} photons/cm^2 from the first pulse and three different photon densities from the second pulse. The second optical pulse is delayed by 6.7 ns with respect to the first pulse and its arrival, i.e., a zero time delay between the second optical pulse and the THz probe pulse, is set to 10 ps on the time axis. Before the second pulse arrives an almost pure 1s exciton population has been built as the absorption peak at ∼3.2 meV indicates. The second pulse then injects the electron-hole plasma at 10 ps. However, signatures of the intraexcitonic transitions remain and decay—depending on the photon density of the second pulse—on a time scale of tens to hundreds of picoseconds. Once intraexcitonic signatures decay, the plasma response increases as a rising absorption below 1.5 meV reveals. Here, the transition of the 1s exciton population into a free electron-hole plasma due to inelastic scattering is caught in the act. For lower photon densities of the second pulse, a small fraction of excitons survives as their signatures are still visible at hundreds of picoseconds [see Fig. 2(a)]. In contrast, higher photon densities lead to a complete decay of the exciton population. Several hundred picoseconds after the second pulse arrives, the electron-hole plasma is cooled down and the reformation of an exciton population starts. After 3 ns, an almost pure exciton population is restored.

A. Inelastic scattering rates

To obtain decay times of the exciton population different approaches are possible. One could analyze the plasma response after the second optical pulse excites the sample. When the exciton population decays into free electron-hole pairs via inelastic scattering, the plasma response increases. A readout of the transients of the absorption at a certain energy below the intraexcitonic resonance is well suited to monitor this increase of the plasma response. However, the plasma response depends on the effective mass of the charge carriers as well as on scattering events. Both are not necessarily constant in this dynamic environment. Therefore, we use another approach as the analysis of the plasma response might be biased.

The approach chosen here is to directly monitor the absorption of the intraexcitonic transitions. When excitons are destroyed by inelastic scattering, they no longer contribute to the intraexcitonic absorption. Hence, the intraexcitonic absorption strength decays. To account for imaginable shifts and broadening effects of intraexcitonic transitions, we integrate the absorption from 2.0 meV to 6.0 meV. In Fig. 3(a), we show the integrated intraexcitonic absorption, i.e., the intraexcitonic oscillator strength, for different time delays for a photon density of 9.8×10^{13} photons/cm^2 of the first pulse and four different densities of the second pulse (vertical offsets are added for clarity). When the second pulse arrives at 10 ps, a clear decay of the intraexcitonic oscillator strength is observed within the first 100 ps. This decay is based on the destruction of the exciton population by inelastic scattering with the electron-hole plasma that is created at 10 ps. By fitting simple biexponential functions we yield the decay times (τ_1) of the exciton population as well as its reformation times (τ_2). In Fig. 3(c), the decay times τ_1 (black data points) are shown for two different photon densities of the first optical pulse.

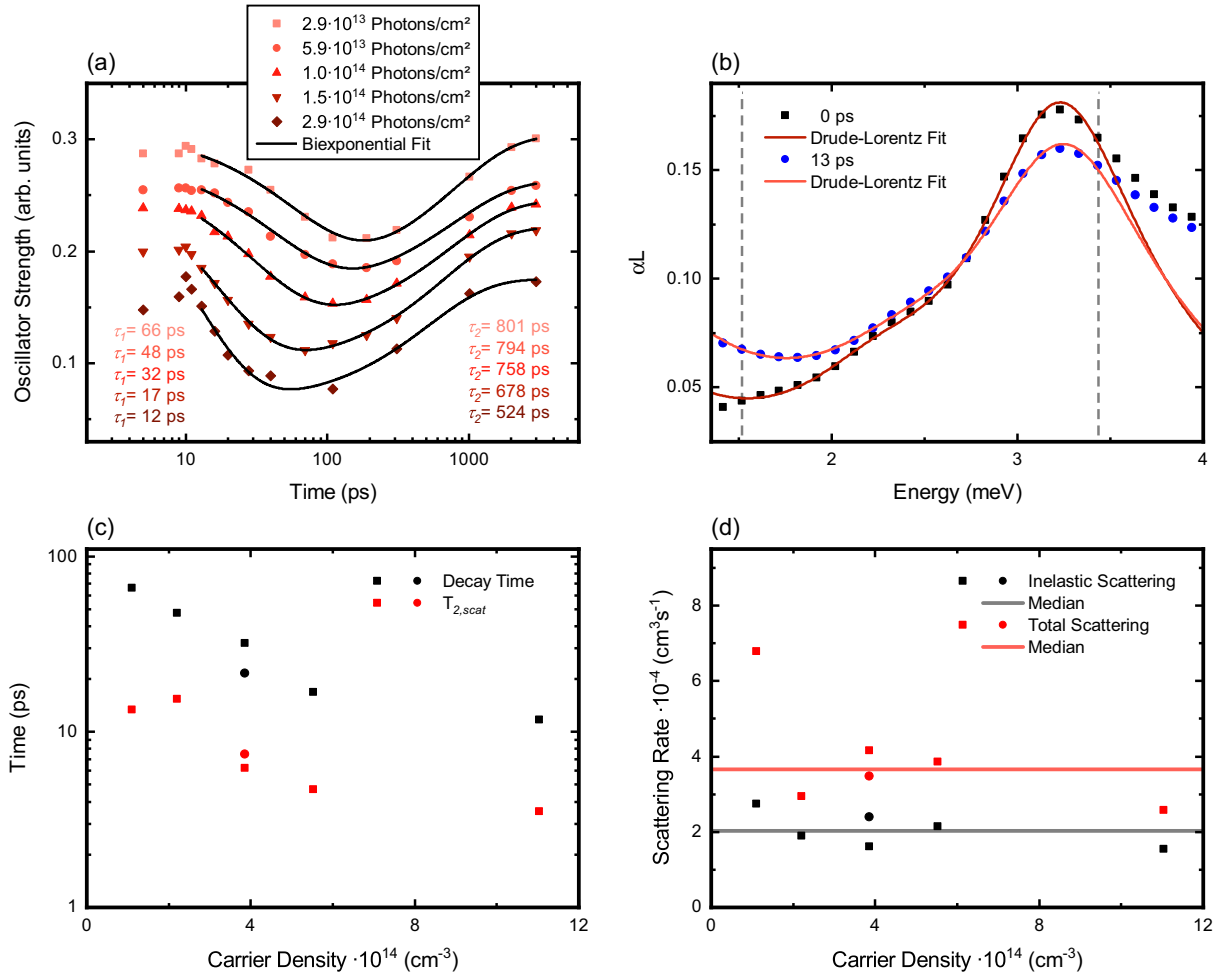

FIG. 3. (a) Intraexcitonic oscillator strength for a photon density of 9.8×10^{13} photons/cm^2 from the first optical pulse and five different densities of the second pulse. For the sake of clarity, the data points have been provided with an offset. A biexponential fit (black) yields the decay as well as the reformation times. (b) Fit of a Drude-Lorentz model to the intraexcitonic $1s-2p$ transition 10 ps before and 3 ps after the second optical pulse injects an electron-hole plasma. The borders of the fit are marked by vertical gray dashed lines. (c) Decay times τ_1 (black data points) from the biexponential fit are plotted together with the additional dephasing due to electron-exciton scattering $T_{2,\mathrm{scat}}$ (red data points), which is calculated via Eq. (7), for photon densities of 9.8×10^{13} photons/cm^2 (squares) and 2.8×10^{14} photons/cm^2 (circles) of the first excitation pulse. (d) The corresponding inelastic and total scattering rates together with the respective median of the data.

The decay times τ_1 are connected with the inelastic scattering rate γ_{in} via $\gamma_{in} = \frac{2}{\tau_1 \cdot n}$, where n is the electron density that is injected into the conduction band by the second optical pulse [24]. Doing so, we yield a median scattering rate of 2.0×10^{-4} cm^3 s^{-1} as shown in Fig. 3(d). This scattering rate is roughly an order of magnitude lower than those observed in Ref. [24] for electron-exciton scattering in bulk gallium arsenide (GaAs). As already stated, Ref. [24] measures the sum of elastic and inelastic scattering, i.e., the total scattering rate. The decay of the intraexcitonic transition investigated here, on the other hand, is only sensitive to inelastic scattering.

B. Linewidth of the intraexcitonic transition

Similar to TRPL or optical transmission experiments [17,19,25,26,28], we can investigate the linewidth of the intraexitonic transition before and after the second optical pulse generates an electron-hole plasma. Here, we use a phenomenological Drude-Lorentz model for a quantitative analysis of the measured spectra [46]. This approach describes the pump-induced changes of the frequency-dependent dielectric function $\Delta\epsilon(\omega) = \Delta\epsilon_1 + i\Delta\sigma_1/(\epsilon_0\omega)$ by means of two components

$$\Delta\epsilon(\omega) = \frac{n_x e^2}{L\epsilon_0\mu}\left(\frac{f_{1s-2p,\parallel}}{\frac{E^2_{\mathrm{res},\parallel}}{\hbar^2}-\omega^2-i\omega\Delta_{\mathrm{hom}}} + \frac{f_{1s-2p,\perp}}{\frac{E^2_{\mathrm{res},\perp}}{\hbar^2}-\omega^2-i\omega\Delta_{\mathrm{hom}}}\right) - \frac{e^2}{L\epsilon_0\mu}\times\frac{n_{fc}}{\omega+i\omega\Gamma}. \quad (5)$$

The first two terms consist of two Lorentzian resonances to account for the two distinct intraexcitonic $1s-2p$ transitions that are caused by the anisotropy of L-valley electrons in bulk Ge [42,47,48]. Since the oscillator strengths $f_{1s-2p,\parallel}$ and $f_{1s-2p,\perp}$ are not determined exactly, we are free to use just one reduced mass μ and one $1s$ exciton density n_x for both oscillators. Furthermore, we assume that both resonances at energies $E_{\mathrm{res},\parallel}$ and $E_{\mathrm{res},\perp}$ have the same homogeneous linewidth Δ_{hom}. The last term represents the Drude response of the free electron-hole plasma. Here, we use just one total free carrier density n_{fc} and assume that we only have one scattering rate Γ. Thus, the remaining fitting parameters are the resonance energies $E_{\mathrm{res},\parallel}$ and $E_{\mathrm{res},\perp}$, the homogeneous linewidth Δ_{hom}, the carrier scattering rate Γ, and the exciton and free carrier densities n_x and n_{fc}. Additional constants in all terms are the electron charge e and the vacuum permeability ϵ_0.

By fitting $2\epsilon_0\omega \cdot \mathrm{Im}\,(\Delta\epsilon(\omega))$ to the experimentally determined absorption spectra as shown exemplarily for two time delays in Fig. 3(b), we receive the linewidth Δ_{hom} of the intraexcitonic $1s-2p$ transition. Since the dephasing time T_2 is connected to the homogeneous linewidth Δ_{hom} via $T_2 = \frac{2}{\Delta_{\mathrm{hom}}}$, the homogeneous line broadening of an intraexcitonic transition gives access to the dephasing due to electron-exciton scattering. Here, we determine the homogeneous linewidth 10 ps before and 3, 6, and 10 ps after the second optical pulse injects the electron-hole plasma. Then, to minimize the error, we average the linewidth for the three time delays (3, 6, and 10 ps) after the second optical excitation and calculate the dephasing time. The determined dephasing time T_2 is then composed of the natural dephasing time of the transition $T_{2,\mathrm{nat}}$, which we obtain from the measurement 10 ps before the second pulse arrives, and the additional dephasing due to electron-exciton scattering $T_{2,\mathrm{scat}}$ via [24]:

$$\frac{1}{T_2} = \frac{1}{T_{2,\mathrm{nat}}} + \frac{1}{T_{2,\mathrm{scat}}}. \tag{6}$$

Converting to $T_{2,\mathrm{scat}}$ results in

$$T_{2,\mathrm{scat}} = \frac{T_2 \cdot T_{2,\mathrm{nat}}}{T_{2,\mathrm{nat}} - T_2}. \tag{7}$$

The dephasing time due to additional scattering $T_{2,\mathrm{scat}}$ is plotted in Fig. 3(c) (red data points) against the carrier density. However, the $1s-2p$ transition consists of two excited states, namely the $1s$ and the $2p$ state, the lifetimes of which are shortened by the additional electron-exciton scattering. Accordingly, $T_{2,\mathrm{scat}}$ consists of the additional dephasing of the $1s$ states ($T_{2,\mathrm{scat},1s}$) as well as the $2p$ states ($T_{2,\mathrm{scat},2p}$) [49]:

$$\frac{1}{T_{2,\mathrm{scat}}} = \frac{1}{T_{2,\mathrm{scat},1s}} + \frac{1}{T_{2,\mathrm{scat},2p}}. \tag{8}$$

Since we only have access to the linewidth of the superposition of both states with THz spectroscopy, we have to make an assumption at this point. Assuming that both states are equally influenced by scattering we get:

$$T_{2,\mathrm{scat},1s} = 2T_{2,\mathrm{scat}}. \tag{9}$$

Herewith we are able to calculate the total scattering rate of the $1s$ exciton state γ_{tot} via:

$$\gamma_{\mathrm{tot}} = \frac{2}{T_{2,\mathrm{scat},1s} \cdot n} = \frac{1}{T_{2,\mathrm{scat}} \cdot n}. \tag{10}$$

By using the median we receive a total electron-exciton scattering rate of $3.7 \times 10^{-4}\,\mathrm{cm^3 s^{-1}}$ as shown in Fig. 3(d). This is roughly a factor of 4 smaller than the electron-exciton scattering rate as determined in Ref. [24] for GaAs. However, in Ref. [24] the scattering rate of optically excited excitonic polarizations with a center-of-mass momentum close to $\vec{K} = 0$ is determined, while we determine the scattering rate of an incoherent exciton population with different center-of-mass momentums. In contrast to Schultheis *et al.* [24], the scattering rate of large-momentum excitons is determined in Ref. [23]. With $9.5 \times 10^{-5}\,\mathrm{cm^3\,s^{-1}}$ the scattering rate from Ref. [23] is approximately a factor of 4 smaller than the scattering rate determined by us and a factor of 17 smaller than the scattering rate determined by Schultheis *et al.* They attribute their much lower scattering rate in comparison to Schultheis *et al.* to drastically reduced scattering of large-momentum excitons with free carriers [23]. Since our unique optical pump-terahertz probe method takes into account excitons of all center-of-mass momentums, it is very reasonable that the scattering rate determined by us lies just between the two values of Ref. [23] and Ref. [24].

The total scattering rate is composed of elastic and inelastic scattering. Since we are able to determine the inelastic scattering rate by the decay of the exciton population, we now have access to the elastic scattering rate as well. The elastic scattering rate is equivalent to the difference between the total and the inelastic scattering rate. This gives us an elastic scattering rate of $1.7 \times 10^{-4}\,\mathrm{cm^3\,s^{-1}}$. Thus, for the excitation conditions used here with an excess energy of the electron-hole plasma of ~50 meV, the elastic scattering rate is comparable to the inelastic scattering rate of $2.0 \times 10^{-4}\,\mathrm{cm^3\,s^{-1}}$.

C. Exciton reformation

After the exciton population has been destroyed by inelastic scattering, the reformation process begins. However, in contrast to the observations for a single excitation pulse that are described in Ref. [42], the exciton formation process is not delayed but starts instantaneously after the exciton population is destroyed. Thus, the scattering and the reformation processes can be described by a simple biexponential fit as shown in Fig. 3(a). For a single excitation pulse, the hot electron-hole plasma has to cool down first via phonons before excitons can form. However, when a second pulse generates a hot electron-hole plasma in the presence of an incoherent exciton population, the plasma can efficiently cool down via inelastic electron-exciton scattering. As a result, a cold electron-hole plasma is present after the scattering, so that the exciton formation can start immediately. In agreement with the findings from Ref. [42], the excitation with a second optical pulse confirms that the exciton formation is faster at higher charge carrier densities. In Fig. 3(a) the reformation time τ_2 decreases continuously from 801 ps for the lowest photon density of the second pulse of $2.9 \times 10^{13}\,\mathrm{photons/cm^2}$ to 524 ps for the highest photon density of $2.9 \times 10^{14}\,\mathrm{photons/cm^2}$. The

photon densities correspond to charge carrier densities of $1.1 \times 10^{14}\,\mathrm{cm}^{-3}$ and $1.1 \times 10^{15}\,\mathrm{cm}^{-3}$, respectively, which are at least one order of magnitude below the Mott transition in Ge [50]. A comparison with the formation times from Ref. [42] shows that at the same charge carrier densities the observed exciton formation is much faster here. This may indicate that even though the initial exciton population is destroyed by inelastic scattering, the reformation process of excitons finds much more favorable conditions than the exciton formation out of an optically excited electron-hole plasma.

IV. CONCLUSION

In conclusion, we present a unique method to experimentally get access to both destructive inelastic and elastic electron-exciton scattering via optical pump-terahertz probe spectroscopy. We monitor the decay of the intraexcitonic transitions of an incoherent exciton population by scattering with an electron-hole plasma which is generated by a second optical pulse in bulk Ge. By analyzing the decay times, we find an inelastic scattering rate of $2.0 \times 10^{-4}\,\mathrm{cm}^3\,\mathrm{s}^{-1}$. An analysis of the linewidth broadening of the intraexcitonic $1s-2p$ transition due to the arrival of the second optical pulse yields a total scattering rate of $3.7 \times 10^{-4}\,\mathrm{cm}^3\,\mathrm{s}^{-1}$. The difference between total and inelastic scattering rate results in the elastic scattering rate, which is $1.7 \times 10^{-4}\,\mathrm{cm}^3\,\mathrm{s}^{-1}$ accordingly. The following reformation of the exciton population is accelerated for higher charge carrier densities.

ACKNOWLEDGMENT

Financial support from the Deutsche Forschungsgemeinschaft via the Collaborative Research Center SFB 1083 is gratefully acknowledged.

[1] V. Gantmakher and Y. Levinson, *Carrier Scattering in Metals and Semiconductors*, Modern Problems in Condensed Matter Sciences (Elsevier Science, Amsterdam, 2012).
[2] D. Derkacs, S. H. Lim, P. Matheu, W. Mar, and E. T. Yu, Appl. Phys. Lett. **89**, 093103 (2006).
[3] J. Xiang, W. Lu, Y. Hu, Y. Wu, H. Yan, and C. M. Lieber, Nature (London) **441**, 489 (2006).
[4] K. Natori, J. Appl. Phys. **76**, 4879 (1994).
[5] S. Takagi, J. L. Hoyt, J. J. Welser, and J. F. Gibbons, J. Appl. Phys. **80**, 1567 (1996).
[6] R. Köhler, A. Tredicucci, F. Beltram, H. E. Beere, E. H. Linfield, A. G. Davies, D. A. Ritchie, R. C. Iotti, and F. Rossi, Nature (London) **417**, 156 (2002).
[7] P. Palestri, D. Esseni, S. Eminente, C. Fiegna, E. Sangiorgi, and L. Selmi, IEEE Trans. Electron Devices **52**, 2727 (2005).
[8] D. Hofstetter, M. Beck, T. Aellen, and J. Faist, Appl. Phys. Lett. **78**, 396 (2001).
[9] R. Binder, D. Scott, A. E. Paul, M. Lindberg, K. Henneberger, and S. W. Koch, Phys. Rev. B **45**, 1107 (1992).
[10] T. R. Nielsen, P. Gartner, and F. Jahnke, Phys. Rev. B **69**, 235314 (2004).
[11] W. Chow, A. Girndt, and S. Koch, Opt. Express **2**, 119 (1998).
[12] M. Hilpert, H. Klann, M. Hofmann, C. Ellmers, M. Oestreich, H. C. Schneider, F. Jahnke, S. W. Koch, W. W. Rühle, H. D. Wolf, D. Bernklau, and H. Riechert, Appl. Phys. Lett. **71**, 3761 (1997).
[13] M. van der Poel, E. Gehrig, O. Hess, D. Birkedal, and J. M. Hvam, IEEE J. Quantum Electron. **41**, 1115 (2005).
[14] G. Malpuech, A. Kavokin, A. Di Carlo, and J. J. Baumberg, Phys. Rev. B **65**, 153310 (2002).
[15] J. Shah, *Ultrafast Spectroscopy of Semiconductors and Semiconductor Nanostructures*, Springer Series in Solid-State Sciences (Springer, Berlin, Heidelberg, 2013).
[16] A. Honold, L. Schultheis, J. Kuhl, and C. W. Tu, Phys. Rev. B **40**, 6442 (1989).
[17] M. Koch, R. Hellmann, G. Bastian, J. Feldmann, E. O. Göbel, and P. Dawson, Phys. Rev. B **51**, 13887 (1995).
[18] R. Hellmann, M. Koch, J. Feldmann, S. T. Cundiff, E. O. Göbel, D. R. Yakovlev, A. Waag, and G. Landwehr, Phys. Rev. B **48**, 2847 (1993).
[19] A. Manassen, E. Cohen, A. Ron, E. Linder, and L. N. Pfeiffer, Phys. Rev. B **54**, 10609 (1996).
[20] V. Capozzi, L. Pavesi, and J. L. Staehli, Phys. Rev. B **47**, 6340 (1993).
[21] D. Huang, H. Y. Chu, Y. C. Chang, R. Houdré, and H. Morkoç, Phys. Rev. B **38**, 1246 (1988).
[22] G. Göger, M. Betz, A. Leitenstorfer, M. Bichler, W. Wegscheider, and G. Abstreiter, Phys. Rev. Lett. **84**, 5812 (2000).
[23] M. Betz, G. Göger, A. Leitenstorfer, M. Bichler, G. Abstreiter, and W. Wegscheider, Phys. Rev. B **65**, 085314 (2002).
[24] L. Schultheis, J. Kuhl, A. Honold, and C. W. Tu, Phys. Rev. Lett. **57**, 1635 (1986).
[25] R. C. C. Leite, J. Shah, and J. P. Gordon, Phys. Rev. Lett. **23**, 1332 (1969).
[26] W. Liu, D. Jiang, K. Luo, Y. Zhang, and X. Yang, Appl. Phys. Lett. **67**, 679 (1995).
[27] H. Wang, K. Ferrio, D. G. Steel, Y. Z. Hu, R. Binder, and S. W. Koch, Phys. Rev. Lett. **71**, 1261 (1993).
[28] D. R. Wake, H. W. Yoon, J. P. Wolfe, and H. Morkoç, Phys. Rev. B **46**, 13452 (1992).
[29] G. Ramon, A. Mann, and E. Cohen, Phys. Rev. B **67**, 045323 (2003).
[30] S. Elkomoss and G. Munschy, J. Phys. Chem. Solids **40**, 431 (1979).
[31] D. H. Auston, K. P. Cheung, J. A. Valdmanis, and D. A. Kleinman, Phys. Rev. Lett. **53**, 1555 (1984).
[32] P. R. Smith, D. H. Auston, and M. C. Nuss, IEEE J. Quantum Electron. **24**, 255 (1988).
[33] R. Sprik, I. N. Duling, C. Chi, and D. Grischkowsky, Appl. Phys. Lett. **51**, 548 (1987).
[34] B. I. Greene, J. F. Federici, D. R. Dykaar, A. F. J. Levi, and L. Pfeiffer, Opt. Lett. **16**, 48 (1991).
[35] R. Groeneveld and D. Grischkowsky, JOSA B **11**, 2502 (1994).
[36] R. Huber, F. Tauser, A. Brodschelm, M. Bichler, G. Abstreiter, and A. Leitenstorfer, Nature (London) **414**, 286 (2001).
[37] R. A. Kaindl, M. A. Carnahan, D. Hägele, R. Lövenich, and D. S. Chemla, Nature (London) **423**, 734 (2003).
[38] T. Suzuki and R. Shimano, Phys. Rev. Lett. **103**, 057401 (2009).

[39] M. Stein, C. Lammers, P.-H. Richter, C. Fuchs, W. Stolz, M. Koch, O. Vänskä, M. J. Weseloh, M. Kira, and S. W. Koch, Phys. Rev. B **97**, 125306 (2018).
[40] Q. Wu and X. Zhang, Appl. Phys. Lett. **67**, 3523 (1995).
[41] A. Nahata, A. S. Weling, and T. F. Heinz, Appl. Phys. Let. **69**, 2321 (1996).
[42] M. Stein, C. Lammers, P. Springer, P.-H. Richter, S. W. Koch, M. Koch, and M. Kira, Phys. Rev. B **95**, 155207 (2017).
[43] R. Ulbricht, E. Hendry, J. Shan, T. F. Heinz, and M. Bonn, Rev. Mod. Phys. **83**, 543 (2011).
[44] S. Elkomoss and G. Munschy, J. Phys. Chem. Solids **38**, 557 (1977).
[45] Y. Feng and H. N. Spector, Superlattices Microstruct. **3**, 459 (1987).
[46] P. Steinleitner, P. Merkl, P. Nagler, J. Mornhinweg, C. Schüller, T. Korn, A. Chernikov, and R. Huber, Nano Lett. **17**, 1455 (2017).
[47] P. Springer, S. W. Koch, and M. Kira, J. Opt. Soc. Am. B **33**, C30 (2016).
[48] M. Stein, C. Lammers, J. T. Steiner, P.-H. Richter, S. W. Koch, M. Koch, and M. Kira, J. Phys. B: At., Mol. Opt. Phys. **51**, 154001 (2018).
[49] D. Andrews and A. Demidov, *An Introduction to Laser Spectroscopy: Second Edition* (Springer US, New York, 2012).
[50] F. Sekiguchi and R. Shimano, Phys. Rev. B **91**, 155202 (2015).

Additional Publications

1. Gain spectroscopy of a type-II VECSEL chip

C. Lammers, **M. Stein**, C. Berger, C. Möller, C. Fuchs, A. Ruiz Perez, A. Rahimi-Iman, J. Hader, J. V. Moloney, W. Stolz, S. W. Koch, and M. Koch, Appl. Phys. Lett. 109, 232107 (2016)

Abstract

Using optical pump-white light probe spectroscopy, the gain dynamics is investigated for a vertical-external-cavity surface-emitting laser chip, which is based on a type-II heterostructure. The active region of the chip consists of a GaAs/(GaIn)As/Ga(AsSb)/(GaIn)As/GaAs multiple quantum well. For this structure, a fully microscopic theory predicts a modal room temperature gain at a wavelength of 1170 nm, which is confirmed by the experimental spectra. The results show a gain buildup on the type-II chip that is delayed relative to that of a type-I chip. This slower gain dynamics is attributed to a diminished cooling rate arising from the reduced electron-hole scattering.

DOI: 10.1063/1.4971333

URL: `https://doi.org/10.1063/1.4971333`

Gain spectroscopy of a type-II VECSEL chip

C. Lammers,[1,a)] M. Stein,[1] C. Berger,[1] C. Möller,[1] C. Fuchs,[1] A. Ruiz Perez,[2] A. Rahimi-Iman,[1] J. Hader,[3] J. V. Moloney,[3] W. Stolz,[1] S. W. Koch,[1] and M. Koch[1]
[1]*Department of Physics and Material Sciences Center, Philipps-Universität Marburg, Renthof 5, 35032 Marburg, Germany*
[2]*NAsP$_{III/V}$ GmbH, Hans-Meerwein-Straße, 35032 Marburg, Germany*
[3]*College of Optical Sciences, University of Arizona, 1630 E. University Blvd., Tucson, Arizona 85721, USA*

(Received 19 August 2016; accepted 16 November 2016; published online 8 December 2016)

Using optical pump–white light probe spectroscopy, the gain dynamics is investigated for a vertical-external-cavity surface-emitting laser chip, which is based on a type-II heterostructure. The active region of the chip consists of a GaAs/(GaIn)As/Ga(AsSb)/(GaIn)As/GaAs multiple quantum well. For this structure, a fully microscopic theory predicts a modal room temperature gain at a wavelength of 1170 nm, which is confirmed by the experimental spectra. The results show a gain buildup on the type-II chip that is delayed relative to that of a type-I chip. This slower gain dynamics is attributed to a diminished cooling rate arising from the reduced electron–hole scattering. *Published by AIP Publishing.* [http://dx.doi.org/10.1063/1.4971333]

Very recently, laser operation has been demonstrated in a type-II vertical-external-cavity surface-emitting laser (VECSEL).[1] The type-II design promises further wavelength flexibility in the infrared as well as reduced Auger losses.[2,3] This makes lasers with a type-II based gain medium promising for many applications, such as optical data transmission.[4]

Important aspects of the optical properties and carrier dynamics of type-II quantum film structures have been investigated already 25 years ago.[5–8] Recently, type-II semiconductor heterostructures with a "W"-type band alignment of the conduction band, spatially separating electron and hole confinement were found promising for laser applications, as reported in Refs. 9 and 10.

Up to date, both edge emitters and surface-emitting quantum well lasers based on type-II material systems have been demonstrated.[11,12] The gain properties of such structures are often characterized by stationary methods such as the Hakki–Paoli technique or the variable-stripe-length method.[13–16] Information on the gain dynamics associated with the carrier dynamics inside the laser medium can be obtained via ultrafast pump–probe experiments.[17–19]

Here, we use optical pump–white light probe spectroscopy to study the gain dynamics of a type-II "W"-VECSEL chip containing 10 × (GaIn)As/Ga(AsSb) "W"-multiple quantum wells. A fully microscopic theory predicts significant modal room temperature gain for this chip at a wavelength around 1170 nm. For comparison, we additionally study a conventional type-I chip. We find that the gain build up is delayed in the type-II structure, as compared to the type-I chip. We attribute this slower dynamics to a reduced carrier cooling rate in the type-II structure.

Our VECSEL chip was grown bottom-up on exact GaAs (001) (±0.1°) substrate in a horizontal AIXTRON AIX 200 Gas Foil Rotation (GFR) metal organic vapor phase epitaxy (MOVPE) reactor system. It consists of a lattice matched (GaIn)P capping layer, a resonant periodic gain (RPG) structure with 10 multi-quantum well heterostructures (MQWHs) and a distributed Bragg reflector (DBR) consisting of 22 1/2 pairs of (AlGa)As/AlAs. The MQWH consists of a "W"-shaped (GaIn)As/Ga(AsSb)/(GaIn)As type-II band alignment, which forms the active region, as can be seen in the inset of Fig. 1(b). The indirect transitions arise from electrons in the conduction band of the (GaIn)As quantum wells (QWs) and holes in the valence band of the Ga(AsSb) QW (dashed double arrows). At least three of them exist: the e1h1, e2h2, and e1h3 transitions, as can be seen in detail for a very similar structure in Ref. 10. The gain dynamics investigated here can be attributed to the e1h1 transition. The active regions are separated by the GaAs/Ga(AsP)/GaAs barriers. In order to obtain a resonant structure, the optical layer thicknesses of the barriers as well as the (GaIn)P capping layer were matched to $\lambda/2$ with respect to the lasing wavelength. The layer thicknesses and compositions of the active region were determined by fitting a fully dynamical simulation to the high-resolution X-ray diffraction (HR-XRD) ((004)-reflection) pattern of the chip structure. This analysis yields a $Ga(As_{1-x}Sb_x)$ ($x = 0.198$)

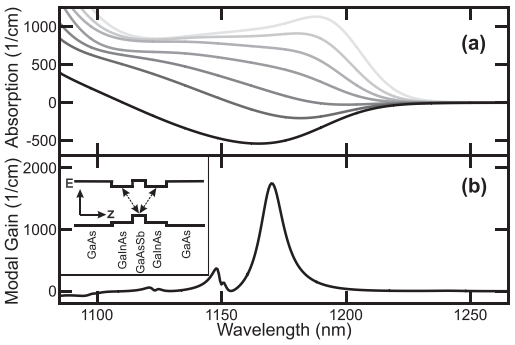

FIG. 1. Theoretical material absorption and modal gain. (a) Calculated material absorption for the active region of the type-II "W"-laser structure is presented for carrier densities ranging from $0.1 \times 10^{12}/cm^2$ up to $3 \times 10^{12}/cm^2$ (bright to dark). (b) A simulation of the modal gain for the full type-II VECSEL system is plotted for a carrier density of $3 \times 10^{12}/cm^2$. The inset schematically illustrates the band alignment of the type-II heterostructure. The dashed double arrows indicate the indirect radiative transitions.

[a)]Electronic mail: christian.lammers@physik.uni-marburg.de

layer thickness of 4.0 nm. The $(Ga_{1-y}In_y)As$ ($y = 0.203$) layer has a thickness of 5.5 nm.

In the following, we present calculations on the basis of the semiconductor Bloch equations (SBE) to predict the gain properties of this structure under optical excitation. In particular, we calculate the changes in absorption and refractive index for various carrier densities.[20–22] To achieve a sufficient level of accuracy in our calculations, we include all terms in the SBE up to the second Born level to take homogeneous broadening into account, i.e., intrinsic microscopic carrier scattering inside the semiconductor.[23,24] Unavoidable and common growth inhomogeneities in such MQWH samples are modeled by an inhomogeneous broadening, a convolution of our theoretical spectra with a Gaussian distribution describing the variation of the band gap energies.[25] Starting point for our calculations are the band structure and the corresponding wavefunctions. All these single-particle properties are accessed evaluating an 8×8 multi band $\mathbf{k} \cdot \mathbf{p}$ model.[23,26] We assume all carriers to be in thermal equilibrium and therefore Fermi distributed in their respective bands. Due to the type-II design, local charge inhomogeneities can arise. Consequently, we solve the Schrödinger–Poisson equation to obtain the changes to the confinement potential.[27] Based on the band structure and the single-particle wavefunctions, we compute the dipole and Coulomb matrix elements.[24]

Having modeled the absorption and refractive index changes induced by a given carrier density, we can derive the overall optical properties of the VECSEL structure. Reflection properties of the sample are calculated using the transfer-matrix method.[22,28] From the transfer-matrix calculations, we obtain a spectral filter function that describes the spatial overlap of the quantum well positions inside the RPG with the intensity maxima of the longitudinal light modes of the optical cavity.[29]

The numerical results for the material absorption of the "W"-type MQWH at 300 K are presented in Fig. 1(a). Here, we assumed an inhomogeneous broadening of 20 meV. As the carrier density is increased from $0.1 \times 10^{12}/cm^2$ up to $3 \times 10^{12}/cm^2$ (bright to dark), the excitonic absorption peak vanishes and the absorption becomes negative. The calculations show that a spectrally broad gain region is formed for this material composition in the RPG. We compute the modal gain for a carrier density of $3 \times 10^{12}/cm^2$, by multiplying the filter function (represented as dashed line in Fig. 2) with the gain of the RPG structure. Thereby, the broad material gain shown in Fig. 1(a) evolves into a narrow modal gain around 1170 nm. This is shown in Fig. 1(b).

Next, we compare the simulated reflectivity to an experimental spectrum in Fig. 2. Here, the measured spectrum plotted in the background of the diagram represents the system under unexcited conditions (yellow shaded area). A direct comparison between experiment and theory shows a good qualitative agreement. Using our theory as a predictive tool, we increase the carrier density up to $3 \times 10^{12}/cm^2$, which leads to the broad material gain, as observed in Fig. 1(a). Thereby, we observe a gradual increase in the reflectivity at the absorption dip in the stop band. Finally, the absorption dip evolves into a gain peak around 1170 nm.

For our optical pump–white light probe gain measurements, we use a 1 kHz, 5 mJ, 35 fs regenerative Ti:sapphire amplifier to acquire time-resolved differential reflectivity spectra. The amplifier drives an optical parametric amplifier (OPA) to provide spectrally tunable fs pump pulses and furthermore generates an fs supercontinuum that is used to probe the gain dynamics in the chip. The pump spot diameter is determined to 150 μm with a knife-edge measurement. An InGaAs-CCD cooled with liquid nitrogen is used as a detector in combination with a Czerny–Turner monochromator with an 80 l/mm diffraction grating as dispersive element. The excitation density of our pump pulse with a central wavelength of 1000 nm is set to $5.6 \times 10^{16}/cm^2$ in order to inject a sufficiently large amount of charge carriers. All experiments are carried out at room temperature. To obtain the gain spectra, the measured differential reflectivity spectra were added to the reflectivity measurements of the unexcited sample.

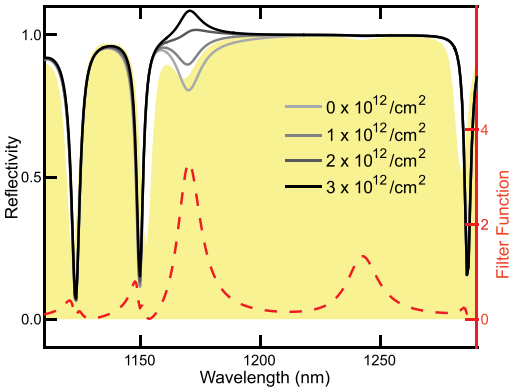

FIG. 2. Theoretical reflectivity (lines) of the type-II gain structure together with its calculated filter function (dashed line). Measured reflectance at room temperature for an unexcited chip is shown as yellow area in the background, while theoretical reflectivity spectra are presented for carrier densities between zero and $3 \times 10^{12}/cm^2$ (solid lines, bright to dark). Again, the system temperature is set to 300 K with an inhomogeneous broadening of 20 meV.

Examples of the reflectivity spectra obtained for different times after the excitation pulse are shown in Fig. 3. For the unexcited sample, one clearly observes the dip in reflection at

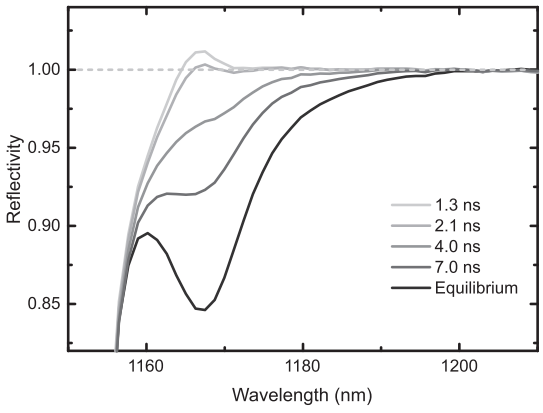

FIG. 3. Experimental reflectivity spectra of a type-II chip for pump–probe time delays between 1.3 and 7.0 ns (solid lines, bright to dark). The maximum gain is reached 1.3 ns after excitation. The equilibrium situation corresponds to the reflectivity measured by the probe pulse without excitation.

1168 nm, which was predicted by theory. It is governed by an interplay of material absorption with the filter function for the employed material and structure, as indicated in Fig. 1. After excitation and carrier relaxation, the sample shows gain, i.e., the reflectivity exceeds one. The gain reaches its maximum after 1.3 ns. It peaks at 1168 nm and has a spectral width of 6 nm. The gain lasts for several hundred picoseconds. At 2.1 ns, it is barely noticeable. Thereafter, i.e., for larger delay times, the reflectivity in this spectral region is below one and gradually reduces.

The black curve in Fig. 4 shows the measured gain dynamics of the type-II chip. To obtain this curve, a region of 1.2 nm width around 1168 nm was spectrally integrated. The gain evolves after 600 ps, reaches its maximum after 1.3 ns and vanishes at 2.1 ns after the optical excitation. For comparison, the same measurements were performed on a type-I VECSEL, exploiting spatially direct transitions. The respective chip, which emits at 1101 nm, has an RPG comprising 10 $(Ga_{0.71}In_{0.29})As$ QWs with a thickness of 5 nm in between GaAs barriers. Again, the filter function is positioned at the edge of the stop band. Hence, all in all one has a similar arrangement as for the type-II VECSEL chip. The grey curve in Fig. 4 shows the gain dynamics of this chip. Once more, we spectrally integrate over a window of 1.2 nm around the gain maximum. In this case, the gain appears at 150 ps and lasts for 1.1 ns. By fitting exponential functions to the decreasing reflectivity, we retrieve charge-carrier lifetimes for both VECSEL structures. These lifetimes amount to 3.3 ns and 7.3 ns for the type-I and type-II chip, respectively. Although the type-I structure produces a higher peak value of 1.016, the time span of gain provided by the material system lasts longer for the type-II structure. As mentioned above, this can be seen as a direct effect of the spatial separation of charge carriers in type-II MQWHs, which exhibit a reduced recombination rate. Hence, high charge-carrier densities, which are a prerequisite for gain, are conserved for a longer period of time in comparison to a type-I heterostructure. It is reasonable to assume that a lower radiative recombination rate in a type-II structure can be a limiting factor with regard to the maximum amount of gain.

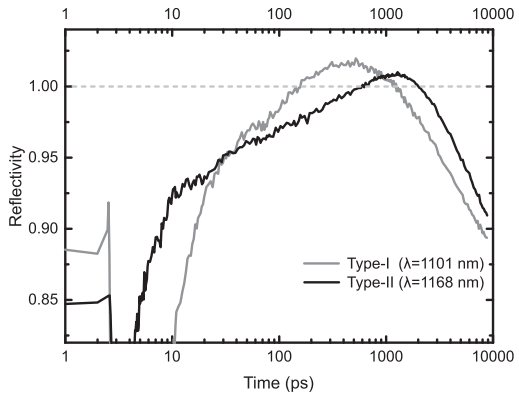

FIG. 4. Semilogarithmic plot showing the gain dynamics of the type-II "W"-VECSEL chip (black line) in comparison to a conventional type-I chip (grey line). For this plot, an offset of 2 ps was applied to the time axis in order to enable a logarithmic illustration.

Nonetheless, reducing the band gap energy in conventional type-I structures leads to an increase in non-radiative losses. Especially, by pushing the wavelength further to the telecom regime, type-II structures might overcome the performance of traditional type-I structures. In general, lowering band gap energies increases potential barrier heights, consequently reducing the overlap of electron and hole wavefunctions in a type-II alignment. However, for increasing carrier densities, band bending effects restore the overlap of the wavefunctions, thus maintaining or even increasing the gain. The slower gain build up in the type-II chip is attributed to a reduced carrier equilibration rate arising from the following situation: after optical excitation, depending on their excess energies, electron and hole distributions emit optical phonons and cool down. The cooling rates for electrons and holes are typically not identical and differ from material to material. Yet, in a type-I sample, electrons and holes can efficiently exchange energy via Coulomb scattering and, hence, the electron and hole distributions have a route to rapidly equilibrate among each other. If the electron distribution cools slower, it can profit from a hole distribution that cools faster—and vice versa. In a type-II sample, electron-hole scattering is significantly diminished due to the reduced spatial overlap of electrons and holes. Hence, it takes more time until a thermal equilibrium among the two distributions is achieved. Yet, a microscopic calculation of this effect for the multi-layer structure studied is beyond the scope of this paper.

In conclusion, we have investigated the gain dynamics of a type-II VECSEL chip using optical pump–white light probe spectroscopy. Experimental gain spectra agree well with a fully microscopic theory. We observe a slower buildup of the modal gain for the type-II chip when compared to a type-I structure. We attribute this to a smaller carrier cooling rate in the type-II chip arising from a reduced electron-hole scattering rate. The smaller scattering rate results from the reduced spatial overlap of electrons' and holes' wave functions in the type-II design. Owing to the fact that a type-II chip can be employed in VECSELs and that the design allows for more wavelength flexibility compared to type-I structures, further efforts will be done in the upcoming investigations in order to optimize the MQWH design with respect to gain and laser output. Recently, similar structures have been grown showing photoluminescence emission up to 1470 nm.[30] Thereby, type-II VECSELs may push available emission wavelengths further to the highly desired telecom wavelengths.

The authors from Marburg acknowledge the financial support from the Deutsche Forschungsgemeinschaft via the Collaborative Research Center 1083 (DFG:SFB1083). The authors from Arizona are supported by the AFOSR Grant No. FA9550-14-1-0062.

[1]C. Möller, C. Fuchs, C. Berger, A. Ruiz Perez, M. Koch, J. Hader, J. V. Moloney, S. W. Koch, and W. Stolz, Appl. Phys. Lett. **108**, 071102 (2016).
[2]W. W. Bewley, J. R. Lindle, C. S. Kim, M. Kim, C. L. Canedy, I. Vurgaftman, and J. R. Meyer, Appl. Phys. Lett. **93**, 041118 (2008).
[3]J. R. Meyer, C. L. Felix, W. W. Bewley, I. Vurgaftman, E. H. Aifer, L. J. Olafsen, J. R. Lindle, C. A. Hoffman, M. J. Yang, B. R. Bennett,

B. V. Shanabrook, H. Lee, C. H. Lin, S. S. Pei, and R. H. Miles, Appl. Phys. Lett. **73**, 2857 (1998).
[4]E. Murphy, Nat. Photonics **4**, 287 (2010).
[5]K. Meissner, B. Fluegel, R. Binder, S. W. Koch, G. Khitrova, and N. Peygambarian, Appl. Phys. Lett. **59**, 259 (1991).
[6]R. Binder, I. Galbraith, and S. W. Koch, Phys. Rev. B **44**, 3031 (1991).
[7]I. Galbraith, P. Dawson, and C. T. Foxon, Phys. Rev. B **45**, 13499 (1992).
[8]J. Feldmann, R. Sattmann, E. O. Göbel, J. Kuhl, J. Hebling, K. Ploog, R. Muralidharan, P. Dawson, and C. T. Foxon, Phys. Rev. Lett. **62**, 1892 (1989).
[9]C. Berger, C. Möller, P. Hens, C. Fuchs, W. Stolz, S. W. Koch, A. Ruiz Perez, J. Hader, and J. V. Moloney, AIP Adv. **5**, 047105 (2015).
[10]S. Gies, C. Kruska, C. Berger, P. Hens, C. Fuchs, A. Ruiz Perez, N. W. Rosemann, J. Veletas, S. Chatterjee, W. Stolz, S. W. Koch, J. Hader, J. V. Moloney, and W. Heimbrodt, Appl. Phys. Lett. **107**, 182104 (2015).
[11]J. F. Klem, O. Blum, S. R. Kurtz, I. J. Fritz, and K. D. Choquette, J. Vac. Sci. Technol. **18**, 1605 (2000).
[12]J. Meyer, L. Olafsen, E. Aifer, W. Bewley, C. Felix, V. Vurgaftman, M. Yang, L. Goldberg, D. Zhang, C.-H. Lin, S. Pei, and D. Chow, IEE Proc.—Optoelectron. **145**, 275 (1998).
[13]B. W. Hakki, J. Appl. Phys. **44**, 4113 (1973).
[14]L. Shterengas, R. Liang, G. Kipshidze, T. Hosoda, S. Suchalkin, and G. Belenky, Appl. Phys. Lett. **103**, 121108 (2013).
[15]K. L. Shaklee, R. E. Nahory, and R. F. Leheny, JOL **7**, 284 (1973).
[16]N. Kirstaedter, O. G. Schmidt, N. N. Ledentsov, D. Bimberg, V. M. Ustinov, A. Y. Egorov, A. E. Zhukov, M. V. Maximov, P. S. Kop'ev, and Z. I. Alferov, Appl. Phys. Lett. **69**, 1226 (1996).
[17]K. L. Hall, J. Mark, E. P. Ippen, and G. Eisenstein, Appl. Phys. Lett. **56**, 1740 (1990).
[18]H. Giessen, U. Woggon, B. Fluegel, G. Mohs, Y. Z. Hu, S. W. Koch, and N. Peyghambarian, Opt. Lett. **21**, 1043 (1996).
[19]C. Lange, S. Chatterjee, C. Schlichenmaier, A. Thränhardt, S. W. Koch, W. W. Rühle, J. Hader, J. V. Moloney, G. Khitrova, and H. M. Gibbs, Appl. Phys. Lett. **90**, 251102 (2007).
[20]M. Lindberg and S. W. Koch, Phys. Rev. B **38**, 3342 (1988).
[21]H. Haug and S. W. Koch, *Quantum Theory of the Optical and Electronic Properties of Semiconductors*, 5th ed. (World Scientific Publication, Singapore, 2009).
[22]M. Kira and S. W. Koch, *Semiconductor Quantum Optics* (Cambridge University Press, Cambridge, 2012).
[23]W. W. Chow and S. W. Koch, *Semiconductor-Laser Fundamentals: Physics of the Gain Materials* (Springer, Berlin, Heidelberg/New York, 1999).
[24]J. Hader, S. W. Koch, and J. V. Moloney, Solid-State Electron. **47**, 513 (2003).
[25]J. Hader, J. V. Moloney, S. W. Koch, and W. W. Chow, IEEE J. Sel. Top. Quantum Electron. **9**, 688 (2003).
[26]J. Hader, N. Linder, and G. H. Döhler, Phys. Rev. B **55**, 6960 (1997).
[27]D. Ahn and S. L. Chuang, J. Appl. Phys. **64**, 6143 (1988).
[28]M. Born and E. Wolf, *Principles of Optics*, 7th ed., Electromagnetic Theory of Propagation, Interference and Diffraction of Light (Cambridge University Press, Cambridge, 1999).
[29]M. Schafer, W. Hoyer, M. Kira, S. W. Koch, and J. V. Moloney, J. Opt. Soc. Am. B **25**, 187 (2008).
[30]C. Fuchs, A. Beyer, K. Volz, and W. Stolz, "MOVPE growth of (GaIn)As/Ga(AsSb)/(GaIn)As type-II heterostructures on GaAs substrate for near infrared laser applications" J. Cryst. Growth (in press).

2. Correlation of optical properties and interface morphology in type-II semiconductor heterostructures

L. Rost, S. Gies, **M. Stein**, C. Fuchs, S. Nau, P. Kükelhan, K. Volz, W. Stolz, M. Koch, and W. Heimbrodt, J. Phys.: Condens. Matter 31 014001 (2018)

Abstract

(Ga,In)As/GaAs/Ga(As,Sb) and (Ga,In)As/GaAs/Ga(N,As) type-II double quantum well heterostructures have been grown by metal-organic vapor phase epitaxy. A growth interruption procedure was used to intentionally modify the morphology of the internal interfaces. The heterostructures were investigated using continuous wave and time-resolved photoluminescence as well as optical pump-optical probe spectroscopy. We find a correlation between the interface morphology and optical and kinetic properties. A growth interruption of about 120 s yielded substantially smoother interfaces both on vertical as well as lateral length scales. On the other hand a considerably enhanced type-II recombination time as well as a longer electron tunneling time are observed. We attribute this to a reduced interface localization in case of smoother interfaces.

DOI: 10.1088/1361-648X/aaee93
URL: https://doi.org/10.1088%2F1361-648x%2Faaee93

IOP Publishing Journal of Physics: Condensed Matter
J. Phys.: Condens. Matter **31** (2019) 014001 (7pp) https://doi.org/10.1088/1361-648X/aaee93

Correlation of optical properties and interface morphology in type-II semiconductor heterostructures

Luise Rost[1], Sebastian Gies[1], Markus Stein[1], Christian Fuchs[1], Siegfried Nau[2], Pirmin Kükelhan[1], Kerstin Volz[1], Wolfgang Stolz[1], Martin Koch[1] and Wolfram Heimbrodt[1,3]

[1] Department of Physics and Material Sciences Center, Philipps-Universität Marburg, Renthof 5, 35032 Marburg, Germany
[2] Fraunhofer Institute for High-Speed Dynamics, Ernst-Mach-Institute, Am Klingelberg 1, 79588 Efringen-Kirchen, Germany

E-mail: Wolfram.Heimbrodt@physik.uni-marburg.de

Received 29 August 2018, revised 22 October 2018
Accepted for publication 6 November 2018
Published 30 November 2018

Abstract

(Ga,In)As/GaAs/Ga(As,Sb) and (Ga,In)As/GaAs/Ga(N,As) type-II double quantum well heterostructures have been grown by metal-organic vapor phase epitaxy. A growth interruption procedure was used to intentionally modify the morphology of the internal interfaces. The heterostructures were investigated using continuous wave and time-resolved photoluminescence as well as optical pump–optical probe spectroscopy. We find a correlation between the interface morphology and optical and kinetic properties. A growth interruption of about 120 s yielded substantially smoother interfaces both on vertical as well as lateral length scales. On the other hand a considerably enhanced type-II recombination time as well as a longer electron tunneling time are observed. We attribute this to a reduced interface localization in case of smoother interfaces.

Keywords: III–V semiconductors, type-II DQWs, time resolved PL, optical pump–optical probe measurements, internal interfaces

(Some figures may appear in colour only in the online journal)

Introduction

Infra-red semiconductor lasers for long-range optical communication using optical fibers are still a highly topical field as the quantum efficiency of the respective III–V laser materials is often limited by non-radiative processes. One of the most dominant processes is Auger recombination [1–4]. A strategy to overcome this issue is the use of type-II devices, where the recombining electrons and holes are spatially separated [5–7]. Additionally, such systems offer more degrees of freedom for device design as the band edges of the electron and the hole confining wells can be varied independently allowing for a wide tuning of the type-II transition energy. A promising heterostructure design for such applications are so called W-laser structures which enable the optimization of the wave function overlap by adding barrier layers to confine carriers [5, 8–10]. With the continuing progress of device miniaturization in mind, the properties of the internal interfaces are getting more and more important [11]. Interfaces (IF) are inevitably connected with lattice imperfections which may act as carrier localization centers, traps and/or non-radiative loss centers. Even though IFs are present in any (type-I or type-II) device there is little to no information on the influence of internal IFs on the optical properties of devices [12]. The aim of the present paper is to study the influence of a morphology change by growth interruptions on the optical properties of charge transfer (CT) processes. We will investigate two different material systems having a type-II band

[3] Present address: Department of Physics and Material Sciences Center, Philipps-Universität Marburg, Renthof 5, 35037 Marburg, Germany

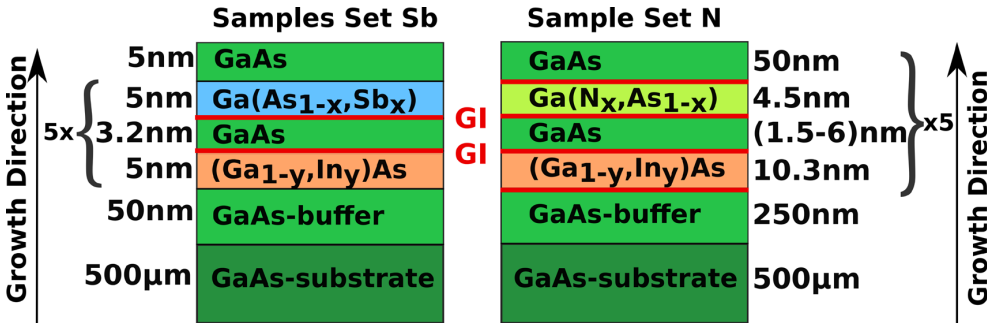

Figure 1. Sample structure of the sample set **Sb** (left) (Ga,In)As/Ga(As,Sb) and sample set **N** (right) (Ga,In)As/Ga(N,As)-based type-II heterostructures.

alignment, namely (Ga,In)As/Ga(N,As) and (Ga,In)As/Ga(As,Sb). Each series of samples was grown on GaAs substrate using nearly the same growth conditions. Therefore, we are able to perform a thorough investigation and correlate the optical properties to the IF morphology. We investigate not only the continuous wave photoluminescence (cw-PL) and time resolved photoluminescence (TRPL) but also optical pump–optical probe (OPOP) measurements under cross-linear-polarized excitation.

Table 1. Measured In, Sb and N concentrations of the investigated MQWHs. The error-bars for the given compositions are $\pm 1\%$ for each material.

Samples	$y_{In}(\%)$	$x_{Sb}(\%)$	$x_N(\%)$
N no GI	23.5	—	5.0
N with 120 s GI	24.5	—	5.0
Sb no GI	19.8	22.7	—
Sb GI (Ga,In)As–GaAs	19.8	23.0	—
Sb GI GaAs–Ga(As,Sb)	19.7	22.9	—

Experimental

The samples were grown in a commercial AIXTRON AIX 200 GFR (gas foil rotation) metal organic vapor phase epitaxy (MOVPE) reactor system. The group-III precursors triethylgallium and trimethylindium were used in combination with unsymmetrical dimethylhydrazine, triethylantimony and the arsenic precursor tertiarybutylarsine (TBAs) for the epitaxial growth. The reactor pressure was set to 50 mbar with H_2 as carrier gas. A TBAs-stabilized bake-out procedure was applied in order to remove the native oxide layer from the GaAs (001) ($\pm 0.15°$) substrate surface.

A schematic picture of the sample structures is given in figure 1. The active region of sample set **N** investigated in this study consists of a 10.3 nm-thick (Ga,In)As quantum well (QW), a GaAs intermediate layer of 1.5 nm, 4 nm or 6 nm, and a 4.5 nm-thick Ga(N,As) QW. The resulting double QW (DQW) was arranged as a 5× DQW-heterostructure separated by 50 nm thick GaAs barriers. The growth temperature was chosen to be 525 °C. For some samples in set **N** the IF modification was introduced by a growth interruption (GI) for 120 s on different positions between the GaAs barrier and the active QWs. The initial partial pressure was held constant over 120 s. The positions of the GIs are depicted in red in figure 1. For comparison a sample was grown without a GI.

The active region of sample set **Sb** consists of a 5× DQW heterostructure again and the growth was carried out at 550 °C. Each DQW is composed of a 5.2 nm thick $(Ga_y, In_{1-y})As$ layer which is followed by a GaAs interlayer of 3.2 nm thickness. The active region is completed by a second 5.0 nm thick quantum well consisting of $Ga(As_{1-x},Sb_x)$ which is followed by a 50 nm thick GaAs barrier. In sample series **Sb** only one IF was modified by a GI, either the IF prior to the GaAs barrier growth or after the growth of the inner barrier, which results in three samples in this series.

The MQWHs are characterized using high resolution x-ray diffraction [5, 13]. The determined In, Sb and N concentrations are summarized in table 1.

The cw-PL spectra were measured using a liquid nitrogen cooled Ge-detector and a 0.25 m grating spectrometer. A frequency-doubled Nd:YAG laser at 532 nm provided the light for the excitation of the samples. The time-resolved PL measurements were performed using a frequency-doubled Nd:YAG at 532 nm and a repetition rate of 10 Hz. The PL was detected using a 0.25 m grating spectrometer and a thermoelectrically cooled (In,Ga)(As,P)/InP photomultiplier. Due to the duration of the laser pulses the time-resolution of our setup is 4 ns.

For the OPOP measurements we used the output of a 1 kHz Ti:sapphire regenerative amplifier system that provides 35 fs long pulses at a central wavelength of 800 nm. The output of the amplifier was split into two parts. One part was tuned to a central energy of 1.34 eV by an optical parametric amplifier and optically excites the sample. The other part experienced a variable delay before it created a white-light supercontinuum via self phase modulation in a sapphire crystal that probed the sample. The transmitted white-light was then detected by a liquid nitrogen cooled spectrometer with a spectral resolution of 1 nm.

We used a highly selective etching procedure to get an image of the interface and to compare the changes with and without growth interruption. Therefore, a GaAs layer has been grown at 525 °C capped with a chemically sufficiently different layer of AlAs. Afterwards, one can wet chemically remove the capping layer. Hydrofluoric acid removes the AlAs layer without effecting the GaAs layer. Hence, an analysis of

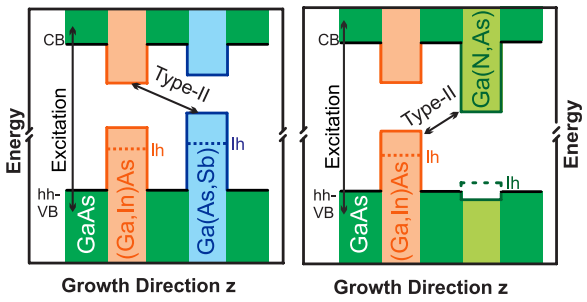

Figure 2. Schematic depiction of the band structure of the two material systems. The solid arrows indicate type-II transitions. Heavy hole and light hole are shown with fine and dotted lines.

the surface as it was grown by means of atomic force microscopy (AFM) is possible [14].

Results and discussion

The influence of the thickness of the internal GaAs barrier on the photoluminescence (PL) spectra was studied earlier for both the (Ga,In)As/GaAs/Ga(N,As) and (Ga,In)As/GaAs/Ga(As,Sb) material systems, respectively [15, 16]. For both type-II systems the CT PL increases strongly with decreasing inner barrier thickness in comparison to the emission of the direct excitons. This increasing PL intensity is accompanied by a decreasing CT exciton lifetime due to the enhanced transition probability.

In figure 2 the bandstructure for both heterosystems are depicted schematically. The arrows indicate the CT transitions. It can be seen that the type-II PL is realized in two different ways.

In the heterosystem (Ga,In)As/GaAs/Ga(N,As), right side in figure 2, the holes are localized in the (Ga,In)As well and the electrons in the Ga(N,As) well. The strong shift of the conduction band to low energies is well known for Ga(N,As) and is caused by the strong interaction of the localized N states with the conduction band edge [17]. The type-I to type-II transition for (Ga,In)As/Ga(N,As) was found already at about 1% N in case of about 20% In [18, 19]. Exactly the opposite happens in the (Ga,In)As/GaAs/Ga(As,Sb) heterosystem. Here the electrons are localized in the (Ga,In)As well and the holes are in the Ga(As,Sb) well [5, 20]. The type-II transition can be tuned to lower transition energies in these DQWs due to the strong valence band shift with higher Sb concentrations [21, 22].

In the following we want to study the influence of modified interfaces on the CT recombination. It is generally assumed, that a growth interruption improves the smoothness of a surface growth [14, 23, 24]. We used growth interruptions for both interfaces of the inner GaAs barrier during the MOVPE growth of our structures. To get information about the respective changes at the buried interfaces a selective etching process was applied to set free the GaAs surface. In figure 3 the AFM images of a GaAs interface without (a) and with a 120 s growth interruption (b) are given as a typical example, since we found the same behavior for the GaAs and GaInAs interfaces [23]. The resolution was one atomic layer

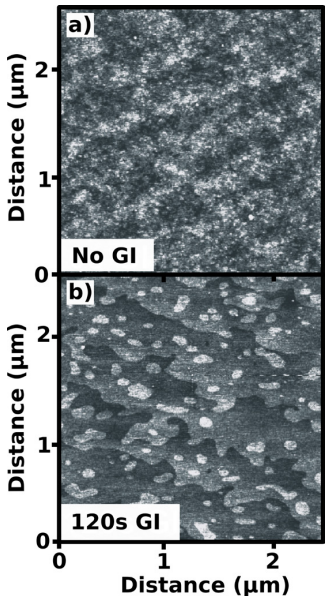

Figure 3. AFM images of a GaAs interface grown at 525 °C (a) without growth interruption, (b) with 120 s growth interruption. Each step in the grey-code between black and white reflects one monolayer yielding a total height of 6 monolayers. Reproduced with permission from [23].

perpendicularly to the surface and about 10 nm in lateral direction. It can be seen, that the growth interruption actually leads to the formation of big, smooth islands. The maximum height difference in the AFM-micrograph of the continuously grown sample amounts to a value of about 6 monolayers by careful line scan-analysis on lateral length scales of about 500 nm to 1 μm. This is the relevant length scale for optical experiments. In the sample with the applied growth interruption on the same lateral length scale the maximum height difference amounts to only 2–3 monolayers. In addition to this reduction in interface modulation the island size is substantially increased due to the growth interruption. Without growth interruption the mean size is about 30 nm and increases to about 150 nm for the 120 s growth interruption.

It should be mentioned at this point, that we also studied the interface configuration of our samples applying high-angle annular dark-field scanning transmission electron microscopy using an aberration-corrected microscope [25, 26]. The results of this true atomically resolved technique for individual group-III- as well as group-V-columns in combination with sophisticated modelling are summarized in a separate paper in this special issue [27]. It is important to note, however, that the optical properties as studied in this paper are primarily correlated to the lateral interface morphology as quantified by the AFM-technique since the excitons experience a mean value of the potential fluctuations caused by the individual atoms.

It is justified to assume the same island growth for the interfaces which underwent the GI in our samples for the optical studies. To correlate the structural changes with the optical properties we investigated the cw-PL. In figure 4 the PL spectra taken at $T = 10$ K are depicted for the (Ga,In)As/

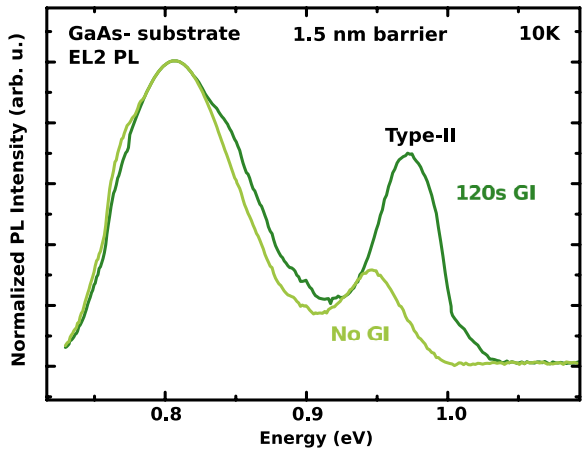

Figure 4. Low temperature photoluminescence of the (Ga,In)As/GaAs/Ga(N,As) heterostructure with growth interruptions at both inner interfaces (light green) and without growth interruption (dark green) at $T = 10$ K.

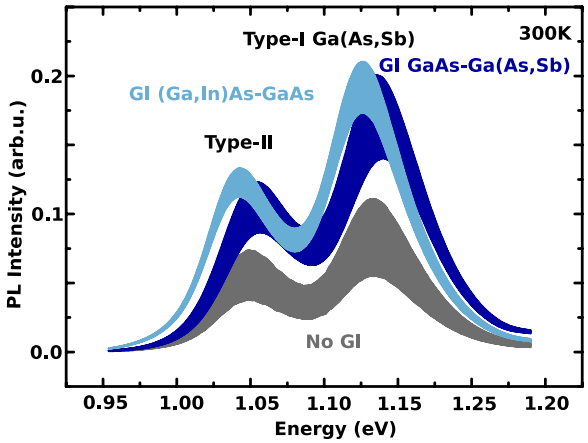

Figure 5. Mean photoluminescence of the (Ga,In)As/GaAs/Ga(As,Sb) heterostructures taken at six different spatial positions.

GaAs/Ga(N,As) DQWs with GI of 120 s and without GI. The spectra are normalized to the EL2 PL emission band. The EL2 PL band originates from the semi-insulating GaAs substrate [28] and can be used as reference to compare the type-II emission. It is obvious that the type-II PL is substantially stronger for the sample with growth interruption. This is a first hint that the growth interruption with the respectively smoother interfaces reduces the number of defects and traps at the interface which can act as losses for the type-II photoluminescence.

In figure 5 the PL spectra are depicted for a (Ga,In)As/GaAs/Ga(As,Sb)-DQW. To answer the question of which of the improved inner interfaces contributes more to the PL enhancement, the GI was applied solely to one or the other inner interface. It should be mentioned, that the PL intensity varies slightly across these samples. Therefore, six different spatial positions on each sample were measured. The shaded area in figure 5 represents the intensity variation between the different positions. The thickness of the inner GaAs barrier was 3.5 nm. The laser excitation energy was above the barrier bandgap energy. Therefore, as discussed in detail in an earlier paper [16, 20], besides the type-II PL the spatially direct exciton of the Ga(As,Sb) can be observed at room temperature as well.

As can be seen in figure 2, the energetically most favorable states for the electrons are in the conduction band of the (Ga,In)As well and for the holes in the Ga(As,Sb) well. Indeed, this transition dominates the spectrum at low temperatures and the Ga(As,Sb) luminescence cannot be observed at 10 K because the electrons tunnel on a timescale faster than the exciton recombination time in Ga(As,Sb). The Ga(As,Sb) emission starts to occur, however, at higher temperatures due to the fact that electrons can occupy higher electronic states by thermal excitation and can return this way to the Ga(As,Sb) QW [16].

Let us now turn to the influence of the growth interruption. As can be seen in figure 5, the GI on either side of the inner barrier enhances the PL intensity at least by a factor of two (blue curves) compared to the sample without a GI. Obviously, loss channels for the type-II recombination exist at the inner IF of the electron well as well as at the IF of the hole well.

It is interesting to note that the type-I transition in the Ga(As,Sb) well is enhanced as well. This seems logical when the GI is applied to the GaAs surface prior to the Ga(As,Sb) growth. But why does this also happen by a GI at the other side of the barrier, i.e. smoothening the (Ga,In)As surface? We attribute this to a flat (Ga,In)As surface, which enables a better 2D growth of the subsequent GaAs barrier and, therefore, also improves the GaAs surface prior to the growth of the Ga(As,Sb) well.

Now, we want to discuss the influence of the smoother interfaces on the dynamics of carriers and excitons. To study the carrier dynamics we performed optical pump-optical probe measurements at 10 K. At an excitation energy of 1.34 eV we create charge carriers in the (Ga,In)As QWs energetically above the 1s-exciton resonance. After optical excitation we observe a bleaching of the excitonic 1s resonance which results in a negative differential absorption. In figure 6 the differential absorption is spectrally integrated over the peak of the excitonic 1s resonance and the time dependence of the differential absorption is depicted for the (Ga,In)As/GaAs/Ga(N,As) samples with inner barrier thicknesses of 6 nm. Here, we compare the time dependence of the differential absorption for the sample with (dark green) and without GI (light green).

To allow a logarithmic plot the temporal overlap of pump and probe is set to 3 ps. At 3 ps, the temporal overlap of pump and probe causes a coherence peak [29]. The following loss of the temporal overlap of pump and probe leads to a rapid recovery of the signal within the first few hundred femtoseconds. Afterwards the cooling of the excited charge carrier population first decreases the differential absorption on a picosecond timescale as can be seen in figure 6 [29–31]. The cooling of the charge carriers is then superimposed by the electron transfer through the barrier from the (Ga,In)As to the Ga(N,As) which takes place within tens of picoseconds. Due to the electron transfer the differential absorption recovers [32, 33].

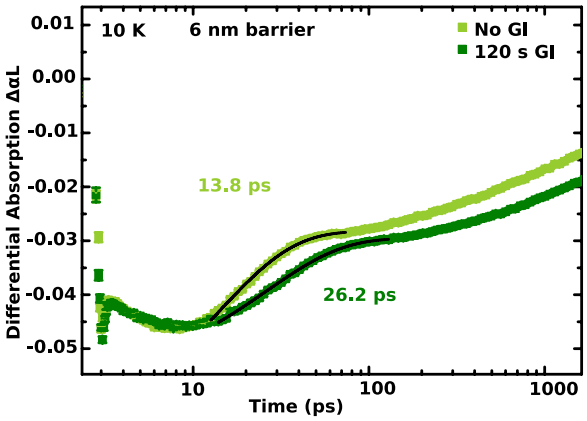

Figure 6. Differential absorption of sample set **N** with a 6 nm barrier at 10 K. The black lines indicate the mono-exponential fit for the transfer time of the electrons through the barrier.

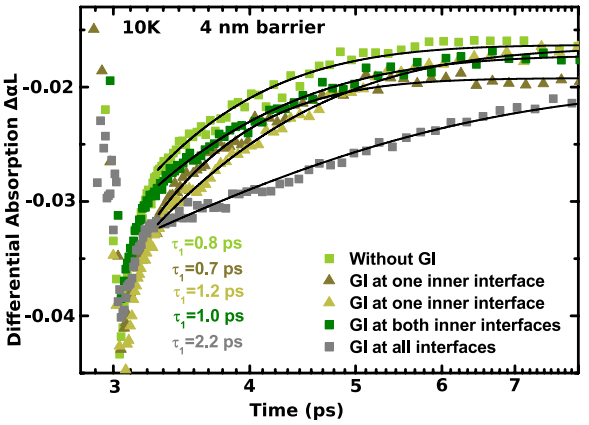

Figure 7. Differential absorption of the sample set **N** with 4 nm barrier at 10 K. The black lines indicate the mono-exponential fit for the transfer times of the electrons through the barrier.

An exponential fit (black lines) yields a 13.8 ps transfer time of the electrons trough the barrier when no GI is present and a 26.2 ps transfer time with GI. Interestingly, the GI slows the electron transfer by almost a factor of 2.

The same measurements are performed for a similar series of (Ga,In)As/GaAs/Ga(N,As) samples but with an internal barrier thickness of 4 nm. Here, after the coherence peak, we observe a charge carrier transfer within the first few picoseconds (see figure 7 for data points and transfer times). The much faster carrier transfer compared to the other set of samples is caused by the thinner inner barrier [34].This set of samples contains samples without any GI, with a GI at one of the two inner interfaces, with GIs at both inner interfaces and with GI at all four interfaces of the double quantum well heterostructure. This allows us to once again compare the transfer time of the sample without any GI with the transfer times of the samples with GI. For the sample without growth interruption we find a transfer time of 0.8 ps. Three of the four samples with GIs show significant longer transfer times of 1.2 ps, 1.0 ps and 2.2 ps as shown in figure 7. However, the sample with the GI at the (Ga,In)As/GaAs interface has a slightly shorter transfer time of 0.7 ps. Since the thickness of the inner barrier is a crucial parameter for the observed transfer times [34], slight sample to sample fluctuations in the growth process have a large impact on the results. Therefore, it is quite possible that a slightly lower barrier thickness leads to the shorter transfer time of the sample with the GI at the (Ga,In)As/GaAs interface.

Accordingly, it is, of course, also possible that a slightly greater barrier thickness of all other samples with GIs leads to a higher transfer time in these samples. However, since three out of four samples with GIs for the sample set with the 4 nm inner barrier and the sample with a GI for the sample set with the 6 nm inner barrier have a significantly longer transfer time than their respective reference sample without GI, we are confident that a longer transfer time is a property of a GI at the inner interface.

Finally, the differential absorption recovers on a nanosecond timescale for both sets of samples. This is a typical recombination time for the type-I transition also for the type-II-transition due to the recombination of the spatially separated charge carriers through the barrier [35].

To reveal the influence of smoother interfaces on the electron hole recombination through the GaAs barrier we performed time resolved PL analysis of the type-II transition at the **Sb** sample set. In figure 8 the transients are depicted for the type-II PL of the (Ga,In)As/GaAs/Ga(As,Sb) heterostructures at room temperature. These were measured at the maximum of the type-II PL band and are normalized to unity. The decay exhibits an exponential behavior. All lifetimes are in the ns range which is typical for type-II transitions [16]. For the sample without GI we find an e^{-1} decay time of $\tau_{3.5\ \mathrm{nm}} = 8$ ns. For both samples with GI the radiative lifetimes increase to 12 ns. Recently, we studied the temperature dependence of the type-II transient in (Ga,In)As/GaAs/Ga(As,Sb) heterostructures and found a surprising behavior [16]. At temperatures above 70 K the PL decay of the type-II recombination is mono-exponential. At 70 K and below the shape of the transients changes drastically, since a slow relaxation mechanism comes into play. This behavior was analyzed in the framework of a rate-equation model. The temporal evolution of the type-II PL with an initial fast decay followed by an additional intensity increase and a slow decay at the end could be explained taking the carrier tunneling, a slow relaxation mechanism and the type-II recombination into account. We ascribed the slow relaxation to a hopping process of the holes in the Ga(As,Sb) well between energetically lower lying states with relatively low hopping probabilities. This explained the respective long feeding times of the type-II PL [16].

We assume the slow relaxation process to be correlated with disorder effects at the interface. Therefore, we measured the decay of the type-II PL at low temperature. The curves are taken again at the maximum of the type-II PL. The PL spectra at 10 K are given in the inset of figure 9. As mentioned above only the type-II PL can be seen. In figure 9 the transients are depicted for the type-II PL of the (Ga,In)As/GaAs/Ga(As,Sb) heterostructures at 10 K. All transients consists of three parts: (i) an initially fast decay followed by (ii) a rise of the curve.

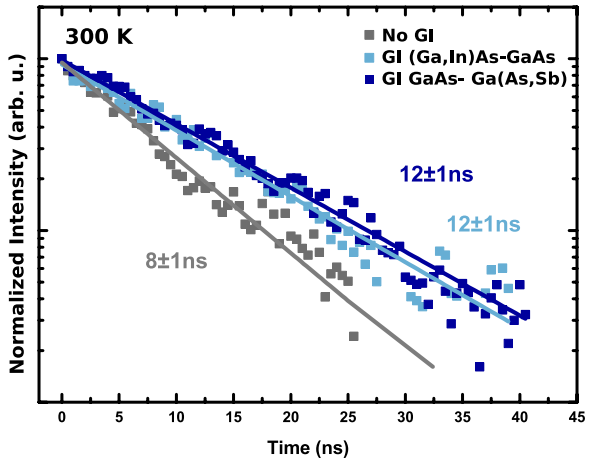

Figure 8. Room-temperature decay curves of the type-II PL for the sample set **Sb** with and without GI. The curves were normalized to unity and were taken at the maximum of the type II peak. The solid curves are the fitted transients obtained by a mono-exponential decay.

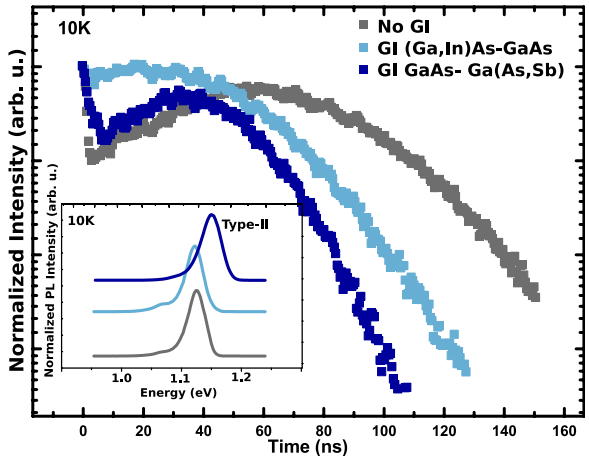

Figure 9. Transients of the type-II PL at 10 K for the sample set **Sb**. The curves are normalized to unity and were taken at the maximum of the type-II peak. The insets shows the normalized cw-PL at 10 K.

The transient reaches a maximum and (iii) declines eventually with a slow decay time. When we apply the model developed in [16] we have to assign the rising part (ii) of our transient to the slow relaxation process. As can be seen in figure 9 the maximum of the transient is reached at about 70 ns for the sample without GI. In case of GI the maximum is reached earlier at about 30 ns. The feeding of the type-II PL is obviously slower without growth interruption. This can be explained in the following way: the slow relaxation, i.e. feeding of type-II PL, is due to hopping but also caused by temporary localization of the carriers at the interface. A decrease of the relaxation time implies a reduction of the number of traps at the interface, which is expected for a smoother interface. It should be mentioned, that the activation energy to release the localized carriers is obviously small, i.e. in the range of a few meV regime. Therefore, the localization does not matter and is not observed at room temperature.

Conclusion

In summary, we could reveal a correlation between the interface morphology and optical and dynamical properties. We were able to show this correlation by means of continuous-wave PL, time-resolved PL and the optical pump–optical probe measurements on (Ga,In)As/GaAs/Ga(As,Sb) and (Ga,In)As/GaAs/Ga(N,As) type-II DWQ heterostructures with or without growth interruptions at the inner barriers. A growth interruption yields a smoother interface with substantially reduced numbers of optical non-radiative loss centers and trap states. As a result we could observe an increased intensity of the type-II PL with growth interruption for both material systems. Furthermore, the TRPL revealed for the sample set **Sb** a slower electron hole recombination time. The OPOP measurements at sample set **N** could show enhanced electron transfer times through the barrier, when the samples were prepared with a growth interruption. This seems to be a very general behavior. Finally, we should mention, that there are still two very different physical reasons for the dynamical changes, namely the reduced transfer and recombination times with increasing IF disorder. One reason is the enhanced quantum-mechanical transition probability through the barrier caused by an increased perturbation. The second reason is the increasing non-radiative recombination which is inevitably connected to the same perturbations. To conclude that findings reported here are of general validity more material systems have to be investigated.

Acknowledgments

We are grateful for financial support by the German Research Foundation (DFG) in the framework of the SFB 1083.

ORCID iDs

Luise Rost https://orcid.org/0000-0002-5188-7751
Pirmin Kükelhan https://orcid.org/0000-0001-5711-228X

References

[1] Andreev A D and O'Reilly E P 2004 *Appl. Phys. Lett.* **84** 1826–8
[2] Zegrya G G and Andreev A D 1995 *Appl. Phys. Lett.* **67** 2681–3
[3] Aydaraliev M, Zotova N V, Karandashov S A, Matveev B A, Stus' N M and Talalakin G N 1993 *Semicond. Sci. Technol.* **8** 1575–80
[4] Meyer J R *et al* 1998 *Appl. Phys. Lett.* **73** 2857
[5] Berger C, Möller C, Hens P, Fuchs C, Stolz W, Koch S W, Ruiz Perez A, Hader J and Moloney J V 2015 *AIP Adv.* **5** 047105
[6] Gies S *et al* 2015 *Appl. Phys. Lett.* **107** 182104
[7] Möller C, Fuchs C, Berger C, Ruiz Perez A, Koch M, Hader J, Moloney J V, Koch S W and Stolz W 2016 *Appl. Phys. Lett.* **108** 071102

[8] Yeh J Y, Mawst L J, Khandekar A A, Kuech T F, Vurgaftman I, Meyer J R and Tansu N 2006 *Appl. Phys. Lett.* **88** 051115
[9] Huang J Y T, Mawst L J, Kuech T F, Song X, Babcock S E, Kim C S, Vurgaftman I, Meyer J R and Holmes A L 2009 *J. Phys. D: Appl. Phys.* **42** 025108
[10] Pan C H and Lee C P 2013 *J. Appl. Phys.* **113** 043112
[11] Kroemer H 2001 *Rev. Mod. Phys.* **73** 783–93
[12] Stein M, Lammers C, Richter P H, Fuchs C, Stolz W, Koch M, Vänskä O, Weseloh M J, Kira M and Koch S W 2018 *Phys. Rev.* B **97** 125306
[13] Caro L D, Giannini C and Tapfer L 1998 *J. Appl. Phys.* **79** 4101
[14] Bernatz G, Nau S, Rettig R, Jänsch H and Stolz W 1999 *J. Appl. Phys.* **86** 6752
[15] Springer P *et al* 2016 *J. Lumin.* **175** 255–9
[16] Gies S, Holz B, Fuchs C, Stolz W and Heimbrodt W 2017 *Nanotechnology* **28** 025701
[17] Shan W, Walukiewicz W, Ager J, Haller E, Geisz J, Friedman D, Olson J and Kurtz S 1999 *Phys. Rev. Lett.* **82** 1221
[18] Grüning H *et al* 2004 *Phys. Status Solidi* c **1** 109–12
[19] Schlichenmaier C *et al* 2005 *Appl. Phys. Lett.* **86** 081903
[20] Gies S, Weseloh M J, Fuchs C, Stolz W, Hader J, Moloney J V, Koch S W and Heimbrodt W 2016 *J. Appl. Phys.* **120** 204303
[21] Peter M, Winkler K, Maier M, Herres N, Wagner J, Fekete D, Bachem K H and Richards D 1995 *Appl. Phys. Lett.* **67** 2639–41
[22] Dinu M, Cunningham J E, Quochi F and Shah J 2003 *J. Appl. Phys.* **94** 1506–12
[23] Nau S 2004 *PhD Thesis* Philipps-Universität Marburg
[24] Gottwaldt L, Pierz K, Ahlers F J, Göbel E O, Nau S, Torunski T and Stolz W 2003 *J. Appl. Phys.* **94** 2464–72
[25] Oelerich J O, Duschek L, Belz J, Beyer A, Baranovskii S D and Volz K 2017 *Ultramicroscopy* **177** 91–6
[26] Kükelhan P, Beyer A, Fuchs C, Weseloh M, Koch S, Stolz W and Volz K 2017 *J. Microsc.* **268** 259–68
[27] Kükelhan P, Beyer A, Fuchs C, Firoozabadi S, Oelerich J, Stolz W and Volz K 2018 *J. Phys.: Condens. Matter* submitted
[28] Leo K, Rühle W W and Haegel N M 1987 *J. Appl. Phys.* **62** 3055–8
[29] Roskos H, Rieck B, Seilmeier A and Kaiser W 1988 *Appl. Phys. Lett.* **53** 2406–8
[30] Meissner K, Fluegel B, Binder R, Koch S W, Khitrova G and Peygambarian N 1991 *Appl. Phys. Lett.* **59** 259–61
[31] Shank C V, Fork R L, Leheny R F and Shah J 1979 *Phys. Rev. Lett.* **42** 112–5
[32] Feldmann J, Sattmann R, Göbel E O, Kuhl J, Hebling J, Ploog K, Muralidharan R, Dawson P and Foxon C T 1989 *Phys. Rev. Lett.* **62** 1892–5
[33] Feldmann J, Nunnenkamp J, Peter G, Göbel E, Kuhl J, Ploog K, Dawson P and Foxon C T 1990 *Phys. Rev.* B **42** 5809–21
[34] Nido M, Alexander M G W, Rühle W W, Schweizer T and Köhler K 1990 *Appl. Phys. Lett.* **56** 355–7
[35] Stein M, Lammers C, Drexler M, Fuchs C, Stolz W and Koch M 2018 *Phys. Rev. Lett.* **121** 017401

3. Room-Temperature Stimulated Emission and Lasing in Recrystallized Cesium Lead Bromide Perovskite Thin Films

N. Pourdavoud, T. Haeger, A. Mayer, P. J. Cegielski, A.-L. Giesecke, R. Heiderhoff, S. Olthof, S. Zaefferer, I. Shutsko, A. Henkel, D. Becker-Koch, **M. Stein**, M. Cehovski, O. Charfi, H.-H. Johannes, D. Rogalla, M. C. Lemme, M. Koch, Y. Vaynzof, K. Meerholz, W. Kowalsky, H.-C. Scheer, P. Görrn, and T. Riedl, Adv. Mater. 31, 1903717 (2019).

Abstract

Cesium lead halide perovskites are of interest for light-emitting diodes and lasers. So far, thin-films of $CsPbX_3$ have typically afforded very low photoluminescence quantum yields (PL-QY $< 20\,\%$) and amplified spontaneous emission (ASE) only at cryogenic temperatures, as defect related nonradiative recombination dominated at room temperature (RT). There is a current belief that, for efficient light emission from lead halide perovskites at RT, the charge carriers/excitons need to be confined on the nanometer scale, like in $CsPbX_3$ nanoparticles (NPs). Here, thin films of cesium lead bromide, which show a high PL-QY of $68\,\%$ and low-threshold ASE at RT, are presented. As-deposited layers are recrystallized by thermal imprint, which results in continuous films ($100\,\%$ coverage of the substrate), composed of large crystals with micrometer lateral extension. Using these layers, the first cesium lead bromide thin-film distributed feedback and vertical cavity surface emitting lasers with ultralow threshold at RT that do not rely on the use of NPs are demonstrated. It is foreseen that these results will have a broader impact beyond perovskite lasers and will advise a revision of the paradigm that efficient light emission from $CsPbX_3$ perovskites can only be achieved with NPs.

DOI: 10.1002/adma.201903717
URL: `https://onlinelibrary.wiley.com/doi/abs/10.1002/adma.201903717`

ADVANCED MATERIALS

www.advmat.de

Room-Temperature Stimulated Emission and Lasing in Recrystallized Cesium Lead Bromide Perovskite Thin Films

*Neda Pourdavoud, Tobias Haeger, Andre Mayer, Piotr Jacek Cegielski, Anna Lena Giesecke, Ralf Heiderhoff, Selina Olthof, Stefan Zaefferer, Ivan Shutsko, Andreas Henkel, David Becker-Koch, Markus Stein, Marko Cehovski, Ouacef Charfi, Hans-Hermann Johannes, Detlef Rogalla, Max Christian Lemme, Martin Koch, Yana Vaynzof, Klaus Meerholz, Wolfgang Kowalsky, Hella-Christin Scheer, Patrick Görrn, and Thomas Riedl**

Cesium lead halide perovskites are of interest for light-emitting diodes and lasers. So far, thin-films of $CsPbX_3$ have typically afforded very low photoluminescence quantum yields (PL-QY < 20%) and amplified spontaneous emission (ASE) only at cryogenic temperatures, as defect related nonradiative recombination dominated at room temperature (RT). There is a current belief that, for efficient light emission from lead halide perovskites at RT, the charge carriers/excitons need to be confined on the nanometer scale, like in $CsPbX_3$ nanoparticles (NPs). Here, thin films of cesium lead bromide, which show a high PL-QY of 68% and low-threshold ASE at RT, are presented. As-deposited layers are recrystallized by thermal imprint, which results in continuous films (100% coverage of the substrate), composed of large crystals with micrometer lateral extension. Using these layers, the first cesium lead bromide thin-film distributed feedback and vertical cavity surface emitting lasers with ultralow threshold at RT that do not rely on the use of NPs are demonstrated. It is foreseen that these results will have a broader impact beyond perovskite lasers and will advise a revision of the paradigm that efficient light emission from $CsPbX_3$ perovskites can only be achieved with NPs.

Metal-halide perovskite semiconductors are of tremendous interest for a variety of applications. Only recently, solar cells based on a representative of this family have been certified with an efficiency in excess of 24%.[1] Aside from their remarkable success in photovoltaics, metal-halide perovskites are also highly promising as light emitters, e.g., in light-emitting diodes (LEDs) or lasers.[2–4] LEDs based on the fruit-fly of these compounds, i.e., methylammonium lead iodide ($CH_3NH_3PbI_3$ or $MAPbI_3$), and other related perovskites have been demonstrated with continuously increasing efficiency.[5–7] For lasers, there is the vision that perovskites may overcome/avoid the typical limitations and loss mechanisms present in organic gain media, such as triplet–singlet annihilation or absorption due to triplet excitons and

N. Pourdavoud, T. Haeger, Dr. R. Heiderhoff, Prof. T. Riedl
Institute of Electronic Devices
University of Wuppertal
Rainer-Gruenter-Str. 21, 42119 Wuppertal, Germany
E-mail: t.riedl@uni-wuppertal.de

Dr. A. Mayer, I. Shutsko, A. Henkel, Prof. H.-C. Scheer, Prof. P. Görrn
Chair of Large Area Optoelectronics
University of Wuppertal
Rainer-Gruenter-Str. 21, 42119 Wuppertal, Germany

P. J. Cegielski, Dr. A. L. Giesecke, Prof. M. C. Lemme
AMO GmbH
Otto-Blumenthal-Straße 25, 52074 Aachen, Germany

P. J. Cegielski, Prof. M. C. Lemme
Elektrotechnik und Informationstechnik
Lehrstuhl für Elektronische Bauelemente
RWTH Aachen University
Otto-Blumenthal-Straße 25, 52074 Aachen, Germany

Dr. S. Olthof, Prof. K. Meerholz
Department of Chemistry
University of Cologne
Luxemburger Straße 116, 50939 Cologne, Germany

The ORCID identification number(s) for the author(s) of this article can be found under https://doi.org/10.1002/adma.201903717.

DOI: 10.1002/adma.201903717

Dr. S. Zaefferer
Max-Planck-Institut für Eisenforschung
Max-Planck-Str. 1, 40237 Düsseldorf, Germany

D. Becker-Koch, Prof. Y. Vaynzof
Kirchhoff-Institut für Physik
Ruprecht-Karls-Universität Heidelberg
Im Neuenheimer Feld 227, 69120 Heidelberg, Germany

D. Becker-Koch, Prof. Y. Vaynzof
Center for Advanced Materials
Ruprecht-Karls-Universität Heidelberg
Im Neuenheimer Feld 225, 69120 Heidelberg, Germany

M. Stein, Prof. M. Koch
Fachbereich Physik
Philipps-Universität Marburg
Renthof 5, 35032 Marburg, Germany

M. Cehovski, O. Charfi, Dr. H.-H. Johannes, Prof. W. Kowalsky
Institut für Hochfrequenztechnik
Technische Universität Braunschweig
Schleinitzstr. 22, 38106 Braunschweig, Germany

M. Cehovski, O. Charfi, Dr. H.-H. Johannes, Prof. W. Kowalsky
Cluster of Excellence PhoenixD (Photonics, Optics, and Engineering – Innovation Across Disciplines)
Welfengarten 1, 30167 Hannover, Germany

Dr. D. Rogalla
RUBION
Ruhr-University Bochum
D-44801 Bochum, Germany

polarons.[8–10] Thus, perovskites currently seed a new promise for the realization of electrically operated laser diodes that can be prepared from solution at low temperatures on virtually any substrate. The marriage of perovskite active materials with silicon (nitride) photonics holds promise to unlock substantial progress in the field of integrated optoelectronics.[11,12] Perovskite lasers also bear the potential to cover the spectral region between 530 and 610 nm, known as the "green-gap,"[13] which is difficult to address at room temperature with established inorganic semiconductor gain media, such as indium-gallium-nitride (InGaN) or aluminum-gallium-indium-phosphide (AlGaInP).

Amplified spontaneous emission (ASE) and optically pumped lasing have been reported for $MAPbI_3$ and other hybrid organic–inorganic lead halide perovskites.[14–19] As a result of the soft nature of this class of materials, photonic resonator structures can be directly patterned into $MAPbX_3$ (X = Br, I) by thermal nanoimprint to achieve low-threshold optically pumped perovskite lasers.[20,21]

Unfortunately, MA-based organic–inorganic halide perovskites lack intrinsic stability.[22,23] For improved thermodynamic stability, the volatile organic moiety can be replaced with inorganic cations, such as Cs.[24,25] The corresponding all-inorganic perovskite semiconductors, i.e., cesium lead halides, have been identified as particularly promising for light-emitting applications.[26]

However, early attempts to use thin-films of $CsPbX_3$ for light emission only led to disappointing results with very low photoluminescence quantum yields (PL-QY) of about 16%.[27] More detrimentally, ASE in $CsPbX_3$ thin-films has only been achieved at cryogenic temperatures below 150 K.[28] The poor performance at higher temperatures has been attributed to nonradiative recombination associated with a high number of defects. It must be noted that the $CsPbBr_3$ thin films used in the above studies showed poor film formation and contained a high number of pinholes. Some attempts to improve on film formation and to mitigate the impact of defects were based on blending the perovskite with additives, such as ZnO nanoparticles[29] or thiocyanate ethyl acetate.[30] However, the luminescence quantum yield could not be increased beyond 20% in these reports. Recently, two-photon pumped ASE has been reported in $CsPbBr_3$ single crystals, albeit at relatively high threshold levels (0.65 mJ cm^{-2}, 35 fs pulse width).[31]

Unlike the case of thin films, $CsPbX_3$ nanoparticles (size < 10 nm) or nanorods showed a high PL-QY and exhibited ASE at room temperature.[32–34] Unfortunately, nanosized grains of lead-halide perovskites have been evidenced to be subject to serious stability issues.[35] Moreover, stabilizing and solubilizing capping ligands are typically required, that not only deteriorate charge transport but may likewise impede thermal transport, which is a particular problem for lasers, especially if electrical and/or continuous wave operation is considered.[36–38] Nevertheless, the impressive results achieved with $CsPbX_3$ nanoparticles nurtured the paradigm that for efficient light emission from lead halide perovskites at room temperature, one needs to confine the charge carriers/excitons on the nanometer scale to prevent their migration to nonradiative defects.[5,39]

Here, we present results that challenge this paradigm. We demonstrate thin films of cesium lead bromide, which show a high photoluminescence quantum yield of 68% and ASE at room temperature with low threshold. The continuous films (≈100% coverage of the substrate) are composed of large crystals with micrometer lateral extension. Our layers result from originally rough as-deposited layers, which were recrystallized by thermal imprint. Using these layers, we demonstrate the first cesium-lead bromide thin-film distributed feedback (DFB) and vertical cavity surface emitting lasers (VCSELs) with ultralow threshold at room temperature, that do not rely on the use of nanoparticles. Our results render this all-inorganic gain medium an excellent material platform for perovskite laser diodes in the future. We also foresee that our results will have a broader impact beyond perovskite lasers and will possibly lead to a revision of the belief that efficient light emission from $CsPbX_3$ perovskites could only be achieved with nanoparticles.

The cesium lead bromide thin films used in this study have been prepared from a solution of cesium bromide (CsBr) and lead bromide ($PbBr_2$) in dimethylsulfoxide (DMSO). The molar ratio of CsBr:$PbBr_2$ was varied between 0.5:1 and 3:1. Initially, a ratio of 1:1 was chosen. The as-deposited layers were recrystallized by a thermal imprint process at 150 °C and a pressure of 100 bar, using a flat piece of silicon wafer as stamp (**Figure 1**a). More details about the film deposition and the thermal imprint process can be found in the Experimental Section.

The as-deposited solution processed cesium lead bromide films are very rough (roughness 23.8 nm, rms) and show a considerable number of pin-hole defects (Figure 1b). The external photoluminescence quantum yield (PL-QY) (η_{ext}) at RT is about 9.3%. This η_{ext} can be translated to an internal PL-QY (η_{int}) of about 43% (see the Supporting Information for details of the determination of η_{int} taking a limited outcoupling probability into account[40]). It is important to note, that with these layers we were not able to achieve amplified spontaneous emission (ASE) at room temperature, even under pulsed excitation at levels of 600 μJ cm^{-2} (λ = 355 nm, pulse duration ≈300 ps), which already marks the onset at which the focused laser beam starts to machine the perovskite thin film. Upon recrystallization by thermal imprint, the layers change strikingly. The layers become very smooth (roughness: 0.5 nm, rms) and are composed of large crystals with micrometer-sized lateral dimensions (Figure 1c). Photographs of pristine and pressed layers (on silicon) clearly demonstrate the mirror-like surface of the pressed layers as opposed to the dull impression of the rough pristine layer. The time resolved analysis of the PL decay dynamics is shown in Figure 1e. The data are fitted by a biexponential decay. For the pristine sample, decay times of τ_1 = 4.1 ns and τ_2 = 10 ns are determined. In the recrystallized layers a notable increase of τ_1 = 5.9 ns and τ_2 = 19 ns is found, which are similar to decay times reported for $CsPbBr_3$ single crystals.[41–43] The PL spectra for pristine and pressed layers are shown in Figure 1f. Most notably, the spectral width (full-width half-maximum) is substantially reduced from $\Delta\lambda$ = 20.1 nm ($\Delta(h\nu)$ = 91 meV) for the pristine layer to 14.5 nm (66 meV) for the pressed layer. Note, while the short-wavelength edge of the PL spectra is very similar, the high-wavelength edge is significantly redshifted in the pristine layers, which indicates recombination via near-band-edge defects.[44] As such, the narrowed PL linewidth supports the conclusion of an overall improved material quality in the pressed layers.

Notably, η_{int} of the recrystallized films increased to 53%. In strong contrast to the pristine layers, the recrystallized

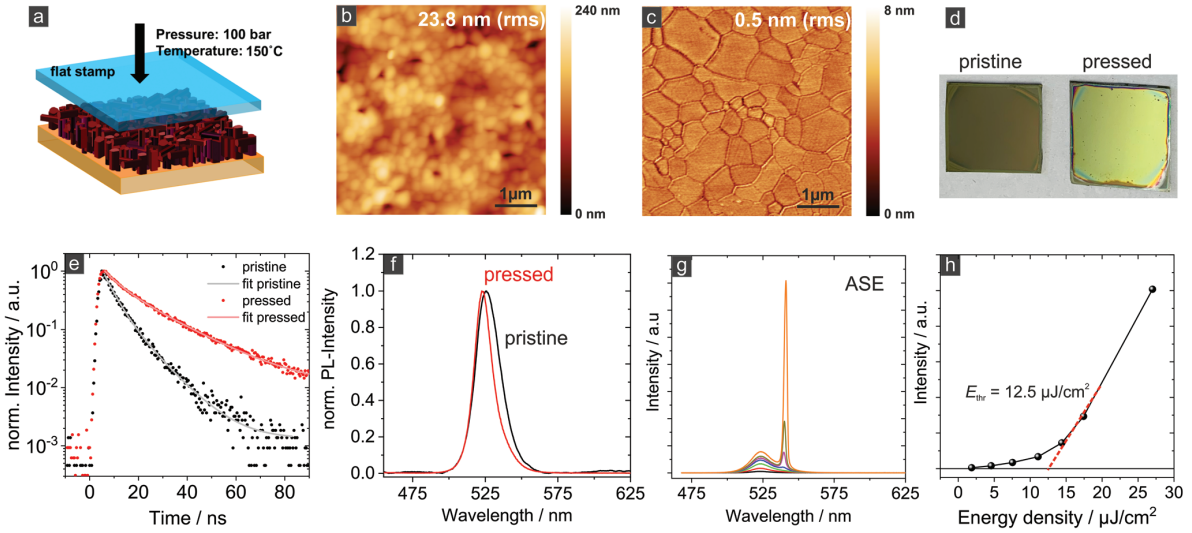

Figure 1. a) Schematic of the thermal imprint process using a flat silicon stamp to recrystallize the as-deposited cesium lead bromide layer. b,c) Atomic force microscopy of layers before (b) and after (c) thermal imprint. The layer thickness is 120 nm. d) Photograph of pristine and pressed layers on silicon substrate. e,f) Time-resolved photoluminescence (PL) decay and PL spectra for pristine (black) and pressed (red) layers at room temperature. Amplified spontaneous emission measurement on a flattened cesium lead bromide thin-film: g) emission spectra and h) corresponding output characteristics.

films show ASE at room temperature (λ_{ASE} = 541 nm, spectral width ≈2.5 nm) under pulsed excitation with a low threshold of 12.5 µJ cm^{-2} (Figure 1g,h).

Taken together, the optical analysis revealed an improved PL-QY and an increased PL lifetime in the recrystallized layers. An increasing grain size in halide perovskite layers has been reported to infer an increased PL lifetime.[45] The finding has been explained by a decreasing radiative rate for larger grains due to the concomitantly decreasing bandgap. Note, we did not observe a similar variation of the bandgap in our films (Figure 1f). On the other hand, de Quilettes et al. provided evidence for the substantial importance of nonradiative recombination at grain boundaries in halide perovskite thin films.[46] The latter result together with the concomitantly observed increase of the PL-QY indicate an effective mitigation of nonradiative recombination in our recrystallized samples, being the key for achieving ASE at room temperature.

To further characterize the structural properties of our samples, we measured the X-ray diffractograms for pristine and pressed layers (**Figure 2**a,b). The pristine sample exclusively shows reflections attributed to the orthorhombic $CsPbBr_3$ phase (ICSD 97851), with a minor peak at 18.62°, which could be due to $PbBr_2$. In striking contrast, the pressed and recrystallized film shows two orders of magnitude more intense peaks, that can be assigned to the tetragonal 2D phase $CsPb_2Br_5$ (i4mcm, JCPDS No. 025–0211, Figure 2b). The dominance of the 002, 004, 006, 008 peaks indicates the high degree of orientation of the crystals, which is also evidenced by electron backscatter diffraction (EBSD) (see Figure S1, Supporting Information). However, it has to be noted that in the pressed layers the reflections due to the 3D $CsPbBr_3$ phase have also gained by a factor of three in intensity compared to the pristine layer (see inset Figure 2b). As such, X-ray diffraction (XRD) provides evidence of substantial recrystallization and an overall improved crystal quality upon thermal imprint. We have also studied the resulting layers by photothermal deflection spectroscopy and THz absorption spectroscopy (Figure S2). The energy gap derived from the absorption spectra is E_g = 2.32 eV (534 nm) for both the pristine and the pressed layer, corresponding to the direct bandgap of $CsPbBr_3$. For $CsPb_2Br_5$ an indirect bandgap of 3 eV or larger has been reported.[47,48] The Urbach energy of the recrystallized layer is 17.4 meV, similar to what has been reported for high-quality $CsPbBr_3$ single crystals[41] and substantially lower than that of the pristine film (20.6 meV), suggesting a lower degree of energetic disorder within the recrystallized films and agrees with the narrowed PL-linewidth (Figure 1f). THz absorption spectroscopy conducted at room temperature revealed sharp absorption peaks in the recrystallized layers at 1.025 THz (34 cm^{-1}), 1.428 THz (47.6 cm^{-1}), and 1.965 THz (65.5 cm^{-1}), whereas the spectrum for the pristine layer only shows less-pronounced features at similar positions. These results are indicative of a substantially reduced number of structural defects in the recrystallized layers.[49] The peak positions agree with the energy of lattice vibrations, reported for single crystals of $CsPbBr_3$ and $CsPb_2Br_5$.[50,51]

Composites of $CsPbBr_3$ and $CsPb_2Br_5$ have recently attracted great attention to improve light emission in nanoparticles and nanoplates.[52,53] The formation of the mixed-phase ($CsPbBr_3$–$CsPb_2Br_5$) perovskite upon annealing $CsPbBr_3$ nanoparticle films has been studied by Manna and co-workers.[54,55] In that report, the pristine layers showed a PL-QY of 19% which decreased to <1% after formation of the mixed $CsPbBr_3$–$CsPb_2Br_5$ phase.

To elucidate the presence of the 2D and 3D phases in our pressed layers, we performed scanning electron microscopy (SEM) and EBSD (Figure 2c,d). Interestingly, the SEM image obtained with backscattered electrons shows a very pronounced contrast of bright and dark crystals, which cannot be explained

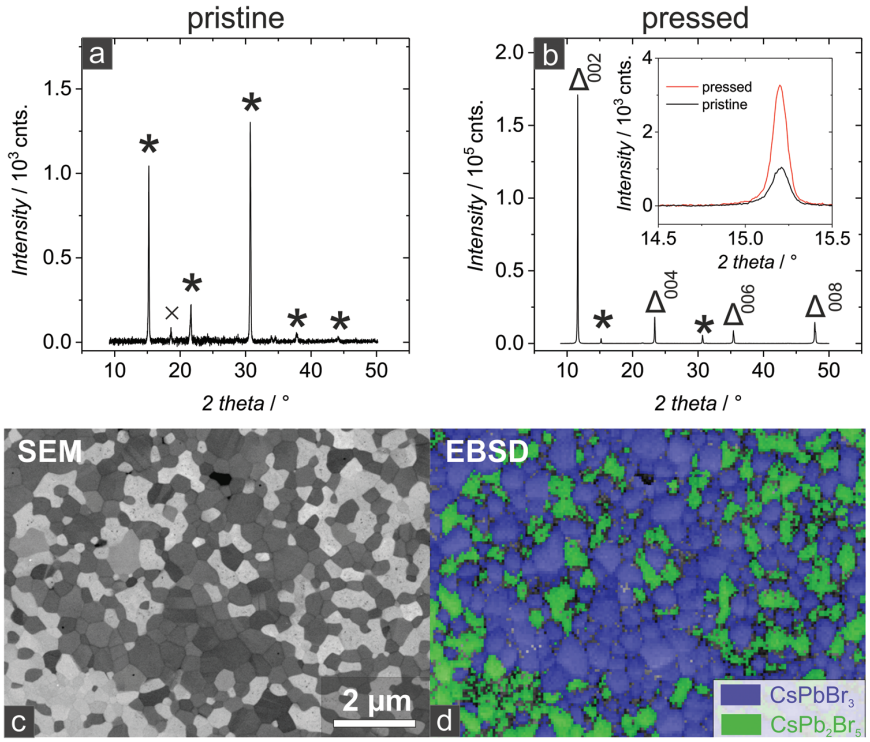

Figure 2. a,b) X-ray diffractograms of pristine (a) and pressed (b) films. The symbols mark diffraction peaks due to $CsPbBr_3$ (*), $CsPb_2Br_5$ (Δ), and $PbBr_2$ (×). Note, the *y*-axis in (b) spans a two orders of magnitude larger scale than that of (a). The inset compares the 110 diffraction peaks of the orthorhombic $CsPbBr_3$ in the pristine and pressed layer. c) Scanning electron microscopy (SEM) image obtained with backscattered electrons, and d) electron backscatter diffraction (EBSD) of a pressed/recrystallized layer. The assignment of the $CsPbBr_3$ and $CsPb_2Br_5$ has been made on the basis of published crystallographic data (see the Experimental Section).

by topography effects. EBSD reveals that the crystals that appear dark in SEM are $CsPbBr_3$ (3D) while those appearing bright are $CsPb_2Br_5$ (2D) (see the Supporting Information). The higher lead content in the 2D phase is expected to cause stronger scattering of electrons, which accounts for the higher brightness in the backscattered SEM image. The pole figures obtained in EBSD for both $CsPbBr_3$ (3D) and $CsPb_2Br_5$ (2D) show a strong 001 orientation, which is particularly pronounced for the 2D phase. (Figure S1, Supporting Information).

Thermal microscopy has shown a similar contrast associated with the 2D and 3D phase in thermal conductivity.[56] The coexistence of the two phases is further supported by optical transmission/PL microscopy (Figure S3, Supporting Information). PL microscopy shows that the light emission results exclusively from the 3D phase while the 2D parts are nonemissive. This is in contrast to earlier reports that claimed that the formation of $CsPb_2Br_5$ inferred a substantial improvement in PL-QY.[57] According to a quantitative analysis of the SEM images using an image processing software, we can determine the relative content of $CsPb_2Br_5$ to be 46% in these samples.

In order to identify whether and to what extent the presence of the nonemissive 2D phase is beneficial for the light emission of the film, i.e., to passivate defects, we aimed to reduce the formation of $CsPb_2Br_5$ by increasing the concentration of CsBr in the precursor solution. Unfortunately, the solubility of CsBr in DMSO is limited and precipitates are forming upon increasing the molar content of CsBr. Rutherford backscattering spectrometry (RBS) shows that precursor solutions with a nominal molar ratio of $CsBr:PbBr_2$ ranging from 0.5:1 to 3:1 afford pristine layers with a substantially lower relative Cs content (**Figure 3**a). For example, for $CsBr:PbBr_2$ = 1:1 in the precursor, we find [Pb]/[Cs] = 1.4 and [Br]/[Pb] = 2.7 in the film. Overall, the [Pb]/[Cs] and [Br]/[Pb] ratio determined by RBS is in favorable agreement with the relative abundance of $CsPb_2Br_5$ and $CsPbBr_3$ identified by the bright and dark regions in the SEM images, respectively (see discussion above). Most notably, a ratio of [Pb]/[Cs] = 1 and [Br]/[Pb] = 3 in the film is found for a nominal ratio of $CsBr:PbBr_2$ = 2.75:1 in the precursor. Indeed, XRD clearly shows a gradual reduction of the abundance of the 2D phase relative to that of the 3D phase in the pressed layers prepared with a $CsBr:PbBr_2$ ratio increased from 1:1 to 2.6:1 (Figure 3b). Finally, for $CsBr:PbBr_2$ = 2.75:1 the signal due to the 2D phase is entirely absent and only intense reflections due to the 3D phase are found. In the SEM image taken from the 2.75:1 sample, no bright/dark contrast as in the mixed phase samples is found (Figure S4). To understand how the presence of the 2D phase affects the ASE threshold we studied the samples under pulsed optical excitation at elevated excitation densities. The corresponding ASE threshold is shown in Figure 3c. Most importantly, the ASE threshold remains constant for a

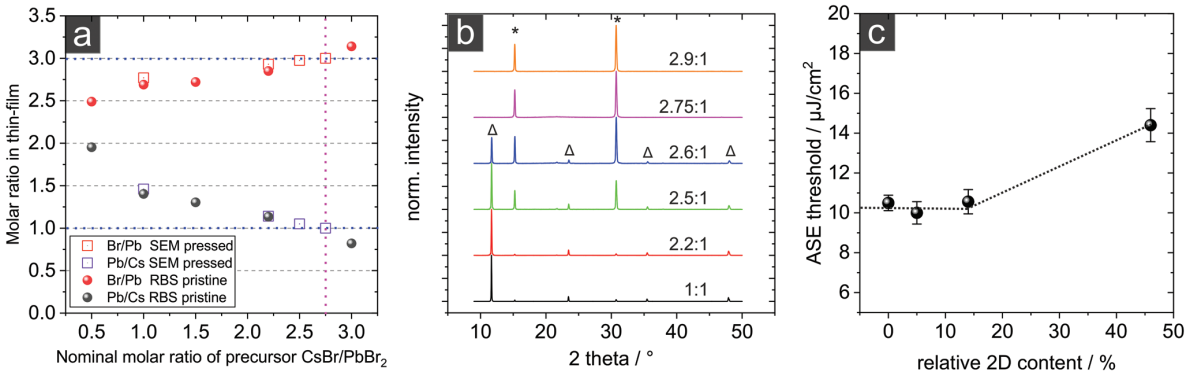

Figure 3. a) Molar ratio Pb/Cs and Br/Pb in the pristine and pressed films versus nominal molar ratio ($CsBr/PbBr_2$) of the precursor. The ratio in the film has been determined by RBS and SEM (see text), respectively. b) X-ray diffractograms of pressed films resulting from a varied $CsBr/PbBr_2$ ratio of the precursor. The symbols mark diffraction peaks due to $CsPbBr_3$ (*), $CsPb_2Br_5$ (Δ). c) ASE threshold of pressed films with varied relative content of 2D phase ($CsPb_2Br_5$).

relative content of 2D phase in the film below 15%. There is a slightly elevated threshold for layers with a higher 2D content of around 50%. This is in part attributed to a strongly reduced amount of active material, as the wide-gap, indirect 2D-phase does not contribute to the ASE. Note, the internal PL-QY for the purely 3D $CsPbBr_3$ thin-film is found to be 68% (see the Supporting Information for details of the determination of the internal PL-QY taking a limited outcoupling probability into account[40]), higher than the 53% we determined for the mixed phase samples (Figure 1f).

Thus, our results clearly demonstrate that the improved optical properties of the layers are not inferred by the formation of 2D $CsPb_2Br_5$, but rather by the overall improved crystal quality due to recrystallization of the $CsPbBr_3$, which mitigates non-radiative recombination. A further important insight results: Efficient light emission in this class of materials is not exclusively linked to nanocrystals, but room-temperature ASE can likewise be provided by thin films, such as our high-quality recrystallized layers.

In the following we utilize the outstanding optical properties of the recrystallized cesium lead bromide in laser structures. First, we consider DFB resonators. To this end, we employ a stamp with a periodic line pattern (3600 lines mm^{-1}, i.e., periodicity: Λ = 278 nm) for the thermal imprint as schematically shown in **Figure 4**a. The stamp is a commercially

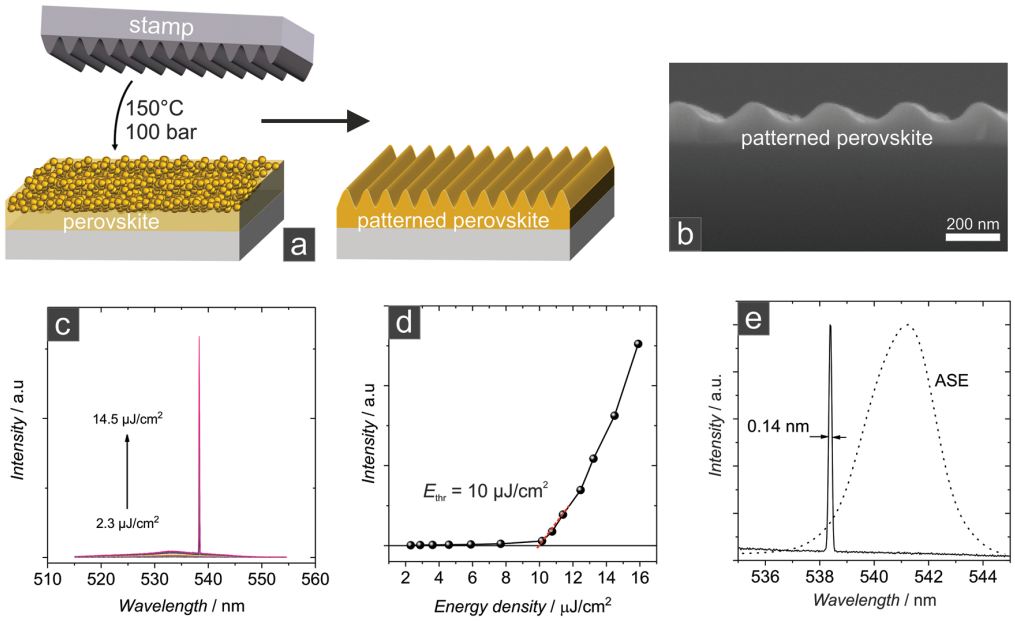

Figure 4. a) Schematic of the direct thermal imprint of a linear grating (periodicity Λ = 278 nm) into the perovskite layer. Glass is used as a substrate. b) SEM image of the cross-section of the patterned perovskite layer. c) Optical emission spectra and d) output intensity upon increasing the pumping energy density. e) High-resolution spectrum of the DFB laser emission line. The ASE spectrum of a flattened layer is shown for comparison (see also Figure 1g).

available diffraction grating (ThorLabs, GH25-36U). The as-casted perovskite layers (on glass substrates) are directly patterned by thermal imprint resulting in a perovskite layer with a sinusoidal grating structure as shown in the SEM image of the cross-section (Figure 4b). Upon pulsed optical pumping, laser emission is found at $\lambda_L = 538.32$ nm above a threshold of 10 μJ cm^{-2} (Figure 4c).

The laser emission is detected perpendicular to the sample surface and the emission spectrum shows a full width at half maximum of 0.14 nm, significantly narrower than the ASE spectrum. The emission wavelength can be understood in the framework of a second order DFB laser, where the Bragg condition is given by $\lambda_L = n_{eff} \times \Lambda$. Accordingly, n_{eff} denoting the effective refractive index of the laser mode is $n_{eff} = 1.938$.

In contrast to the direct patterning of the perovskite layer, we can also use a prepatterned substrate to form a DFB perovskite laser (**Figure 5**). Specifically, glass substrates are coated with a polymer resin (Ormocore, micro resist technology GmbH), which is optically highly transparent and can be patterned by thermal imprint. For the patterning of the Ormocore layer, we again use the diffraction grating as stamp. The perovskite layer is coated on top of these prepatterned substrates and is subsequently recrystallized and flattened by thermal imprint using a flat silicon stamp (Figure 5a). The SEM cross-section image shows the perfect filling of the grooves of the substrate with the perovskite and the flat surface of the perovskite layer. Upon pulsed optical pumping, lasing can be achieved with a likewise low threshold of 7.2 μJ cm^{-2} (at $\lambda = 539.1$ nm) and narrow linewidth (Figure 5b–d). The inset in Figure 5d shows the dual lobed far-field emission spectrum above threshold, which is characteristic for DFB lasers with predominant complex coupling.[58] As verified in Figure 5e the emission is characterized by a typical strong linear polarization.

Aside from DFB resonators, VCSELs are very attractive for a number of applications, due to their circular beam profile and potentially small footprint. The only all-inorganic perovskite VCSELs reported so far were based on $CsPbBr_3$ nanocrystals as gain medium.[59,60] Here, we employ recrystallized thin films instead to achieve ultralow threshold levels. Specifically, we utilize commercially available dielectric flat mirrors (ThorLabs, FD1M) with transmission characteristics as shown in Figure S5. Importantly, these mirrors show a reflection of up to 99.79% in the spectral region of 530–570 nm. The VCSEL layout in this study is schematically shown in **Figure 6**a.

Briefly, we use one of the dielectric mirrors as a substrate onto which a cesium lead bromide layer is coated. An identical mirror is then used as a stamp for the thermal imprint/recrystallization

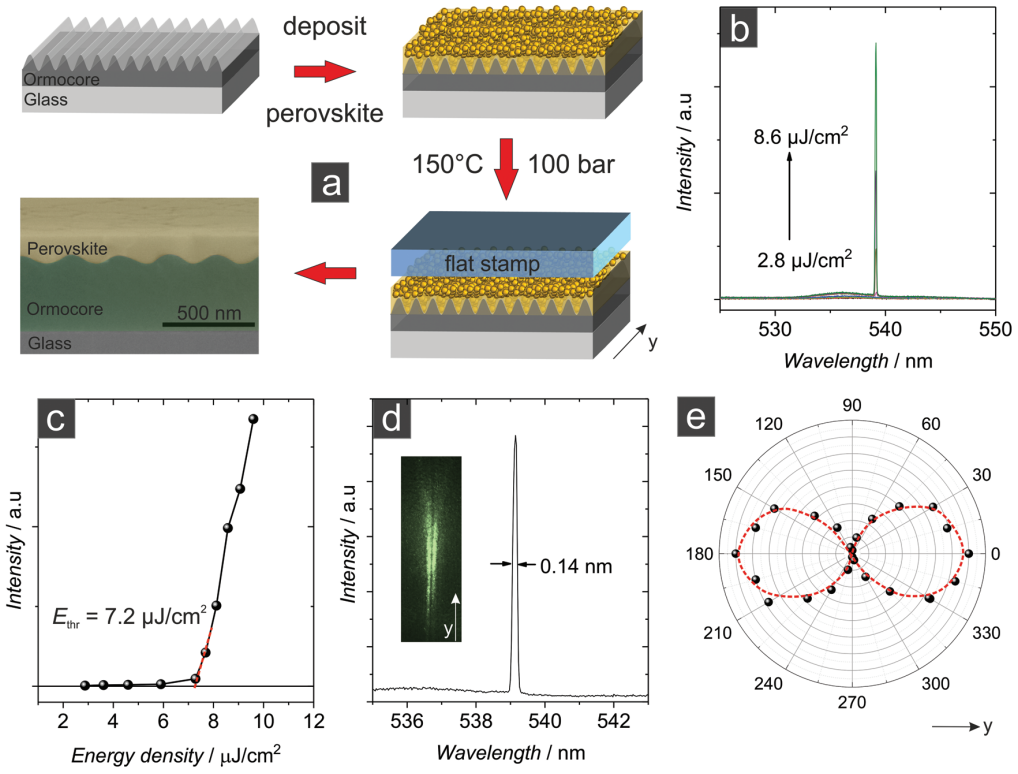

Figure 5. a) Schematic of preparing perovskite DFB laser on a prepatterned carrier. b) Optical emission spectra and c) output intensity upon increasing the pumping energy density. d) High-resolution spectrum of the laser emission line (inset: photograph of the far-field emission profile). e) Polarization characteristics of the second order DFB laser emission. The results shown in this figure and in Figure 4 represent the first all-inorganic $CsPbBr_3$ thin-film distributed feedback lasers. Their low-threshold operation at room temperature is made possible by the recrystallization by thermal imprint.

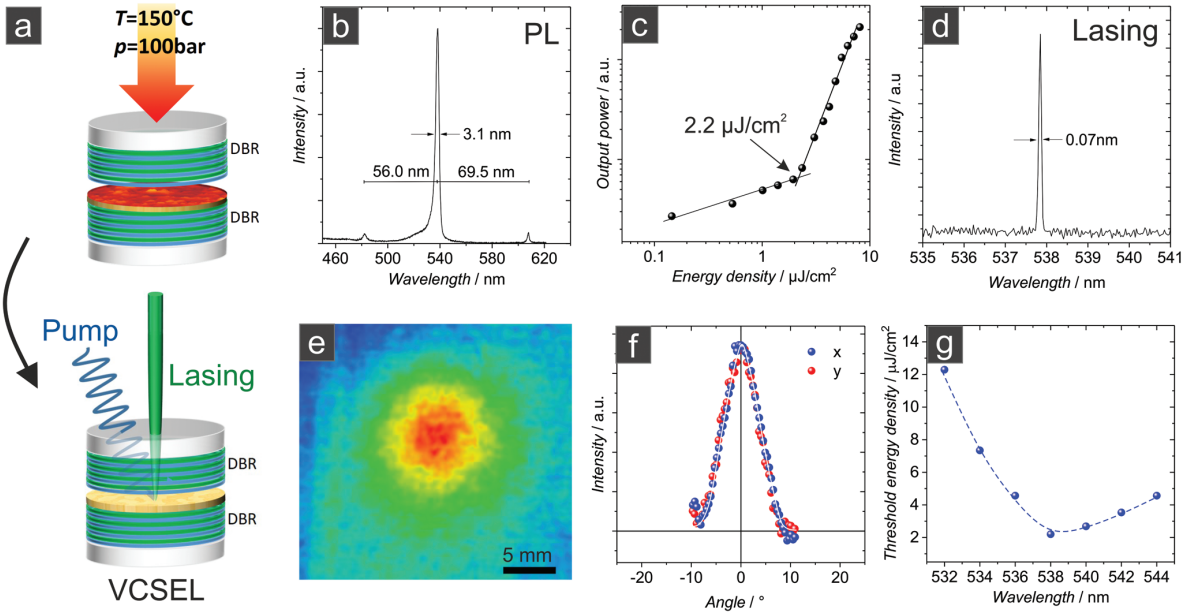

Figure 6. a) Schematic of VCSEL setup. b) Cavity mode spectrum below threshold. c) Output power versus pump energy density. d) Emission spectrum and e,f) far-field beam characteristics of the VCSEL above threshold. The laser beam has been directed on a sandblasted glass screen that had been positioned in a distance of 3 cm from the VCSEL surface. g) Laser threshold energy density in dependence on the emission wavelength.

process (150 °C, 100 bar). Afterward, the stamp is left attached on top of the recrystallized perovskite layer, and the entire assembly forms the VCSEL. Below threshold the luminescence spectrum is characterized by marked resonator modes (Figure 6b). The respective spacing ($\Delta\lambda$) of these modes allows us to derive the effective cavity length $L_{\text{eff}} = \lambda^2/(2 \times \Delta\lambda)$ ≈2.3 µm. Note, the perovskite layer is about 110 nm thick. Upon pulsed excitation, the VCSEL shows lasing with a threshold of 2.2 µJ cm^{-2}.

Note, for VCSELs based on $CsPbBr_3$ nanocrystals as gain media a threshold of 0.39 µJ cm^{-2} has been reported by Huang et al., albeit upon pumping with fs-pulses.[59] When the authors used ns-pulses instead, they observed an increase of the threshold by more than two orders of magnitude to 98 µJ cm^{-2}. This striking phenomenon was attributed to an increased thermal load under ns-excitation because the thermally insulating shell of the ligands attached to the nanocrystals prevented efficient thermal transport. At the same time, the authors found a decay time of ≈10 ps for stimulated emission, which could likewise account for the marked increase of threshold upon ns-pumping. A similar increase of the ASE threshold from 5.3 to 450 µJ cm^{-2} has been found by Yakunin et al. when going from fs- to ns-excitation.[32] The authors explained their finding with the duration of the pump pulse either being substantially shorter or longer compared with the ASE decay time of ≈100 ps of the gain medium. Compared to the fs-data in these reports, our $CsPbBr_3$ thin-film VCSELs were pumped with relatively "long" pulses of 300 ps. As such, the low threshold level of 2.2 µJ cm^{-2} for our lasers is therefore even more notable and points to the excellent material quality of the gain medium. The VCSEL emission spectrum is very narrow ($\Delta\lambda$ = 0.7 Å, limit of the spectral resolution of the spectrometer) and the emitted beam shows circular symmetry (Figure 6 e,f). Thanks to a slight (unintentional) variation of the perovskite layer thickness, which leads to some tuning of the resonator length, we were able to likewise tune the laser emission spectrum between λ = 532–544 nm (Figure 6 g). Note, the reflectance of the DBR mirrors remains essentially unchanged in this region, which is why we can attribute the variation in the threshold energy density to correspond to the spectral shape of the gain spectrum of the active medium.

In summary we have shown highly efficient photoluminescence (PL-QY = 68%), amplified spontaneous emission, and low-threshold lasing in thin-films of cesium lead bromide at room temperature for the first time. Importantly, our layers are not based on nanocrystals or quantum dots but consist of extended continuous layers, which formed upon recrystallization of as-deposited layers by thermal imprint (100 bar, 150 °C). We were able to prepare phase pure 3D $CsPbBr_3$ films, and we provided evidence, that the presence of the 2D $CsPb_2Br_5$ phase is not required to render these layers excellent light emitters and active gain media. Building on these recrystallized layers, we demonstrated the first cesium lead bromide thin-film DFB and VCSELs with ultralow threshold (2.2 µJ cm^{-2}, 300 ps pump pulses) at room temperature, that do not rely on the use of nanoparticles. Our results render cesium lead bromide thin-films an excellent material platform for perovskite laser diodes in the future. We also expect that our results will impact perovskite device research beyond lasers and should lead to the revision of the paradigm that efficient room-temperature light emission from $CsPbX_3$ perovskites could only be achieved with nanoparticles.

Experimental Section

Cesium Lead Bromide Layer Preparation: Lead bromide (purity 99.999%, ultradry) (Alfa Aesar) and cesium bromide (99.999%, trace metal basis) (Sigma-Aldrich) were dissolved in anhydrous DMSO with molar ratio of CsBr to $PbBr_2$ varied between 0.5:1 and 3:1 (stirred and heated over night at 60 °C in a nitrogen-filled glovebox). The solution was filtered using a 0.2 µm filter before use.

Borofloat glass substrates were used for the lasers and silicon wafers for SEM, EBSD, and RBS characterization. For PL-QY measurements silicon wafers with 1.5 µm of thermal oxide on top were used. For PDS and THz spectroscopy, quartz substrates were used. All substrates were cleaned by sonication in citric acid, deionized water, and isopropanol (each step 15 min). After drying, the substrates were transferred to a nitrogen-filled glovebox. The perovskite layers were prepared by spin-coating the precursor solution at 4000 rpm, 120 s, and 11 s ramp. After spin-coating, the films were annealed on hotplate at 100 °C for 20 min.

Thermal Nanoimprint and Hot Pressing: Thermal nanoimprint and planar hot pressing experiments were performed in a parallel plate-based imprint system.[61] During heat-up of the system to the processing temperature of 150 °C, which, in this case, took about 20 min, the pressure of 100 bar was applied. When the imprint temperature was reached, the pressure was kept constant for 5 min. Afterward the system was cooled down and the pressure was released slowly as soon as the temperature was below 30 °C. The stamp used for nanoimprint is a commercial diffraction grating (3600 lines mm^{-1}, i.e., periodicity: $\Lambda = 278$ nm, ThorLabs, GH25-36U) and provided with an antisticking layer.[62,63] For the prepatterned gratings Ormostamp (microresist, Berlin) was patterned. For planar hot pressing the stamp was unpatterned silicon, again provided with an antisticking layer. The procedure for planar hot pressing was similar to the imprint procedure; the prepressure used was 100 bar and the pressing time was increased to 30 min. The laser devices were based on the films resulting from a nominal 1:1 molar ratio of CsBr to $PbBr_2$.

Characterization of Materials: XRD was measured using a Panalytical Empyrean system with a Cu Kα anode ($\lambda = 1.54056$ Å). For XRD, layers on glass substrates were used. For the SEM studies layers on Si substrates were investigated using a Philips XL30S FEG microscope with a field emission cathode. AFM measurements were conducted with a Bruker Innova system in tapping mode (tip: RTESPA-300; tip radius: <12 nm).

The microstructure of the material was further studied using EBSD mapping. No specific sample preparation was applied. A Bruker nanosystem with an X-flash EBSD camera, installed on a Zeiss Merlin SEM, was used for the measurements. The measurements were done at 30 kV acceleration voltage and 2 nA beam current. The patterns were binned to 160 × 120 pixel size and exposed for 30 ms, resulting in a measurement rate of 33 frames per second. The analysis of the measured maps was carried out using the EDAX/TSL software OIM DC. Further details can be found in the Supporting Information.

Absorption spectra were measured by photothermal deflection spectroscopy (PDS). The samples were submerged in an inert liquid (Fluorinert FC-770), which acts as deflecting medium for a probing laser beam (REO R-31008) of 633 nm wavelength and passes parallel to the samples surface. Its deflection, measured by a position sensitive detector (Thorlabs PDP90A) amplified by a lock-in amplifier (Ametec 7230), was directly linked to the absorption of the sample, and caused by the heat created from the absorbed pumping light in the sample. The chopped excitation light was provided by a Xenon arc lamp (Ushio 150W with Abet housing) and a subsequent monochromator.

RBS was performed at the 4 MV tandem accelerator of the RUBION facility (University of Bochum, Germany). A 2 MeV $^4He^+$ ion beam (beam current of 20–40 nA) in combination with a silicon surface barrier detector at an angle of 160° was used.

For photoluminescence (PL) measurements, a laser diode ($\lambda = 450$ nm, power density 0.2 W cm^{-2}) was used. The PL spectra were dispersed in a monochromator (Princeton Instruments, Acton SP2500, gratings: 300 and 1200 lines mm^{-1}) and detected by a thermoelectrically cooled charge coupled device camera (Princeton Instruments).

External PL-QY was measured using a focused continuous wave laser beam (RLDE405M-50-5, Roithner-Lasertechnik, wavelength: 405 nm, power density: 15 W cm^{-2}). As substrates for the perovskite layers Si wafers covered with 1.5 µm thermal SiO_2 were used. The sample was attached to one of the ports of an integrating sphere (RTC-060-SF, Labsphere). The excitation signal was blocked from entering the detector by a filter (03FCG065, Melles Griot) and the PL signal was detected with a power meter (PM100USB, Thorlabs).

The time-resolved PL measurements were done using a Streak camera (Hamamatsu Streak scope C4334). The samples were optically pumped with a Nd:YVO laser (3rd harmonic, wavelength: 355 nm, pulse width: 700 ps, repetition rate: 1 kHz, energy density: 1.5 µJ cm^{-2}). An optical fiber attached to the Streak camera and a lens system collected part of the emitted light from the samples.

The THz absorption spectroscopy was conducted using the output of a 1 kHz titanium-sapphire-based regenerative amplifier system with 35 fs pulses spectrally centered at 800 nm. The output of the amplifier was split into two parts. One part drove a low-temperature grown large aperture Galliumarsenide antenna, which emitted spectrally broad THz pulses ranging from 0.2 to 3 THz. The THz radiation was focused onto the sample by a pair of parabolic mirrors. The transmitted THz pulse was detected phase-sensitive via electro-optical sampling in an 800 µm thick Zinctelluride crystal by the other part of the amplifier output and autobalanced photodiodes. The beam path of the THz radiation was purged with nitrogen gas to avoid water vapor absorption. Two measurements were performed, one with the pure quartz substrate as the sample ($E_0(t)$) and one with the quartz substrate spin-coated by the perovskite layers ($E_p(t)$). Fourier transformation converted the THz pulses into the frequency domain where the absorption can be calculated using: $\alpha \sim \ln\left(\frac{|E_0(\omega)|^2}{|E_p(\omega)|^2}\right)$.

Optical constants were determined by spectroscopic ellipsometry at 75.48° angle (J.A. Wollam M-2000F).

Characterization of Laser Devices: The perovskite laser samples were optically pumped by a frequency-tripled diode-pumped solid-state laser (PowerChip NanoLaser, TEEM Photonics, France) with $\lambda = 355$ nm, a pulse duration of ≈0.3 ns, and a repetition rate of 1 kHz. The excitation spot had an area of 0.45 mm^2. The excitation density was varied by a neutral density filter wheel. The power of the pump laser was measured with a thermal sensor head (S470C, ThorLabs).

The far field emission characteristics of the DFB laser and VCSEL were recorded by using a sand-blasted glass screen positioned at a distance of about 2–3 cm from the sample surface and a Si CMOS camera (DCC1545M, ThorLabs) with a 25 mm fixed focal length objective.

Supporting Information

Supporting Information is available from the Wiley Online Library or from the author.

Acknowledgements

The authors acknowledge the German Federal Ministry for Education and Research (Grant No. 13N13819) and the DFG (Deutsche Forschungsgemeinschaft) (Grant No. RI1551/9-1) for financial support. This project received funding from the European Research Council (ERC) under the European Union's Horizon 2020 research and innovation programme (Grant Agreement No. 637367). Collaborations of the involved institutions were also funded by the Deutsche Forschungsgemeinschaft (DFG, German Research Foundation) under Germany's Excellence Strategy within the Cluster of Excellence PhoenixD (EXC 2122, Project ID 390833453). Y.V. and D.B.-K. thank the DFG for funding (SFB 1249, Project C04). K.M. and S.O. acknowledge funding within the PeroBOOSt project (EFRE). The authors acknowledge Dr. Stephan Suckow (AMO GmbH) for fruitful discussions and his support.

Conflict of Interest

The authors declare no conflict of interest.

Keywords

cesium lead halide perovskite, distributed feedback lasers, perovskite vertical cavity surface emitting lasers, recrystallization, thermal imprint, thin films

Received: June 11, 2019
Revised: July 15, 2019
Published online: August 12, 2019

[1] *Best Research-Cell Efficiency Chart*, https://www.nrel.gov/pv/assets/pdfs/best-research-cell-efficiencies.20190703.pdf (accessed: July 2019).
[2] B. R. Sutherland, E. H. Sargent, *Nat. Photonics* **2016**, *10*, 295.
[3] S. D. Stranks, H. J. Snaith, *Nat. Nanotechnol.* **2015**, *10*, 391.
[4] S. Adjokatse, H.-H. Fang, M. A. Loi, *Mater. Today* **2017**, *20*, 413.
[5] H. Cho, S.-H. Jeong, M.-H. Park, Y.-H. Kim, C. Wolf, C.-L. Lee, J. H. Heo, A. Sadhanala, N. Myoung, S. Yoo, S. H. Im, R. H. Friend, T.-W. Lee, *Science* **2015**, *350*, 1222.
[6] W. Xu, Q. Hu, S. Bai, C. Bao, Y. Miao, Z. Yuan, T. Borzda, A. J. Barker, E. Tyukalova, Z. Hu, M. Kawecki, H. Wang, Z. Yan, X. Liu, X. Shi, K. Uvdal, M. Fahlman, W. Zhang, M. Duchamp, J.-M. Liu, A. Petrozza, J. Wang, L.-M. Liu, W. Huang, F. Gao, *Nat. Photonics* **2019**, *13*, 418.
[7] K. Lin, J. Xing, L. N. Quan, F. P. G. de Arquer, X. Gong, J. Lu, L. Xie, W. Zhao, D. Zhang, C. Yan, W. Li, X. Liu, Y. Lu, J. Kirman, E. H. Sargent, Q. Xiong, Z. Wei, *Nature* **2018**, *562*, 245.
[8] M. Lehnhardt, T. Riedl, T. Weimann, W. Kowalsky, *Phys. Rev. B* **2010**, *81*, 165206.
[9] T. Rabe, P. Görrn, M. Lehnhardt, M. Tilgner, T. Riedl, W. Kowalsky, *Phys. Rev. Lett.* **2009**, *102*, 137401.
[10] M. Lehnhardt, T. Riedl, U. Scherf, T. Rabe, W. Kowalsky, *Org. Electron.* **2011**, *12*, 1346.
[11] P. J. Cegielski, S. Neutzner, C. Porschatis, H. Lerch, J. Bolten, S. Suckow, A. R. S. Kandada, B. Chmielak, A. Petrozza, T. Wahlbrink, A. L. Giesecke, *Opt. Express* **2017**, *25*, 13199.
[12] P. J. Cegielski, A. L. Giesecke, S. Neutzner, C. Porschatis, M. Gandini, D. Schall, C. A. R. Perini, J. Bolten, S. Suckow, S. Kataria, B. Chmielak, T. Wahlbrink, A. Petrozza, M. C. Lemme, *Nano Lett.* **2018**, *18*, 6915.
[13] T. Langer, A. Kruse, F. A. Ketzer, A. Schwiegel, L. Hoffmann, H. Jönen, H. Bremers, U. Rossow, A. Hangleiter, *Phys. Status Solidi C* **2011**, *8*, 2170.
[14] G. Xing, N. Mathews, S. S. Lim, N. Yantara, X. Liu, D. Sabba, M. Grätzel, S. Mhaisalkar, T. C. Sum, *Nat. Mater.* **2014**, *13*, 476.
[15] F. Deschler, M. Price, S. Pathak, L. E. Klintberg, D.-D. Jarausch, R. Higler, S. Hüttner, T. Leijtens, S. D. Stranks, H. J. Snaith, M. Atatüre, R. T. Phillips, R. H. Friend, *J. Phys. Chem. Lett.* **2014**, *5*, 1421.
[16] B. R. Sutherland, S. Hoogland, M. M. Adachi, C. T. O. Wong, E. H. Sargent, *ACS Nano* **2014**, *8*, 10947.
[17] S. Chen, K. Roh, J. Lee, W. K. Chong, Y. Lu, N. Mathews, T. C. Sum, A. Nurmikko, *ACS Nano* **2016**, *10*, 3959.
[18] Y. Jia, R. A. Kerner, A. J. Grede, A. N. Brigeman, B. P. Rand, N. C. Giebink, *Nano Lett.* **2016**, *16*, 4624.
[19] S. Chen, A. Nurmikko, *ACS Photonics* **2017**, *4*, 2486.
[20] N. Pourdavoud, S. Wang, A. Mayer, T. Hu, Y. Chen, A. Marianovich, W. Kowalsky, R. Heiderhoff, H.-C. Scheer, T. Riedl, *Adv. Mater.* **2017**, *29*, 1605003.
[21] N. Pourdavoud, A. Mayer, M. Buchmüller, K. Brinkmann, T. Häger, T. Hu, R. Heiderhoff, I. Shutsko, P. Görrn, Y. Chen, H.-C. Scheer, T. Riedl, *Adv. Mater. Technol.* **2018**, *3*, 1700253.
[22] B. Conings, J. Drijkoningen, N. Gauquelin, A. Babayigit, J. D'Haen, L. D'Olieslaeger, A. Ethirajan, J. Verbeeck, J. Manca, E. Mosconi, F. D. Angelis, H.-G. Boyen, *Adv. Energy Mater.* **2015**, *5*, 1500477.
[23] E. J. Juarez-Perez, Z. Hawash, S. R. Raga, L. K. Ono, Y. Qi, *Energy Environ. Sci.* **2016**, *9*, 3406.
[24] M. Kulbak, S. Gupta, N. Kedem, I. Levine, T. Bendikov, G. Hodes, D. Cahen, *J. Phys. Chem. Lett.* **2016**, *7*, 167.
[25] A. F. Akbulatov, S. Y. Luchkin, L. A. Frolova, N. N. Dremova, K. L. Gerasimov, I. S. Zhidkov, D. V. Anokhin, E. Z. Kurmaev, K. J. Stevenson, P. A. Troshin, *J. Phys. Chem. Lett.* **2017**, *8*, 1211.
[26] S. A. Veldhuis, P. P. Boix, N. Yantara, M. Li, T. C. Sum, N. Mathews, S. G. Mhaisalkar, *Adv. Mater.* **2016**, *28*, 6804.
[27] N. Yantara, S. Bhaumik, F. Yan, D. Sabba, H. A. Dewi, N. Mathews, P. P. Boix, H. V. Demir, S. Mhaisalkar, *J. Phys. Chem. Lett.* **2015**, *6*, 4360.
[28] M. L. De Giorgi, A. Perulli, N. Yantara, P. P. Boix, M. Anni, *J. Phys. Chem. C* **2017**, *121*, 14772.
[29] C. Li, Z. Zang, C. Han, Z. Hu, X. Tang, J. Du, Y. Leng, K. Sun, *Nano Energy* **2017**, *40*, 195.
[30] X. Zhang, Z. Jin, J. Zhang, D. Bai, H. Bian, K. Wang, J. Sun, Q. Wang, S. F. Liu, *ACS Appl. Mater. Interfaces* **2018**, *10*, 7145.
[31] C. Zhao, W. Tian, J. Liu, Q. Sun, J. Luo, H. Yuan, B. Gai, J. Tang, J. Guo, S. Jin, *J. Phys. Chem. Lett.* **2019**, *10*, 2357.
[32] S. Yakunin, L. Protesescu, F. Krieg, M. I. Bodnarchuk, G. Nedelcu, M. Humer, G. De Luca, M. Fiebig, W. Heiss, M. V. Kovalenko, *Nat. Commun.* **2015**, *6*, 8056.
[33] S. Kondo, K. Takahashi, T. Nakanish, T. Saito, H. Asada, H. Nakagawa, *Curr. Appl. Phys.* **2007**, *7*, 1.
[34] Y. Fu, H. Zhu, C. C. Stoumpos, Q. Ding, J. Wang, M. G. Kanatzidis, X. Zhu, S. Jin, *ACS Nano* **2016**, *10*, 7963.
[35] Q. Sun, P. Fassl, D. Becker-Koch, A. Bausch, B. Rivkin, S. Bai, P. E. Hopkinson, H. J. Snaith, Y. Vaynzof, *Adv. Energy Mater.* **2017**, *7*, 1700977.
[36] H. Huang, M. I. Bodnarchuk, S. V. Kershaw, M. V. Kovalenko, A. L. Rogach, *ACS Energy Lett.* **2017**, *2*, 2071.
[37] M. Cadelano, V. Sarritzu, N. Sestu, D. Marongiu, F. Chen, R. Piras, R. Corpino, C. M. Carbonaro, F. Quochi, M. Saba, A. Mura, G. Bongiovanni, *Adv. Opt. Mater.* **2015**, *3*, 1557.
[38] Y. Jia, R. A. Kerner, A. J. Grede, A. N. Brigeman, B. P. Rand, N. C. Giebink, *Nano Lett.* **2016**, *16*, 4624.
[39] Z. Xiao, R. A. Kerner, L. Zhao, N. L. Tran, K. M. Lee, T.-W. Koh, G. D. Scholes, B. P. Rand, *Nat. Photonics* **2017**, *11*, 108.
[40] J. M. Richter, M. Abdi-Jalebi, A. Sadhanala, M. Tabachnyk, J. P. H. Rivett, L. M. Pazos-Outón, K. C. Gödel, M. Price, F. Deschler, R. H. Friend, *Nat. Commun.* **2016**, *7*, 13941.
[41] Y. Rakita, N. Kedem, S. Gupta, A. Sadhanala, V. Kalchenko, M. L. Böhm, M. Kulbak, R. H. Friend, D. Cahen, G. Hodes, *Cryst. Growth Des.* **2016**, *16*, 5717.
[42] J. Song, Q. Cui, J. Li, J. Xu, Y. Wang, L. Xu, J. Xue, Y. Dong, T. Tian, H. Sun, H. Zeng, *Adv. Opt. Mater.* **2017**, *5*, 1700157.
[43] X. Li, Y. Wu, S. Zhang, B. Cai, Y. Gu, J. Song, H. Zeng, *Adv. Funct. Mater.* **2016**, *26*, 2435.
[44] J. I. Pankove, *Optical Processes in Semiconductors*, Dover, Mineola, NY, USA **1975**.
[45] V. D'Innocenzo, A. R. Srimath Kandada, M. De Bastiani, M. Gandini, A. Petrozza, *J. Am. Chem. Soc.* **2014**, *136*, 17730.
[46] D. W. de Quilettes, S. M. Vorpahl, S. D. Stranks, H. Nagaoka, G. E. Eperon, M. E. Ziffer, H. J. Snaith, D. S. Ginger, *Science* **2015**, *348*, 683.
[47] I. Dursun, M. De Bastiani, B. Turedi, B. Alamer, A. Shkurenko, J. Yin, A. M. El-Zohry, I. Gereige, A. AlSaggaf, O. F. Mohammed, M. Eddaoudi, O. M. Bakr, *ChemSusChem* **2017**, *10*, 3746.

[48] G. Li, H. Wang, Z. Zhu, Y. Chang, T. Zhang, Z. Song, Y. Jiang, *Chem. Commun.* **2016**, *52*, 11296.
[49] J. Wang, E. Motaharifar, L. N. S. Murthy, M. Higgins, D. Barrera, T. B. Daunis, Y. Zheng, A. V. Malko, F. Ely, M. Quevedo-Lopez, M. Lee, J. W. P. Hsu, *J. Appl. Phys.* **2019**, *125*, 025706.
[50] H. Shi, X. Zhang, X. Sun, X. Zhang, *Nanoscale* **2018**, *10*, 9892.
[51] O. Yaffe, Y. Guo, L. Z. Tan, D. A. Egger, T. Hull, C. C. Stoumpos, F. Zheng, T. F. Heinz, L. Kronik, M. G. Kanatzidis, J. S. Owen, A. M. Rappe, M. A. Pimenta, L. E. Brus, *Phys. Rev. Lett.* **2017**, *118*, 136001.
[52] X. Tang, Z. Hu, W. Yuan, W. Hu, H. Shao, D. Han, J. Zheng, J. Hao, Z. Zang, J. Du, Y. Leng, L. Fang, M. Zhou, *Adv. Opt. Mater.* **2017**, *5*, 1600788.
[53] X. Zhang, B. Xu, J. Zhang, Y. Gao, Y. Zheng, K. Wang, X. W. Sun, *Adv. Funct. Mater.* **2016**, *26*, 4595.
[54] F. Palazon, S. Dogan, S. Marras, F. Locardi, I. Nelli, P. Rastogi, M. Ferretti, M. Prato, R. Krahne, L. Manna, *J. Phys. Chem. C* **2017**, *121*, 11956.
[55] F. Palazon, F. Di Stasio, S. Lauciello, R. Krahne, M. Prato, L. Manna, *J. Mater. Chem. C* **2016**, *4*, 9179.
[56] T. Haeger, M. Wilmes, R. Heiderhoff, T. Riedl, *J. Phys. Chem. Lett.* **2019**, *10*, 3019.
[57] B. Turedi, K. J. Lee, I. Dursun, B. Alamer, Z. Wu, E. Alarousu, O. F. Mohammed, N. Cho, O. M. Bakr, *J. Phys. Chem. C* **2018**, *122*, 14128.
[58] M. Kasraian, D. Botez, *Appl. Phys. Lett.* **1995**, *67*, 2783.
[59] C.-Y. Huang, C. Zou, C. Mao, K. L. Corp, Y.-C. Yao, Y.-J. Lee, C. W. Schlenker, A. K. Y. Jen, L. Y. Lin, *ACS Photonics* **2017**, *4*, 2281.
[60] Y. Wang, X. Li, V. Nalla, H. Zeng, H. Sun, *Adv. Funct. Mater.* **2017**, *27*, 1605088.
[61] A. Mayer, S. Moellenbeck, K. Dhima, S. Wang, H.-C. Scheer, *J. Vac. Sci. Technol., B: Nanotechnol. Microelectron.: Mater., Process., Meas., Phenom.* **2011**, *29*, 06FC13.
[62] C. Steinberg, K. Dhima, D. Blenskens, A. Mayer, S. Wang, M. Papenheim, H.-C. Scheer, J. Zajadacz, K. Zimmer, *Microelectron. Eng.* **2014**, *123*, 4.
[63] M. Papenheim, C. Steinberg, K. Dhima, S. Wang, H.-C. Scheer, *J. Vac. Sci. Technol., B: Nanotechnol. Microelectron.: Mater., Process., Meas., Phenom.* **2015**, *33*, 06F601.

Danksagung

An dieser Stelle möchte ich die Gelegenheit nutzen, um mich bei all denen zu bedanken, die mich in meiner Promotionszeit unterstützt und begleitet haben.
Bei Prof. Dr. Martin Koch möchte ich mich nicht nur für die Aufnahme in die Arbeitsgruppe und die Möglichkeit bedanken, hier meine Dissertation anzufertigen, sondern vor allem auch für das mir entgegengebrachte Vertrauen. Das Vertrauen, das es mir ermöglichte eigene Ideen zu verfolgen, das Vertrauen, dass die nächsten 100 Liter Helium dafür gebraucht und nicht verschwendet werden und das Vertrauen, jederzeit kommen und gehen zu können ohne sich je dafür rechtfertigen zu müssen. Ich weiß, dass das alles andere als selbstverständlich ist und bin sehr dankbar dafür.
Bei Prof. Dr. Stephan W. Koch möchte ich mich sowohl für die Erstellung des Zweitgutachtens bedanken, als auch dafür, dass er immer ein offenes Ohr für unsere experimentellen Ergebnisse hatte und zusammen mit Prof. Dr. Mackillo Kira nicht zögerte, diese in ihrer Arbeitsgruppe theoretisch modellieren oder einzelne Aspekte durch Rechnungen überprüfen zu lassen. Diesbezüglich gilt mein Dank insbesondere auch Dr. Christian Berger, Dr. Philip Springer, Maria Weseloh, Dr. Osmo Vänskä und Dr. Hanno Steiner, die während meiner Promotionszeit alle mindestens einmal experimentelle Daten von uns theoretisch modellieren durften oder mussten. Hier gilt mein Dank nicht nur den durchgeführten theoretischen Rechnungen, sondern auch den damit verbundenen Diskussionen, die mein bescheidenes Verständnis der Theorie erweitert haben und oft genug auch Inspiration für neue Experimente im Labor waren.
Ganz besonders hervorheben möchte ich an dieser Stelle Dr. Osmo Vänskä, der zusätzlich zu den stundenlangen Diskussionen über Charge-Transfer Exzitonen auch nach seiner Zeit in Marburg noch seine Freizeit opferte, um mir in seitenlangen Mails und mit einer Engelsgeduld auch noch die Fragen zu beantworten, die sich erst bei der Erstellung der theoretischen Grundlagen dieser Arbeit ergeben haben. Herzlichen Dank dafür, Osmo.
Des Weiteren gilt mein Dank Prof. Dr. Martin R. Hofmann und Prof. Dr. Wolfgang Stolz für die Mitarbeit in meiner Prüfungskommission sowie Prof. Dr. Peter Lenz für die Übernahme des Vorsitzes meiner Prüfungskommission.
Prof. Dr. Wolfgang Stolz und Dr. Christian Fuchs danke ich außerdem für die Erstellung der zahlreichen Proben, ohne die viele experimentelle Untersuchungen in dieser Arbeit gar nicht möglich gewesen wären.
Schließlich möchte ich noch meinen Kollegen und Mitarbeitern aus der Arbeitsgruppe von Prof. Martin Koch danken.
Mein ganz besonderer Dank gilt hier meinen Kameraden Dr. Christian Lammers und Philipp Richter aus dem VLab-Team. Es war mir eine Freude und Ehre sich mit euch die Nächte im Labor um die Ohren zu schlagen und ich würde jederzeit wieder eine Nacht opfern, um mit euch beiden auf Exzitonenjagd zu gehen.
Außerdem möchte ich mich bei allen Studenten bedanken, die während meiner Pro-

motionszeit im VLab-Team waren, uns unterstützt haben und maßgeblich zu dieser tollen Arbeitsatmosphäre beigetragen haben an die ich mich immer gerne zurückerinnern werde. Hier sind zu nennen Melanie Fey, Ebru Kartal, Leonie Gomell und allen voran mein ehemaliger Student Felix Schäfer, der rund um die Uhr zur Verfügung stand, um meine Probleme zu lösen. Danke.